BRUNEL UNIVERSITY LONDON

COLLEGE OF ENGINEERING, DESIGN AND PHYSICAL SCIENCES

DEPARTMENT OF MECHANICAL AND AEROSPACE ENGINEERING

**PhD**

**SELAMAWIT GETACHEW ABATE**

# DESIGNING AN OPTIMISED HINGED MAGNETIC FLUX LEAKAGE (MFL) SYSTEM FOR REMOTE LOCALISED DEFECT MONITORING IN TANK FLOORS AND PIPELINES

This thesis is submitted in partial fulfilment of the requirements for the degree of *Doctor of Philosophy*



July 2025

This page intentionally left blank

COLLEGE OF ENGINEERING, DESIGN AND PHYSICAL SCIENCES

DEPARTMENT OF MECHANICAL AND AEROSPACE ENGINEERING

PhD

Academic Year 2021 - 2025

**SELAMAWIT GETACHEW ABATE**

# DESIGNING AN OPTIMISED HINGED MAGNETIC FLUX LEAKAGE (MFL) SYSTEM FOR REMOTE LOCALISED DEFECT MONITORING IN TANK FLOORS AND PIPELINES

This thesis is submitted in partial fulfilment of the requirements for the degree of *Doctor of Philosophy*

# ABSTRACT

A significant demand exists for magnetic flux leakage (MFL) systems designed for permanent installation in difficult-to-access areas, such as pipe elbows, where localised corrosion occurrences are prevalent. These systems enable continuous and long-term remote monitoring. Designing a magnetic circuit is a critical stage in MFL development, ensuring that induced magnetisation intensity and uniform flux distribution are maintained to facilitate effective defect detection. This work aims to develop a novel optimal-performance and compact MFL system that can be used to inspect a wide range of inspection components, such as flat plates and pipes, including pipe elbows.

This research was based on a simulation-led design of an MFL circuit using finite element analysis (FEA) and optimisation algorithms, and an experimental programme to verify and validate the developed designs. Analyses and optimisation of the magnetic circuit were performed by parametric study of a reference configuration, followed by optimisation of multiple magnetic circuit parameters, resulting in the identification of alternative solutions.

Three magnetic circuit types were developed: a reference (Ref) circuit with improved design parameters, a novel hinged (Hin) based circuit and a novel optimised (Opt) circuit. Using a comprehensive simulation program, the MFL reference configuration underwent a detailed parametric study based on sensitivity analysis of the circuit components. This led to an improved Ref circuit, considering the specified sample magnetisation level, recommended operation points on the **B-H** curve, and improved uniformity of magnetic flux density within the sample. The next step in the design process was the development of a new magnetic circuit with a hinged magnet bridge, which allowed for improved MFL application on non-flat inspection surfaces, e.g. pipes and elbows. Out of the four hinged configurations, the most suitable was adopted for further parameter and topology optimisations using Bound Optimisation by Quadratic Approximation (BOBYQA) and Method of Moving Asymptotes (MMA) algorithms.

The simulation-based design was validated experimentally for all three (Ref, Hin and Opt) circuits by characterising machined cylindrical imperfections on three object shapes: flat plates, pipe and pipe elbow. The Opt circuit demonstrated the best performance, is more compact and can be used for a range of inspection object shapes, including plates, pipes and elbows. The discrepancy between experimental and simulation results was below 2% for all tests. The

sensitivity analysis of the novel devices was performed for defects of different depths, radii, locations and sensor lift-offs.

# DECLARATION

I hereby declare that the work presented in this thesis has not been submitted for any other degree or professional qualification and is the result of my own independent work.

**Selamawit Getachew Abate**

Brunel University London, Uxbridge, 2025

# ACKNOWLEDGEMENTS

First and foremost, I would like to thank my Lord and Saviour, Jesus Christ, for His unfailing love, abundant grace, guidance, countless blessings and provision throughout this journey. He has strengthened me during challenges, providing clarity, comfort and peace. I am forever grateful, and to Him be all the glory and praise.

I would like to express my deep and sincere gratitude to my academic supervisors, Dr Nenad Djordjevic and Prof Rade Vignjevic, and industrial supervisor, Dr Owen Rees-Lloyd, for their invaluable guidance and support throughout the PhD journey. It was a great privilege and honour to work under your supervision.

I would like to extend my deepest gratitude to my family and friends, especially my parents and siblings for their love, prayers, encouragement, sacrifices, support and understanding throughout this journey. You have been my inspiration and a true blessing. Thank you for believing in my potential and empowering your daughter/sister through education, especially my Dad (Abiye).

This work was made possible by the sponsorship and support of Lloyd's Register Foundation and Brunel University London. The work was enabled through, and undertaken at, the National Structural Integrity Research Centre (NSIRC), a postgraduate engineering facility for industry-led research into structural integrity established and managed by TWI through a network of both national and international Universities. Lloyd's Register Foundation helps to protect life and property by supporting engineering-related education, public engagement and the application of research.

# DEDICATION

I dedicate this work to my Dad, Getachew, Mom, Amarech and siblings: Fikirte, Kibrlab, Tihitina, Yosef, Esrael and Aysanew. I am eternally grateful for everything you have done.

# LIST OF PUBLICATIONS/PRESENTATIONS

Getachew Abate, S., Djordjevic, N., Vignjevic, R., & Rees Lloyd, O. ‘‘Magnetic-Based Approach for Characterization of Pipelines Corrosion’’, National Structural Integrity Research Centre, NSIRC Research and Innovation Conference proceedings/presentation, Cambridge, UK, 21st -22nd July 2022.

Getachew Abate, S., Djordjevic, N., Vignjevic, R., & Rees Lloyd, O. ‘‘Sensitivity Analysis of Magnetic Circuit Components of Magnetic Flux Leakage Device for Appropriate Magnetisation’’, NSIRC Research and Innovation Conference proceedings/presentation, Cambridge, UK, 14th -15th June 2023.

# TABLE OF CONTENTS

# LIST OF FIGURES

# LIST OF TABLES

# LIST OF ABBREVIATIONS

| | |
|---|---|
| AC | Alternating Current |
| API | American petroleum Institute |
| AISI | American Iron and Steel Institute |
| ANSI | American National Standards Institute |
| ASME | American Society of Mechanical Engineers |
| ASTM | American Society for Testing and Materials |
| BOBQA | Bound Optimisation by Quadratic Approximation |
| BS EN | British Standard European Norm |
| COBYLA | Constrained Optimisation by Linear Approximations |
| DAS | Data Acquisition System |
| DC | Direct Current |
| DPP | Distance between Peak to Peak |
| EGIG | European Gas Pipeline Incident Data Group |
| EMAT | Electromagnetic Acoustic Transducer |
| EMF | Electromotive Force |
| FE | Finite Element |
| FEA | Finite Element Analysis |
| FEM | Finite Element Modelling |
| FMS | Ferromagnetic Support |
| GDP | Gross Domestic Product |
| GM | Gaussmeter |
| Hin | Hinged |
| ILI | In-line Inspection |
| LPT | Liquid Penetrant Testing |

| | |
|---|---|
| MAGMA | Magnetic Materials and Application |
| MCE | Magnetic Compression Effect |
| MFL | Magnetic Flux Leakage Testing |
| MFNC | Magnetic Fields, No Currents |
| MMA | Method of Moving Asymptotes |
| MMF | Magnetomotive Force |
| NDE | Non-destructive Evaluation |
| NDE | Non-destructive Examination |
| NDI | Non-destructive Inspection |
| NDT | Non-destructive Testing |
| NDT & E | Non-destructive Testing and Evaluation |
| NFMS | Non-Ferromagnetic Support |
| NSIRC | National Structural Integrity Research Centre |
| Opt | Optimised |
| PC | Pulsed Current |
| PDF | Partial Differential Equation |
| PHMSA | Pipeline and Hazardous Materials Safety Administration |
| PIG | Pipeline Inspection Gauge |
| PLA | Polylactic Acid |
| P-P | Peak to Peak |
| Ref | Reference |
| RBI | Risk-Based Inspection |
| SHM | Structural Health Monitoring |
| SIMP | Solid Isotropic Material with Penalisation |
| SNOPT | Sparse Nonlinear Optimiser |
| SNR | Signal-to-Noise Ratio |

| | |
|---|---|
| TWI | The Welding Institute |
| WA | Wavelet Analysis |

# LIST OF SYMBOLS

| | |
|---|---|
| A | Area |
| $\mathbf{B}_r$ | Remnant flux density |
| $\mathbf{B}_s$ | Saturation magnetisation |
| **B** | Magnetic flux density |
| $\mathbf{B}_g$ | Average gap magnetic flux density |
| $\mathbf{B}_x$ | Magnetic flux density component in x-direction |
| $\mathbf{B}_y$ | Magnetic flux density component in y-direction |
| $\mathbf{B}_z$ | Magnetic flux density component in z-direction |
| C | Capacitor |
| **D** | Electric flux density or electric displacement |
| d | Distance between two poles |
| **E** | Electric field intensity |
| F | Magnetomotive force |
| G | Vector-valued function (scalar-valued in case of a single constraint) |
| **H** | Magnetic field strength |
| I | Current |
| **J** | Current density |
| k | Proportionality constant |
| L | Length of magnetic path |
| lb | Lower bound |
| **M** | Magnetisation |
| $\mathbf{M_s}$ | Saturation magnetisation |
| NdFeB | Neodymium iron boron or neodymium magnet |
| $P_1, P_2$ | Poles |

| | |
|---|---|
| $Q$ | Scalar-valued objective function |
| $P$ | Permeance |
| $P^{SIMP}$ | Solid Isotropic Material with Penalisation exponent |
| $R$ | Reluctance or magnetic resistance |
| $R$ | Resistor |
| $S_m$ | Area of the magnet |
| $SmCo$ | Samarium cobalt magnet |
| $ub$ | ub upper bound |
| $V$ | Voltage |
| $V_m$ | Magnetic scalar potential |
| $\chi_m$ | Magnetic susceptibility |
| $\xi$ | Vector of control variables |
| $\mu$ | Permeability of the material |
| $\mu_i$ | Initial permeability |
| $\mu_o$ | Permeability of free space |
| $\mu_r$ | Relative permeability |
| $\phi$ | Magnetic flux |
| $\phi_{\mathbf{B}}$ | Magnetic Flux |
| $\theta$ | Theta (Angle) |
| $\theta_{min}$ | Minimum penalised volume fraction |
| $\rho$ | Electric charge density |

# 1. INTRODUCTION

## 1.1. Motivation and Industrial Context

Oil and gas account for a significant portion of the global total energy supply, contributing over 50% of the world's primary energy consumption [1], [2]. Therefore, transportation of oil and gas is vital to the energy sector and the economy of the country. Pipelines and storage tanks are critical components of oil and gas industries used to transport and store oil and gas. Pipelines are the safest, energy-efficient, eco-friendly and economical way to transport oil and gas over long distances, either within the geographical boundary of a country or beyond it [3]. Steel pipelines and storage tanks are widely used as a long-distance transportation and storage means to transport and store oil and gas due to their excellent mechanical and thermal properties and low cost. However, since most pipelines and storage tanks are buried underground, exposed to harsh external environments and carry substances that can facilitate corrosion, they are prone to corrosion [4] [5]. Corrosion is the process of metal deterioration due to environmental reactions and dissolution [6], [7]. It is one of the leading causes of pipeline failures reported by the European Gas Pipeline Incident Data Group (EGIG) between 2010 and 2019 [8], as illustrated in Figure 1.1.

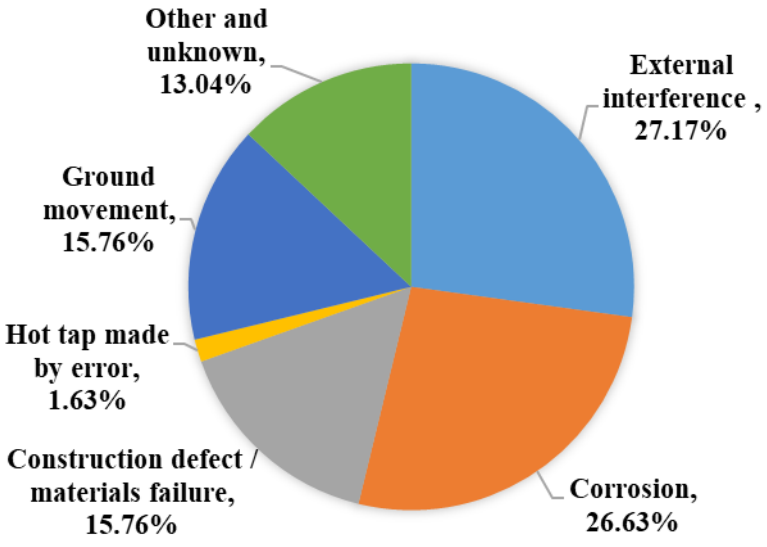


**Figure 1.1.** Incident distribution per cause in gas pipelines during the period 2010 to 2019 reported by the European Gas Pipeline Incident Data Group (EGIG) [8].

There are two broad categories of corrosion: general/uniform corrosion and localised corrosion [9]. General corrosion occurs equivalently throughout the exposed surface, whereas localised

corrosion occurs due to an intense attack at localised sites. The most commonly occurring localised corrosion types in oil and gas industries are pitting, flow-accelerated corrosion and erosion-corrosion [10], [11], [12], [13], [14], [15]. Figure 1.2 shows Pitting, erosion-corrosion and flow-accelerated corrosion [7], [16], [17].

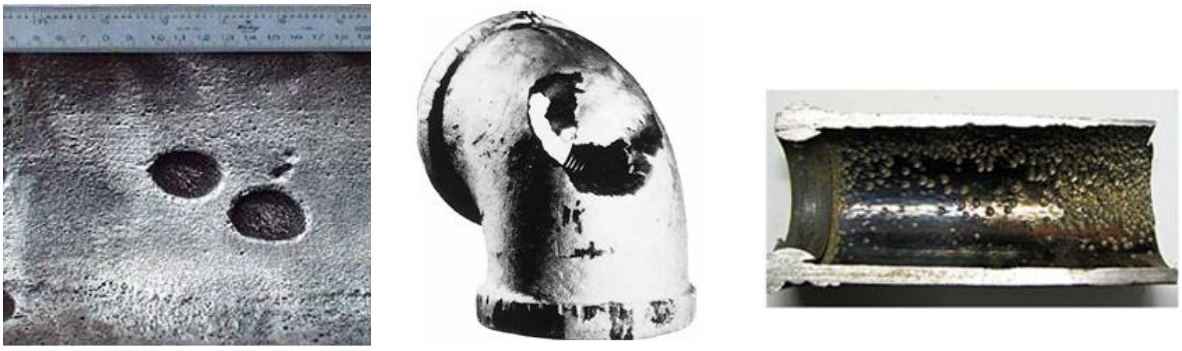

(a) (b) (c)

**Figure 1.2.** (a) Pitting corrosion shows deep, localised pits on a metal surface that can lead to significant material loss over time [16], (b) erosion-corrosion on a pipe elbow damage concentrated in areas experiencing high fluid velocity, leading to material loss and surface degradation [7], and (c) flow-accelerated corrosion inside a pipe exhibiting uneven thinning due to fast-flowing water removing the oxide layer [17].

Pitting occurs due to the deterioration of the protective oxide layer, initiated by physical damage in the presence of aggressive anions [18]. Erosion-corrosion involves the combined effect of mechanical erosion due to fluid flow and impingement of particles, along with electrochemical corrosion processes that remove the protective film and base metal [19] [20]. It commonly occurs at bends, where the fluid changes its direction and fluid velocity is high. Figure 1.3 shows measurements of wall thickness loss per year (in mm/year) taken at various ultrasonic transducer locations, highlighting where the most significant erosion occurred, which is 14.7 mm/year or $3.93 \times 10^{-4}$ mm/kg at the pipe elbow bend (marked in yellow and circled in red dots) [21]. Erosion-corrosion has been known for an extended period as a potential source of problems in oil and gas production systems [22]. The combined effects of erosion and corrosion lead to severe pits in the underlying material [19]. Flow-accelerated corrosion occurs when the fast-flowing fluid dissolves the protective oxide layer on a metallic surface [23] [24].

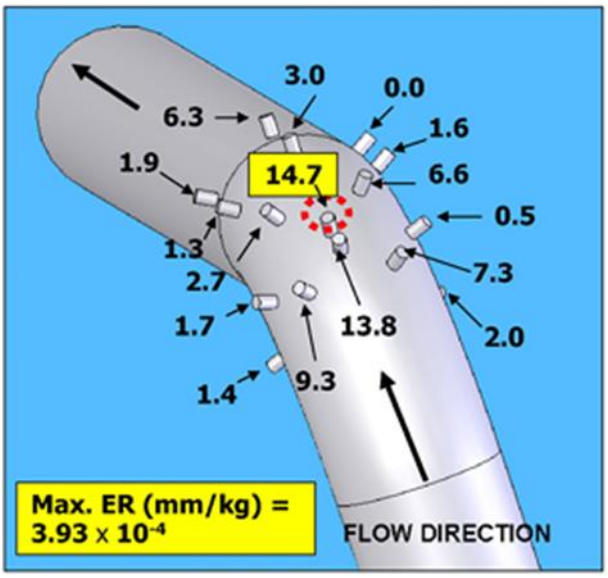


**Figure 1.3.** Specific erosion rates were measured at each transducer location, highlighting the maximum erosion rate measured at a pipe elbow bend, circled with red dots. The maximum erosion rate is 14.7 mm/year or $3.93 \times 10^{-4}$ mm/kg (highlighted in yellow) [21].

Corrosion can cause catastrophic pipeline failure, resulting in fires, explosions, environmental pollution and human losses [25] [26], [27]. The global cost of corrosion is roughly US $2.5 trillion, equivalent to 3.4% of the global gross domestic product (GDP) [28]. The most severe liquefied petroleum gas accident in history occurred in San Juanico, Mexico, due to pitting corrosion, resulting in a series of chain-reaction explosions that injured 64000 people and killed 650 [29], [18].

Conoco Humber refinery failure in the United Kingdom is one of the major engineering failures due to erosion-corrosion. It resulted from thinning of a 7.11 mm thick pipe elbow to 0.3 mm and finally bursting catastrophically. Figure 1.4 shows the failed pipe elbow and the extent of the pipe elbow wall thinning. The resulting fire and explosions affected infrastructure, individuals, the surrounding community and the environment [30]. Figure 1.5 shows a large fire and explosion resulting from the ruptured pipe elbow, which released a large cloud containing 90% ethane, propane and butane, subsequently igniting the gas cloud [31]. Although the pipe had been inspected periodically in accordance with API code requirements, there was a lack of risk-based inspection for the elbow [30].

**Figure 1.4.** Failed pipe elbow at Conoco Humber refinery in the United Kingdom due to erosion corrosion [30].

**Figure 1.5.** A significant fire and explosion resulting from the rupture of the pipe elbow [31].

A number of structural health monitoring (SHM) and non-destructive testing and evaluation (NDT & E) techniques have been developed to inspect integrity of the pipelines and reduce the occurrence of catastrophic corrosion failures. One of them is magnetic flux leakage (MFL). MFL is an efficient, low-cost, easy-to-implement inspection technique for detecting internal and external defects compared to other NDT techniques [25], [32]. It does not require couplants and surface preparation and is suitable for automated inspection without manual intervention [33], [34], making it ideal for continuous monitoring.

According to ASME B31.8S and API 570, the maximum integrity assessment interval for pipelines is between five and ten years based on the operating and predicted failure pressures

[35], [36]. Periodic inspections are crucial for ensuring safety and integrity of pipeline systems. However, there are corrosion-susceptible areas, such as pipe elbows, where the corrosion rate is higher [37], [38]. Current inspection practices often rely on general intervals rather than focusing specifically on vulnerable components. API 580 suggests risk-based inspection (RBI) for high-risk or corrosion-susceptible areas based on the operating conditions and specific needs and circumstances [39].

As the oil and gas industry continues to push for improved safety, reliability and cost-effectiveness, developing new and optimised magnetic circuit designs for MFL systems for continuous and long-term corrosion monitoring has become increasingly important. For this reason, a novel magnetic flux leakage (MFL) system needs to be developed for continuous and long-term remote monitoring in corrosion-susceptible, hazardous and difficult-to-access areas such as pipe elbows, critical areas of pipes and tank floors. These areas are where localised corrosion is frequent, the inspection cost is high, and conventional wall thickness inspections, such as pipeline inspection gauges (PIG) and other scanning devices, inspection cycles are not sufficient and convenient.

## 1.2. Research Aims and Objectives

The main aim of this study is to develop a novel optimal-performance and compact MFL system that can be permanently installed for continuous and long-term remote monitoring in corrosion-prone, hazardous and difficult-to-access areas, such as pipe elbows, high-risk areas of pipes and tank floors. Optimising the design of an MFL circuit is essential for adequate magnetisation level and uniform flux distribution, which are required for efficient defect detection and characterisation.

Objectives of this work are presented below:

- Starting from parametric and sensitivity analysis of an existing/initial MFL circuit configuration, designing a reference (Ref) circuit with improved design parameters. This is based on the specified requirements for sample magnetisation, recommended operation points on the **B-H** curve and improved magnetic field uniformity within the sample.
- Developing a novel hinged (Hin) circuit design to improve the MFL circuit performance and minimise the field dispersion when inspecting flat and non-flat surfaces.

- Using different optimisation algorithms, design an optimised (Opt) circuit with required performance, and reduced fringing effect, unintended leakage field and weight and the ability to inspect flat and curved surfaces.
- Validation of numerical results experimentally for all three circuits on a flat plate, pipe and pipe elbow using machined cylindrical defects of known dimensions.
- Sensitivity analysis of the novel devices to machined cylindrical defects of different depths (0%, 20%, 40%, 60% and 80% of the wall thickness loss), radii (2 mm, 5 mm, 8 mm, and 11 mm), locations (near and far surface) and sensor lift-offs (0.5 mm, 1 mm, 2 mm, 3 mm, 4 mm and 5 mm) by measuring magnetic flux leakage signals.

The methodology proposed in this work consists of a simulation-led design based on finite element analysis (FEA) using COMSOL Multiphysics software with optimisation algorithms. The simulation-led design allows for a large number of iterations through design solutions at no/minimum cost; however, it requires experimental validation. Therefore, an experimental programme is developed to verify and validate simulation results and accurately detect and characterise defects.

## 1.3. Contribution to Knowledge

For integrity assessment in the oil and gas industry, previous studies have explored various non-destructive testing techniques and MFL for in-line and periodic inspections. However, none have focused extensively on the design optimisation of MFL systems for permanent installation and continuous long-term remote monitoring in corrosion-susceptible areas of pipelines and tank floors. Moreover, the impact of pipe and pipe elbow curvatures on MFL inspections has not been thoroughly studied. Therefore, this research addresses the gap by developing a novel optimised MFL system for corrosion monitoring on flat and curved surfaces. It starts with sensitivity analysis to improve a reference circuit, introduces hinges, which allows for improved circuit application on flat and non-flat inspection surfaces, and optimises using different algorithms.

A summary of the contribution to knowledge of this work is presented below:

- Develop an improved Ref circuit by analysing circuit parameters and considering magnetisation level and uniform flux distribution in the inspection component.
- Introduce a novel Hin circuit to minimise the field dispersion when inspecting flat and non-flat surfaces.

- Design a novel, optimised, permanently installable MFL system with the best performance, and reduced fringing effect, unintended leakage field, weight and size using different algorithms to monitor corrosion-susceptible areas of flat and curved surfaces.
- Provide new insights into magnetic field distribution behaviour in flat and curved surfaces.
- Demonstrate that circuit design and inspection component geometry affect the magnetisation level and, therefore, MFL inspection accuracy, which has not been investigated before.
- Validate the novel designs experimentally on flat and non-flat inspection surfaces by introducing a machined cylindrical defect.
- Conduct a comprehensive sensitivity analysis of the novel MFL designs for different defect depths, radii, locations and sensor lift-offs experimentally.
- Novel contribution to industry is providing a novel MFL system that enables efficient, continuous and long-term remote monitoring of defects in difficult-to-access, hazardous and corrosion-prone areas.

## 1.4. Thesis Structure

The thesis comprises six chapters, and its structure is described as follows:

- Chapter 1 outlines the motivation and industrial context, research aims and objectives, contribution to knowledge and thesis structure.
- Chapter 2 presents a background relevant to this research, pipeline and storage tank failure mechanisms, the resulting accidents and their impacts. It gives an overview of the most commonly used NDT techniques, focusing more on MFL. It discusses the characteristics of ferromagnetic materials, factors governing MFL inspection, MFL circuit design requirements, and MFL-based devices. It reviews the literature on MFL circuit design, focusing on critical theories, methodologies, and findings from previous studies and highlights the gaps this research aims to address.
- Chapter 3 describes the materials and methodology used to conduct the study. It details the materials, their magnetic properties and instruments used. It outlines the

comprehensive approach to investigating and optimising the MFL system, focusing on numerical and experimental aspects. It presents a finite element (FE) modelling approach describing FE models, derivation of Maxwell's equation, optimisation techniques and algorithms. The experimental programme, procedures and protocols followed for consistent and accurate data collection are presented.

- Chapter 4 reports a simulation-led design development of a novel MFL system based on 3D finite element analysis (FEA). It describes three MFL circuit types: a reference circuit with improved design parameters, a novel hinged circuit with a hinged magnet bridge and a novel optimised circuit with optimal performance in the range of applications, including flat and non-flat inspection objects. It describes each of the design solutions and evaluates their performance.

- Chapter 5 describes the experimental setup and procedures for validating simulation results. Simulation results are validated experimentally for three circuit configurations on a flat plate, pipe and pipe elbow by introducing a range of machined defects. The chapter presents a sensitivity analysis of the prototypes to a range of defect parameters, including depth, radius, locations and sensor lift-off, to understand their impact on defect detection.

- Chapter 6 summarises the key findings of the research, providing conclusions drawn from the simulation and experimental findings. It suggests future directions for further research and development.

# 2. LITERATURE REVIEW

## 2.1. Introduction

Localised corrosion, including pitting, erosion-corrosion and flow-accelerated corrosion, is especially dangerous because it often progresses without any warning and can lead to unexpected pipeline rupture due to rapid and severe damage at specific sites. Conoco Humber pipeline failure is an example of this type of failure caused by erosion-corrosion [30]. Localised corrosion requires advanced non-destructive testing (NDT) techniques for detection and monitoring. Magnetic Flux Leakage (MFL) inspection stands out due to its simplicity and effectiveness in identifying and characterising defects.

The MFL technique involves magnetising the pipeline and detecting the leakage field caused by different types of anomalies. The MFL inspection is affected by several design factors. This chapter reviews NDT techniques, focusing on the MFL method. The discussion includes magnetic materials characteristics, working principles of MFL inspection, factors that affect MFL inspection, design requirements of the MFL system, which are essential for optimising the performance in detecting and characterising defects, and MFL-based devices.

Despite the advancements in MFL technology, there is a significant gap in the design optimisation of MFL systems for enhanced localised defect monitoring in flat and curved inspection components. The literature review examines pipeline and storage tank failures due to localised corrosion and the resulting accidents and their impacts, critically reviews the current state of MFL inspection technology, identifies areas for further research and proposes strategies for enhancing the design and application of MFL systems to bridge the gap.

## 2.2. Corrosion and Failures in the Pipelines and Storage Tanks

Steel pipelines and storage tanks are most commonly used for oil and gas transportation and storage. However, they are susceptible to various failures, with corrosion being a predominant cause of pipeline and storage tank failures. Corrosion is the deteriorative loss of a metal as a result of the electrochemical reaction between metal and surrounding environments. The rusting of steel in water containing dissolved oxygen occurs in two steps. First, iron gets oxidised and oxygen gains electrons, which form hydroxide ions. The iron ions react with hydroxide ions to form iron (II) hydroxide, as shown in Equation 2.1. In the second stage, iron (II) hydroxide oxidises to iron (III) hydroxide in the presence of oxygen and water, as shown

in Equation 2.2. The compound iron (III) hydroxide is rust [7]. General corrosion occurs equivalently throughout the exposed surface, whereas localised corrosion occurs due to an intense attack at localised sites. The most commonly occurring localised corrosion types in oil and gas industries are pitting, flow-accelerated corrosion and erosion-corrosion [10], [11], [12], [13], [14], [15].

$$Fe + \frac{1}{2}O_2 + H_2O = Fe^{2+} + 2OH^- = Fe(OH)_2 \quad 2.1$$

$$2Fe(OH)_2 + \frac{1}{2}O_2 + H_2O = 2Fe(OH)_3 \quad 2.2$$

The total annual direct cost of corrosion for hazardous materials storage (underground and over-ground storage tanks) and gas and liquid pipelines is US $14 billion in the United States alone [40]. The pipeline failure data presented by the Pipeline and Hazardous Materials Safety Administration (PHMSA) in the United States shows an average of 640 pipeline incidents, 14 fatalities, and 57 injuries occur annually [41]. Corrosion is one of the main causes of pipeline failures [8]. Oil and gas pipeline failure can cause fire, explosions, environmental damage, injuries and the deaths of people [42]. Localised corrosion is more dangerous and difficult to detect, predict and control. It occurs in difficult-to-access areas, propagates rapidly and causes unexpected catastrophic failure without warning [43], [44]. This makes localised corrosion more challenging to detect and manage in pipeline systems. Table 2.1 highlights some corrosion accidents that occurred due to localised corrosion and their consequences. Therefore, it is essential to monitor localised corrosion to effectively control it and prevent catastrophic failures.

**Table 2.1.** Accidents caused by localised corrosion and their resulting consequences.

| Accidents | Cause | Consequences |
|---|---|---|
| San Juanico, Mexico | Pitting | 650 killed, 6400 injured, two of the multiple explosions had an intensity of 0.5 Richter scales, destroyed 100 parked trucks loaded with household gas cylinder, scattering of spheres and cylinders (some weighting 30 tons) over distances up to 1.2 km, destroyed 150 homes and damaged a few hundred homes, evacuated 200,000 people from the area, financial damage US $29 million [45], [46], [47], [48]. |
| Piper Alpha North Sea, UK | Localised corrosion | 167 killed, 62 injured, involved multiple explosions and fires resulting in significant environmental damage, financial damage US $1.27 billion [11], [49], [50], [51]. |
| Carlsbad, New Mexico, USA | Pitting | 12 killed, severely damaged two nearby suspension bridges, destruction of three vehicles, destruction of vegetation along both riverbanks due to the fire, release of natural gas into the environment, financial damage US $998,296 [52]. |
| Conoco Humber, UK | Erosion-corrosion | 3 injured, released flammable liquids and gases including hydrogen sulphide, destroyed the refinery which cost over US $750 million to build, fined £895,000 for breaching health and safety, extensive damage to the nearby buildings and properties within a 1-kilometer radius of the site [30], [31]. |

## 2.3. Overview of Non-destructive Testing (NDT) Techniques

Non-destructive testing (NDT), also known as non-destructive examination (NDE), non-destructive inspection (NDI) or non-destructive evaluation (NDE), examines, inspects and evaluates materials, components or assemblies without impairing their future usefulness [53], [54]. NDE involves not only detecting defects and locating their position but also providing information about defects' size, shape, and orientation [55] and characterising the physical/mechanical properties of materials [56]. It is performed to improve the safety and reliability of a component by correlating NDT data with the quality and serviceability

requirements of the evaluated item [57]. It also provides significant data to improve design, production and maintenance [58]. The most commonly used techniques are discussed below, and each method has its benefits, limitations and suitability for various applications.

### 2.3.1. Visual Testing

Visual testing or visual inspection is, foremost, the oldest and most commonly used non-destructive testing technique across all industries [57], [59]. Visual testing involves illuminating a test object with a light source whose lighting level is in the recommended illuminance range suitable for human eyes (500 and 2000 lx) [55], [60], [61]. It relies on aided and unaided eyes to detect a number of defects, including cracks, corrosion, porosity, indentation, undercut or misalignment [55], [57]. The size of the defect to be detected by visual testing needs to be approximately 6.35 mm and larger. This is due to the human eye's ability to detect discontinuities, the limitations of visual inspection techniques and the need to maintain a balance between inspection efficiency and reliability [62]. Figure 2.1 (a) shows a typical visual testing setup with angle and distance measurements from the test object [55]. The eye of the inspector needs to be positioned within 24 inches of radius from the test object and at an angle not less than 30°. The 24-inch distance and 30° angle enable optimal focal distance for defect visibility and contrast, minimise glare and reflection, reduce eye strain, and ensure repeatability [55]. Figure 2.1 (b) shows bridge inspection using visual testing [63]. Visual testing uses mechanical and/or optical aids for accurate inspection, such as callipers, micrometres, mirrors, various gauges, magnifying glasses, microscopes, endoscopes, borescopes, closed-circuit television (CCTV) systems and others [55], [64]. Visual testing is the first inspection method to detect any visible discontinuities, and it can locate part of the specimen to be inspected further using other NDT techniques [55], [59], [62]. Some NDT techniques, such as dye penetrant and magnetic particle testing, rely on visual testing [55], [57], [62]. The advantages of using visual testing are that it is simple, direct, inexpensive, and fast and that it can examine any specimen [55], [64], [65]. The drawbacks of visual testing are that its qualitative assessment is limited to surface examination (inaccessible areas cannot be inspected), does not detect defects located deeper within the material (far-surface defects) and whose size is less than 6.35 mm, is labour-intensive, requires an experienced inspector, the surfaces need to be cleaned prior to the examination, and the paint should be removed [55], [62], [66]. A study conducted on highway bridges to examine the reliability and accuracy of the visual testing showed that visual testing results can be significantly variable with different inspectors (3.9% of inspectors correctly identified the presence of crack indications) [63]. For

the above reasons, mainly due to its limitation to surface examination, inability to detect far-surface defects and defect size less than 6.35 mm, visual testing is not suitable for remote defect monitoring in difficult-to-access areas.

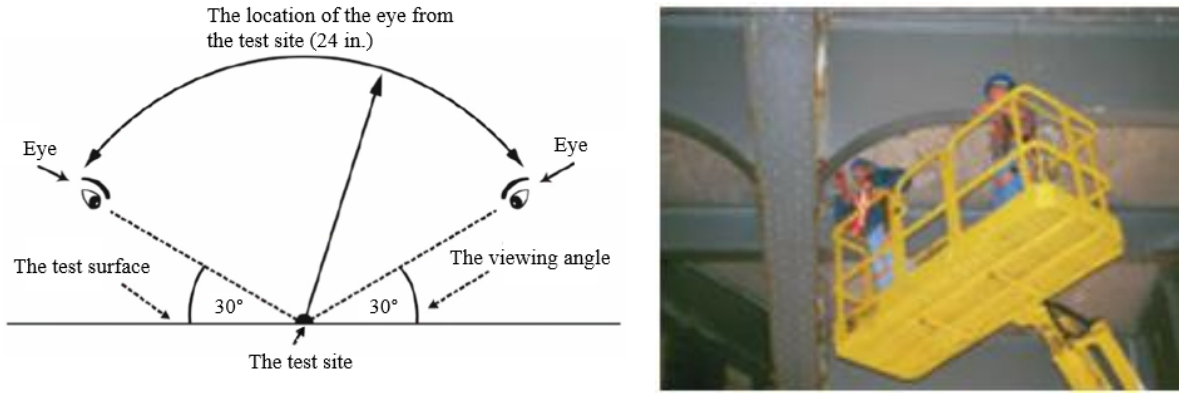


(a) (b)

**Figure 2.1.** (a) During visual testing, the standard distance and viewing angle of the human eye from the test object [55]. (b) Highway bridge inspection using visual testing [63].

### 2.3.2. Ultrasonic Testing

Ultrasonic testing is one of the most popular NDT techniques used in a wide range of industries to detect flaws in different materials [56], [57], [67], [68]. Ultrasonic testing uses sound waves with frequencies above the audible range of human hearing, above 20 kHz up to 50 MHz [56], [67]. Figure 2.2 shows the ultrasonic testing system setup, which consists of a pulser/receiver, transducer, display devices and test object. A pulser/receiver produces high-voltage electrical pulses, which drive the transducer to generate high-frequency ultrasonic energy [69]. The transducer is coupled to the test object using gel, oil or water. When high-frequency sound waves pass through the test object, a defect-free part allows the passage of sound waves easily, whereas a defective part results in sound waves being reflected and scattered, resulting in energy loss. The reflected wave signal is transformed into an electrical signal by the transducer and is displayed on a screen [56], [68], [69]. There are two basic types of ultrasonic testing: pulse-echo technique and through transmission technique. In the pulse-echo technique, uses a single transducer, and access to only one specimen surface is needed. In contrast, uses two transducers, and access to both sides of the specimen is necessary for the through transmission technique [56], [67], [68]. Some of the advantages of ultrasonic testing are that it inspects different materials such as metals, ceramics, plastics, composites and concrete, has broad applications such as thickness measurement, physical properties and metallurgical structure evaluations. It has high accuracy for determining the depth of internal

flaws and the thickness of parts with parallel surfaces [56], [67], [68], [69]. Some of the limitations of ultrasonic testing are: the surface must be accessible to transmit ultrasound, requires a coupling medium, has reduced sensitivity for volumetric flaws (corrosion), may have false positive results, paint must be removed, requires experienced technicians for inspection and data interpretation, reduced resolution for dense and crystalline materials due to higher attenuation and coarse-grained, rough, irregular, small/thin and heterogeneous materials are challenging to inspect [67], [68], [69]. Additionally, some of the challenges of using ultrasonic testing for remote corrosion monitoring are its limitations in detecting localised corrosions such as erosion-corrosion and pitting. Localised corrosions cause ultrasonic wave scattering, leading to inaccurate or weak reflections. This results in inaccurate defect measurements or missed defects [70], [71], [72], [73]. Inaccessible or hazardous locations present significant challenges for maintaining continuous power supply and data transmission. The use of coupling agents (e.g., gels or water) complicates field deployment, especially on rough or coated surfaces. Environmental factors, such as temperature and humidity fluctuations, affect signal velocity, necessitating frequent calibration to ensure accuracy. However, recalibration, maintenance, and repairs become particularly difficult in hard-to-reach or hazardous environments. Additionally, turbulent surfaces can scatter or absorb ultrasonic waves, reducing measurement accuracy, and ultrasonic arrays are often expensive [74], [75].

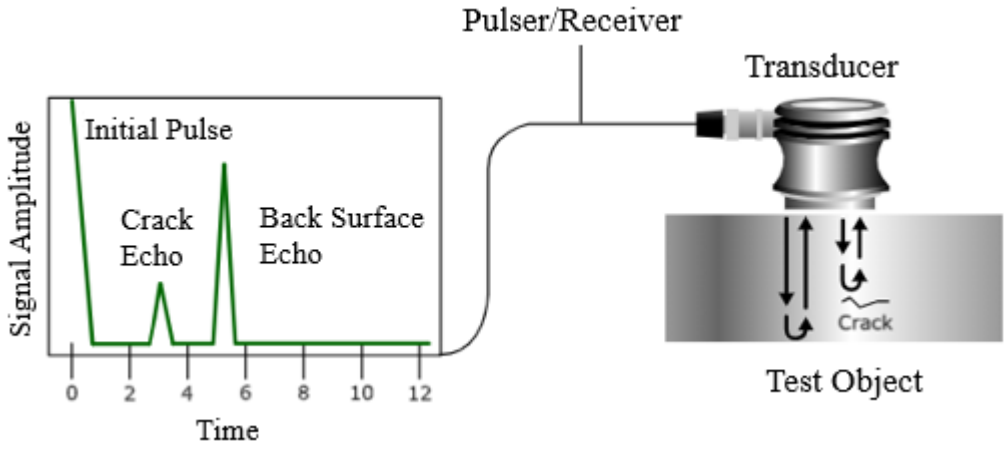


**Figure 2.2**. Ultrasonic testing setup consisting of a pulser/receiver, transducer, display devices and test object [69].

### 2.3.3. Acoustic Emission Testing

Acoustic emission testing is an NDT technique that detects high-frequency sound waves or vibrations released from defects when the material is subject to an external stimulus (change in pressure, load, or temperature) [57], [76], [77], [78], [79]. These sound waves result from

the energy the defects release as they respond to the applied stress. Figure 2.3 illustrates the setup of the acoustic emission testing system, including an Acoustic emission (AE) sensor, preamplifier, filter and amplifier, display, and storage devices such as oscilloscopes, voltmeters, and computer [80], [81]. An acoustic emission sensor is typically a piezoelectric transducer that converts mechanical movement into an electrical voltage signal. Preamplifiers eliminate unwanted signals and boost the voltage. The filter eliminates low frequencies (background noise) and high frequencies. The signal then travels to the acoustic system mainframe for further filtering, if necessary, analysis, and storage [76], [77], [78]. Some of the advantages of acoustic emission testing are that it has versatile applications, such as assessing structural integrity, detecting flaws, testing for leaks or monitoring weld quality. The sensor can be fixed in one place to inspect the whole structure, and only a few sensors can be used. Acoustic emission testing inspects different types of materials and detects the formation of new defects or the progression of existing defects. The limitation of acoustic emission testing or acoustic emission testing is not well-suited for remote localised corrosion monitoring since it cannot detect defects that are present but do not move or grow. It is more sensitive to active crack growth rather than slow, gradual material loss due to corrosion. The defects may be undetected if the loading is not high enough (less than the trigger level) to cause an acoustic wave and the fluid flow environment has high background noise reducing corrosion signal. Acoustic emission testing provides only qualitative data about the defect; therefore, further inspection using another NDT technique is required to obtain quantitative data [76], [77], [78], [79].

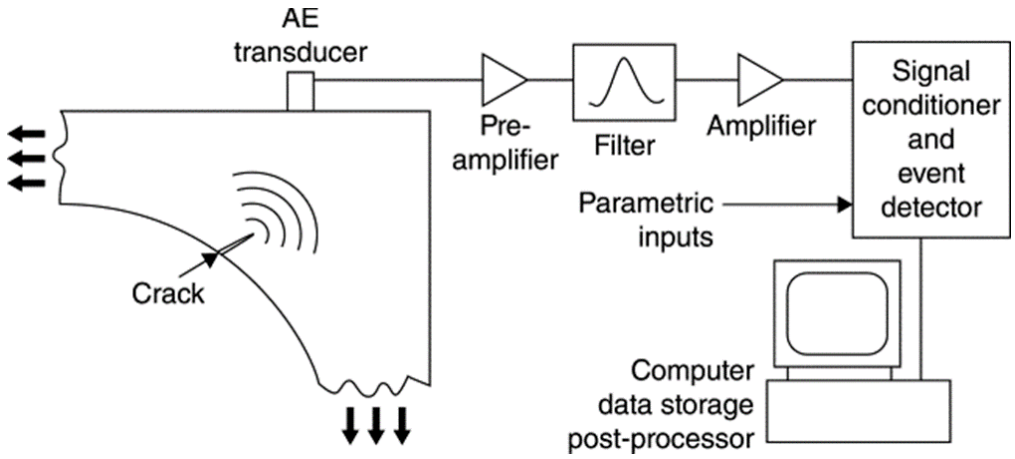


**Figure 2.3**. Schematic of an acoustic emission system setup for defect detection. The AE transducer detects stress waves from crack propagation, which are amplified, filtered, and processed through a signal conditioner and event detector. The data is then stored and analysed using a computer post-processor [80].

### 2.3.4. Radiographic Testing

Radiographic testing is a widely used and effective NDT technique due to its universal acceptance in industries [56], [82]. It uses either x-rays or gamma rays and radiography and inspects most solid materials [56], [57], [82], [83]. Several imaging techniques exist, such as film, real-time, computed and digital radiography [83]. Figure 2.4 shows the radiographic testing system setup, with a test object between a radiation source and a radiography (detector) [82]. When radiation passes through a test object with defects, attenuation is less and more photons reach the film; however, in a defect-free test object, there will be more attenuation, and fewer photons will reach the film [57], [82], [83]. Some advantages of radiographic testing include its high accuracy and effectiveness for detecting internal defects, such as cracks and voids in various materials and its permanent record of test data [82], [83], [84], [85]. Limitations of radiographic testing include the following: It is expensive, time-consuming, and requires a large space due to bulky and heavy radiation generators. It poses potential health and environmental hazards due to radioactive waste. The detection of defects depends on the orientation of radiation (thin cracks can be missed if radiation is parallel to the defect). It is limited in detecting localised and early-stage corrosion. Both sides of the test object must be accessible, which is impractical for remote and difficult-to-access areas [82], [84], [85], [86], [87]. For the above reasons, radiographic testing is impractical for remote corrosion monitoring.

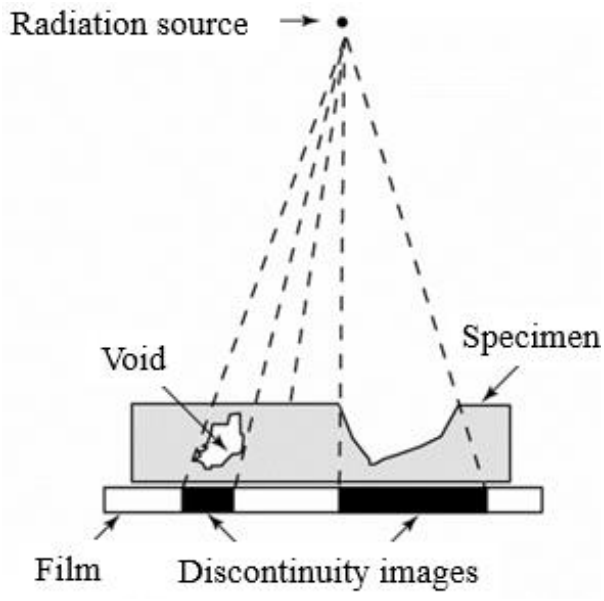


**Figure 2.4.** Radiographic testing system setup consists of an inspection object between the radiation source and the radiography film [82].

### 2.3.5. Penetrant Testing

Penetrant testing, or liquid penetrant testing, is an NDT technique to detect surface flaws in nonporous solid materials [57], [88]. Before the penetrant testing examination, the target area of an inspection object needs to be cleaned using detergents, organic solvents, descaling solutions, paint removers and others. The surface then needs to be dry. Fluorescent or visible penetrant enters very small openings of defects when applied on the surface by capillary action. After penetration time, any excess penetrant is removed by spraying with water or with a lint-free cloth/paper. A wet or dry developer is applied on the surface to draw out the penetrant trapped in surface-breaking defects, making them more visible to the inspector. Thus, red-colour bleeding through the white background of the developer provides a clear indication of defects while using visible penetrants in bright light, as shown in Figure 2.5 (a). A bright yellow-green fluorescence against a dark background is observed for fluorescent penetrants in a dark room [57], [89], [90], as shown in Figure 2.5 (b) [91]. Some of the advantages of using penetrant testing include: it is very sensitive to surface cracks [89], [90], [92], can be used in uneven [90] and complex geometric shapes [93], is portable and relatively simple to apply [90] and is a simple, low-cost method [92]. Some of the drawbacks of penetrant testing include: it is only suitable for surface defects and cannot detect subsurface defects [94]. It is affected by surface cleanness, roughness or porosity [90] and environmental conditions (temperature and humidity) [94]. It is time-consuming and may have false indications caused by localised surface

irregularities due to machining marks [89]. It leaves no permanent record, does not provide quantitative data and defects may not be detected if it filled with dirt or oxide [90]. Penetrant testing is a manual process requiring multiple steps such as pre-cleaning, drying, applying penetrant and developer, cleaning excess penetrant and visual inspection. Remote corrosion monitoring requires automation and minimal human intervention. Therefore, Penetrant testing is not suitable for remote corrosion monitoring.

(a) (b)

**Figure 2.5.** Crack presence indications while using (a) Visible penetrant and (b) Fluorescent penetrant [91].

### 2.3.6. Eddy Current Testing

Eddy current testing is one of the oldest and most extensively used NDT techniques to inspect electrically conductive materials [54], [95], [96]. Eddy current testing is used not only to detect flaws but also to measure the thickness of non-conductive material adhering to conductive material, conductivity measurements for material identification, heat damage detection or other applications and characterisation of inhomogeneities in metals [54], [95], [97], [98]. Eddy current testing's working principle is based on the electromagnetic principle, as shown in Figure 2.6 [96], [99]. When an alternative current (AC) passes through an eddy current testing coil, it generates a changing magnetic field around it. When the coil is situated close to an electrically conductive material, the primary changing magnetic field penetrates the material and induces a circular eddy current in the conductor according to Faraday's law of electromagnetic induction. Faraday's law states that changing magnetic field induces an electric current in a conductor, as shown in Equation 2.3. The eddy current results in a secondary magnetic field of its own, which opposes the initial magnetic field produced by the coil due to Lenz's law. Lenz's law describes that eddy currents create their own magnetic field that opposes the original field from the coil, as shown in Equation 2.5. It also affects the current

and voltage flowing in the coil. If the material has any defect, the eddy current flow will be disrupted, and the changes in eddy current can be measured using the primary or secondary detector coil [95], [96], [97], [100], [101].

$$\nabla \times \mathbf{E} = -\frac{\partial \mathbf{B}}{\partial \mathrm{t}} \qquad 2.3$$

Where **E** is electric field intensity, **B** is magnetic flux density, and t is time.

$$\mathcal{E} = -\frac{\mathrm{d}\Phi}{\mathrm{dt}} \qquad 2.4$$

Where $\mathcal{E}$ is the electromotive force, and $\Phi$ is magnetic flux.

The orientation of defects to the eddy current flow is essential for defect detection, which is determined by the orientation of the coil to an inspection component. Thin crack-type defects may not be detected if it is oriented parallel to the eddy current flow [54], [100], as shown in Figure 2.7 [54]. Some of the advantages of eddy current testing are that it detects different types of defects in ferromagnetic and non-ferromagnetic materials, is a non-contact method, can detect near and far-surface defects, is portable and lightweight, does not need any couplant, requires minimum surface preparation, gives immediate test results, inspects objects with complex geometries and can be automated to inspect uniform parts [54], [95], [96], [97], [98]. Eddy current testing's drawbacks are that it is used to inspect only electrically conducting materials, cannot detect thin defects parallel to eddy current flow direction, requires skill and training for inspection and signal interpretation and is affected by conductivity of material, permeability, test frequency, lift-off, geometry of material and coil design. Depth of penetration decreases with an increase in conductivity, frequency and permeability. Therefore, it is challenging to detect subsurface defects in ferromagnetic materials due to their high permeability and in non-ferromagnetic materials, due to variations in conductivity and frequency. The coil diameter affects flux field distribution and eddy current penetration. Eddy current shows skin effect, i.e. current density decreases with depth. Thus, test sensitivity decreases with increasing depth [54], [97], [98], [100]. Overall, eddy current testing is less reliable for subsurface remote corrosion monitoring in ferromagnetic components due to components' high permeability decreasing penetration depth.

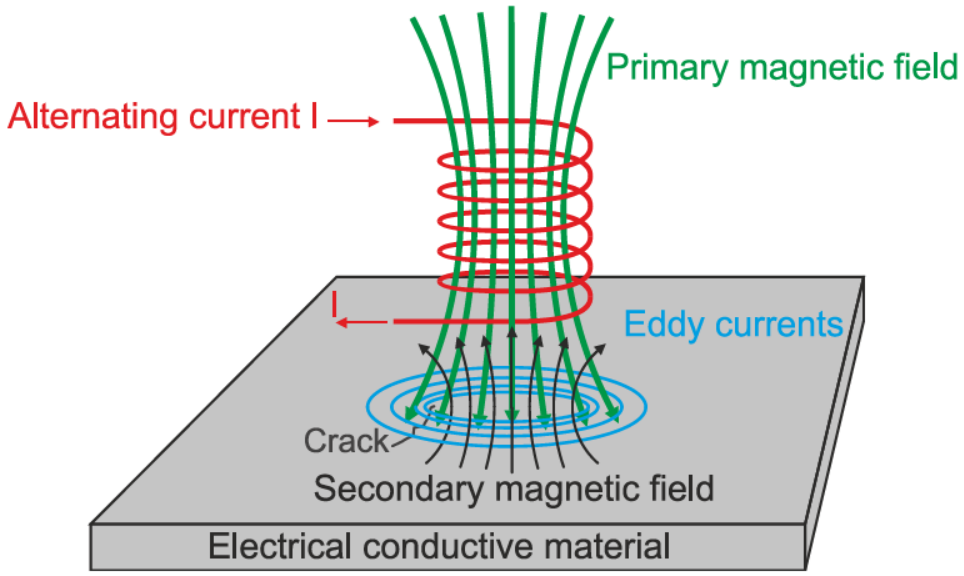


**Figure 2.6.** Working principles of eddy current testing [96], [99].

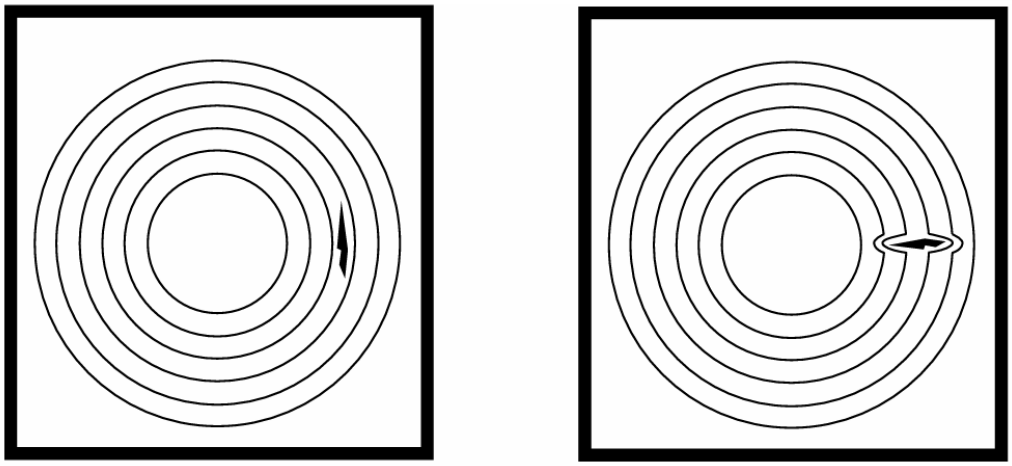

(a) (b)

**Figure 2.7.** (a) Defect parallel to eddy current flow direction, and (b) Defect perpendicular to eddy current flow direction [54].

### 2.3.7. Magnetic Particle Testing

Magnetic particle testing is a long-established and widely used electromagnetic NDT technique to detect surface and subsurface defects in ferromagnetic materials [102], [103], [104], [105]. It combines two NDT techniques: magnetic flux leakage testing and visual inspection [102]. Figure 2.8 (a) shows magnetic particle testing system setup [106]. Magnetic particle testing involves inducing a magnetic field to magnetise an inspection component. Dry or wet high-contrast or fluorescent colour or fluorescent-coated magnetic particles are applied on the surface of the inspection component for detection. Dry magnetic particles are powdered iron

filings dusted on the inspection surface. Wet magnetic particles are particles suspended in liquid carriers, either water or oil and sprayed over the inspection surface for an even distribution of particles. The magnetic field leak and magnetic particles cluster most densely on a defective area when there is a discontinuity in the magnetised inspection component [102], [103], [107], [108], [109], as shown in Figure 2.8 (b) [105]. The clustered magnetic particles indicate the extent, location, size and shape of the defect [102]. Magnetic particle testing does not quantify the size of a defect. However, an experienced operator can estimate it from the extent and pattern of the gathered particles at the defect area [103]. Some advantages of using magnetic particle testing include its simplicity, speed, sensitivity, versatility, applicability to irregular shapes, low cost and minimal training and equipment requirements [102], [103], [104], [107], [108], [109]. It does not need precleaning for examination, and defects which are filled with foreign materials can be detected [102], [109], is user-friendly [104], has a clear indication of defects on the surface [103], [107], [109] and is not hazardous [109]. Some of the limitations of magnetic particle testing are that it inspects only ferromagnetic materials, requires the inspection components to be adequately magnetised, does not have test results permanent record, does not provide quantitative corrosion data, the inspection surface needs to be accessible, requires a very high current to magnetise large inspection parts which might result in overheating, needs demagnetisation after the test and demand inspector's skill and experience [102], [103], [107], [109]. Magnetic particle testing is a manual process requiring magnetic particle application and visual inspection. Therefore, it is not suitable for remote corrosion monitoring, which needs less human intervention.

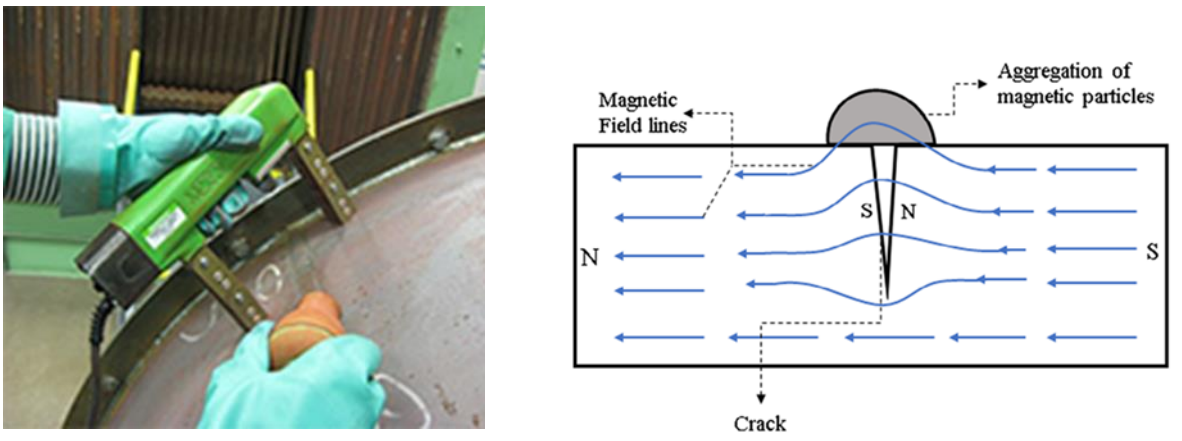


(a) (b)

**Figure 2.8.** (a) Magnetic particle Testing system setup with a magnetising yoke, an inspection object and magnetic particles [106]. (b) Principle of magnetic particle testing [105].

### 2.3.8. Magnetic Flux Leakage (MFL) Inspection

Magnetic flux leakage (MFL) is one of the most commonly used NDT techniques for detecting different types of defects in ferromagnetic structures in the petrochemical, transportation, energy and metal industries [4], [110], [111]. It is a widely used, reliable, low-cost, easy-to-implement and efficient inspection technique [25], [4], [112]. MFL does not require surface preparation for the inspection. It is a non-contact method [112]. It detects internal and external defects [32]. It has high detection accuracy, quick detection speed, a straightforward structure and no requirement for coupling agents [33]. The signal interpretation is relatively easy and highly sensitive to volumetric defects due to corrosion and erosion. The MFL method and device are simple and suitable for in-line and automatic quantitative defect measurements [34]. For the above reasons, the MFL is the most popular and widely used NDT method in oil and gas pipelines and storage tanks [4], [113].

The MFL demonstrates distinct advantages over other NDT methods for remote localised corrosion monitoring in ferromagnetic components. Unlike ultrasonic testing, MFL is highly sensitive to volumetric loss such as pitting and erosion-corrosion, does not need surface preparation and couplant and is a low-cost and easy-to-implement technique. Unlike eddy current testing, MFL detects both surface and subsurface defects.

Some of the limitations of MFL are that it is used to inspect only ferromagnetic materials [114], [115], conventional MFL is limited/not able to detect small cracks or crack-like defects, especially far surface cracks [88], [116], and detection and sizing accuracy is affected by the strength of a magnet used [117]. MFL is governed by several factors, such as scanning velocity for moving MFL, defect orientation, sensor configuration, lift-off, induced magnetisation in the inspection component, thickness of the inspection component and circuit configurations [4], [114], [118], [119], [120]. Data interpretation is challenging and requires skilled personnel [114], [115], [121], [122].

MFL has a magnetic circuit and a sensor. Figure 2.9 shows the magnetic circuit of an MFL device. It consists of magnetic circuit components such as permanent magnets, pole pieces, a magnet bridge, an inspection component along with a sensor. The permanent magnets are the sources of a magnetic field in the circuit. The pole pieces are ferromagnetic materials that transfer magnetic flux from the magnets to the inspection components and protect the magnets from damage due to direct contact with the inspection component. The magnet bridge is made of a ferromagnetic material and connects/bridges the two magnet poles. The inspection

component is a ferromagnetic material, a plate, pipe or pipe elbow. The sensor detects any magnetic flux leakage. It is positioned at the midpoint between the magnetic poles, the magnetic neutral point [123]. The magnetiser lift-off is a gap between the MFL device and the inspection component. The sensor lift-off is a gap between the sensor and the sample under inspection.

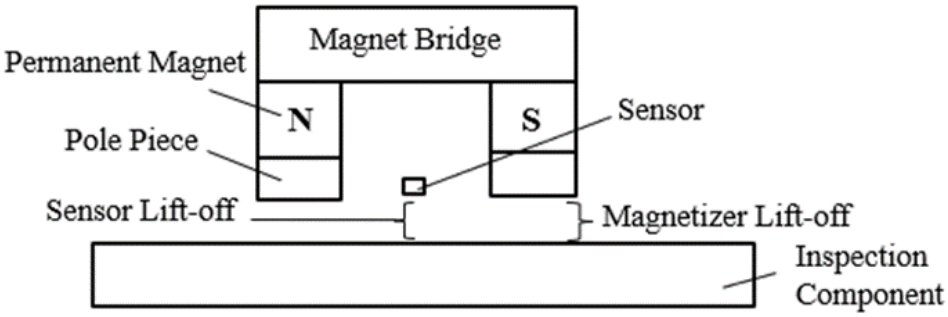


**Figure 2.9.** The magnetic circuit of an MFL device. The magnetic circuit components are permanent magnets, pole pieces, a magnet bridge, an inspection component along with a sensor.

## 2.4. Magnetic Flux Leakage (MFL) Inspection

### 2.4.1. Magnetism and Magnetic Materials Characteristics

Magnetism is an interaction (attraction or repulsion) between magnetic poles, regions in magnets where forces of attraction and repulsion originate, separated by a distance [124], [125]. The force between magnet poles is proportional to the product of their pole strength, $P_1$ and $P_2$ and inversely proportional to the square of the distance d between them, as shown in Equation 2.5 [125]. This equation describes magnetic force as an interaction between two distinct magnetic poles based on pole strength and distance and is used in fundamental magnetostatics.

$$F = k \frac{P_1 P_2}{d^2} \qquad 2.5$$

Where k is the proportionality constant.

There are three basic categories of magnetism based on the response of materials when an external magnetic field is applied: paramagnetism, diamagnetism and ferromagnetism. Paramagnetic materials are not strongly attracted to a magnet. A magnet repels diamagnetic materials, and ferromagnetic materials manifest large and permanent magnetisation. The classification of these materials is based on their magnetic susceptibility, $\chi_m$. It is a measure of the degree of magnetisation in an applied magnetic field, as shown in Equation 2.6. The

magnetic susceptibility of diamagnetic, paramagnetic and ferromagnetic materials is given in Table 2.2. Since the magnetic susceptibility of diamagnetic and paramagnetic materials are close to zero, they are considered non-magnetic [126].

$$\chi_m = \frac{\mathbf{M}}{\mathbf{H}} \qquad 2.6$$

Where **M** is magnetisation, a process of making materials temporarily or permanently magnetic by inducing a magnetic field, and **H** is magnetic field strength.

**Table 2.2**. The magnetic susceptibility of diamagnetic, paramagnetic and ferromagnetic materials.

| Material Type | Magnetic susceptibility ( $\chi_m$) | Characteristics |
|---|---|---|
| Diamagnetic | $\chi_m < 0$ (negative, small, typically around $-10^{-5}$) | Weakly repelled by a magnetic field, no permanent magnetic moment. |
| Paramagnetic | $\chi_m > 0$ (positive, small, typically around $10^{-3}$ to $10^{-5}$) | Weakly attracted by a magnetic field, with temporary alignment of magnetic moments. |
| Ferromagnetic | $\chi_m >> 0$ (positive, large, can be 50 to 10,000) | Strongly attracted by a magnetic field, with permanent magnetic moments. |

The magnetic properties of materials can be discussed using relative permeability, $\mu_r$. It measures the degree to which a material allows induction of a magnetic field, compared to a vacuum, as shown in Equation 2.7. Equation 2.8 relates relative permeability to magnetic susceptibility.

$$\mu_r = \frac{\mu}{\mu_0} \qquad 2.7$$

$$\chi_m = \mu_r - 1 \qquad 2.8$$

Where $\mu$ is the permeability of the material, and $\mu_0$ is the permeability of free space and equal to $4\pi\times10^{-7}$ H.m$^{-1}$.

Magnetic permeability, $\mu$, is a property of materials where the applied magnetic field strength passes, and magnetic flux density is measured:

$$\mu = \frac{\mathbf{B}}{\mathbf{H}} \qquad 2.9$$

Where **B** is magnetic flux density or magnetic induction.

Magnetic flux density measures the magnitude of an internal field strength when a magnetic field is applied. In Figure 2.10, magnetic flux density shows how tightly field lines are packed. Magnetic flux, $\phi$, is a measure of the total magnetic field passing through a given surface area, A, as shown in Equation 2.10.

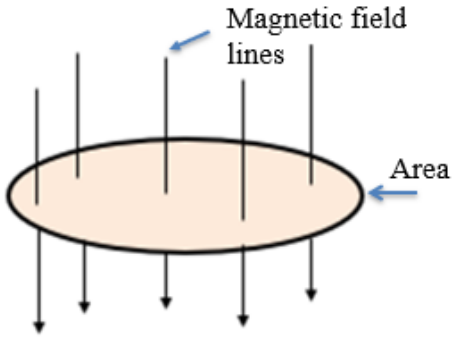


**Figure 2.10.** Magnetic flux through the area.

$$\phi = \mathbf{B}A\cos(\theta) \qquad 2.10$$

Where $\theta$ is an angle between the magnetic field lines and the surface.

Magnetic flux density is a vector component with $\mathbf{B}_x$, $\mathbf{B}_y$ and $\mathbf{B}_z$ components in three-dimensional space. The norm of magnetic flux density (**B**) implies the magnitude or strength of the magnetic flux density and is given in Equation 2.11.

$$\|\mathbf{B}\| = \sqrt{\mathbf{B}_x{}^2 + \mathbf{B}_y{}^2 + \mathbf{B}_z{}^2} \qquad 2.11$$

Where $\mathbf{B}_x$, $\mathbf{B}_y$ and $\mathbf{B}_z$ are magnetic flux density components in the x, y and z directions, respectively.

Permeance **(**P) measures the ease with which magnetic flux can be admitted through a material or magnetic circuit, as shown in Equation 2.12. Reluctance or magnetic resistance is the reciprocal of permeance. It is a property of the magnetic material to oppose the flow of a magnetic field through it.

$$P = \frac{\phi}{\mathbf{F}} = \frac{\mu A}{L} \qquad 2.12$$

Where **F** is magnetomotive force, a quantity that quantifies the sum of magnetising force along a circuit, and L is the length of magnetic path.

Magnetic Flux Leakage refers to the magnetic flux that does not follow the intended path in a magnetic circuit but instead "leaks" into the surrounding space. Fringing flux is a part of the produced flux that distributes and bends outside the magnetic circuit due to an air gap (a non-magnetic region) in the magnetic circuit. The fringing effect increases with increasing the air gap, as shown in Figure 2.11 [127]. As shown in Equation 2.12 a larger air gap increases the reluctance, reducing the flux density and causing fringing flux. A smaller air gap minimises reluctance, leading to a higher flux concentration.

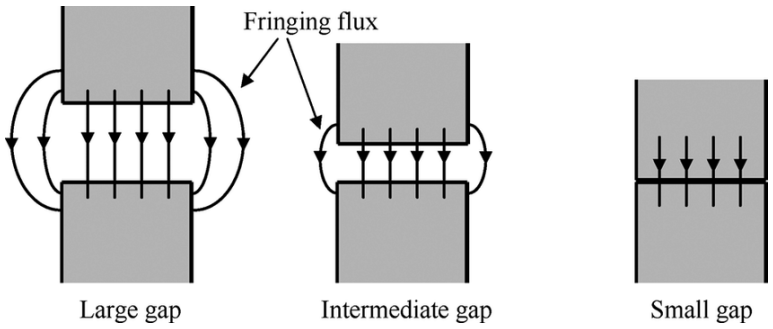


**Figure 2.11**. Fringing effect as a function of the air gap, the fringing effect increasing with the air gap [127].

The magnetisation of the ferromagnetic materials depends on their magnetic properties. All ferromagnetic materials exhibit distinct magnetic characteristics described through their magnetic hysteresis curve [102] Figure 2.12. Magnetic hysteresis is the phenomenon where the response of magnetic flux density (**B**) lags behind changes in the applied magnetic field strength (**H**). This is due to the inherent properties of ferromagnetic materials and their tendency to retain a certain level of magnetisation even after the external magnetic field is removed [7], [57], [125]. Ferromagnetic materials show nonlinear behaviour between magnetic flux density and applied magnetic field strength [102].

The magnetic hysteresis loop or curve is a four-quadrant S-shaped loop that shows the hysteresis property of a system, as shown in Figure 2.12. Figure 2.13 illustrates an increased degree of domain growth and alignment with increased magnetic field strength (labelled O through a). The magnetic domains are randomly oriented, and there is no net **B** in unmagnetised ferromagnetic materials (inset O). As magnetic field is applied, domains that are favourably oriented with respect to the field begin to grow at the expense of unfavourably oriented ones. This growth occurs through the movement of domain boundaries and leads to a rapid increase

in magnetic flux density (insets V through X). As the field strength continues to increase, most of the favourably oriented domains have grown significantly, and the material approaches a nearly single-domain state (inset Y), where further growth is limited. Eventually, the material reaches a point where most domain growth has occurred, and the remaining increase in magnetisation happens by rotation of the domains toward the field direction (inset a). This final stage marks the saturation magnetisation ($\mathbf{B}_s$), where the material is fully magnetised in the direction of the applied field. The 0-a segment of the magnetic hysteresis curve is an initial **B-H** curve; see Figure 2.12 and Figure 2.13. The **B-H** curve refers to the capability of a material to induce the magnetic flux density as a function of the applied magnetic field strength.

When the applied magnetic field is reduced from the saturation point, the magnetic flux density slowly decreases along a different path, as shown in Figure 2.12. It does not follow the initial curve, indicating a lag in response. The lag shows that materials retain some magnetisation level even as the magnetic field strength decreases. When the magnetic field is reduced to zero, the material retains some magnetisation (point b), known as remnant flux density ($\mathbf{B}_r$). Point b shows residual or remanence magnetism, the amount of retained flux density when field intensity is zero. Retentivity is the ability of magnetic materials to maintain a certain amount of magnetism after magnetisation.

A magnetic field must be applied in opposite direction to remove retained magnetism. Applying magnetic field strength in the opposite direction decreases magnetic flux density slowly and finally to zero (point c). The amount of magnetic field strength required to reduce the magnetic flux density to zero is called coercive force. Coercivity measures a material's resistance to demagnetisation.

As the reversed magnetic field strength increases beyond point c ($\mathbf{B} = 0$), the domains align in the opposite direction, and the magnetic flux density changes its polarity. Initially, **B** increases rapidly and gradually slows down, reaching negative saturation (point f). A further increase in applied magnetic field after point f will not increase **B**. When the reversed magnetic field strength is reduced to zero after point f, residual magnetism is obtained in the negative direction (point e). When a positive magnetic field is applied again to remove retained magnetism, the magnetic flux density eventually returns to zero at the positive coercive field (point d). A further increase in the magnetic field strength increases the magnetic flux density towards positive saturation (point a), thus completing the hysteresis loop [7], [57], [125].

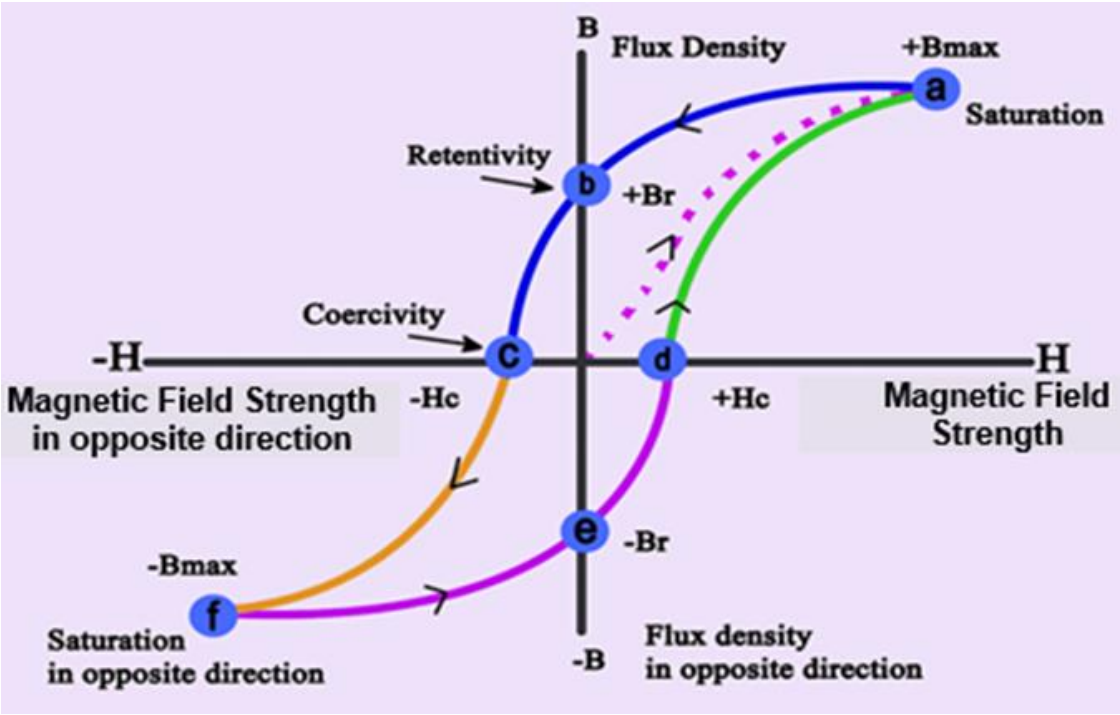


**Figure 2.12.** Magnetic hysteresis curve [128].

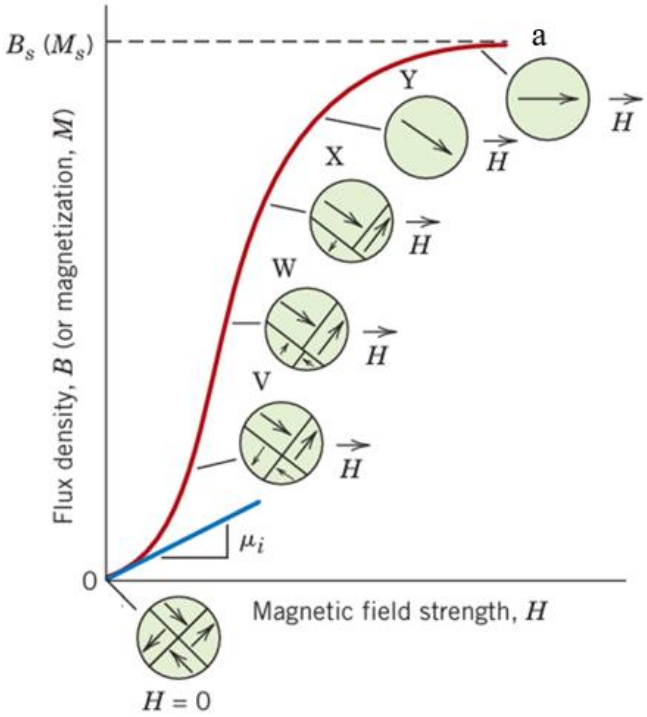


**Figure 2.13.** Initial magnetisation (**B-H**) curve with magnetic domain configuration during stages of magnetisation. **B**s and **M**s are saturation magnetic flux density and magnetisation, respectively and µi is initial permeability [7], [129].

Hysteresis is an irreversible process where the area enclosed by the hysteresis loop indicates the magnetic energy loss per unit volume of material in the form of heat during each

magnetisation and demagnetisation cycle. Based on their hysteresis characteristics, ferromagnetic materials can be classified as magnetically soft and hard materials, as shown in Figure 2.14. Soft magnetic materials have narrow hysteresis loops, high relative permeability, low coercivity and minimal energy loss. Therefore, they are easy to magnetise and demagnetise and are used to build the MFL circuit. In contrast, hard magnetic materials have wide hysteresis loops, low relative permeability, high coercivity and remanence. They are used for permanent magnets [7].

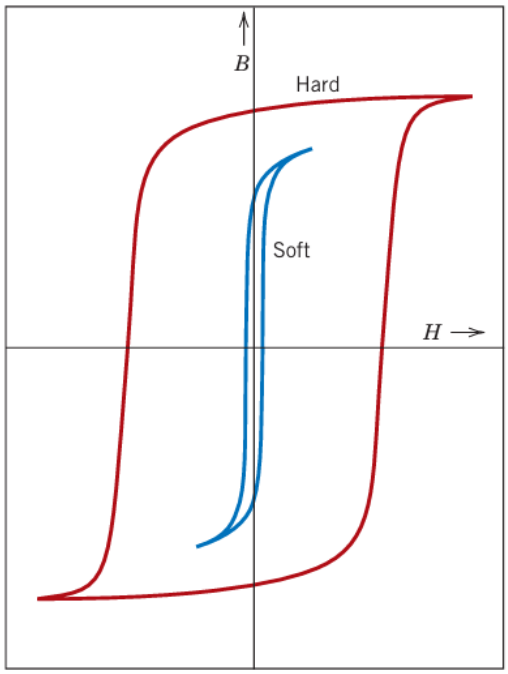


**Figure 2.14.** Magnetic hysteresis curves for soft and hard magnetic materials [7].

Magnetic properties of materials are affected by temperature. When temperature increases, the thermal motion of atoms randomises aligned magnetic moments. Saturation magnetisation is maximum at 0 K where thermal vibration is minimum, decreases with increasing temperature, and then abruptly drops to zero at Curie temperature, Tc. Above Tc, ferromagnetic materials become paramagnetic [7], [130], [131], [132].

### 2.4.2. Working Principles of Magnetic Flux Leakage (MFL)

The MFL-based device working principle is illustrated in Figure 2.15. It requires inducing a magnetic field in an inspection component and measuring the leakage field. Most magnetic flux passes through the inspection component when MFL is used on a defect-free sample [4], as shown in Figure 2.15 (a). However, in the presence of a defect, the magnetic field leaks into the surrounding medium [133], [134], as depicted in Figure 2.15 (b). The leakage is due to the

defect reducing the cross-sectional area/volume material, and the permeability of the flawed material part (air) is lower than that of the defect-free part [4], [57], [112].

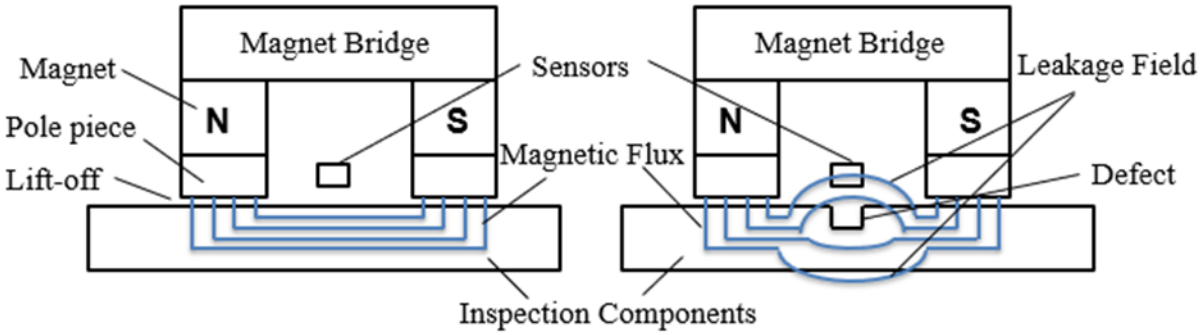


**Figure 2.15.** Working principle of the MFL: The left side shows the inspection component without defect, and on the right, the inspection component with defect.

The defect leakage signal is a vector quantity with three components, $\mathbf{B}_x$, $\mathbf{B}_y$, and $\mathbf{B}_z$, representing the leakage field in the x, y, and z axes, respectively, as shown in Figure 2.16 [4]. The orientation of defect leakage signals is based on the magnetisation direction [135]. The $\mathbf{B}_x$ (horizontal) component is parallel to the magnetisation direction. The $\mathbf{B}_z$ (normal) component is perpendicular to the inspection component, and the $\mathbf{B}_y$ (vertical) component is perpendicular to $\mathbf{B}_x$ and $\mathbf{B}_z$ [136]. For example, if the inspection component is a pipe, the $\mathbf{B}_x$, $\mathbf{B}_z$**, and** $\mathbf{B}_y$ are the axial, radial and tangential components, respectively; see Figure 2.16 [4]. The horizontal component signal along the magnetisation direction and the normal component, perpendicular to the inspection component, are most commonly used to analyse and predict defects due to their larger signal strength and better defect detection performance [136].

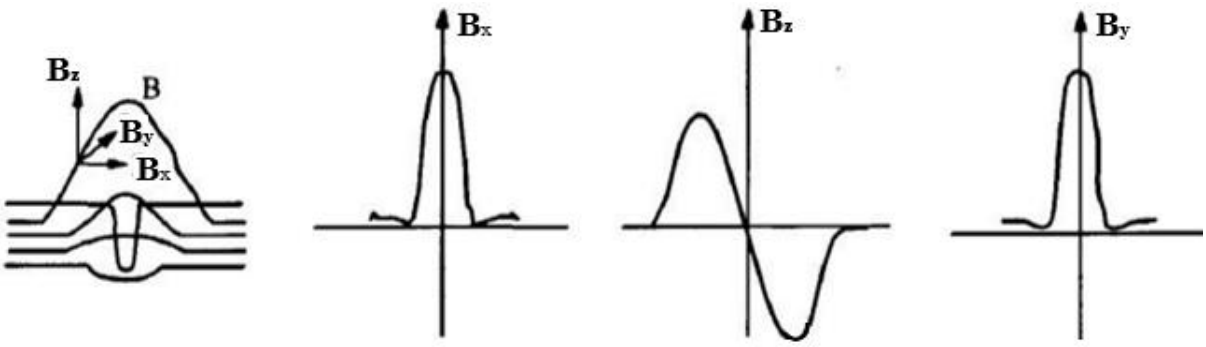


(a) (b) (c) (d)

**Figure 2.16.** (a) Defect leakage field and its components, (b) Axial component, (c) Radial component, and (d) Tangential component [4].

The typical spatial distribution of the leakage flux density, $\mathbf{B}_z$, components are peak amplitude (peak to peak value, P-P value) and peak to peak width, P-P width (distance between peak to peak, DPP) [137], [138], [139], [140], as shown in Figure 2.17 [137]. The spatial distribution of the leakage flux density, $\mathbf{B}_x$, has peak amplitude, bottom value and slope of the baseline components, as shown in Figure 2.18. The peak amplitude is the difference between the maximum and minimum magnetic flux density values. The bottom value is the minimum tangential magnetic induction. The slope of the baseline indicates the slope of the tangent line of the leakage flux density curve distant from the defect. Thus, the larger peak amplitude, smaller bottom value and shallower slope of the baseline are beneficial for detecting anomalies [141].

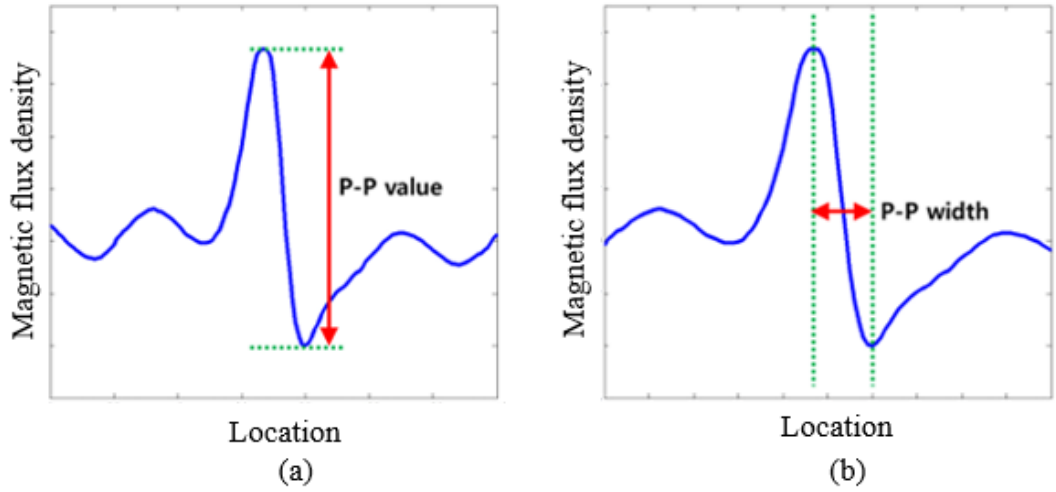


**Figure 2.17.** Typical $\mathbf{B}_z$ components: (a) Peak-to-Peak value (P-P value), and (b) Peak-to peak width (P-P width) [137].

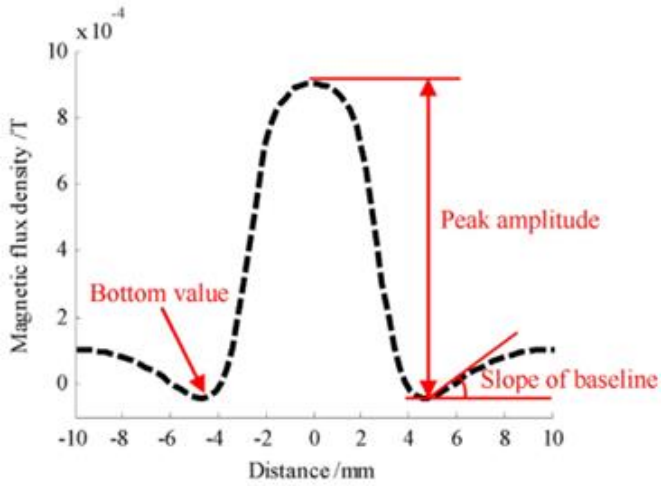


**Figure 2.18.** Spatial distribution of leakage flux density, $\mathbf{B}_x$, with three components [141].

### 2.4.3. Factors Govern Magnetic Flux Leakage (MFL) Inspection and MFL Circuit Design Requirements

MFL is governed by several factors such as magnetisation, magnetic properties of the circuit components, sensing method and defect size, shape, location and orientation.

Magnetisation is the most significant factor for reliable and accurate MFL inspection [25], [142]. The credibility and accuracy of the magnetic leakage field resulting from defects depends on the magnetisation of the inspection components [143]. The magnetisation level of the inspection component significantly impacts the ability of the MFL technique to detect defects [144], [145].

Magnetisation depends on the excitation techniques used, material properties, the dimensions and geometry of the circuit parameters. Magnetisation is generated by either a permanent magnet or an electromagnet. A permanent magnet generates a static magnetic field and does not need any external power supply. Permanent magnets are produced by heat-treating specially formulated alloys in an intense magnetic field. During the heat treatment, the magnetic domains align and remain aligned after removing the external magnetic field [146]. Permanent magnets are generally smaller and lighter than electromagnets. The most commonly used permanent magnets are ferrite, neodymium iron boron (NdFeB) and samarium cobalt (SmCo) magnets [147]. NdFeB and SmCo are the strongest permanent magnets, and NdFeB magnet has the highest magnetic strength of all permanent magnets [148], [149]. SmCo magnet can be used in higher temperature applications [150] and is more expensive [151], [152].

Electromagnets require an external power supply to generate a magnetic field. The external power supply can be direct current (DC), alternating current (AC) or pulsed current (PC). Electromagnets are typically larger and heavier than permanent magnets. However, electromagnets offer the advantage of controlling and adjusting magnetisation intensity by varying the supplied current.

The **B-H** curve is divided into three zones, as illustrate Figure 2.19. Zone-1 (under saturation) is when the material is not sufficiently magnetised. In this region, magnetic flux density (**B**) increases almost linearly and rapidly with a small change in magnetic field strength (**H**). Zone-2 (near saturation) is when the material is magnetised, and **B** still increases, but at a reduced rate with increasing **H**. Zone-3 indicates material saturation, and increasing **H** has minimal effect on **B**. For the states of material in Zone-1, where there is a lack of proper magnetisation,

the leakage field from the defects is not strong enough, does not and remains in the inspection component wall. Optimal defect detection in MFL inspections is typically achieved within Zone-2 of the **B-H** curve. When the material is magnetised, there is a significant change in the leakage signal from no defect to the presence of a defect. The material states in Zone-3 can lead to flux leakage even in the absence of defects, which is called background magnetic field (BMF) [123], [153], [154], [155]. This can diminish a defect signal-to-noise ratio and reduce defect resolution ability [4], [123], [153], [154], [155]. Increasing the BMF leads to the magnetic compression effect, which compresses and reduces the volume and density of leakage signals from defects, thereby impairing defect detection [156]. Consequently, the sensitivity of the MFL sensor depends on the operating point on the **B-H** curve of the specimen [141]. Therefore, maintaining the magnetisation level within the operating region of the **B-H** curve is essential for ensuring efficient MFL inspection.

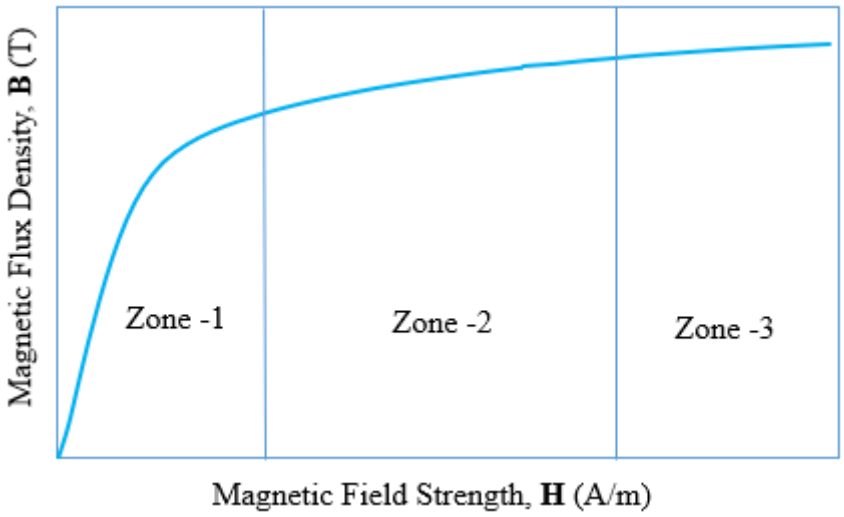


Figure 2.19. Three zones of the B-H curve: Zone-1 (under saturation), Zone-2 (near saturation) and Zone-3 (saturation).

The dimensions and geometry of the magnetic circuit determine the induced magnetisation intensity and uniform flux distribution, which are important for efficient defect detection. The geometrical design and the material properties of the magnetic circuit determine the level and quality of the magnetisation of the inspection component [144]. The reliability of the MFL inspection can be significantly improved by ensuring proper design of the magnetising system that provides appropriate magnetisation [157].

The dimensions of the magnet bridge strongly affect the performance of the magnetic circuit [154]. The length of the magnet bridge significantly impacts the efficiency of the magnetic circuit [154]. It plays the most crucial role in distributing the magnetic field generated by the magnets/electromagnets to other geometrical parameters and uniformity of magnetic flux in the inspection component, which is crucial for accurately detecting defects [144]. When there is a uniform flux distribution, smoother, more predictable and consistent leaked signals from various defects will be obtained. Unlike this, when there is a non-uniform flux distribution, a disintegrated signal will be received, resulting in an interpretation error and poor detection of flaws. The magnet bridge length significantly impacts reluctance [144], [158]. It plays the most important role in the size of the MFL device and provides space for accommodating the rest of the circuit components [144], [154]. Increasing the length of the magnet bridge increases reluctance [158], results in a heavier magnetic circuit (reduces handling) [159], causes magnetic field reduction in the inspection component [25], improves the uniformity of magnetic flux until a particular value [144], [155], which improves the detectability of far-side defects [155] and decreases the coupled magnetic field in the air, which enhances the inspection sensitivity [25]. When the magnet bridge is short, the MFL circuit will be smaller, easier to handle and require a smaller magnet. However, a magnet bridge that is too short is not desirable because it needs to have enough room to accommodate other components and a too-short magnet bridge results in a smaller magnet that will not magnetise the inspection components properly [144], [154].

The magnet bridge height significantly impacts the performance of the magnetic circuit, the magnetic field density in the circuit [154] and the spatial distribution of the leakage flux density caused by defects [141]. Increasing this parameter increases the distribution of the leakage flux density from defects [141]. Reduction in the magnet bridge height limits the flow of magnetic flux, affecting the magnetic field density in the circuit [154]. As the pole piece is a path for magnetic flux, decreasing the height of the pole piece will reduce the flux spreading into the air and increases magnetic strength in the inspection component [25]. Since permanent magnets provide a finite/constant magnetic flux, the magnetisation level achieved on the inspection component depends on its thickness [120] and length [25]. The induced magnetic flux density in the inspection component drops with increasing its area when the same level of magnetic field strength is applied [120], [25].

Magnet dimensions significantly affect the magnetisation of the inspection component [25], [155]. Figure 2.20 shows the relation between the magnetic flux density and the magnet

dimensions, width and thickness. While increasing magnet width, magnetic flux density increases sharply at first and slows down once the inspection component is saturated. The magnetic flux density increases slightly with increasing magnet thickness. Thus, the magnet width has a more significant effect on the magnetisation level of the inspection component than the magnet thickness. The area of the magnet is directly proportional to the magnetic force and the gap magnetic flux density, as given in Equation 2.13. This equation describes magnetic force due to a magnetic field in an air gap and is used in practical applications where magnetic circuits and air gaps are involved. The gap magnetic flux density is the amount of magnetic flux passing through a unit area in the gap between the pole pieces and the surface being inspected [25].

$$F = \frac{B_g{}^2 S_m}{2\mu_0} \qquad 2.13$$

Where F is the magnetic force, $B_g$ is the average gap magnetic flux density, and $S_m$ is the area of the magnet.

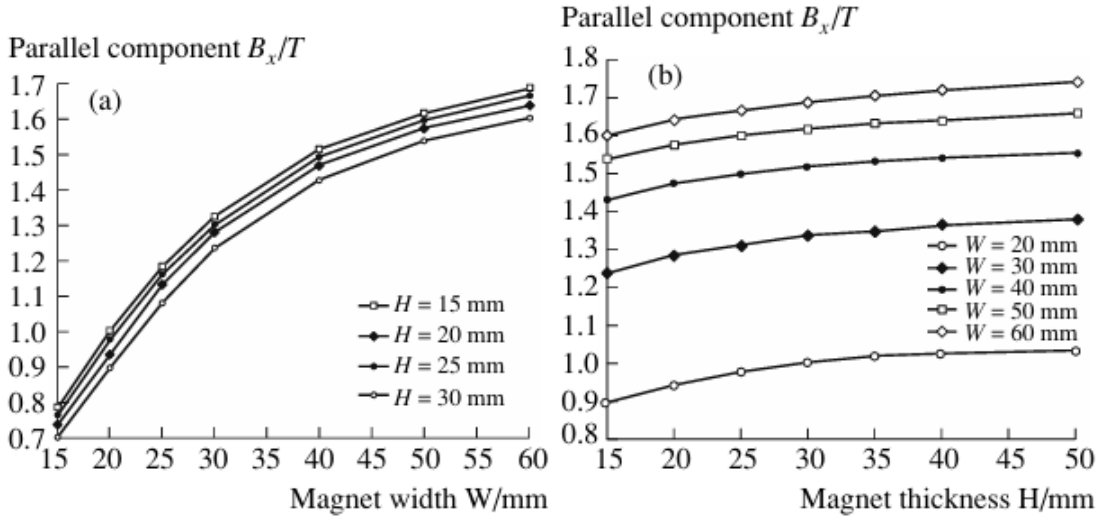


**Figure 2.20**. (a) Magnet width and (b) magnet thickness influence on the magnetisation level of the inspection component [25].

Lift-off (sensor, magnetiser and both) is a gap in the magnetic circuit caused by debris, welds, coating thickness, or wear-resistant material employed to prevent sensors or high-hardness sediments on the internal surface of the pipe [160], [161], [162], [163], [164], [165]. Lift-off affects the magnetisation and measurement steps of the MFL testing process, as shown in Figure 2.21 [161]. The magnetiser lift-off significantly affects the magnetisation step by influencing the magnetic circuit's ability to magnetise the inspection component sufficiently

and produce a strong leakage field in the presence of defects [155], [161]. The sensor lift-off notably influences the sensor's ability to measure the actual flux leakage field accurately [161], [163], [164] and determine the exact location of defects [161]. It results in a fringing effect. Lift-off results in a reduction of measured peak and baseline MFL amplitude [161], [163], [164]. Figure 2.22 (a) and (b) show simulation results of leakage signal for the magnetiser, sensor and the two lift-offs simultaneously, and the leakage amplitude was measured while varying the three types of lift-offs, respectively [163]. When comparing the same magnitude of sensor and magnetiser lift-off, sensor lift-off has a more significant effect on the measured peak MFL amplitude than magnetiser lift-off [161], [163], [164]. Increasing the two lift-offs will result in the most significant reduction in peak MFL amplitude [161], [163], [164]. Inaccurate MFL signal measurement results in either missing small defects or underestimating big defects [161], [163], [164], which can impair the ability and reliability of the MFL device to detect defects [162], [164]. Even a small lift-off can significantly reduce the magnitude of the measured MFL signals [161], [163], [164]. Therefore, reducing the lift-off is important to prevent the missing or under-sizing of defects [161], [163], [164].

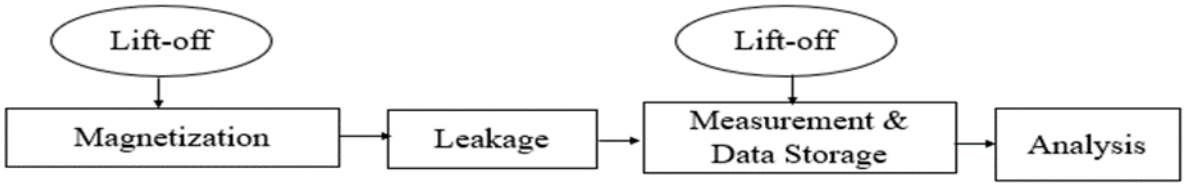


**Figure 2.21.** Effects of lift-off on the magnetisation and measurement stages [161].

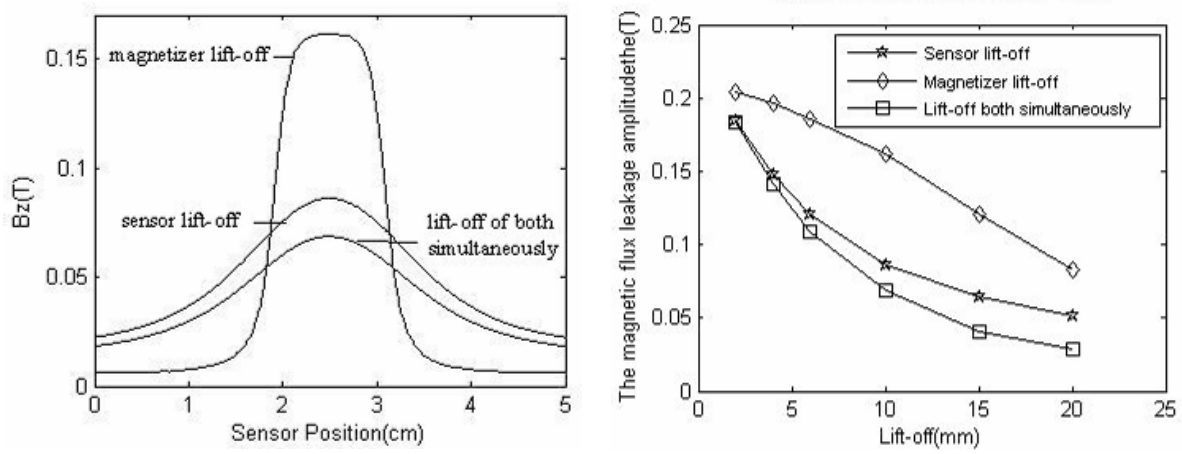


(a) (b)

**Figure 2.22.** (a) The defect leakage signals for the magnetiser, sensor and the two lift-offs simultaneously, and (b) The magnetic flux leakage amplitude while varying the lift-offs [163].

The MFL inspection is significantly affected by various characteristics of the defects, including their size, shape, location and orientation.

The size of a defect, particularly its length, width and depth, affects the magnitude and shape of the MFL signals. A number of parameters can be extracted from the MFL leakage signals [166]. The length of a defect can be obtained from the distribution of leakage signals, as shown in Figure 2.23. It can be extracted from the lateral distance between positive and negative peak values (distance between peak to peak (DPP)) of the normal component of the MFL signal [167], [168], [169], [170], [171], [172] and the pulse width of 65% of the peak amplitude of the horizontal component of the MFL signal [167], [169]. The width of the defect is determined from the pulse width of 65% of the peak amplitude of the horizontal component of the MFL signal [169]. The peak amplitude of the horizontal and normal components of the MFL signals are mainly dependent on the defect depth [140], [167], [169], [173], [174], [175]. The peak amplitudes increase with defect depth [176], [177], [178]. The length and width of defects are typically more directly measured parameters [166]. The depth of a defect is the most critical factor in defect identification, as it reveals how close the defect is to potentially causing a leak. It is the most difficult parameter to identify [166], [168], [174], [177], [179]. This is due to the amplitude of the leakage signal depends not only on the defect depth but also the defect length and width [169], [174], [177], [180], narrow-deep and wide-shallow defects are challenging to predict [168], [170], and complex relationship between the MFL signals and geometry of defects [181]. Therefore, using secondary signal parameters to predict difficult-to-identify defects [170] or using advanced MFL signal analysis techniques, such as machine learning methods [182], [183], wavelet analysis [184], neural networks [4], [113], [166], deep learning methods [185], statistical analysis [186] and others are important for reliable and accurate defect detection.

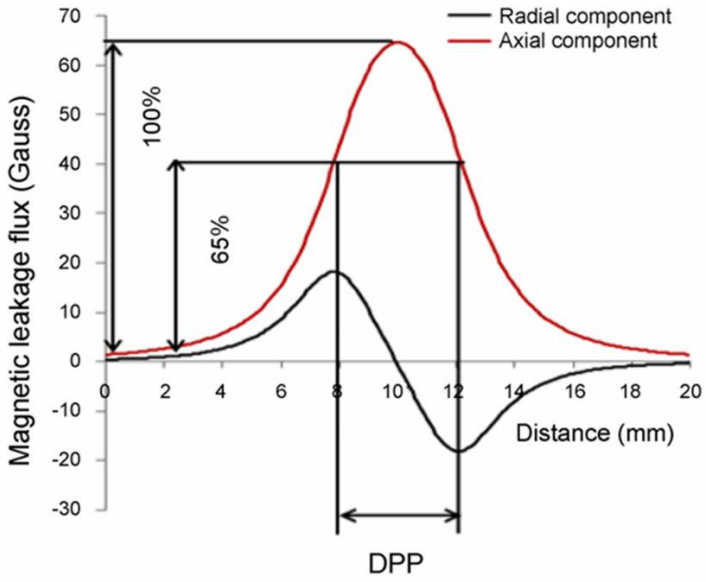


**Figure 2.23.** The horizontal and normal components of the MFL signal distributions indicate the length of the defect [167].

The shape of a defect also plays a critical role in the MFL signal. Defects with sharp edges generate stronger signals compared to those with rounded edges. This is because sharp edges cause an abrupt change in the magnetic flux direction [168], [184], [187], [188].

The location of a defect within the inspection component affects the MFL signal. Defects closer to the surface (near-surface defects) create stronger leakage fields. In contrast, those located deeper within the material (far-surface defects) produce weaker signals since the defects are further from the sensor and the presence of a ferromagnetic wall between them [189], [190]. Figure 2.24 shows the MFL signals obtained from near- and far-surface defects [189]. The difference in signals for the same dimension defect for near and far-surface defects could lead to an underestimation of their size or even result in the defect being missed entirely. For this reason, various techniques have been developed to differentiate near- and far-surface defects [122], [189], [191], [192], [193].

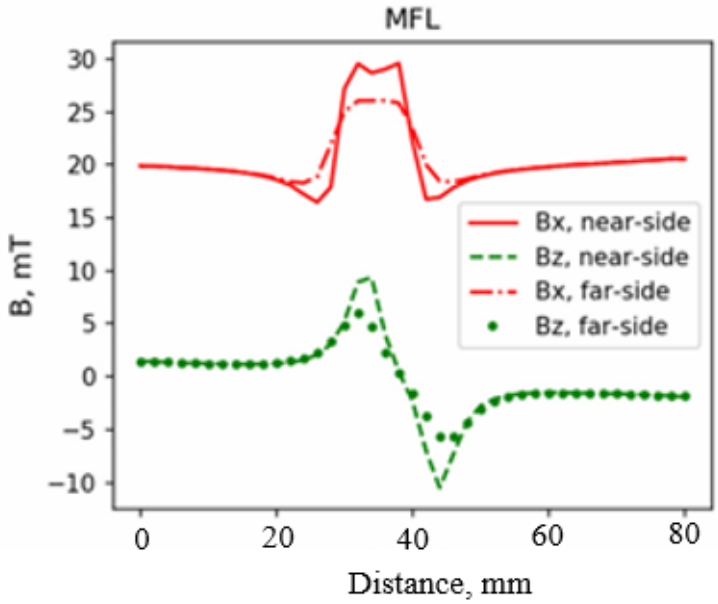


**Figure 2.24**. The horizontal and normal components of the MFL signals for near- and far-surface defects [189].

Finally, the orientation of the defect relative to the direction of magnetisation is another crucial factor. Figure 2.25 shows the relationship between the MFL signals and defect orientation [194]. Defects aligned perpendicular to the magnetic field lines typically produce the strongest MFL signals, as they disrupt the field more effectively. In contrast, defects parallel to the magnetic field produce weaker signals [102], [194]. Although the amplitude is small, detecting cracks parallel to the magnetisation direction is possible [195], [196]. This directional sensitivity requires careful consideration during inspection planning to ensure that the magnetic field is applied to maximise defect detectability.

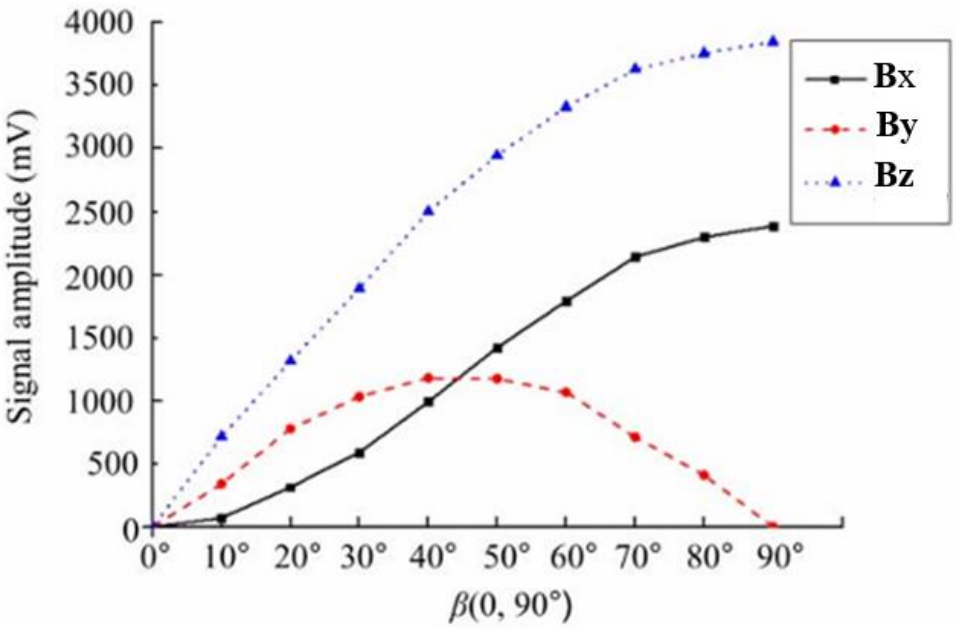


**Figure 2.25**. Effect of the angle between magnetisation and defect on the MFL signal amplitudes [194].

### 2.4.4. Existing Magnetic Flux Leakage (MFL) Devices

A pipeline inspection gauge (PIG) is a robotic tool commonly used to either clean (a cleaning PIG) or inspect (a smart PIG) oil and gas pipelines [197], [198], [199]. Smart PIGs employ a single or different integrated NDT technique such as MFL, UT, ECT and Electromagnetic Acoustic Transducer (EMAT) [198], [200]. An MFL PIG is the most commonly used inline inspection (ILI) tool to determine the integrity of pipelines and identify both internal and external defects [144], [201], as shown in Figure 2.26 (a) [202]. The MFL PIG is the most widely used ILI technique due to its high efficiency, robustness, ability to detect different types of defects, high degree of automation, working principle simplicity, not being affected by transportation media and good applicability to both oil and gas pipelines [201], [203], [204]. These PIGs are inserted into the pipeline from one end and propelled by the oil and gas flow to the other end of the pipeline, performing inspections without interrupting service [144], [199], [205], [206]. The MFL PIG surveys are typically carried out every ten years unless certain factors necessitate more frequent inspections [207], [208], [209]. Typical MFL PIG has a battery module (power supply), a position-tracking module (PIG locator with odometer), a data acquisition system (DAS), and many MFL circuits (magnetic module) [154], [199], as shown in Figure 2.26 (b) [154]. The battery module provides the energy needed by the position-tracking module and the data acquisition system. The position tracking module logs the MFL signal and maps the geographical coordinates of the pipeline where the magnetic flux leakage

occurs, indicating the locations of potential defects. An array of magnetic circuits mounted on the MFL PIG induces a magnetic field in the pipeline wall as the PIG travels through, and sensors mounted on the PIG between the magnetic poles detect and record the leakage field in the presence of defects [154], [206]. After the tool is removed from the other end of the pipeline, experts analyse the gathered data to estimate the severity and location of defects [144]. One of the drawbacks of the MFL PIG is its difficulty navigating narrow bends, valves, connectors and welded joints [206].

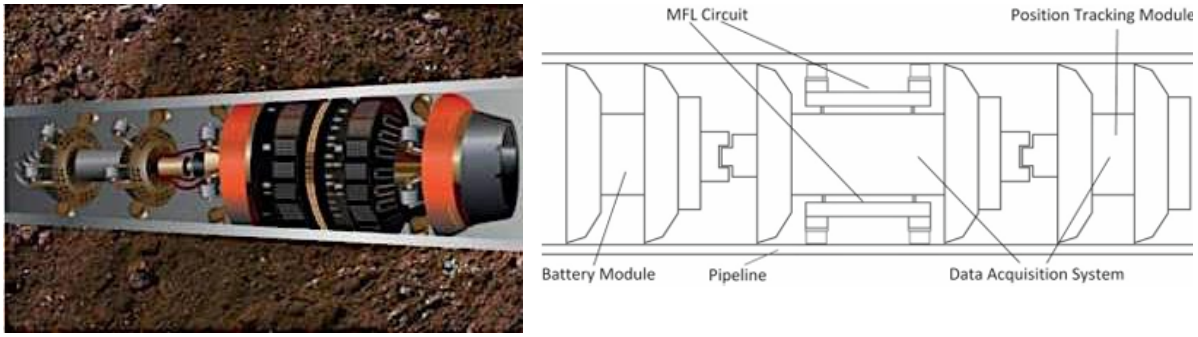


(a) (b)

**Figure 2.26.** A typical MFL pipeline inspection gauge (PIG) system (a) [202] and schematic of its components (b) [154].

An MFL tank floor scanner is a device used for non-destructive testing of storage tanks over large areas, providing high-speed and efficient inspection [192], [210], [211], [212]. Figure 2.27 (a) and (b) show an MFL tank floor scanner and a person running an MFL tank floor scanner, respectively. Unlike PIG, which is done while in service, the MFL tank floor scanner inspection must be carried out after emptying and cleaning the storage tanks [193]. The MFL tank floor scanner has the following key components: scanning head, mainframe (main handle section), user control, tablet, and batteries, as shown in Figure 2.27 (a). The scanning head is a crucial component that connects to the mainframe. It mainly includes the variable-strength magnetic bridge and the MFL sensors, which induce a magnetic field and detect defects on the tank floor. It also includes a magnetic position indicator to identify the level of magnetic strength applied to the inspection surface, a bridge height adjuster to adjust the bridge height position, a cover plate to protect the magnet bridge and the MFL sensors head during scanning and cable ports to connect the scanning head to the main frame. The mainframe contains the essential electronics and processing units. It links the user control and tablet to the scanning head and is the central data acquisition and control hub during inspections. The user control enables the operator to interact with the scanner, providing controls for navigation, data acquisition and all necessary operational functions. It ensures the scanner can be manoeuvred

effectively across the tank floor. The tablet is equipped with the SIMS GO data acquisition software, which controls the scanner and processes the data collected during inspections. It provides an interface for operators to monitor and adjust the scanning process. The scanner is powered by rechargeable batteries, which provide the necessary energy for the operation of the scanning head, mainframe and other components [213].

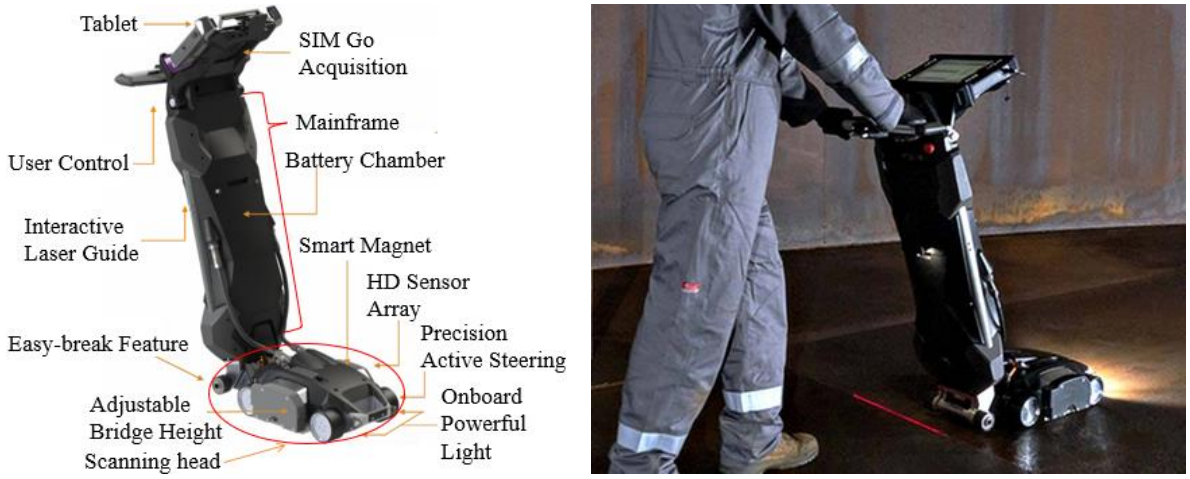


(a) (b)

**Figure 2.27.** (a) An MFL tank floor scanner and its components [213], and (b) A person running the scanning manually [214].

## 2.5. State-of-the-art in Magnetic Circuit Design Improvement

A number of studies were conducted to improve the magnetic circuit design and enhance the MFL inspection. Parra-Raad and Roa-prada [154] proposed a multi-objective optimisation approach using a 2D finite element analysis, a Lumped model and a genetic algorithm to optimise the design of the magnetic circuit of an MFL device. The objective was to minimise the dimensions of a magnetic circuit of an MFL PIG by adjusting magnet bridge length, magnet bridge thickness and lift-off dimensions while obtaining maximum leakage field from flaws. The Lumped model was used to build a physical circuit and compare its results with the 2D finite element model. The genetic algorithm was used to design the optimum magnetic circuit by improving the magnetisation level of the inspection component at the midpoint between magnets. The normalised flux density in the sample, $\mathbf{B}_t$, is directly proportional to magnet bridge thickness and inversely proportional to magnet bridge length and lift-off. Figure 2.28 (a) shows the optimal magnetic circuit. However, the optimised lift-off, 24 mm, is too big. The experimental validation of an optimum magnetic circuit design showed the best performance compared to non-optimal circuits when introducing a 5 mm radius and 6 mm depth defect, as shown in Figure 2.28 (b).

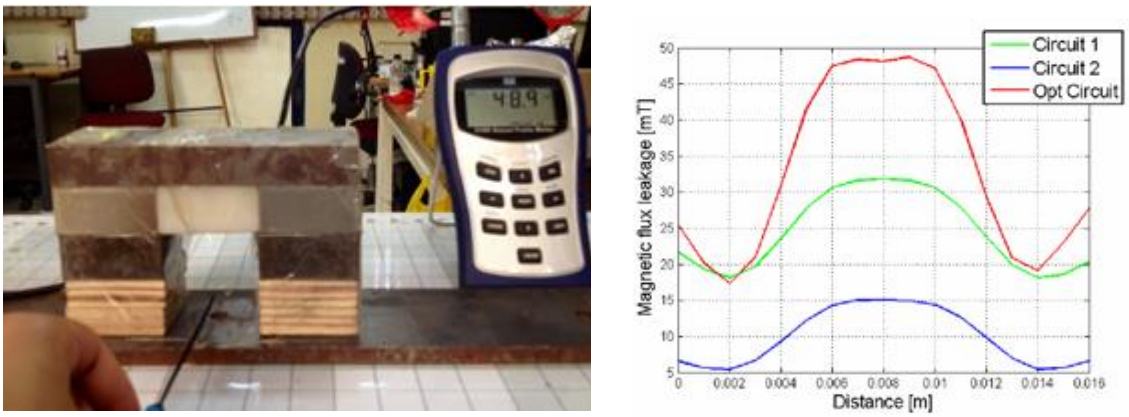


(a) (b)

**Figure 2.28.** (a) The optimal magnetic circuit, and (b) Comparsion of the performance of the optimal magnetic circuit with two non-optimal circuits [154].

Xiao-chun [25] conducted a 3D finite element analysis to improve the defect detection performance of the magnetic circuit of the MFL system by analysing magnet size, magnet pole spacing and pole piece thickness. The output parameters for selecting the magnet size were magnetisation level, gap magnetic flux density and magnetic force, whereas signal-to-noise ratio (SNR) was measured to determine the magnet pole spacing and pole piece thickness. Experimental analysis was carried out to verify the flow detection capability of a designed magnetic circuit for inspecting components with and without defects. The result showed a distinct difference between the leakage signal obtained with and without defects. It was concluded that the designed magnetic circuit could effectively magnetise the inspection component, and a detectable leakage field would be generated in the presence of a defect.

Ou et al. [215] proposed a pot-shaped magnetic circuit structure to address the edge effect caused while using a conventional U-type magnetic circuit using a 3D finite element analysis. Figure 2.29 shows the U-type and the pot-shaped magnetic circuit structure models. The main objective was to use the pot-shaped circuit structure and improve the magnetisation level of the inspection component between the two magnets, which determines the leakage field in the presence of defects and enhances defect detection. The magnetisation level was compared using the two magnetic circuit structures in simulation. The pot-shaped magnetic circuit structure had a higher magnetisation level and did not show any edge effect (the magnetic field in the inspection component was concentrated between the two magnets). For the U-shaped magnetic circuit structure, the magnetisation level achieved was lower, and the magnetic field was spread out throughout the width of a plate. When increasing the plate width, the magnetic flux density of the U-type magnetic circuit structure significantly decreases. In contrast, the

pot-shaped magnetic circuit structure was not affected by the plate width, as shown in Figure 2.30. The experimental validation of the pot-shaped magnetic circuit structure creating a defect showed a significant correlation with simulation.

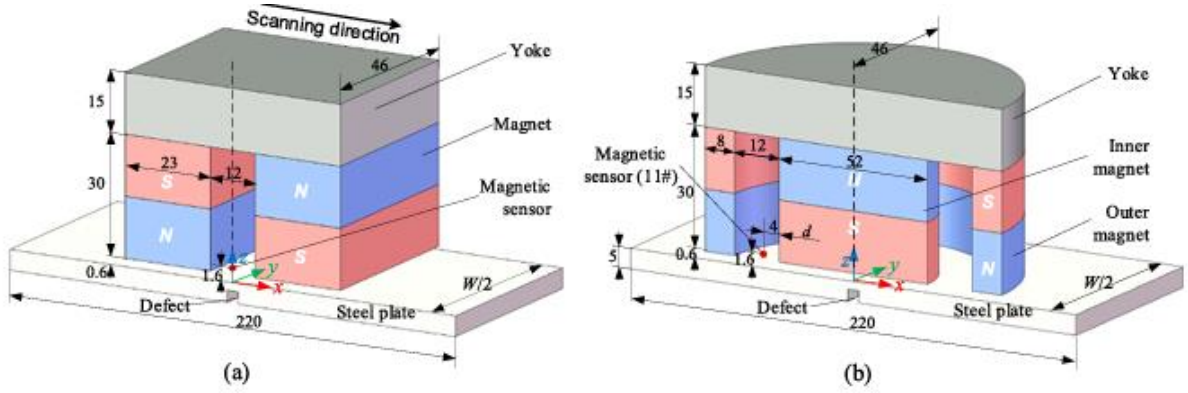


**Figure 2.29.** Half-section of: (a) Conventional U-type magnetic circuit, (b) Pot-shaped magnetic circuit [215].

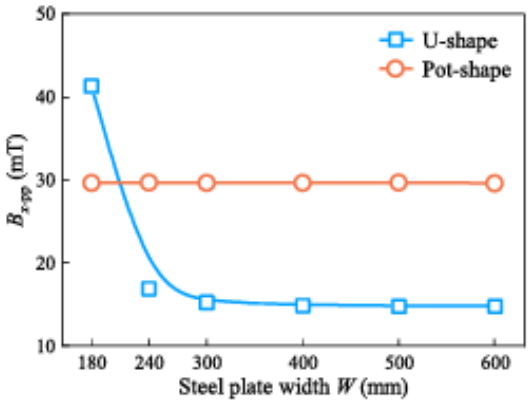


**Figure 2.30.** The effect of the plate using U-shaped and pot-shaped magnetic circuits [215].

Norouzi and Ravanbod [144] studied different magnet bridge lengths to find the optimal length by measuring the quality of the flux distribution inside the sample or flux smoothness length using a 2D finite element method. The width of the magnet required to reach a 1.8 T saturation point was determined by trial and error. Three different magnet bridge lengths, optimal length, shorter and longer lengths, were developed. The flaw detection sensitivity of optimal (35 cm), shorter (20 cm) and longer (50 cm) magnet bridge lengths was studied by simulating various groove flaws with different depth and width. The results showed the highest sensitivity using the optimal magnet bridge for different defect widths; however, all the magnet bridge lengths have almost the same sensitivity for different defect depths. It was concluded that the optimisation goal was to have uniform flux distribution inside the magnet bridge. Flaw detection sensitivity also improved with optimal magnet bridge length.

Kara and Çelik [123] proposed a non-linear magnetic equivalent circuit (MEC) model based on Kirchhoff's voltage law to determine the MFL system's dimensions affecting flux distribution. The MEC model incorporated various factors affecting magnetic flux, including non-linear behaviours of magnetic materials, winding leakage flux, horizontal leakage flux and fringing effects. The research found that the widths of the pole and the distance between the two poles significantly impact the performance of the MFL system, particularly in terms of flux density and error rates in defect detection.

The background magnetic field in the air (without defects) causes the magnetic compression effect (MCE), which reduces and compresses the leakage signal from defects [156], [216]. Since magnetic field lines do not cross each other [217] and magnetic diffusion is impeded in areas with high magnetic flux, the leakage signal from the defect is inversely proportional to the background magnetic field [156], [216]. Thus, Sun and Kang [218] proposed magnetic shielding on the MFL system to get a near-zero background magnetic field and increase leakage signal from defects, as shown in Figure 2.31. The shielding was introduced to collect and drive away the background magnetic flux and create a near-zero background magnetic region in the shielded space. The simulation and experimental results showed an increased leakage signal while using shielding compared to the conventional MFL system. Figure 2.32 shows the simulation result of the x and y-component leakage signals using shielding and a conventional MFL device.

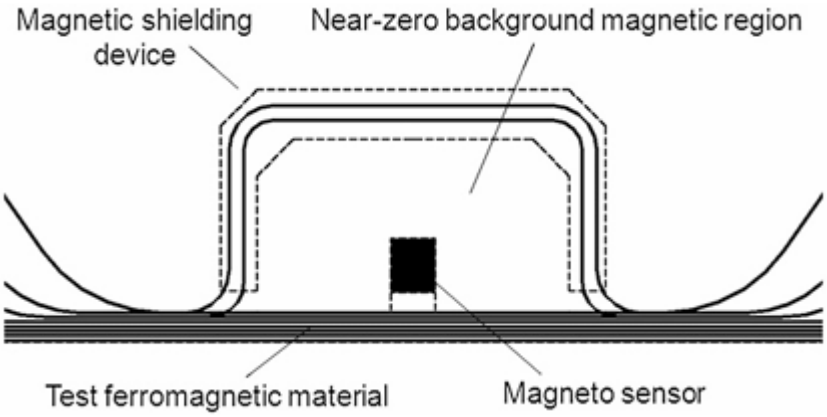


**Figure 2.31.** Magnetic shielding to create near-zero background magnetic region [218].

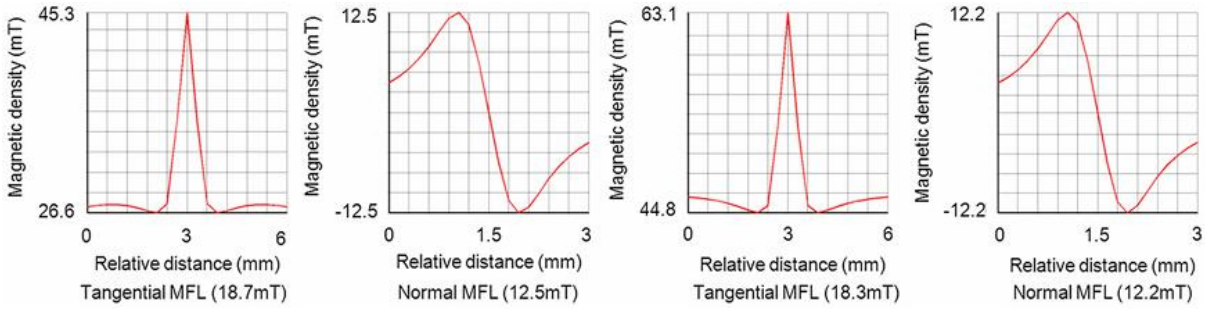


(a) (b) (c) (d)

**Figure 2.32.** The horizontal component of the MFL signal (a) and z (b) components of leakage signals using magnetic shielding in the MFL device. The horizontal (c) and z (d) components of leaking signals using conventional MFL device for a notch defect of 1 mm width, 1 mm depth and 20 mm length in all cases [218].

In conventional MFL, sensors are installed in a non-ferromagnetic protecting support (NFMS). NFMS is a protective material support for sensors made from non-ferromagnetic material. However, its thickness introduces lift-off distance from the inspection surface, which reduces sensitivity during testing, as magnetic field strength decreases with distance. Wu et al. [219] suggested a high-permeability ferromagnetic support (FMS). FMS is a protective material support for sensors made from high-permeability ferromagnetic material. It guides more leaked magnetic fields from defects into the sensor location based on Hopkinson's law, which can improve the sensitivity. Hopkinson's law states that materials with high reluctance reduce flux, while materials with high magnetic permeability allow more flux, as shown in Equation 2.12. Figure 2.33 (a) shows the MFL probe with the non-ferromagnetic and ferromagnetic support. The leakage signal amplitude obtained using FMS was approximately 31.6% greater than that of NFMS at a higher magnetisation current. Figure 2.33 (b) shows numerical simulation leakage signals obtained using FMS and NFMS.

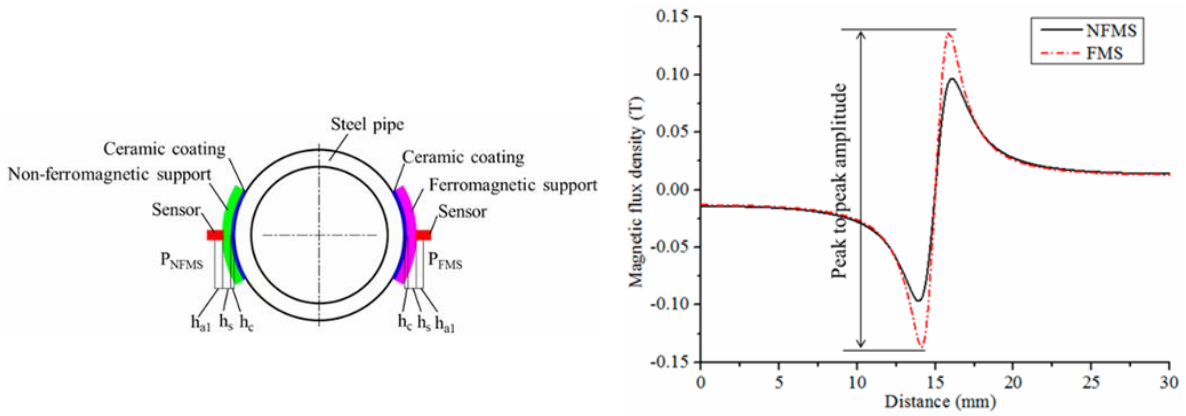


(a) (b)

**Figure 2.33.** (a) The left side of the pipe shows the MFL probe with the non-ferromagnetic support (NFMS) and the right side is the probe with the ferromagnetic support (FMS). (b) The numerical leakage signal obtained using NFMS and FMS [219].

A sensor lift-off layer based on air or non-ferromagnetic wear-resistant material has been used to prevent sensors from wearing. However, this layer causes attenuation of the leakage signal. Therefore, Tang et al. [160], [220] introduced a ferromagnetic sensor lift-off layer with a through groove design to enhance the MFL detection sensitivity and the leakage signal amplitude while addressing common challenges in the conventional MFL method. Figure 2.34 shows the conventional and the new MFL methods. The leakage signal amplitude and signal peak obtained using the new and conventional methods were compared in simulation and experimentally, respectively. Figure 2.35 shows the signal peak obtained using the conventional and the new method with and without slot on the ferromagnetic lift-off layer. The leakage signal amplitude obtained while using the new method with slotted ferromagnetic lift-off layer was higher and lift-off tolerant than those obtained by the conventional method. When comparing conventional method with non-grooved ferromagnetic lift-off layer, non-grooved ferromagnetic lift-off layer improves the performance of the MFL for lift-off layer less than 1.5 mm above this lift-off conventional method performs better. However, Wu et al. [219] claimed using non-slotted ferromagnetic guiding improves the MFL performance. This was since Wu et al. [219] used 0.5 mm lift-off layer. Moreover, Tan et al. [160] considered groove and crack widths from 0.2 mm to 1 mm with a 0.2 mm gap. However, the groove width needs to be adjusted (has optimal width) according to the defect width, which is difficult for real-life applications due to various defect sizes.

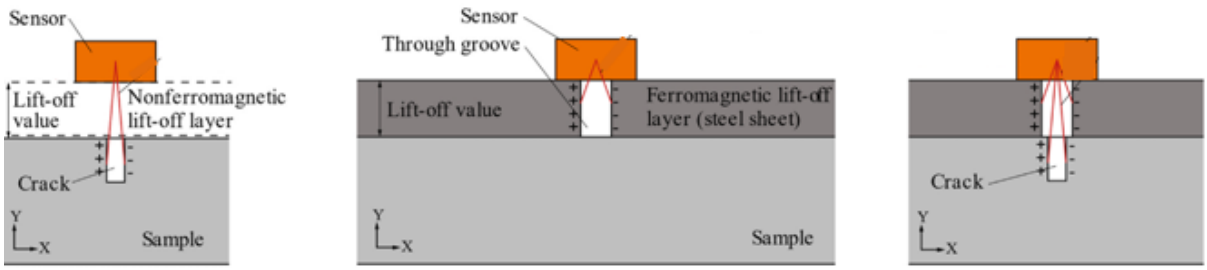


(a) (b) (c)

**Figure 2.34.** An MFL system based on (a) Non-ferromagnetic lift-off later, (b) Ferromagnetic lift-off layer with slot for an inspection component without a defect, and (c) Ferromagnetic lift-off layer with slot for an inspection component with a defect [160].

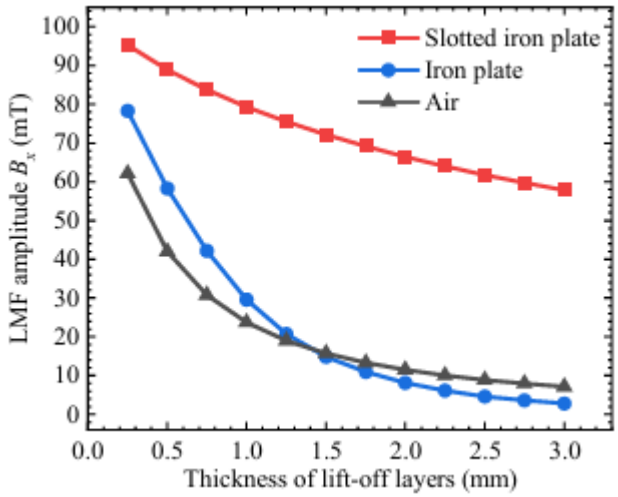


**Figure 2.35.** The leakage signal amplitude vs thickness of lift-off layers for slotted iron plate, iron plate without slot and air lift-off layer [220].

## 2.6. Gaps Identified from Literature Review

The current state-of-the-art describes the effect of a limited number of magnetic circuit parameters on the magnetisation, uniform flux distribution, defect detection and compactness of the MFL device. To date, little research has been conducted on the design optimisation and the comprehensive effect of multiple magnetic circuit parameters of the MFL system for a range of sample geometries, such as flat plates and curved surfaces, pipes and elbows. The effects of sample geometries on the performance of MFL devices have not been studied. Previous studies have considered 2D models and/or used plates in 3D models to represent pipes. However, signals obtained in the 3D analyses are significantly reduced compared to its 2D equivalent. This is due to the confinement of magnetic flux within a plane in the 2D model [111], [175]. The 3D models help to get accurate results [175], [221]. Additionally, the most

commonly used MFL system such as the pipeline inspection gauge (PIG) inspection cycle is 10 years, which is not sufficient and frequent for corrosion susceptible areas. Therefore, this research designs a remote, permanently installable MFL system for monitoring localised corrosions in corrosion-susceptible, hazardous and difficult-to-access regions of plates, pipes and elbows using 3D FEA, optimisation algorithms and experimental study. The effect of sample geometries on the performance of the MFL system is studied using both flat and curved surfaces.

# 3. MATERIALS AND METHODS

## 3.1. Introduction

The methodology proposed to investigate and optimise the MFL system consists of a simulation-led design development based on 3D finite element analysis (FEA) using COMSOL Multiphysics software with its AC/DC and Optimisation Modules. Moreover, an experimental programme was used to verify and validate the developed design and characterise different defect parameters. The simulation-led design development technique for the MFL problems was first used before the experimental investigation because it allows for a large number of iterations through design solutions at no/minimum cost and high accuracy.

The implementation of the finite element (FE) model is described, including the derivation of Maxwell's equations that form the foundation of the simulation and experiment to understand the basic theory in which the research methodology used in this project is established. FE model development is presented, highlighting the mesh generation and a mesh convergence study. The simulation-led design development involves parametric analysis and parametric and topology optimisation to refine the model and improve its accuracy. An overview of the optimisation strategy is provided, highlighting the optimisation algorithm implemented and the type of optimisation used. The chapter also covers the experimental procedures to validate the 3D FEA results. The materials used in the study and their magnetic properties are presented.

## 3.2.Materials

The material types and magnetic properties of the magnetic circuit components are given in Table 3.1. A strong permanent neodymium-iron-boron (NdFeB) magnet was used as a magnetic field source in the circuit. NdFeB is the strongest permanent magnet and has a high remnant flux density. The magnet bridge and pole pieces were made of the same ferromagnetic material, AISI 1020 steel. The AISI 1020 steel has a high saturation magnetisation, the maximum magnetisation that a material can attain in an applied magnetic field, allowing the circulation of the magnetic field in the circuit without being saturated. The inspection components, plate and straight pipe, were made of S275 and API 5L X42 steels, respectively. S275 steel is low-carbon steel commonly used in oil and gas industry storage tanks [222], [223] due to its strength, durability, versatility and cost-effectiveness [224]. API 5L X42 is widely used in oil and gas pipelines due to its excellent durability, cost-effectiveness, low maintenance, good balance of strength, toughness, formability and weldability [225], [226],

[227], [228]. It is less prone to weld defects and has reduced welding costs. It has shorter lead times; thus, it is widely available [228]. The final inspection component, a 90-degree pipe elbow, was made of ASTM A234 (ASME/ANSI B16.9). ASTM A234 steel elbow is a widely used pipe fitting in oil and gas pipelines due to its strength, durability, and ability to withstand pressure and temperature [229], [230]. The 90-degree pipe elbows are widely used in transportation pipelines [231]. Due to the elbows' curved nature (radii), a centrifugal force is generated, which plays a significant role in the flow dynamics [232]. All tests were completed in the air. The chemical and composition magnetic susceptibility of the three samples are presented in Appendix A Table A.1 and A.2, respectively.

**Table 3.1.** The material types used and their magnetic properties.

| Component | Material | Magnetic Properties |
|---|---|---|
| Magnet | NdFeB | Permanent magnet |
| Magnet bridge | AISI 1020 Steel | Ferromagnetic |
| Pole piece | AISI 1020 Steel | Ferromagnetic |
| Plate | S275 | Ferromagnetic |
| Pipe | API 5L X42 | Ferromagnetic |
| Elbow | ASTM A234 | Ferromagnetic |
| Environment | Air | Paramagnetic |

## 3.3. Materials Magnetic properties

The **B-H** loop (hysteresis loop) shows the relationship between the induced magnetic flux density (**B**) and the magnetic field (**H**). It shows how materials respond to an applied magnetic field, providing insight into its magnetic properties. The **B-H** curve (initial magnetisation curve) provides a guideline to determine whether the specimen is sufficiently magnetised. The **B-H** loop and curves of the inspection components, i.e., plate, pipe and elbow, were obtained using a DC magnetic characterisation system at Cardiff University Magnetic Materials and Application (MAGMA) research group, as shown in Figure 3.1. Table 3.2 presents the dimensions of the plate, pipe, and elbow test samples used for DC magnetic characterisation.

Figure 3.2 shows a sample covered with electrical insulation tape fitted between pole pieces of an electromagnet with 5. 7 cm pole tips diameter and pole gaps are equal to the sample lengths as it is a closed-circuit measurement. The measurements were carried out following the BS EN 60404-4 [233], [234]. The measurement parameters used were magnetic flux density and magnetic field strength. Magnetic flux density was measured from a 10-turn **B**-coil connected to an integrating fluxmeter, while the magnetic field strength was measured using a Hall sensor connected to a Gaussmeter. A current-controlled bipolar power supply was employed to drive an electromagnet with adjustable pole pieces. The full loop takes approximately 5 minutes to avoid any dynamic effects.

Figure 3.3 shows the experimentally measured **B-H** curves for the plate, pipe and elbow. The **B-H** curves of plate, pipe and elbow are characterised by steepness, which refers to a fast increase in the **B** with a slight increase in the **H**, i.e. these materials have high permeability, allowing them to become easily magnetised. Figure 3.4 shows complete **B-H** loops of the plate, pipe and elbow, indicating that they are soft ferromagnetic materials characterised by narrow hysteresis loops. It indicates minimal energy loss as heat during each magnetisation cycle.

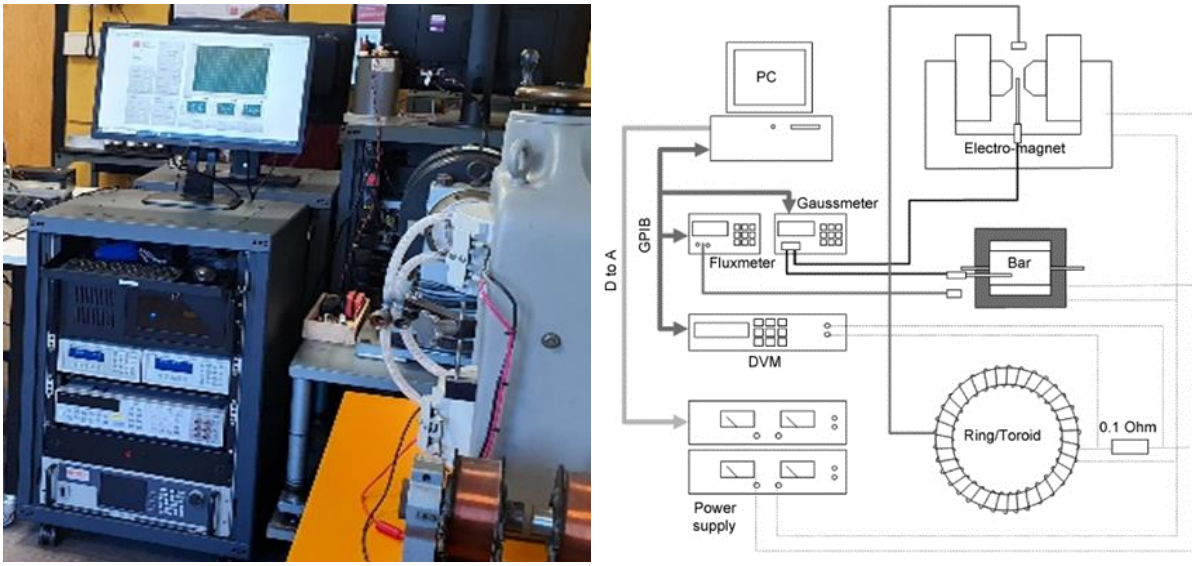


**Figure 3.1.** (a) DC magnetic measurement system. (b) Schematic of the DC measurement system [234].

**Table 3.2.** Dimensions of the plate, pipe, and elbow test samples used for DC magnetic characterisation.

| Sample | Length (mm) | Width (mm) | Thickness (mm) |
|---|---|---|---|
| Plate | 20 | 32.0 | 7.85 |
| Pipe | 20 | 30.8 | 6.48 |
| Elbow | 20 | 29.5 | 10.00 |

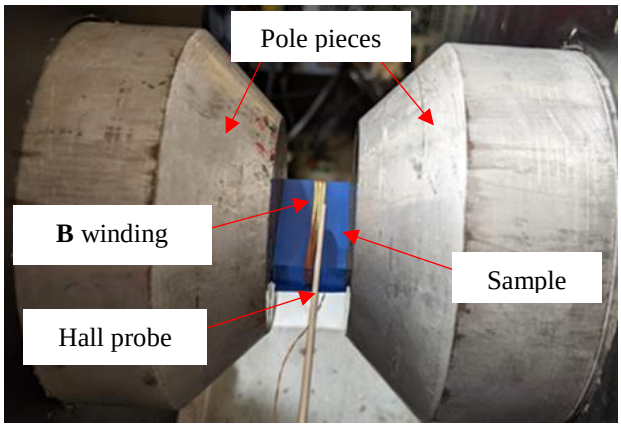


**Figure 3.2.** The sample covered with electrical insulation tape fitted between pole pieces of an electromagnet with 10-turn **B** winding and a Hall probe.

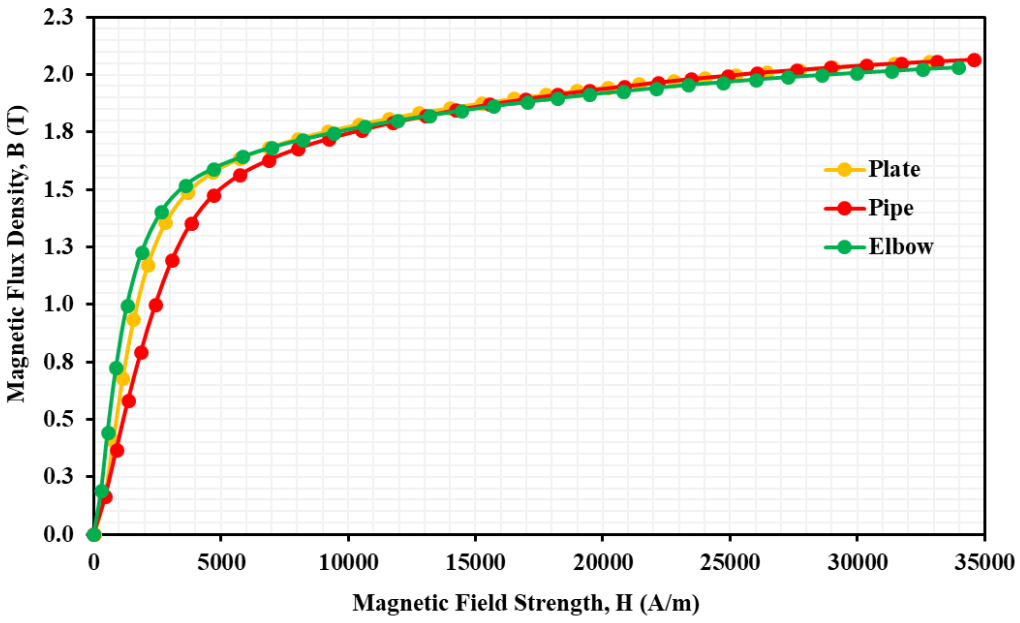


**Figure 3.3**.The initial magnetisation curves (the **B-H** curves) of the plate, pipe and elbow measured on the DC magnetic measurement system.

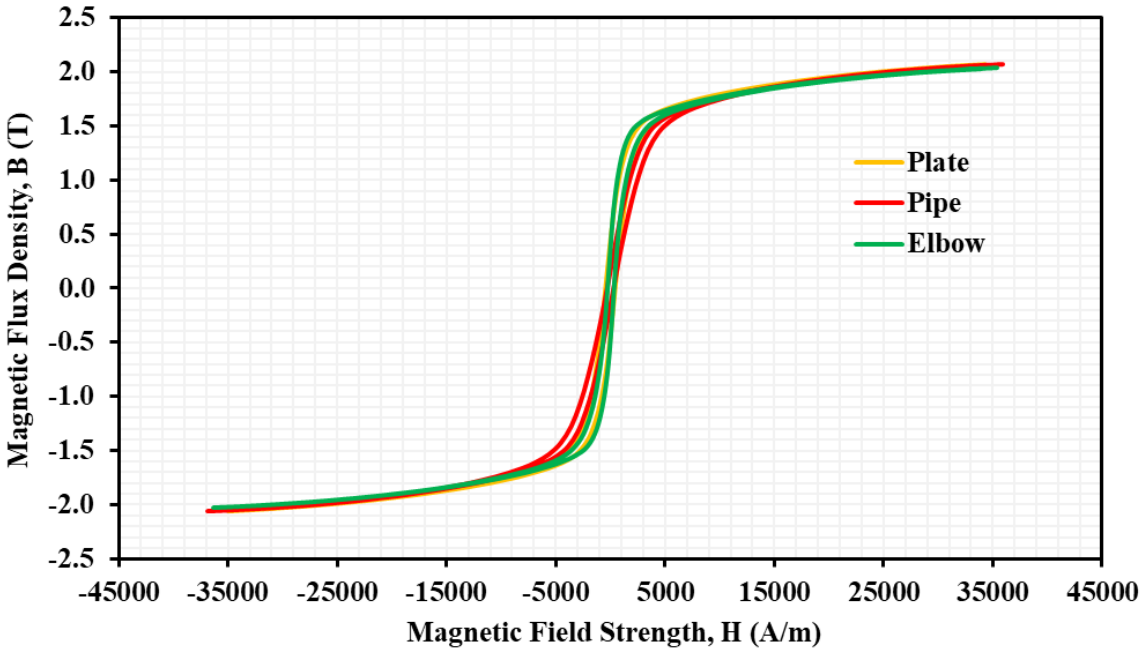


**Figure 3.4.** Complete **B-H** loops of the plate, pipe and elbow measured on the DC Magnetic measurement system.

## 3.4. Finite Element Method (FEM)

The MFL modelling techniques developed to date can be broadly classified into analytical and numerical modelling.

Analytical models for MFL are based on the magnetic dipole model or Maxwell's equations in the closed form, which describe the MFL signal and provide a quick and simple analysis [4], [235]. These methods are great for basic understanding and quick checks but are limited and may miss the details in more complicated cases, in handling complex defect geometries and real-world problems [236], [237], [238], [239]. Analytical models often rely on simplified assumptions and consider the permeability of materials linear, leading to inaccurate representation of real-world conditions and discrepancies between model predictions and actual measurements [237], [240]. Solving equations using analytical methods is almost impossible in three-dimensional space, which involves boundary conditions [111], [241], [242].

One common approach within analytical methods is two-dimensional magnetic dipole modelling due to a notch defect developed by Zatsepin and Shcherbinin [235]. This model assumes defects as magnetic dipoles (dots, lines and bands). Figure 3.5 shows a schematic diagram of a typical 2D magnetic dipole model [110]. 2a and b are defect width and depth,

respectively. The magnetic charge density is $dp = \sigma_m dy$ for a line with infinitesimal length dy [110] and causes the magnetic field distribution on the defect surface [243]. The 2D magnetic dipole model provides expressions for the tangential and normal components of the leakage field using equations derived from dipole theory, Equation 3.1 and Equation 3.2, respectively. The dipole is assumed to be distributed uniformly at the defect surfaces with density, $\sigma_m$ since the defect is relatively small compared with the radius of the pipeline [203]. However, this assumption leads to a significant error when calculating the intensity of the leakage magnetic field since the magnetic dipole (the magnetic field) along the defect depth is not constant [244].

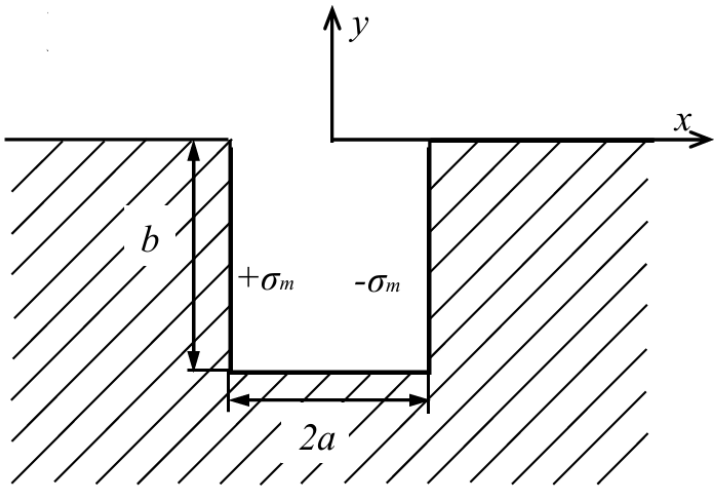


**Figure 3.5.** 2D magnetic dipole model for MFL calculation as presented by Zatsepin and Shcherbinin for a rectangular defect [110].

$$Hx = \frac{\sigma_m}{2\pi}\left[\arctan\frac{b(x+a)}{(x+a)^2 + y(y+b)} - \arctan\frac{b(x-a)}{(x-a)^2 + y(y+b)}\right] \quad 3.1$$

$$Hy = \frac{\sigma_m}{4\pi} ln\left[\frac{[(x+a)^2 + (y+b)^2][(x-a)^2 + y^2]}{[(x+a)^2 + y^2][(x-a)^2 + (y+b)^2]}\right] \quad 3.2$$

According to Edwards and Palmer [239], the magnetic charge density, $\sigma_m$, can be calculated using the following formula:

$$\sigma_m = H_0 \frac{\pi n(\mu - 1)}{\arctan n(n - \mu)} \quad 3.3$$

Where $H_0$ is a uniform applied magnetic field along the x-axis, and n is the ratio of the defect depth and the half of the width, i.e. $n = b/a$.

Numerical modelling uses computational methods to solve governing equations for magnetic fields in materials. It relies on algorithms and iterative procedures leading to approximate solutions. This technique can handle complex geometries, material properties, boundary conditions and scenarios that are difficult or impossible to solve analytically [4], [104], [169], [236]. It has high accuracy [203], [245] and offers greater flexibility [104]. For this reason, numerical modelling is preferred over the analytical method.

Finite Element Method (FEM) is one of the most commonly used numerical methods. It discretises a complex structure or object into smaller, simpler finite elements. These elements are interconnected at points called nodes, forming a mesh that represents the entire structure. Each element is analysed individually with specific mathematical equations, and the solutions are assembled to give an approximate solution for the entire system [246]. FEM can be used for a wide range of problems and boundary conditions, can incorporate varied and complex material properties, including non-linear and anisotropic materials and can handle complex and irregular geometries. Hwang and Lord used FEM for the first time to simulate MFL signals for detecting surface-breaking cracks in ferromagnetic materials [247]. Numerical methods like the boundary element and finite difference methods are best suited for linear problems. Thus, they are unsuitable for MFL problems as the specimen is always non-linear (ferromagnetic material) [248]. Therefore, FEM is the best approach for the MFL problem as it has the highest accuracy and ability to handle non-linearities.

There are a number of software packages and solvers based on the FEM. COMSOL Multiphysics was used in this project due to its powerful Multiphysics integration, user-friendly interface, detailed electromagnetic analysis, robust meshing and solver capabilities. It allows users to model and analyse complex physical systems involving multiple coupled and single physics phenomena. It enables users to directly input user-defined physics descriptions, equations and expressions into the user interface. This feature enables the modelling of unique physics phenomena not covered by the built-in physics interfaces. COMSOL Multiphysics provides parametric sweeps, design studies, and optimisation tools, enabling users to explore and optimise their designs for various operating conditions and design parameters [249].

AC/DC COMSOL Module was used in 3D FEA simulations. This module predicts and models electric and magnetic fields in static, quasi-static, transient, and time-harmonic simulations. It has a range of predefined AC/DC physics interfaces, as shown in Figure 3.6. AC/DC physics interfaces are fully Multiphysics enabled to construct and solve electromagnetics field

simulations such as electrostatics, electric currents in conductive media, magnetostatics, low-frequency electromagnetics and others. The physics interfaces formulate and solve the differential form of Maxwell's equations with initial and boundary conditions using physical quantities such as electric scalar potential V, magnetic vector potential A and magnetic scalar potential $V_m$ as dependent variables.

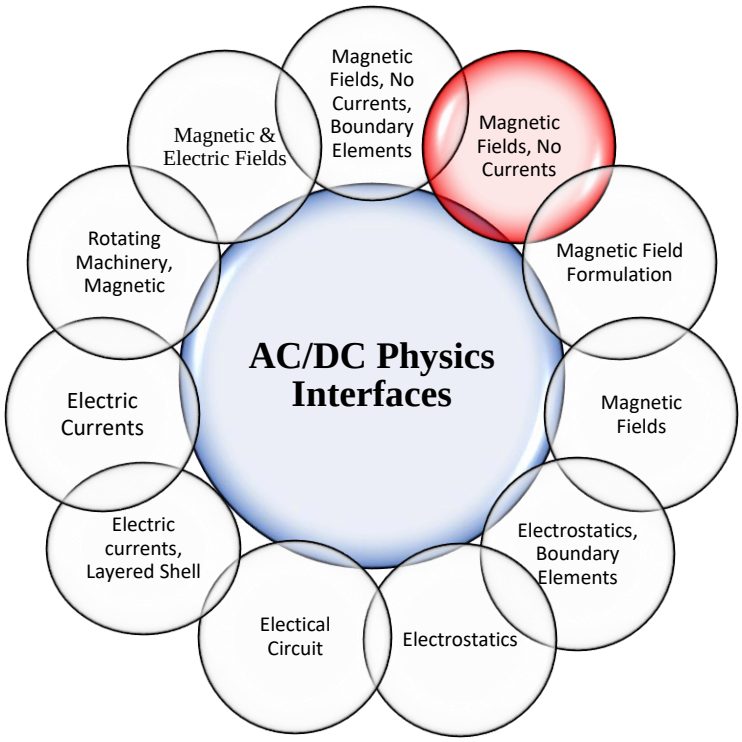


**Figure 3.6.** AC/DC physics interfaces with magnetic fields, no currents (mfnc) used in this work highlighted in red [249].

AC/DC COMOSOL Module uses Maxwell's four partial differential equations to describe electricity and magnetism for electromagnetic analysis [250]. Maxwell's equations are given as:

$$\nabla . \mathbf{D} = \rho \tag{3.4}$$

$$\nabla \times \mathbf{E} = -\frac{\partial \mathbf{B}}{\partial t} \tag{3.5}$$

$$\nabla . \mathbf{B} = 0 \tag{3.6}$$

$$\nabla \times \mathbf{H} = \frac{\partial \mathbf{D}}{\partial t} + \mathbf{J} \tag{3.7}$$

Where **D** is electric flux density or displacement, ρ is electric charge density, **E** is electric field intensity, **B** is magnetic flux density, **H** is magnetic field strength, and **J** is current density.

The equations were derived from Gauss's, Faraday's and Ampere's laws. Equation 3.4, known as Gauss's law for electricity, describes that the outward electric flux per unit volume from a point is directly proportional to the free electric charge density at that point. Equation 3.5 is Faraday's law of electromagnetic induction. It states that an electromotive force (emf) is induced in a conductor or a coil when there is a change in the magnetic flux linked with that conductor or coil over time.

Gauss's law for magnetism, Equation 3.6, describes the number of magnetic field lines entering a closed surface equal to the number of magnetic field lines that exit that surface, as illustrated in Figure 3.7. Therefore, the net magnetic flux density **B**, divergence of **B**, is zero for the closed surface. That means, unlike electric charges that come in two types, positive and negative charges, and exist independently, magnets exist as a dipole; a north pole always comes with a south pole. Thus, no magnetic monopole exists.

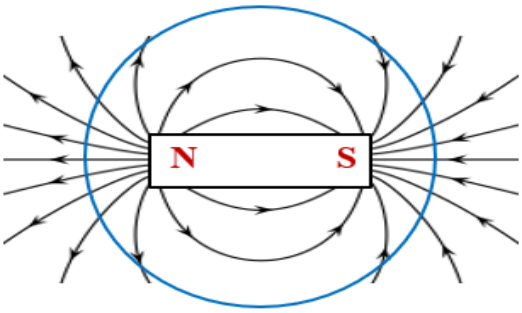


**Figure 3.7.** A closed surface (blue circle) with a bar magnet (rectangle with the North and south poles) shows an equal number of magnetic lines, indicated by black arrows, entering and exiting the surface.

Gauss's law for magnetism, Equation 3.6, can be derived by considering magnetic flux in the closed surface. Since the magnets exist as a dipole, the magnetic flux in a closed sphere equals zero, Equation 3.9.

$$\mathbf{B} = \frac{\Phi}{A} \qquad 3.8$$

$$\Phi_{\mathbf{B}} = \oint \mathbf{B}.\mathbf{ds} = 0 \qquad 3.9$$

Where $\phi_{\mathbf{B}}$ magnetic flux, A is the area through which the magnetic flux is passing, and s is a small vector area element on the surface through which the magnetic flux is being calculated.

By Gauss's divergence theorem, the surface integral changes to a volume integral, then Equation 3.9 becomes:

$$\oint \mathbf{B}.\mathbf{ds} = \oint (\nabla.\mathbf{B})\mathbf{dv} = 0 \qquad 3.10$$

$$\nabla.\mathbf{B} = 0 \qquad 3.11$$

### 3.4.1. Governing Equations and Boundary Conditions

The Magnetic fields, no Currents (mfnc) physics interface is found under the AC/DC physics interface, as highlighted in Figure 3.6. It is used in this research for the MFL analysis. It computes magnetostatics fields (no time-varying or steady fields) from permanent magnets, where magnetic sources are current-free. The main assumptions in the mfnc interface are magnetic fields arise solely from permanent magnets, the field is magnetostatics (no time-varying field) and no electric current exists. A stationary solver was used since magnetostatics is time-invariant. Two of Maxwell's equations, Equations 3.6 and 3.7, govern magnetostatics problems and are used in their differential forms to provide approximate solutions in the mfnc interface. The mfnc interface solves the two differential forms of Maxwell's equations with the boundary conditions and the constitutive relations for the magnetic scalar potential, which is a dependent (field) variable.

Maxwell – Ampere's law, Equation 3.7, says the magnetic field circulates around electric current and changing electric flux. To derive the magnetostatics equation for the mfnc interface, Gauss's law for magnetism needs to be solved using the scalar magnetic potential, which is a dependent (field) variable. Since there is no electric current in magnetostatics problems, Ampere – Maxwell's equation, Equation 3.7, will be written as:

$$\nabla \times \mathbf{H} = 0 \qquad 3.12$$

This implies that analogous to the definition of electric potential for static electric fields, magnetic scalar potential $V_m$ can be written as:

$$\mathbf{H} = -\nabla V_m \qquad 3.13$$

Where $V_m$ is magnetic scalar potential.

A constitutive relation that relates the magnetic induction to the magnetic field is:

$$\mathbf{B} = \mu_0 (\mathbf{H} + \mathbf{M}) \quad 3.14$$

Where **M** is magnetisation.

Using Equations 3.13 and 3.14, Gauss's law for magnetism, Equation 3.6, becomes:

$$-\nabla.(\mu_0 \nabla V_m - \mu_0 \mathbf{M}) = 0 \quad 3.15$$

The mfnc interface used for MFL analysis computes Equation 3.15 above or a similar equation depending on the selected constitutive relation for magnetic scalar potential.

There are three material conditions or constitutive relations based on how materials respond to a magnetic field: linear (paramagnetic and diamagnetic) materials, non-linear (ferromagnetic) materials and permanent magnets. The mfnc interface equation for MFL analysis, Equation 3.15, changes accordingly based on selected constitutive relations.

Paramagnetic and diamagnetic materials have a linear relationship between the magnetisation **M** and the magnetic field **H**. Thus, the magnetisation is:

$$\mathbf{M} = \chi_m \mathbf{H} \quad 3.16$$

Where $\chi_m$ is magnetic susceptibility, and $\mu_r$ is relative permeability.

The constitutive relation for linear materials is:

$$\mathbf{B} = \mu_0 (1 + \chi_m) \mathbf{H} = \mu_0 \mu_r \mathbf{H} = \mu \mathbf{H} \quad 3.17$$

Where $\mu_r$ is relative permeability.

Then, solving Gauss's law for linear materials by using Equations 3.13 and 3.17 provides:

$$-\nabla.(\mu \nabla V_m) = 0 \quad 3.18$$

The mfnc uses Equation 3.18 to compute magnetic scalar potential for linear materials.

Ferromagnetic materials have a non-linear relationship between the magnetisation **M** and the magnetic field **H**. It emerges due to permeability variation with the intensity of the magnetic field strength, history of the field distribution, and hysteresis effects.

$$\mathbf{B} = f(|\mathbf{H}|) \quad 3.19$$

Where the function $f$, $f$: $R_0^+ \rightarrow R_0^+$, is magnetisation or **B-H** curve.

Then, Gauss's law for the non-linear materials using Equations 3.13 and 3.19 gives:

$$-\nabla . f(\nabla V_m) = 0 \qquad 3.20$$

The constitutive equation for a permanent magnet is:

$$\mathbf{B} = \mu_0 \mu_r \mathbf{H} + \mathbf{B_r} = \mu \mathbf{H} + \mathbf{B_r} \qquad 3.21$$

Where **B**r is the remnant magnetic flux density, which is the magnetic flux density in the absence of a magnetic field.

Then, computing Gauss's law for the permanent magnet using Equations 3.13 and 3.21 provides:

$$-\nabla . (\mu \nabla V_m - \mathbf{B}r) = 0 \qquad 3.22$$

The mfnc interface for MFL analysis uses Equation 3.15 or a similar equation based on the selected constitutive relation. For linear materials, it uses Equation 3.18; for non-linear materials, it applies Equation 3.20; and for permanent magnets, it employs Equation 3.22. It computes scalar magnetic potential and provides an interface for defining the constitutive relation and the relevant material properties. The magnetic flux conservation node is the primary node in the mfnc interface.

The boundary conditions used for MFL analysis for this research are as follows: The default boundary condition is the magnetic insulation node. It uses the boundary condition of the normal component of magnetic flux density equal to zero to provide magnetic insulation. It prevents magnetic field lines from penetrating or crossing the boundary.

$$n . \mathbf{B} = 0 \qquad 3.23$$

A zero magnetic scalar potential boundary condition sets the magnetic scalar potential to zero at the boundary, providing a fixed reference point that ensures a unique solution to the magnetic field equations.

$$V_{\mathbf{m}} = 0 \qquad 3.24$$

### 3.4.2. Finite Element Model Development

Discretisation involves selecting the type of element and conducting a mesh refinement study. The accuracy and efficiency of the simulation depend significantly on the type of elements used and the mesh refinement study. High-quality elements and a finer mesh should be applied

to the area of interest, while a coarser mesh can be used in regions where finer detail is unnecessary to reduce computational costs. A hexahedral element was used due to its higher accuracy and efficiency. COMSOL supports hexahedral meshing for geometries compatible with mapped or swept meshing techniques. For mapped mesh, the domain should resemble a brick or wedges. Meanwhile, a swept mesh requires structured geometry with aligned source and destination faces. It involves extruding a surface mesh throughout the domain. Therefore, a swept mesh was used splitting the geometry into sweep-compatible subdomains. The magnetic circuit and the plate were meshed with hexahedron elements (swept mesh), as shown in Figure 3.8 (a). An extremely fine tetrahedral mesh was used to model the air volume, as shown in Figure 3.9. This choice of mesh was used to reduce unnecessary computational time, and it did not affect the results for magnetic flux density in the MFL circuit. A mesh convergence study was performed to ensure that the simulation results were independent of the mesh density. This involved systematically refining the mesh and comparing the results at each stage to ensure that further increases in mesh density did not significantly alter the outcomes. Magnetic energy density is a built-in variable which is derived from the magnetostatics Maxwell equations (Maxwell–Ampère's Law and Gauss's Law for Magnetism) combined with the constitutive relation. As shown in Figure 3.8 (b), convergence of the simulation result for the energy density was achieved at an element size of 2 mm. Accordingly, a 2 mm mesh size was used for the magnetic circuit before introducing hinge and defect. Following the introduction of the hinge and defect features, local mesh refinement was applied in these critical regions to improve simulation accuracy. Local swept mesh refinement requires domain partitioning to allow different mesh controls. Therefore, the hinge and defect areas were partitioned and meshed with maximum and minimum element sizes of 0.5 mm and 0.1 mm, respectively, as shown in Figure 3.10 (a) and (b).

Quadratic Lagrange polynomials were used to interpolate the magnetic scalar potential in the Ref models before introducing defects. Cubic Lagrange polynomials were used in models with defects and the hinge to capture finer details and improve accuracy. The solver used the default iterative configuration, with a relative tolerance of $1\times10^{-3}$, to ensure convergence in the stationary magnetic field simulations. Based on the defined physics interface, mesh type and boundary conditions, COMSOL automatically generates the weak form, computes the element matrices, and assembles them into the global system for solving.

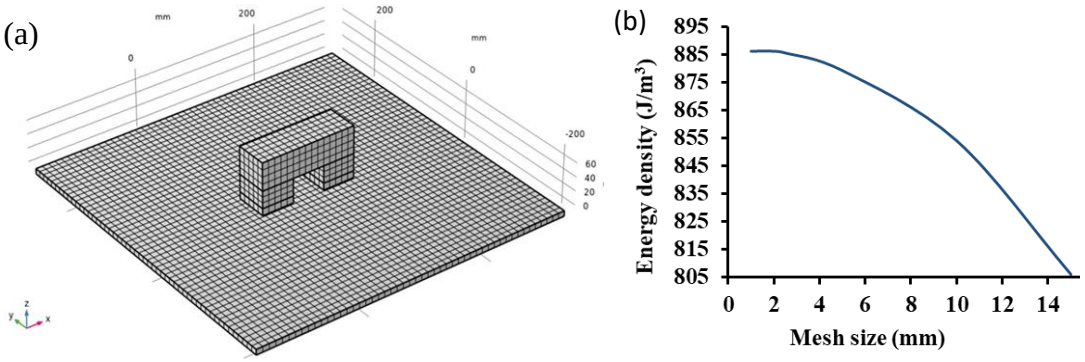


**Figure 3.8.** (a) The magnetic circuit and the plate meshed with hexahedron elements. (b) Mesh convergence study.

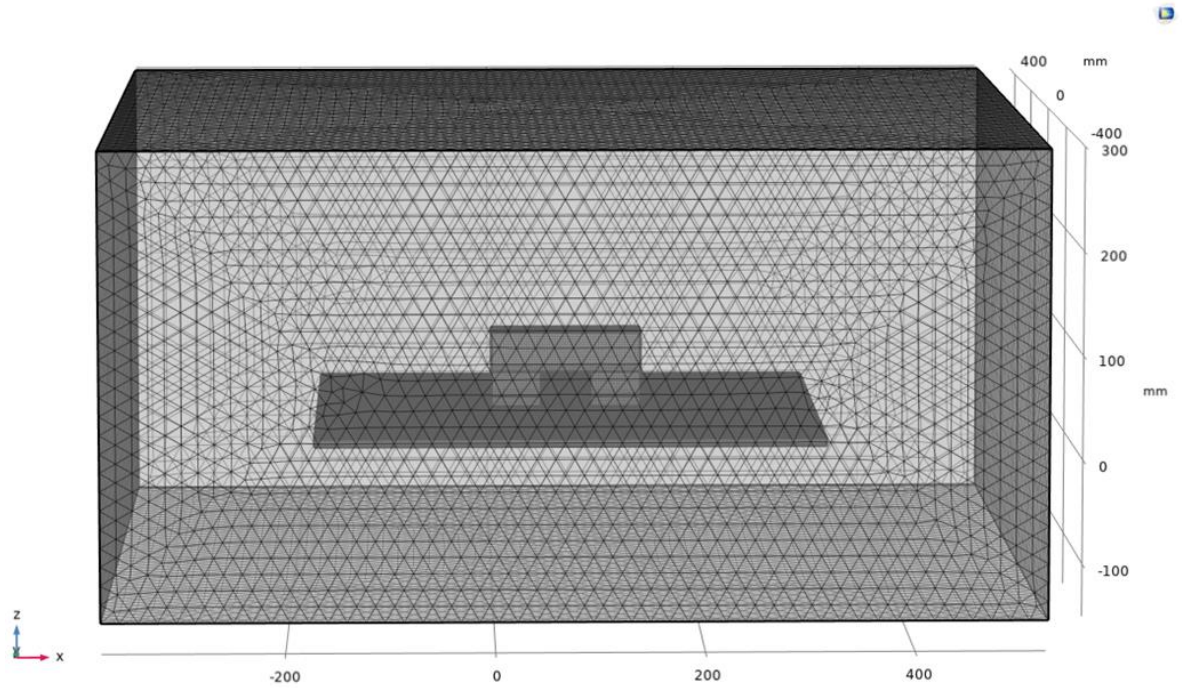


**Figure 3.9.** Air volume meshed with an extremely fine tetrahedral mesh.

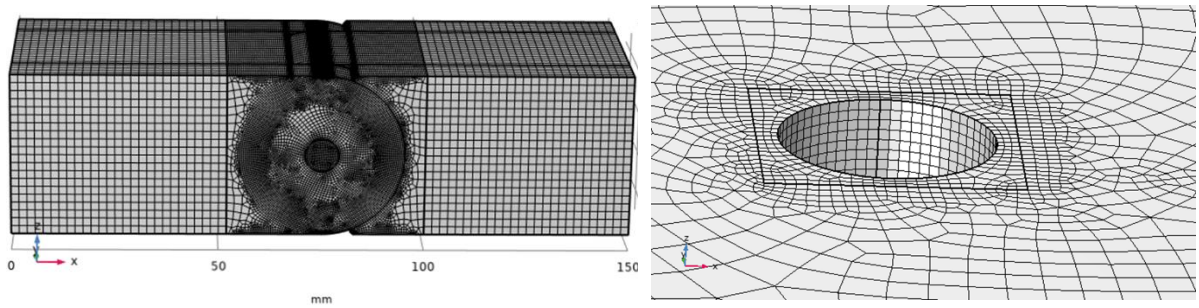


(a) (b)

**Figure 3.10**. Local mesh refinement in (a) the hinge region and (b) the zoomed-in defect area, with maximum and minimum element sizes of 0.5 mm and 0.1 mm, respectively.

### 3.4.3. Outline of the Optimisation

The Optimisation Module of COMSOL Multiphysics 6.0 was used to achieve optimal design by defining objective functions, design variables and constraints [251]. The design or control variables and parameters can be any model inputs such as geometrical dimensions, shapes, material properties or material distributions. The objective function is a target model output to be achieved. The constraints define a set of viable values for the control variables.

The module offers several algorithms, both derivative-based and derivative-free. The derivative-based or gradient-based solvers use gradient information (derivatives) of the objective function with respect to the control variables to guide the optimisation process towards the optimal solution iteratively. They are used when the derivative of the objective function is available, smooth and continuous. The gradient-based solvers available in COMSOL include sparse nonlinear optimiser (SNOPT), method of moving asymptotes (MMA) and Levenberg–Marquardt. The gradient-free solvers do not require gradient information. They are suitable for problems where the objective function or constraints are non-smooth, discontinuous, noisy, or their derivatives are not available or computationally expensive to evaluate. The gradient-free solvers in COMSOL include coordinate search, Nelder–Mead, constrained optimisation by linear approximations (COBYLA) and bound optimisation by quadratic approximation (BOBYQA). Figure 3.11 presents a flow chart that outlines the process for selecting the most suitable algorithm.

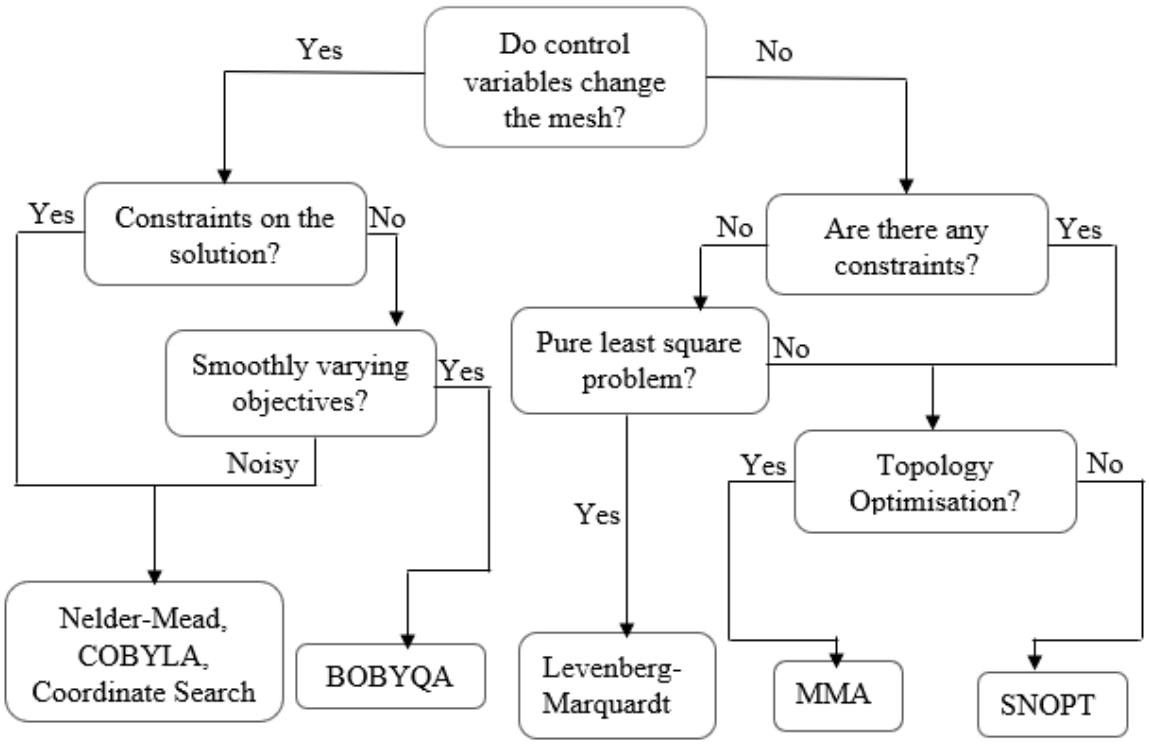


**Figure 3.11.** The process for selecting the most suitable algorithm for optimisation [252].

Optimisation solvers evaluate the gradient of the objective function analytically or numerically to approximate the gradient and determine how to move through the parameter space towards the optimal solutions. Equations 3.25, 3.26 and 3.27 state a general formulation of an optimisation problem. Equations 3.25 defines an objective function, $Q$, to be minimised. The goal is to find a value of the control variable, $\xi$, that minimises the objective function. Equation 3.26 indicates the feasible region where the control variable belongs to the set of constraints, $C$. Equation 3.27 defines the feasible set $C$ as the set of all values of the control variable for which the constraint function $G\ (\xi)$ lies between a lower bond ($lb$) and lower bound ($ub$).

$$min\ Q\ (\xi) \tag{3.25}$$

$$\xi\ \in\ C \tag{3.26}$$

$$\mathrm{C} = \{\, \xi : \mathrm{lb}\ \leq \mathrm{G}\ (\xi)\ \leq\ \mathrm{ub}\, \} \tag{3.27}$$

Where $\xi$ is a vector of control variables, $Q$ is the scalar-valued objective function, $C$ is a set of constraints (the feasible set), $G$ is a vector-valued function (scalar-valued in case of a single constraint), and $lb$ and $ub$ are upper and lower bounds respectively.

Optimisation of the MFL system was carried out using both topology and parameter optimisation in conjunction with the magnetic fields, no currents physics interface to model the magnetostatics field. Parameter optimisation was used to optimise the geometry/dimensions of circuit components, including pole piece height, magnet bridge length and magnet bridge height. The BOBYQA solver was used for the parametric optimisation because control variables define geometric dimensions.

In addition, topology optimisation was employed to enhance the circuit performance and minimise its size by optimising the distribution of materials in the magnetic circuit. The MMA, a gradient-based approach, was used because of its fast computation, no need for re-meshing and capability to handle problems with many control variables. The topology optimisation solves for theta ($\theta$) variable, which controls material distribution within a design space to maximise (or minimise) an objective function [253]. The control variables, representing ferromagnetic materials, are defined in the density model. These materials use the **B**-**H** curve to evaluate magnetisation level. However, using of relative permeability instead of the **B**-**H** curve for topology optimisation is more convenient. The **B**-**H** curve was defined using relative permeability, $\mu_r$, as written in Equation 3.28.

$$\mu_r, (|\mathbf{H}|) = \frac{\mathbf{B}(|\mathbf{H}|)}{\mu_0|\mathbf{H}|} \qquad 3.28$$

The relative permeability of the design space was defined in terms of the penalty material volume factor, $\theta_p$, as given in Equations 3.29 and 3.30. Equation 3.29 uses Equation 3.30 to compute the effective relative permeability between air and ferromagnetic material using interpolation. The penalty material volume factor represents the final, penalised material distribution throughout the design domain in a topology optimisation problem. Its physical significance is to ensure that optimised structures converge towards distinct regions of solid material or void rather than intermediate densities. Intermediate densities have ambiguous physical interpretations and create manufacturing challenges; therefore, the penalty material volume factor helps to produce physically manufacturable designs with clear material boundaries. $\theta_{min}$, the minimum penalised volume fraction, represents a minimum, non-zero material property value assigned to void regions to maintain numerical stability and design feasibility in the optimisation process. In the MFL analysis for this research, the minimum penalised volume fraction is the minimum relative permeability value of $1e^{-3}$ assigned to void regions to prevent the complete removal of material that would cause the finite element analysis

to fail. $\Theta^{P_{SIMP}}$, penalised design variable, represents the raw penalised form of the design variable θ raised to the exponent $P^{SIMP}$ to push the design towards a binary solution (solid (θ ≈ 1) or void (θ ≈ 0)) to shape the topology. Equation 3.29 interpolates the material's relative permeability in topology optimisation, allowing regions to transition between air (μ=1, $\Theta_p$= θmin) and ferromagnetic material (μr ≫ 1, $\Theta_p$=1) based on the penalised design variable $\Theta_p$. Equation 3.30 penalises intermediate densities to have a clear solid or void design.

$$\mu_r(\Theta_p, |\mathbf{H}|) = 1 + \Theta_p\left(\frac{\mathbf{B}(|\mathbf{H}|)}{\mu_0|\mathbf{H}|} - 1\right) \quad 3.29$$

$$\Theta_p = \Theta_{min} + (1 - \Theta_{min})\Theta^{P_{SIMP}} \quad 3.30$$

Where $\Theta_{min}$ is the minimum penalised volume fraction, and $P^{SIMP}$ is the Solid Isotropic Material with Penalisation (SIMP) exponent.

In the topology optimisation process, filtering and projection techniques were employed to ensure numerical stability and promote discrete, manufacturable designs. First, a Helmholtz-type partial differential equation, Equation 3.31, was used to filter the raw/unfiltered design variable, $\Theta_c$, to produce a smoothed and filtered design variable, $\theta_f$. This filtering step makes the solution independent of the mesh resolution and suppresses non-physical patterns such as checkerboarding by imposing minimum length scale, $R_{min}$, via a Helmholtz filter.

$$\theta_f = R_{min}{}^2\nabla^2\theta_f + \Theta_c \quad 3.31$$

Where $\Theta_c$ is unfiltered design variable representing material distribution that can contain noise or oscillations that cause non-manufacturable results., $\theta_f$ is the filtered design variable, representing a physically meaningful and manufacturable material distribution obtained by smoothing the raw design variable, $R_{min}$ is a length scale parameter that defines the minimum allowable size of material features in the optimised design. In this study, it was defined from mesh, and $\nabla^2\theta_f$ is the Laplacian operator, representing spatial diffusion or smoothing. This spreads out the values of $\theta_f$ based on its neighbours.

The filtered design variable can then be transformed to projected design variable, θ, which represents the material layout driven toward a binary (0 or 1) solution using a hyperbolic tangent projection function, as shown in Equation 3.32.

$$\theta = \frac{(\tanh\left(\beta(\theta_f - \theta_\beta)\right) + \tanh(\beta\theta_\beta))}{(\tanh\left(\beta(1 - \theta_\beta)\right) + \tanh(\beta\theta_\beta))} \quad 3.32$$

Where $\theta_\beta$ is threshold parameter at which the projected design variable switches from material (1) to void (0). It was 0.5 in this study. $\beta$ is sharpness parameter that governs how binary the final material layout becomes. In this study, the default value of $\theta_\beta$ and $\beta$ were 0.5 and 8, respectively. In this study, the threshold and sharpness parameters were set to 0.5 and 8, respectively, to ensure a clear separation between material and void regions.

In both optimisation approaches, the optimisation process was carried out iteratively with the magnetostatics PDE solved via FEM at each iteration. In each case, the design variables were updated and the process continued until convergence was achieved, using a predefined optimality tolerance of 0.001.

## 3.5. Experimental Method

Maxwell's equations also govern the experimental system of MFL investigation. They provide the fundamental framework for understanding how magnetic fields generate, propagate, behave around a material, and interact with defects.

Generally, there are two types of model validation: external validation and sensitivity analysis [254]. External validation involves comparing simulation results against experimental data. Sensitivity analysis offers insights into the impact of input parameters on the model output and identifies critical factors that influence the performance of the system. The experimental investigation is based on validating the numerical results by characterising cylindrical defects. The sensitivity analysis of defects in terms of depths, radii, locations (near and far-surface) and sensor lift-offs were analysed experimentally. The measured signals from different inspection components were analysed. The MFL experimental set-up consists of the magnetic circuit machined and assembled using an excitation source (NdFeB magnet), soft ferromagnetic steels (AISI 1020, S275, X42 and ASTM A234 WPB), a 3D printed plastic sensor holder made of polylactic acid (PLA) to provide an accurate position for the sensor during the tests and ensure repeatability and a Gaussmeter which consists of a Hall effect sensor to measure leakage signals.

Hall effect sensors detect and measure magnetic fields based on the Hall effect principle. They consist of a thin sheet of conductive material carrying a current. When a current-carrying

conductor is exposed to a magnetic field perpendicular to the direction of current flow, the magnetic field exerts a transverse force on the moving charge carriers within the conductor. This force causes the charge carriers to accumulate on one side of the conductor, creating a potential difference known as the Hall voltage across the conductor, which was discovered by Edwin Hall in 1879 [255]. The Hall voltage generated is directly proportional to the current flowing through the conductor and the strength of the applied magnetic field. Hall effect sensors measure this Hall voltage to determine the magnitude and polarity of the magnetic field [256]. Hall Effect sensors have a higher sensitivity, stability and operating temperature than coil sensors, and they are also suitable for detecting high magnetic fields, compared to giant magnetoresistance and tunnel magnetoresistance sensors, whose sensitivity decreases with increasing magnetic field [116].

A summary of the methodology used in this work is shown in Figure 3.12.

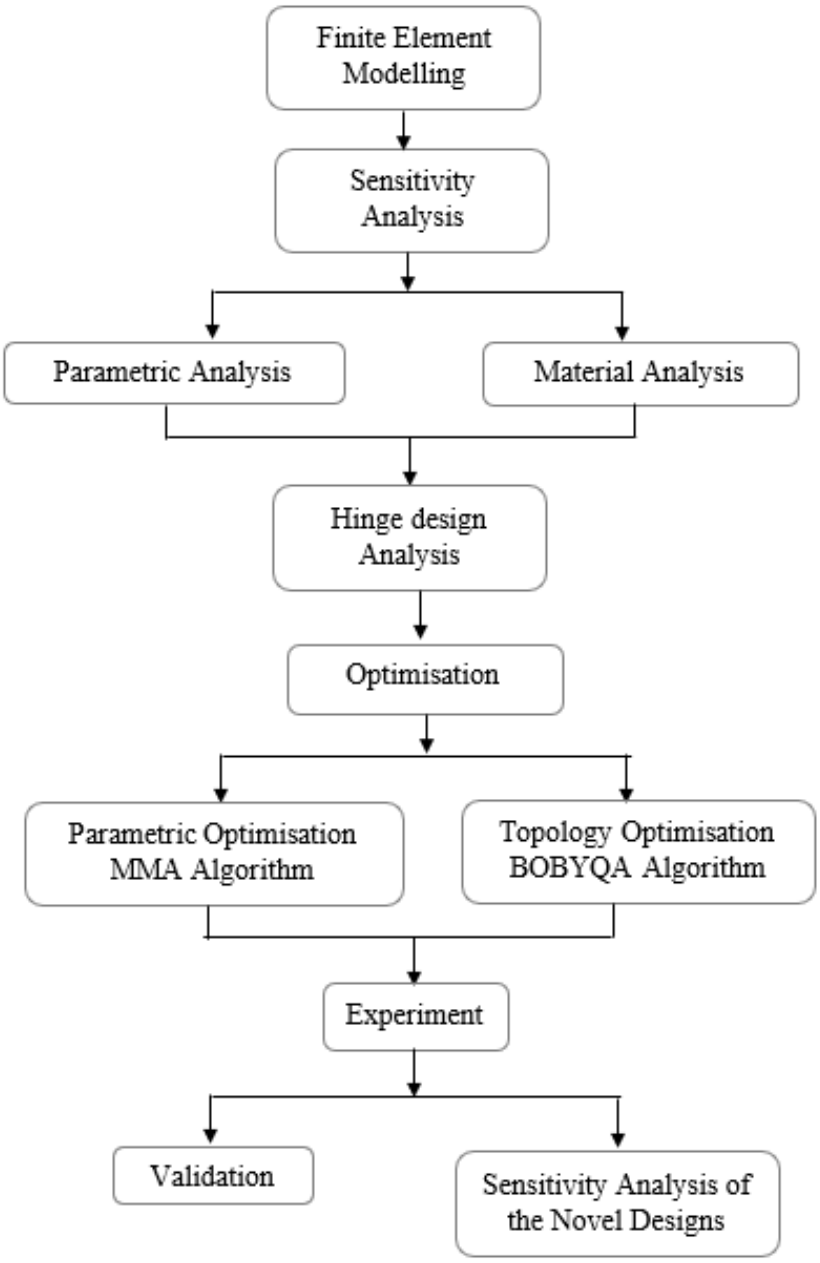


**Figure 3.12.** Flow chart of the summary of the methodology used in this work.

## 3.6. Summary

The finite element (FE) modelling approach was presented, providing an in-depth explanation of the FE model development, starting with the derivation of Maxwell's equations relevant to the study. The FE model setup was described, including the mesh generation, mesh convergence study and the application of boundary conditions. Optimisation techniques used to enhance the model were presented.

The experimental programme was designed to validate the 3D FEA results. The equipment used, the measurement techniques employed and the protocols followed to ensure consistency and accuracy in data collection were presented.

# 4. SIMULATION RESULTS AND DISCUSSIONS

## 4.1. Introduction

One significant step in developing an efficient MFL system is the design of an MFL circuit. A clear set of design requirements was established to develop a simulation-led design of an MFL system that can be permanently installed in difficult-to-access areas. The design requirements include increasing the magnetisation level to the recommended operating region in the **B-H** curve, obtaining uniform flux distribution in the sample, reducing fringing and unintended leakage fields, developing a compact magnetic circuit with optimal performance that can be used to inspect a wide range of inspection components and enhancing accurate defect signal detection.

Based on these design requirements, three magnetic circuit designs were developed and evaluated. The iterative design development process is based on building upon the insights and shortcomings of the previous iteration achieved. By conducting a comprehensive simulation program, an improved reference (Ref) circuit with improved design parameters is developed by performing a parametric study based on the sensitivity analysis of the circuit components. Building upon the insights gained from the Ref circuit, a new hinged (Hin) circuit introduces a hinged magnet bridge to enhance the performance of the MFL system on non-flat inspection surfaces, e.g. pipes and elbows. These changes are intended to address the shortcomings identified in the Ref design while using it on non-planar inspection surfaces, thereby improving the overall detection capability of the system for both planar and non-planar surfaces. Four hinge designs were investigated with 3D FEA. The most suitable hinge design is adopted from the hinged configurations. A novel optimised (Opt) circuit is developed by performing parametric and topology optimisation of the best-performance Hin circuit using algorithms. Parameter optimisation is used to optimise the dimensions of circuit components to enhance performance. Topology optimisation is employed to improve the circuit performance and minimise its size by optimising the distribution of materials in the magnetic circuit.

This chapter provides a detailed overview of each design development phase, including the methodology, approach taken to achieve significant improvements, specific enhancements implemented and comparative analyses of the three designs.

## 4.2. Reference (Ref) Circuit

In this research, the 3D FEM simulations used magnetic fields, no currents physics interface, based on the main assumptions that magnetic fields originate from permanent magnets, the field is magnetostatics (time-invariant), and no electric currents are present. It is governed by magnetostatics Maxwell equations combined with the constitutive relations. Materials used were considered homogeneous and isotropic, with non-linear **B**-**H** curves for ferromagnetic materials and constant **B**r for the permanent magnets surrounded by air. Interfaces were assumed to be perfectly bonded with no air gaps. Magnetic insulation and zero magnetic scalar potential boundary conditions were used to prevent magnetic flux from crossing the boundaries and ensure a unique and stable solution. Mesh refinement was performed. The finite element modelling methodology, such as governing equations, assumptions, boundary conditions, and solver and mesh settings used in the simulations are described in detail in Chapter 3. Table 4.1 below summarises the finite element modelling setup defined in COMSOL Multiphysics for the simulation results presented throughout the thesis. These include governing equations, material properties, mesh settings, solver tolerances, and assumptions used to obtain simulation data.

The Ref circuit was designed based on sensitivity analysis of various circuit parameters. These parameters include the material of the magnet, magnet bridge dimensions, inspection component size (boundary effects) and pole piece dimensions. A conventional U-type, existing MFL circuit with a flat inspection component was used as an initial geometry, as shown in Figure 4.1 (a). The dimensions are listed in Table 4.2. The sensitivity and the following analyses and optimisation studies are based on the magnetisation level of the inspection components achieved at the point of interest, in the middle of the inspection components, i.e., halfway through the thickness in the centre plane of the MFL device, as illustrated in Figure 4.1 (b). This point of interest, the measurement point, is for simulation work to analyse the magnetisation level.

**Table 4.1**. Summary of FEM methodology, including boundary conditions, assumptions, input parameters, mesh and solver settings used in the simulations presented throughout this thesis.

| Feature | Description |
|---|---|
| Physics interface | Magnetic Fields, No Currents (3D), time-invariant, current free magnetostatics fields from permanent magnets |
| Governing equations | Magnetostatics (Maxwell's equations), Scalar potential formulation |
| Solver type | Stationary (iterative) |
| Solver tolerance | Relative tolerance = $10^{-3}$ |
| Element interpolation | Quadratic (Ref circuit models); Cubic (models with defects and hinges) |
| Mesh type | Hexahedral (swept mesh) |
| Mesh element size | 2 mm for Ref circuit verified by convergence study |
| Local mesh refinement | 0.5 mm (max), 0.1 mm (min) for hinge and defect zones |
| Steels properties | Experimentally measured non-linear **B**-**H** curves |
| Magnets properties | Sintered N52 $\mathbf{B}_r$ = 1.4 T and N42 $\mathbf{B}_r$ = 1.3 T |
| Boundary conditions | Magnetic insulation and zero scalar potential at external boundary (air domain) |
| Field evaluation | Domain point probe at point of interest for magnetisation and 2 mm lift-off, moving 2.4 mm for leakage field measurement |
| Weak form handling | Automatically generated by COMSOL; Matrices assembled and solved internally |

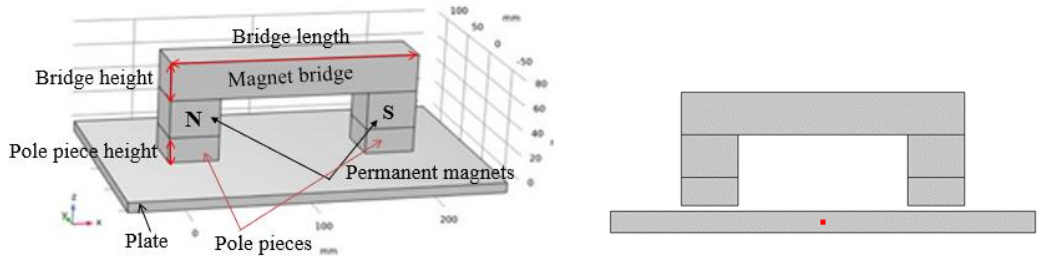


(a) (b)

**Figure 4.1.** (a) Initial geometry of the existing MFL circuit, with labelled dimensions for the magnet bridge, permanent magnets and pole pieces. (b) Point of interest marked red in the model symmetry plane.

**Table 4.2.** Dimensions of the initial magnetic circuit.

| Components | Dimensions (mm) |
|---|---|
| Magnet | 40 × 40 × 30 |
| Magnet bridge | 200 × 40 × 30 |
| Pole piece | 40 × 40 × 20 |
| Plate | 350 × 200 × 10 |
| Air | 400 × 250 × 150 |

### 4.2.1. Magnet

A range of neodymium magnets (NdFeB) were considered from commercial off-the-shelf magnets to magnetise the inspection components to a suitable extent. The grade and size of the NdFeB magnet determine the magnetomotive force supplied by the magnet. Four NdFeB magnets were considered here: an N42 NdFeB magnet with dimensions of 40 mm × 40 mm × 30 mm and with an 84 kg pull, an N42 NdFeB magnet with dimensions of 50 mm × 50 mm × 25 mm and with a 95 kg pull, an N52 NdFeB magnet with dimensions of 40 mm × 40 mm × 20 mm and with a 100 kg pull and an N52 NdFeB magnet with dimensions of 50 mm × 50 mm × 25 mm and a pull of 116 kg. The simulation results of these four magnets is shown in Figure 4.2. The magnetisation level achieved using N52 NdFeB 50 mm × 50 mm × 25 mm magnet was the highest over the other options and was found to lie within/close to zone 2 of the **B-H**

curve, based on experimentally measured **B-H** data, see Figure 2.19 and Figure 3.3. Previous studies state that higher-grade and volume magnets exhibit greater remanence and coercivity, significantly influencing the induced magnetisation intensity [25], [155], [257]. Consequently, this magnet was selected.

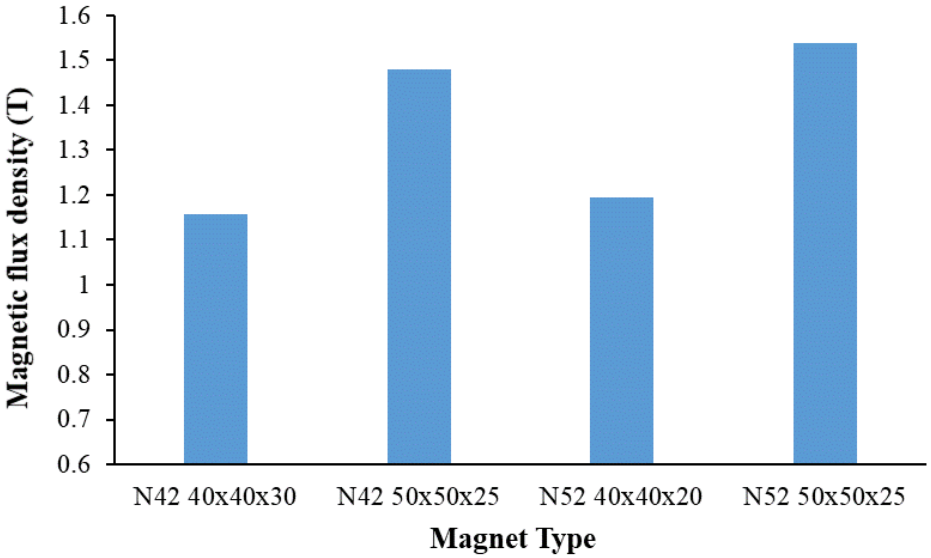


**Figure 4.2.** Magnetic flux density obtained using different grades and sizes of the NdFeB magnet types.

### 4.2.2. Magnet Bridge Dimensions

The bridge length effect was investigated to study how the length of the bridge affects the magnetisation level of the plate in the range from 125 to 300 mm. The 3D FEA simulation result in Figure 4.4 (a) shows that the norm of magnetic flux density (**B**) decreases with increasing bridge length. This is because a longer bridge leads to a longer magnetic path, increasing reluctance and decreasing magnetic flux density [25], [258]. Reluctance is directly proportional to the magnetic path length, as shown in Equation 4.1. Shortening the bridge length increases the magnetic flux density [144], [154]. However, reducing the bridge length leads to a leakage field due to a direct interaction between the two magnet poles, resulting in a non-uniform flux flow in the circuit. This effect is illustrated in Figure 4.3, which compares bridge lengths of 120 mm and 150 mm. Results are 2D XZ-plane slices taken midway through the bridge width. As a result, a bridge length of 150 mm was selected for the Ref circuit.

$$R = \frac{L}{\mu A} \qquad 4.1$$

Where R is reluctance, L is magnetic path length, μ is magnetic permeability, and A is cross-sectional area of the magnetic path.

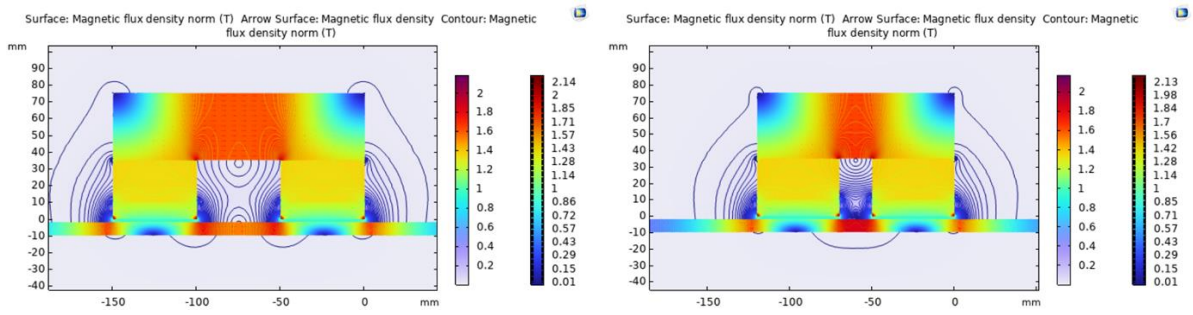


(a) (b)

**Figure 4.3**. Magnetic flux distribution for 120 mm (a) and 150 mm (b) magnet bridge lengths, showing increased leakage and non-uniformity with the shorter bridge. The results are 2D slices in the XZ plane, taken midway through the bridge width.

The magnet bridge height influence on the magnetisation level of the plate was studied in the range from 10 to 50 mm, as its width was determined by magnet width. Figure 4.4 (b) shows that the magnetic flux density initially increases with bridge height, as the increased cross-sectional area allows more magnetic flux to pass through the bridge/circuit [154]. However, further increase of the bridge height beyond 40 mm did not show the same effect, as the magnetic flux density remained constant, which means that the increased area does not alter the amount of magnetic field circulating in the circuit and the maximum of the magnetic field in this circuit is reached. Therefore, the bridge thickness of 40 mm was chosen for the Ref circuit.

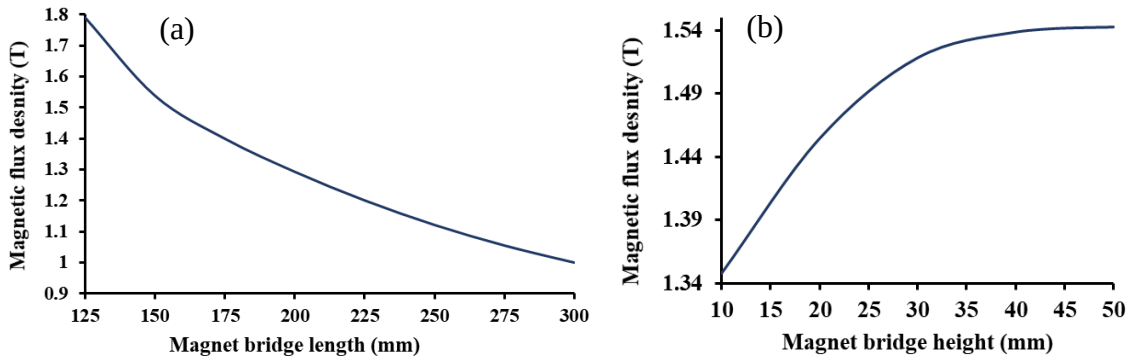


**Figure 4.4.** 3D FEA results of the magnet bridge length, on the left (a), and the magnet bridge height, on the right side (b) vs magnetic flux density.

### 4.2.3. Inspection Plate Size

The effect of the inspection plate size (plate length and width) on the magnetisation level was studied for a 7.85 mm thick plate from 100 to 500 mm, while all the other circuit parameters were kept constant. Figure 4.5 (a) and (b) show that the inspection sample boundaries affect the magnetic flux density obtained at the point of interest, which tremendously drops with increasing plate size, up to a specific size, beyond which the boundary effects disappear. The observed decrease in magnetisation level with increased plate width aligns with findings from previous research [215]. Consequently, a 500 mm × 500 mm plate was selected as a reference flat sample for this study.

Moreover, the effect of plate thickness was studied by increasing the plate thickness from 3.85 mm to 13.85 mm with 2 mm gaps, as shown Figure 4.6. The results show that magnetic flux density drops with increasing plate thickness. Thicker plates require more magnetic field strength to achieve the same magnetisation level as thinner plates. Previous research has shown magnetisation level drops with increased plate thickness due to a finite amount of flux that can be supplied into the plate from a permanent magnet [120]. Therefore, 7.85 mm plate thickness was used since it is the most commonly used thickness.

Regarding plate size (length and width), practical applications use plate sizes bigger than 500 mm × 500 mm, where the boundary effect disappears. Therefore, a bigger plate size for practical application will not affect the magnetisation level as the boundary effect disappears after a certain size. When it comes to plate thickness, the plate thickness of 7.85 mm was chosen for this study because it falls within the most commonly used plate thickness range. While using a thicker plate, the magnet size has to be adjusted accordingly.

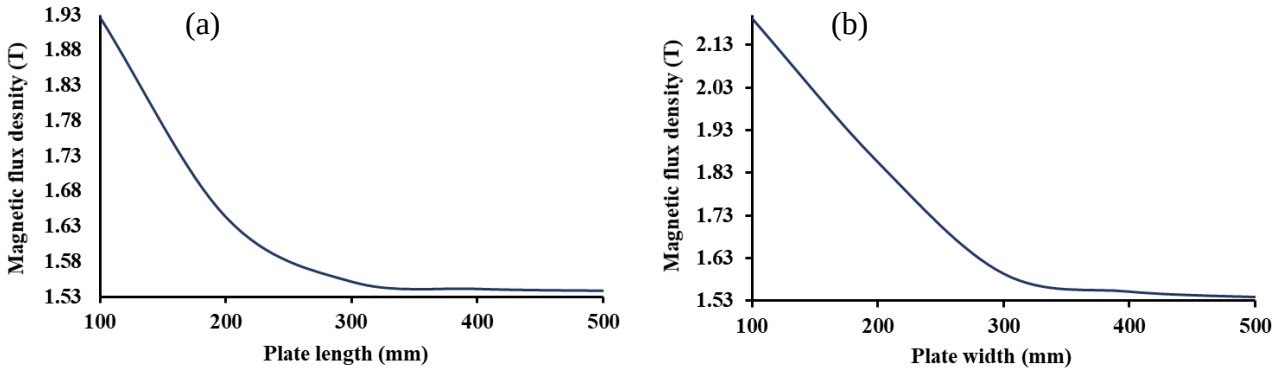


**Figure 4.5.** 3D FEA results for the magnetic flux density relative to: (a) the plate length and (b) the plate width.

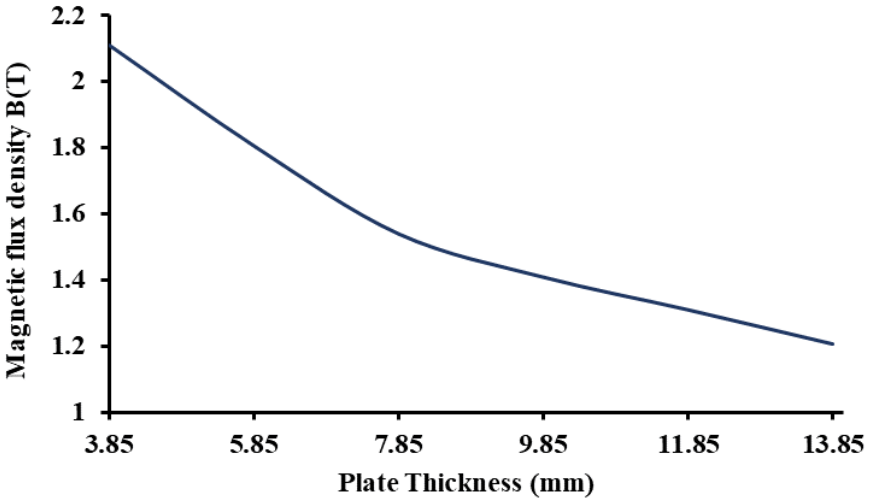


**Figure 4.6.** 3D FEA results of the magnetic flux density vs plate thickness.

### 4.2.4. Pole Piece Dimensions and Magnetiser Lift-off

The effect of pole piece height on the magnetisation level was investigated from 10 mm to 30 mm, as its length and width were determined by the size of the magnet. The pole pieces play a vital role in guiding and transferring the magnetic field between the magnets and the inspection plate. Increasing the pole pieces' height decreases the magnetic flux density in the plate, see Figure 4.7 (a), due to increased magnetic path length resulting in reluctance. However, removing the pole pieces was not considered because they guide the magnetic field lines in the circuit and protect the magnets from chipping and shattering during installation and removal. Field lines were spread outside the circuit when no pole pieces were used. Thus, the preferred pole piece height for this study was 10 mm.

The effect of magnetiser lift-off on the magnetisation level of the plate was studied in the range from 2 mm to 20 mm. When the magnetiser lift-off increases, the magnetisation level in the plate drops due to the fringing effects, as shown in Figure 4.7 (b). The observed drop in magnetisation level with increasing magnetiser lift-off aligns with findings in prior studies [155], [161]. Therefore, the magnetiser lift-off should be kept at a minimum. This study used a 2 mm lift-off to allow for coating thickness on the inspection components.

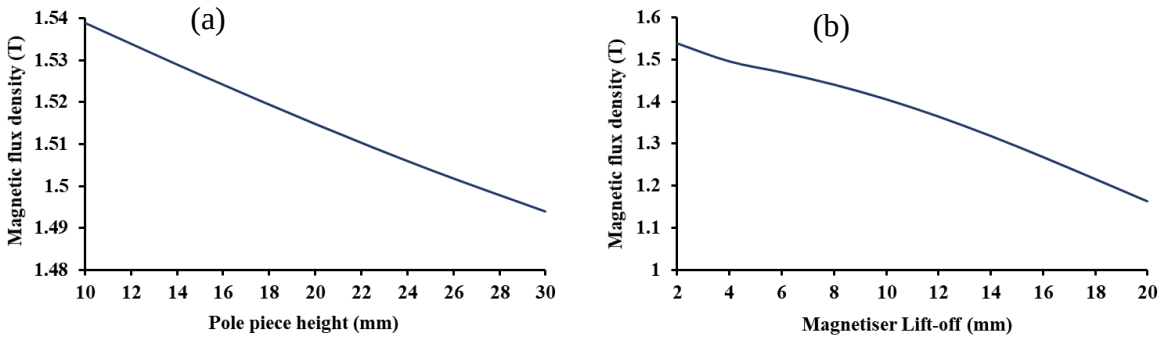


**Figure 4.7.** 3D FEA results of the pole piece height, on the left (a), and the magnetiser lift-off, on the right side (b) vs magnetic flux density.

Table 4.3 provides a summary of the dimensions of the Ref circuit components obtained from a detailed parametric study, which are subsequently used in newly developed circuits. After analysing the parametric study results for the flat plate inspection component, a 500 mm long pipe and a 90-degree elbow with an outer diameter of 168.3 mm and a wall thickness of 7.11 mm were chosen as the inspection components of interest. The dimensions of the pipe and elbow used are listed in Table 4.4. Figure **4.8** illustrates the magnetic flux density distribution obtained in the 3D FEA for the Ref circuit with the flat inspection plate. The magnetic flux density norm at the point of interest in the Ref circuit is 1.54 T.

**Table 4.3.** Dimensions of the magnet circuit components.

| Components | Dimensions (mm) |
|---|---|
| Magnet | 50 × 50 × 25 |
| Magnet bridge | 150 × 50 × 40 |
| Pole piece | 50 × 50 × 10 |
| Plate | 500 × 500 × 7.85 |
| Magnetiser lift-off | 2 |
| Air domain box | 700 × 850 × 550 |

**Table 4.4.** Dimensions of the pipe and elbow.

| Components | Outside Diameter (mm) | Wall Thickness (mm) |
|---|---|---|
| Pipe | 168.3 | 7.11 |
| Elbow | 168.3 | 7.11 |

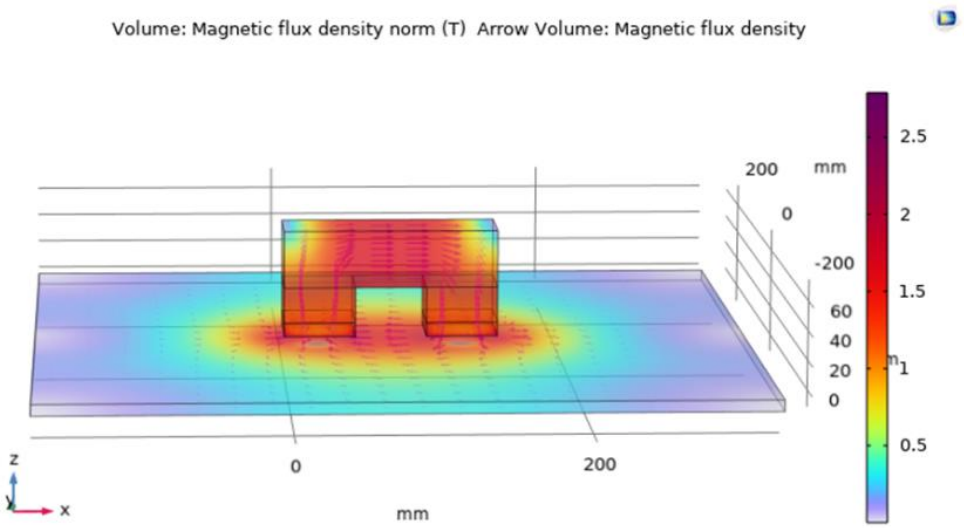


**Figure 4.8.** Magnetic flux density behaviour in 3D FEA model.

## 4.3. Hinged (Hin) Circuit

When the Ref circuit is used on the pipe and elbow, the magnetisation level decreases due to the additional lift-off induced by the surface curvature. This results in the magnetic field dispersing outside the magnetic circuit. In this work, four new hinge-based designs of the magnet bridge were proposed to improve the MFL circuit performance and minimise the field dispersion in the inspection of the non-flat surfaces. Figure 4.9 shows the proposed four hinge designs, including assembly on the left and its respective components on the right. The Hin circuit enables a smooth magnetic field flow with a minimised air gap between the flat-pole piece surface and the curved surface (pipe and elbow) by adjusting the hinge angle. Figure 4.10 shows the FEA results for magnetic field distribution obtained on the plate with the four hinge designs on the left and the magnetic field distribution in the symmetry plane of the hinged magnetic bridge by slicing halfway through the magnet bridge width, exposing the 2D cross-sectional surface on the right.

Although hinge design-1 allows for the maximum angle between the inspection surfaces, the small contact areas/lines and the large gaps across the hinge led to leakage and a reduction in magnetisation, as evidenced in Figure 4.10 (a). The magnetic flux density obtained for hinge design-1 was 1.52 T, below the result obtained with the Ref circuit (1.54 T).

Hinge design-2 was developed to reduce the leak and large gap across the hinge, as shown in Figure 4.10 (b). However, the contact and the gap remained large. The magnetic flux density measured for hinge design-2 was 1.52 T. As a result, hinge design-3 and 4 were designed by chamfering the rectangular ends of the hinge parts to semi-circular ends. This change increased the contact area and closed the gaps between the parts of the hinge, as shown in Figure 4.9 (c) and (d) and Figure 4.10 (c) and (d). The magnetic flux density for both hinge design-3 and 4 was 1.54 T. Since hinge design-4 is more complicated to machine and offers no performance improvement over design-3, it was decided to proceed with optimising and developing hinge design-3 further.

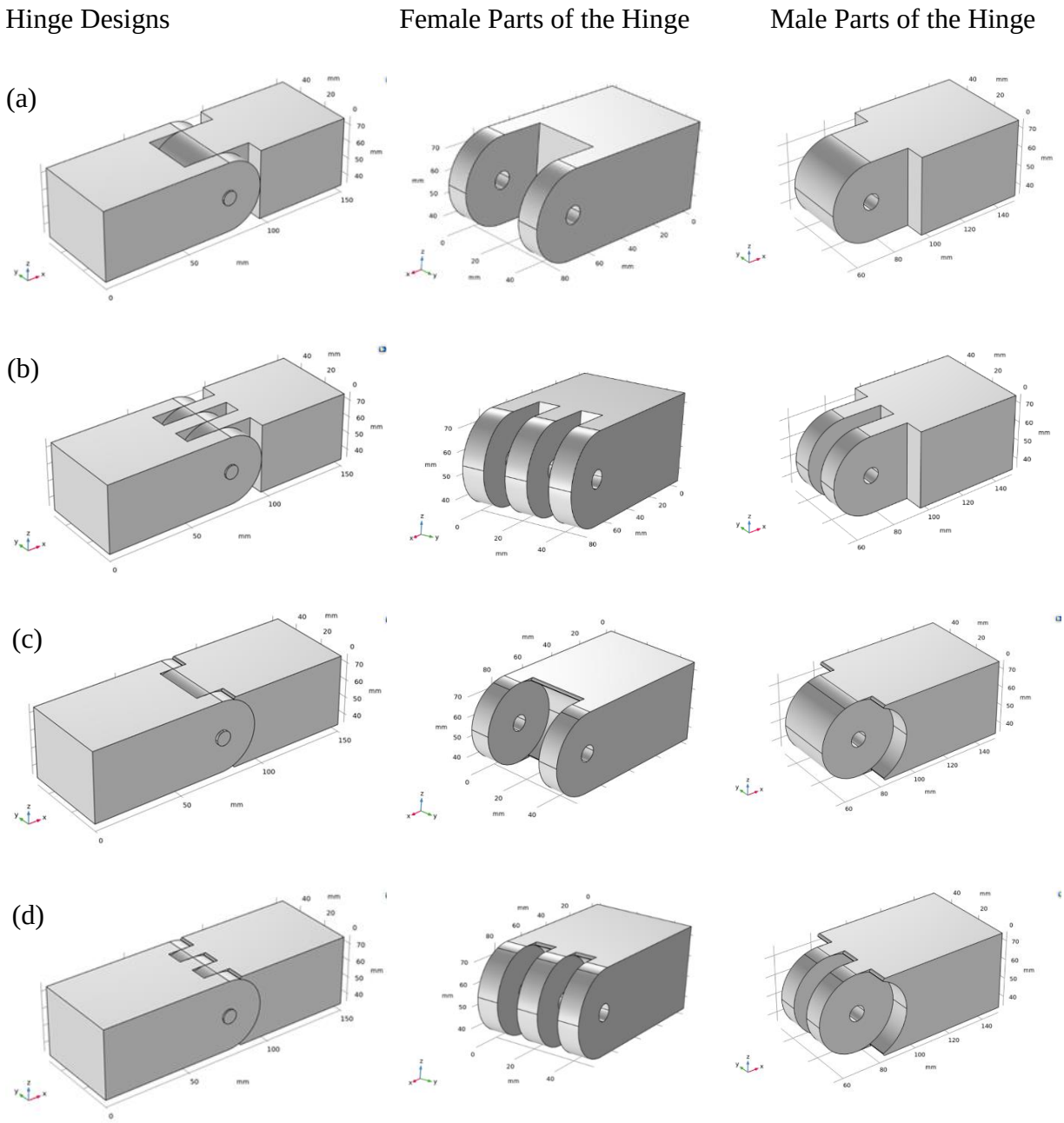


**Figure 4.9.** New magnetic bridge hinge designs assemblies and components: (a) Hinge design 1 - single hinge pole design with a line contact, (b) Hinge design 2 - double hinge pole design with a line contact, (c) Hinge design 3 – single hinge pole design with a surface contact, and (d) Hinge design 4 – double hinge pole design with a surface contact.

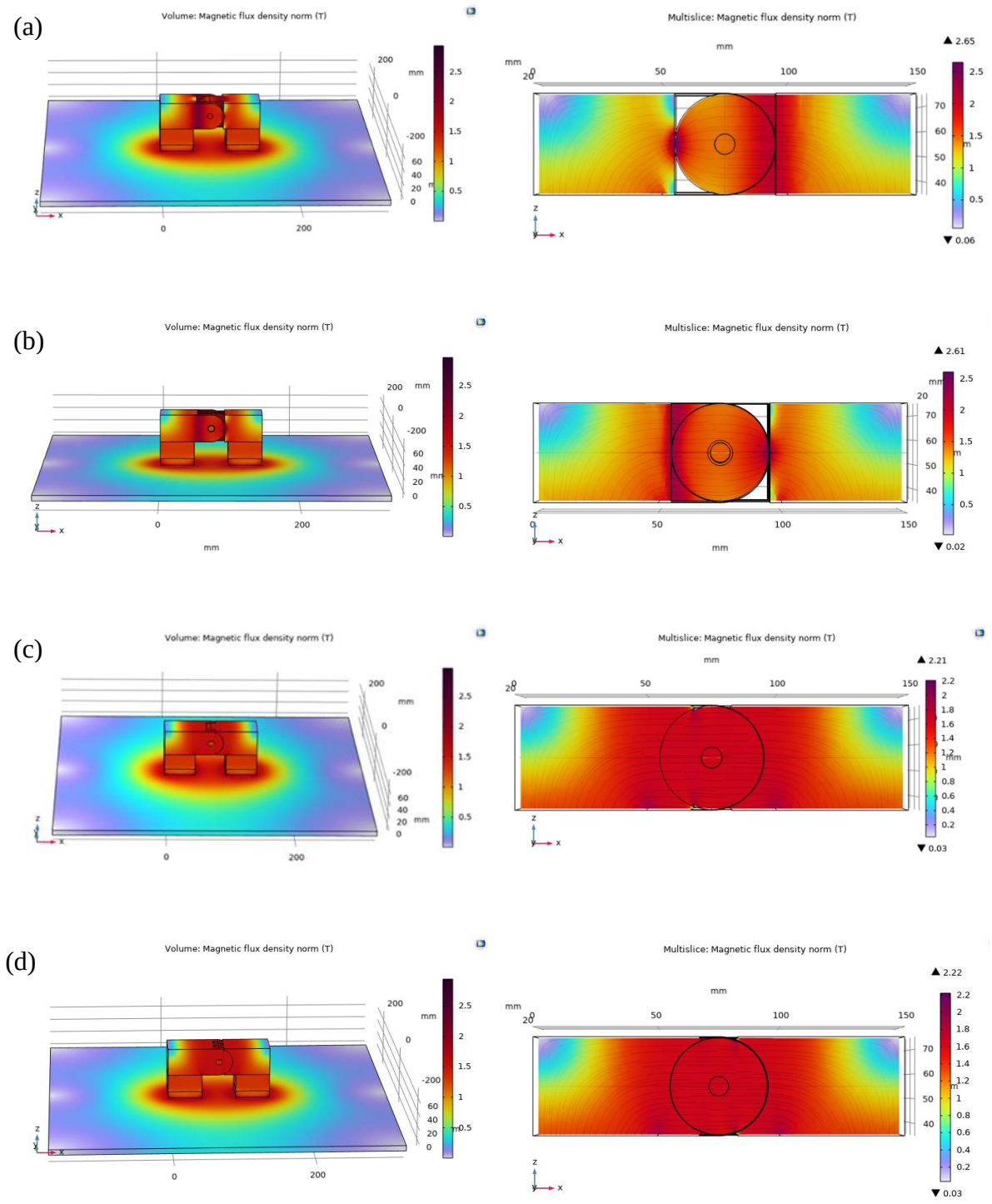


**Figure 4.10.** 3D FEA results for magnetic flux density obtained with four new hinged magnetic bridges, with a 3D view shown on the left, and the magnetic field distribution in the symmetry plane across the hinged bridge obtained by vertically slicing the magnet bridge through the midpoint of its width, resulting in a 2D cross-sectional view shown on the right. (a) Hinge design-1, (b) Hinge design-2, (c) Hinge design-3, and (d) Hinge design-4.

The performance of the Ref circuit was compared with the hinge design-3 on the pipe and pipe elbow, measuring the amount of magnetisation achieved using magnetic flux density in simulation, as shown in Figure 4.11. It was observed that there was a significant improvement in magnetisation level while using the hinge design-3 for both the pipe and pipe elbow, see Figure 4.12.

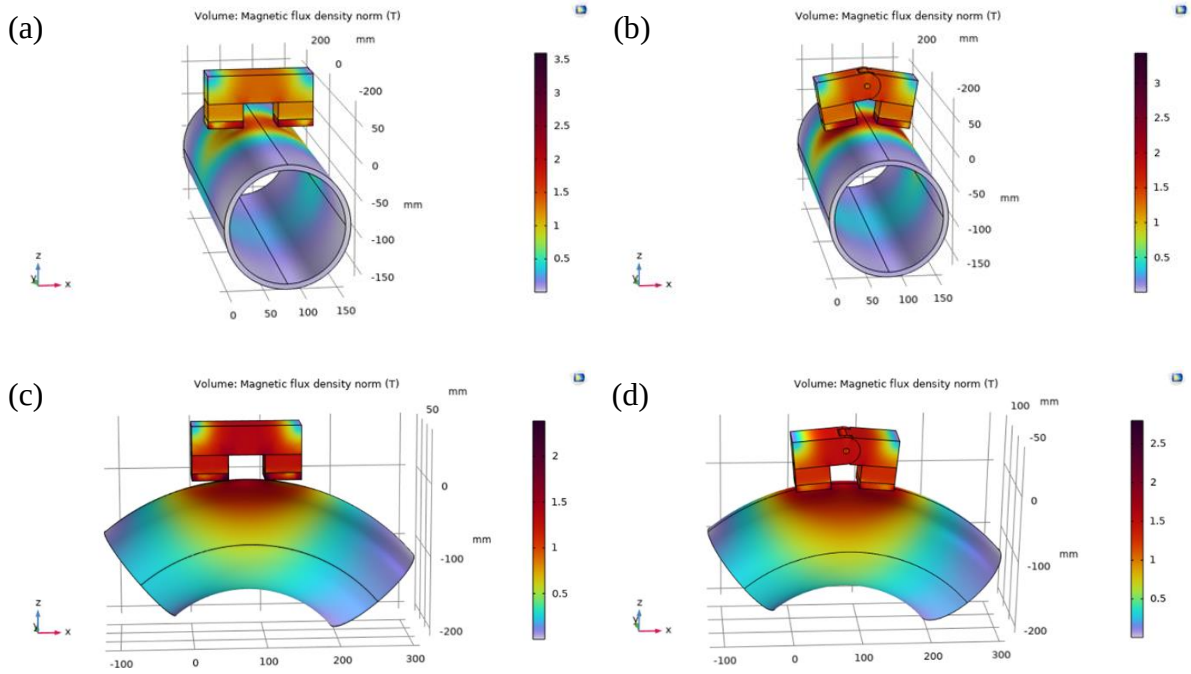


**Figure 4.11.** Comparison of FEA results for magnetic flux density obtained with the Ref and Hin circuit used on the pipe and elbow. (a) Ref circuit with pipe, (b) Hin circuit with pipe, (c) Ref circuit with elbow, and (d) Hin circuit with elbow.

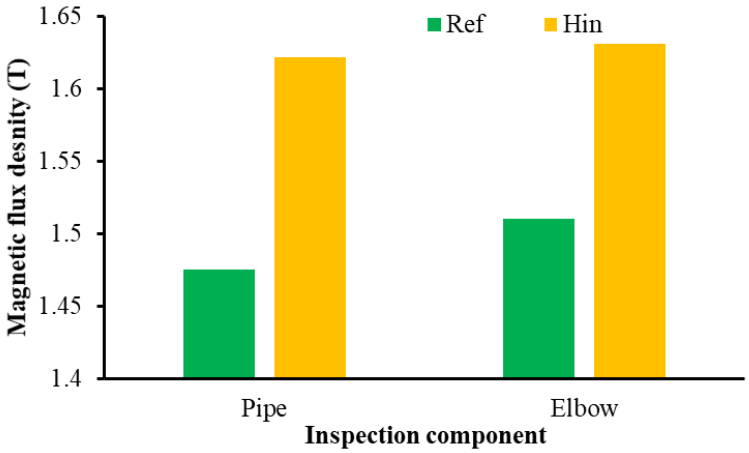


**Figure 4.12.** Magnetisation level achieve with Ref and Hin circuit on pipe and elbow.

## 4.4. Optimised (Opt) Circuit

Optimisation was conducted using the Optimisation 6.0 module in COMSOL [251] to achieve optimal circuit performance through parametric and topology optimisations coupling the FEM model to the optimisation solver. Table 4.5 summarises the optimisation setup used in this study, including solver configurations, objective function, design variables, filtering and projection methods, and constraints. A detailed description of the optimisation procedures is provided in Chapter 3. Since the optimisation is fully coupled with the magnetic fields, no currents physics interface, it uses the same numerical settings summarised in Table 4.1.

**Table 4.5.** Summary of the optimisation setup used in this study.

| Feature | Description |
|---|---|
| Optimisation type | Parametric and topology optimisation (coupled with FEM model) |
| Solvers used | BOBYQA (parametric), MMA (topology) |
| Objective function | Achieve magnetisation in operating region of **B**-**H** curve (target: 1.7 **T**); reduce circuit size; qualitatively increase flux uniformity |
| Design variables | Bridge length, bridge height, pole piece height |
| Parametric constraints | Upper and lower bounds for design variables |
| Topology constraints | Maximum 20% material removal |
| Projection parameters | Threshold: 0.5; Sharpness: 8 |
| Filtering and projection methods | Helmholtz filter and hyperbolic tangent projection function applied to design variable field |
| Penalisation Strategy | Minimum relative permeability: $1e^{-3}$ assigned to void regions to avoid singularities |
| Optimisation tolerance | Optimality tolerance: 0.001 |

### 4.4.1. Parametric Optimisation

Parametric optimisation was conducted using the bound optimisation by quadratic approximation (BOBYQA) algorithm. This method is effective for smooth objective functions that lack gradient information, refining parameter estimates through a quadratic model. BOBYQA efficiently explores the parameter space within bounds, ensuring convergence to an optimal solution. Parametric optimisation enables the examination of numerous parameters simultaneously, whereas parametric studies are conducted by focusing on one parameter at a time. The objective of the optimisation was to increase the magnetisation level of the inspection component towards the recommended operating region of the **B**-**H** curve, with a target magnetic flux density of 1.7 T. In parallel, achieving a uniform flux distribution. This uniformity was qualitatively observed to depend on the bridge length, as illustrated in Figures Figure 4.3. Other objectives of the design optimisation of the MFL circuit was to make its size compact so that it could be permanently installed in space-constrained and/or difficult-to-access areas. In such cases, a compact design is essential. The control variables were the pole piece height, magnet bridge length and magnet bridge thickness. The constraints were the upper and lower values of the control variables, as listed in Table 4.6. Using a single initial value for the control variable leads to parametric optimisation results closer to the initial values. Therefore, a parametric sweep of initial values within the range between lower and upper values was used. The optimisation results have several combinations of the control variables' values as listed in Table B.1 in Appendix B. Increasing bridge length further leads to a longer magnetic path length, increasing reluctance and decreasing magnetic flux density while resulting in a heavier magnetic circuit (reduces handling) [144], [158]. While shorter bridge length increases magnetic flux density, however, it leads to a leakage field due to a direct interaction between the two magnet poles. Therefore, based on an evaluation of key performance factors such as the magnetisation level, uniform flux distribution, reluctance and overall circuit size, a bridge length of 150 mm and a thickness of 40 mm were selected. These values also aligned with dimensions identified during the earlier parametric study. Moreover, the pole piece height of 5 mm was selected, which contributed to a more compact circuit design and enhanced the performance. As a result of the optimisation, the magnetic flux density at the target region increased to 1.55 T, indicating a modest yet meaningful improvement in the field strength, along with improved flux distribution (see Figure 4.3, which compares short and long bridge configurations) and reduced circuit volume. The results were then used in the topology optimisation, as described in the following Section 4.4.2.

**Table 4.6.** Control variables and constraints.

| Parameters | Initial values (mm) | Lower bounds (mm) | Upper bounds (mm) |
|---|---|---|---|
| Magnet bridge length | Range (100, 50, 200) | 100 | 200 |
| Magnet bridge thickness | Range (10, 10, 50) | 10 | 50 |
| Pole piece height | Range (0, 5, 30) | 0 | 30 |

### 4.4.2. Topology Optimisation

The topology optimisation was carried out using the method of moving asymptotes (MMA) algorithm. The objective of topology optimisation was to enhance the magnetisation level of the inspection component to 1.7 T at the point of interest, while minimising the magnetic field spreading outside the circuit and the overall weight of the MFL device by constraining the amount of material. The control variables were magnet bridge and pole pieces volume, defined in COMSOL density model. The **B**-**H** curves of the control variables were defined in terms of relative permeability, which was defined in terms of penalised material volume factor (PMVF (dtopo1thata-p)). In the physics section, the PMVF was used to link the control variables from the density model, ensuring that these variables are incorporated into the material physics. The constraint was set to remove 20% of the control variables, such as the magnet bridge and the pole piece materials. Figure 4.13 shows the results of the topology optimisation, with the blue region representing the removed part ($\Theta = 0$) and the red region indicating the retained part ($\Theta = 1$) of the design space. The topology optimisation result shows that the sharp corners of the bridge and pole pieces were removed. In the Ref and Hin circuits' simulation results, it was observed that these sharp corners were not in the path of the magnetic field, causing flux leakage and increasing the weight of the circuits. Figure 4.14 (a) shows the optimum circuit design based on the topology optimisation results and performing additional simulation analysis. The weight of the Opt circuit was reduced by 20%. Figure 4.14 (b), (c) and (d) show the 3D FEA results of the Opt circuit installed on the pipe, plate and elbow, respectively. The magnetic flux density obtained for plate, pipe and elbow using the Opt circuit was significantly increased compared to the Ref and Hin circuits, as shown in Figure 4.15.

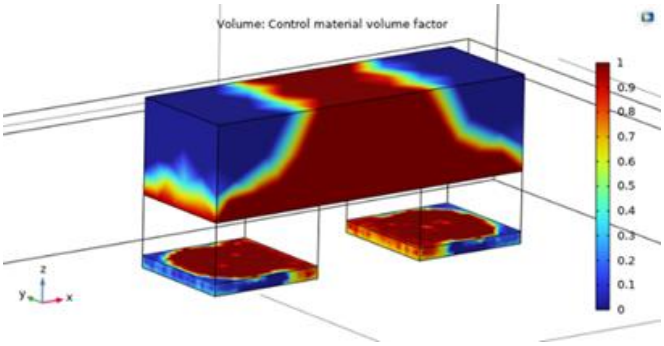


**Figure 4.13.** Topology optimisation results, removed (blue) and retained (red) parts in the design space.

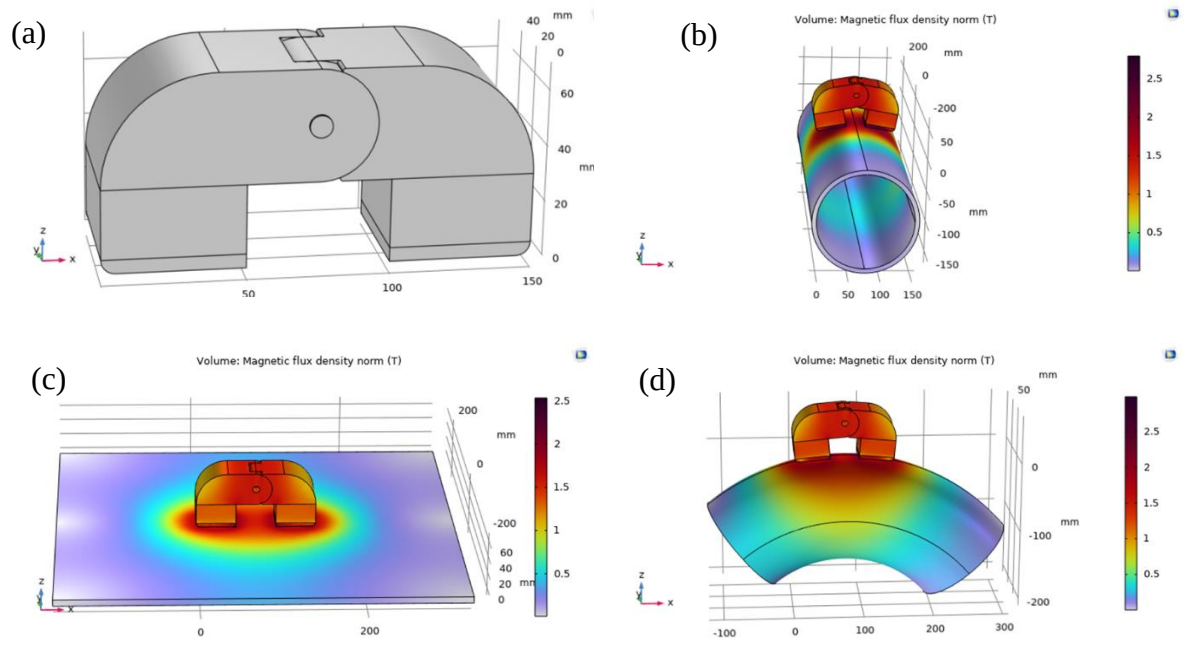


**Figure 4.14.** (a) Opt circuit design, (b) 3D FEA results of the Opt circuit installed on the pipe, (c) The Opt circuit installed on the plate, and (d) The Opt circuit installed on the elbow.

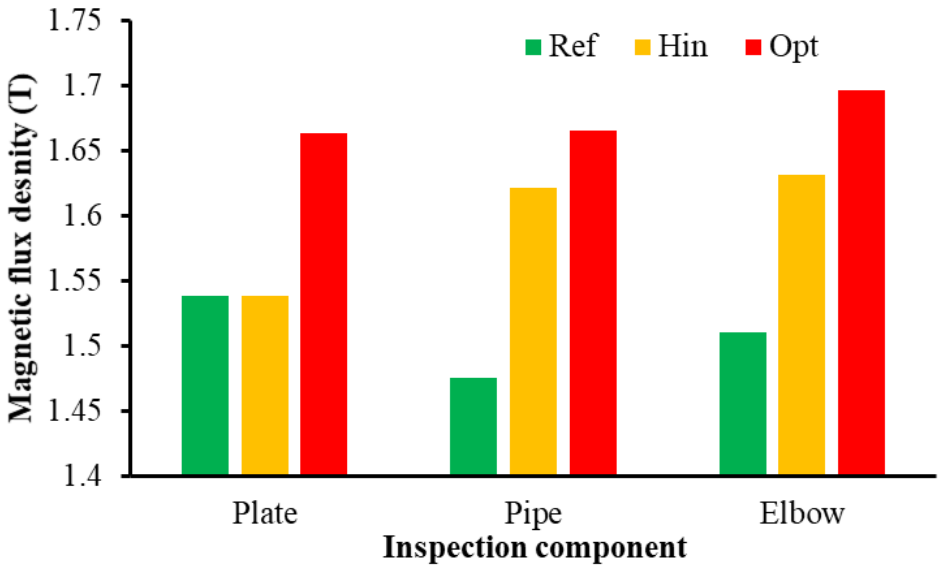


**Figure 4.15.** Magnetic flux density obtained using the Ref, Hin and Opt circuit on the plate, pipe and elbow.

## 4.5. Summary

In this chapter, a simulation-led design of the MFL circuit based on 3D FEA and the optimisation module of COMSOL Multiphysics was developed for permanent and long-term corrosion monitoring in challenging-to-access areas where localised corrosion occurrence is prevalent. After conducting an extensive parametric study to analyse the MFL reference configuration, an improved reference (Ref) circuit was developed based on the specified sample magnetisation level, recommended operation points on the **B-H** curve and increased uniformity of magnetic flux density inside the sample. While using the Ref circuit on non-planar surfaces such as pipes and pipe elbows, the circuit performance drops. Subsequently, a new hinged (Hin) circuit with a hinged magnet bridge was designed, which improved the performance of the system for non-planar surfaces. Four hinge types were considered, and the most suitable one was chosen. A novel Opt circuit was developed by performing parametric and topology optimisation of the best-performance Hin circuit to optimise the performance and reduce the overall weight of the device. The comparative analyses of the three designs reveal that the Opt circuit has optimal performance, is more compact and can be used on flat and curved inspection components such as plates, pipes and pipe elbows. Its compactness allows it to be installed permanently and easily in difficult-to-access areas.

# 5. EXPERIMENT

## 5.1. Introduction

In Chapter 4, a reference circuit with improved design parameters, a novel hinged-based design and a novel optimised design were developed. Ensuring the accuracy and reliability of these systems is critical, particularly when developing new magnetic circuit designs. This chapter presents validation of the simulation results by introducing defects and performing a thorough sensitivity analysis. Experimental validation helps to ensure that the simulation accurately predicts real-world behaviour. Sensitivity analysis evaluates the performance of the new designs under varied conditions.

This chapter presents the experimental validation of the new MFL system by introducing artificial cylindrical defects of known dimensions. The simulated leakage signal is compared with experimental measurements. This provides information about the model's accuracy and predictive capabilities. Furthermore, sensitivity analysis helps to understand the impact of defect parameters such as defect depth, radius, location, and sensor configurations on the MFL signal. This ensures the designs' accuracy in detecting and characterising defects of varying depths, radii, and locations and accounts for variations in sensor lift-off, thus confirming the system's robustness and reliability under diverse conditions. By analysing the strength and shape of the leakage signal, it is possible to estimate the severity of the defect and the capability of the MFL device to detect different defect sizes.

In this chapter, the experimental procedure, the baseline signal without defect and how defects change the baseline signal and the validation of simulation results for the Ref, Hin and Opt magnetic circuits on a plate, a pipe and a pipe elbow are presented by introducing machined cylindrical defects on the inspection components. The sensitivity analysis of several defects in terms of their radius, depth, location and sensor lift-off is discussed. The magnetic flux leakage signals are measured and compared.

## 5.2. Experimental Procedure

The Ref, Hin, and Opt circuits and artificial cylindrical defects with a range of depths, radii and locations were manufactured for experimental validation and sensitivity analysis. The cylindrical defects on the plates were machined using a reamer, while spark erosion was used to produce defects in the pipe and pipe elbow with high dimensional accuracy. Reaming typically achieves tolerances between ±0.005 mm to ±0.025 mm [259], whereas spark erosion

can attain a precision of up to ±0.005 mm [260]. The measured dimensions with errors of the defects on the inspection components are given in Appendix M Table M.1. The defects located on the pipe elbow and far surface of the pipe were internal and, therefore, not directly measurable. Figure 5.1 shows machined cylindrical defects on plates with different widths and depths, and on a pipe with different depths.

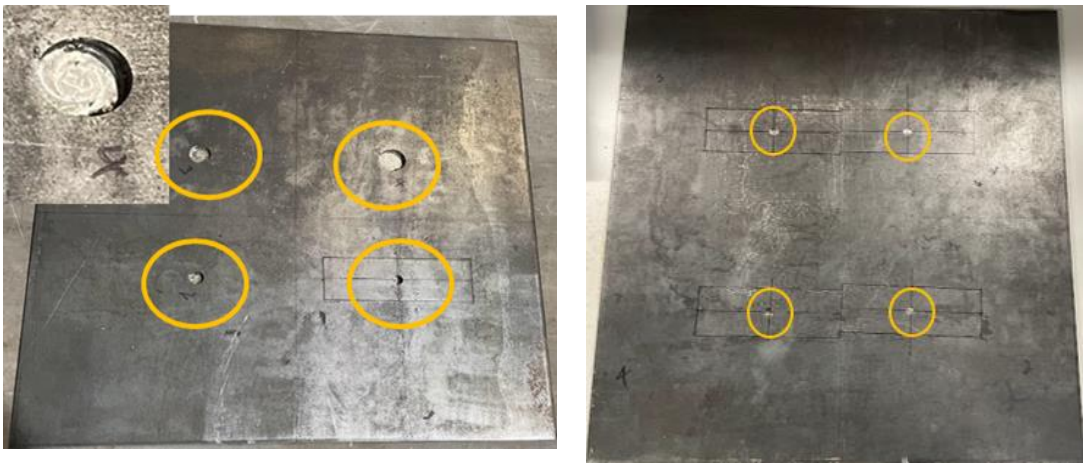

(a) (b)

(c)

**Figure 5.1**. Machined cylindrical defects on test specimens. (a) Plate with varying defect widths, (b) Plate with varying defect depths, and (c) Pipe with varying defect depths.

A GM08 handheld gaussmeter was used to measure the strength and polarity of magnetic flux density in milli Tesla (mT). It has a long, thin, semi-flexible rectangular transverse Hall probe measuring 1 mm thickness and 4 mm width, with a Hall effect sensor. The transverse probe with a measurement range/sensitivity of 0 - 29.99 mT, was used to detect magnetic flux leakage from defects.

A polylactic acid (PLA) plastic probe/sensor holder was designed with holes of 1 mm length and 4 mm height in the x-direction (magnet bridge length direction) and 3D-printed to secure the sensor in place during $\mathbf{B}_x$ measurements, ensuring precise positioning and repeatability of

the results. Figure 5.2 shows the sensor holder designs for curved and flat surfaces to measure $\mathbf{B}_x$. The holes were evenly spaced in both directions from the central line of the defect, with a gap of 2.4 mm between them. The number of holes in the probe holder depends on the defect radius. With a larger defect radius, more inspection points. Figure 5.3 shows the magnetic circuits with sensor holders fitted to measure $\mathbf{B}_x$ in flat plate and curved surfaces.

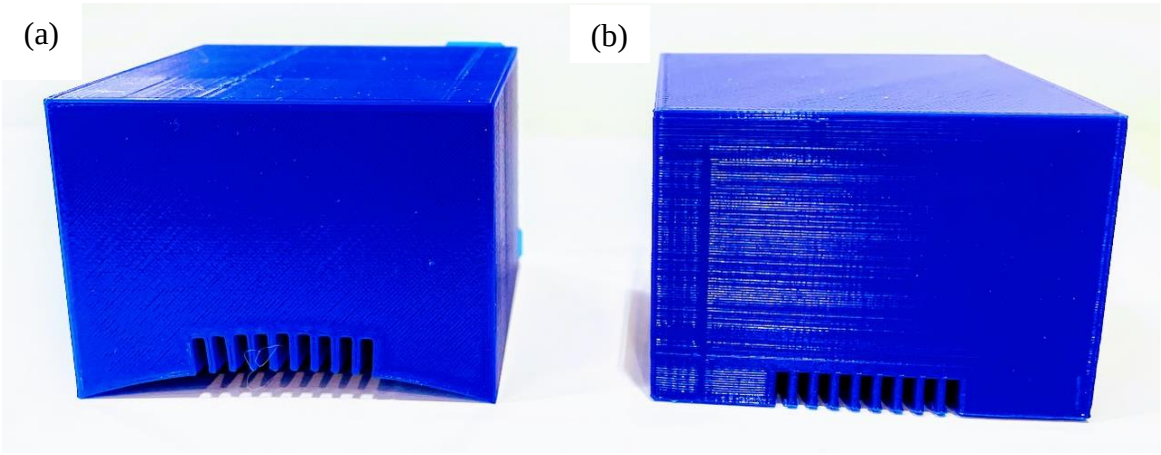


**Figure 5.2.** (a) The Ref circuit probe holder for curved surfaces, and (b) the Ref circuit probe holder for flat surfaces.

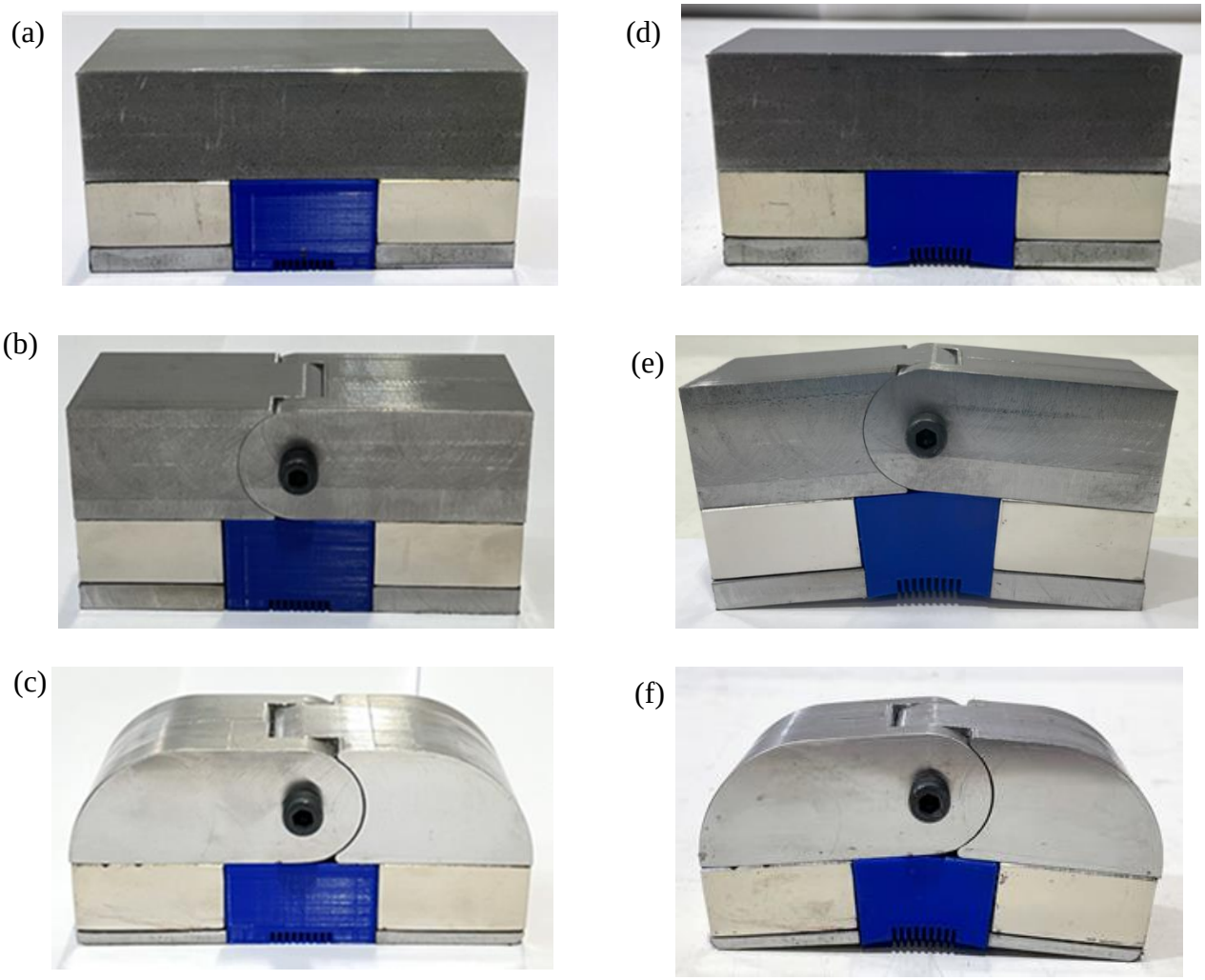


**Figure 5.3.** (a) The Ref circuit with the probe holder, (b) the Hin circuit with the probe holder, and (c) the Opt circuit with the probe holder to inspect the flat plate. (d) The Ref circuit with the probe holder, (e) the Hin circuit with the probe holder, and (f) the Opt circuit with the probe holder to inspect the curved surface.

Experiments were conducted using the Ref, Hin and Opt circuits on the inspection objects with and without defects. The material types and dimensions used for the circuits and inspection components were same as to those employed in the simulations. The leakage magnetic flux density in the x-direction, $\mathbf{B}_x$, and z-direction, $\mathbf{B}_z$, are in the magnetisation direction and perpendicular to the magnetisation direction, respectively. $\mathbf{B}_x$ and $\mathbf{B}_z$ were measured by moving the sensor from the centre of the defect in both positive and negative x-directions with a 2.4 mm gap at different inspection points based on the radius of the defect while keeping the magnetiser lift-off zero. Figure 5.4 and Figure 5.5 show the experimental systems where the Opt circuit was used on the flat plate and pipe elbow, respectively.

During the $\mathbf{B}_x$ measurement, the transverse Hall probe was precisely oriented perpendicular or 90° to the magnetisation direction by inserting it in the PLA sensor holder slot. This slot has a 1 mm length and 4 mm height designed to accommodate the probe in a fixed orientation securely. Due to the semiflexible and handheld nature of the device, the probe was manually handheld during measurement to maintain the correct alignment, unlike Figure 5.4 and Figure 5.5, where the probe is unsupported to take pictures. The sensor lift-off during $\mathbf{B}_x$ measurement was 2 mm, as the active Hall element is embedded at the centre of the 4 mm width probe.

The $\mathbf{B}_z$ component of the signal was measured by moving the probe aligned parallel to the magnetisation direction with the help of a calliper in the magnet bridge length direction using a PLA plastic probe holder to ensure consistent probe positioning and lift-off during scanning. The PLA plastic holder used for $\mathbf{B}_z$ measurement has a 1 mm thickness from the surface of the inspection component to create a sensor lift-off between the Hall sensor and the surface of the inspection component. This allows for maintaining a 2 mm sensor lift-off during $\mathbf{B}_z$ scanning as $\mathbf{B}_x$, with a 1 mm lift-off due to the probe holder thickness and a 1 mm lift-off from the probe thickness. The plastic probe holder has a central horizontal slot or hole with 1 mm height and without internal partitions, allowing it to accommodate a 4 mm wide Hall probe, free to move laterally across a 2.4 mm gap of nine measurement points. During $\mathbf{B}_z$ measurements, the probe was aligned parallel to the magnetisation direction by holding and aligning the probe along the length of the sample.

The correct orientation of the Hall probe during MFL measurements was achieved by aligning its sensitive axis perpendicular to the magnetic field component being measured. For $\mathbf{B}_x$ (the horizontal component), the probe was positioned with its sensing face oriented perpendicular to the x-direction of the magnetic field. While measuring Bz (the vertical component), the sensing face was aligned perpendicular to the z-direction. The probe is designed with a visible sensing element near the tip, allowing users to physically align the probe relative to the sample and the expected magnetic field direction.

A method was established to accurately locate the (0,0) coordinate of the defect relative to the magnet bridge edges. The zero position on the scan-axis (0, 0) was defined as a point in the centre of a defect. The zero position on the scan-axis was aligned with the defect centre by first measuring using a calliper, then manually marking the defect centre line and the region where the magnetic circuit would be placed before placing the circuit on the specimen surface, using reference edges on the specimen. The PLA plastic probe holders were designed to align the

scan-axis (Y = 0 mm) with the defect centre by stopping the active Hall probe element (located 3.5 mm behind the probe tip) at the centre of the defect by limiting the probe's forward movement. The holder is configured to stop 3.5 mm beyond the defect centre, ensuring that the active sensing element aligns precisely with the centre of the defect. A preliminary scan was performed across the defect to verify or correct the scanning origin aligns with the defect centre. The MFL signal was analysed for symmetry, peak amplitude and zero-crossing points (where flux transitions from positive to negative), which occur at the defect centre. Bidirectional scans were used to compare signal patterns in both directions, helping to identify and confirm the central position of the defect accurately. The scan axis was adjusted as needed to ensure that the scanning (0,0) coordinate aligned with the defect centre using the explained method.

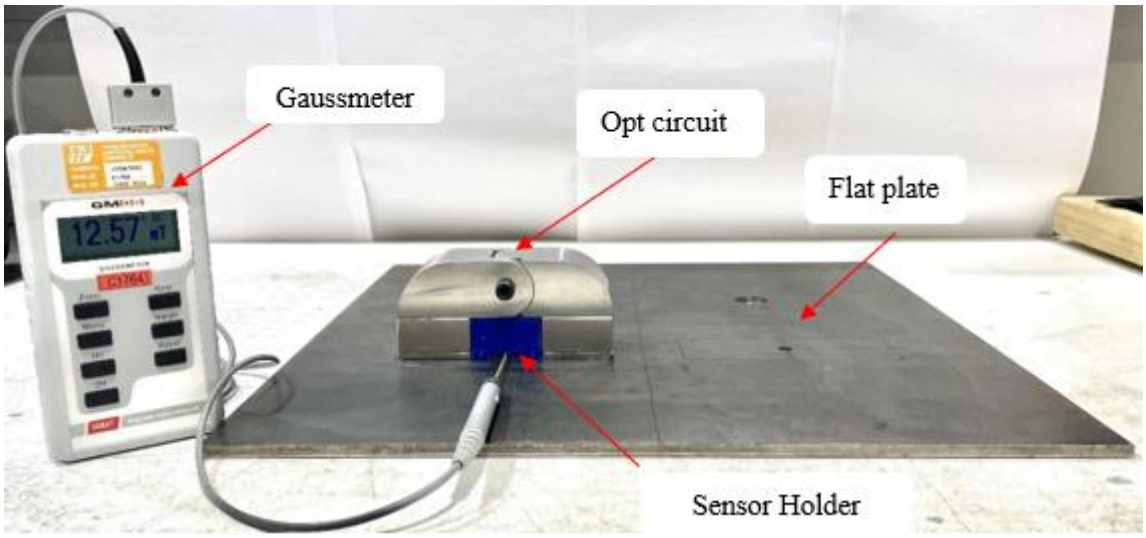


**Figure 5.4.** The experimental system for MFL measurements using the Opt circuit on the plate.

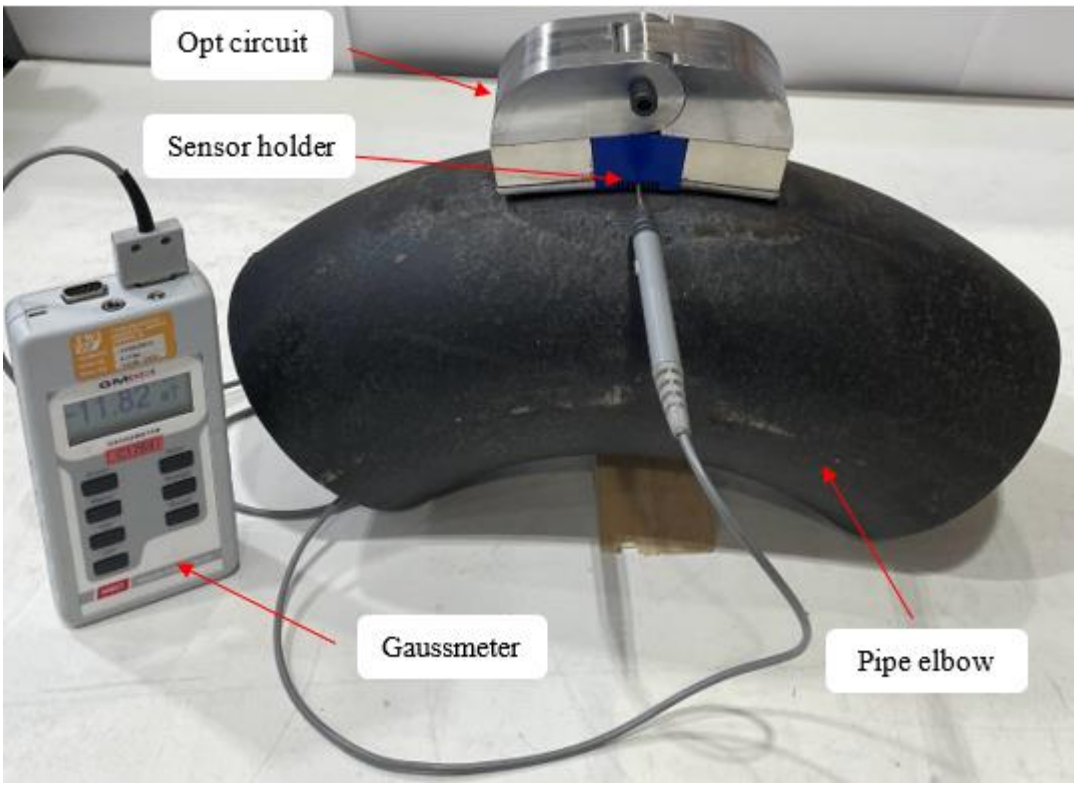


**Figure 5.5**. The experimental setup for the MFL measurements using the Opt circuit on the pipe elbow.

## 5.3. Validation of Numerical Results

The numerical results were validated experimentally by introducing defects. The 3D FEA modelling of flux leakage from defects employs magnetic fields, no currents physics interface in a stationary solver. It is governed by the magnetostatics form of Maxwell's equations, as described in Section 3.4.1. The same boundary conditions outlined in Section 3.4.1 were applied, and a mesh refinement study was conducted in the defect region, following the approach detailed in Section 3.4.2. For the plate and pipe, near-surface (external) cylindrical defects of 5 mm radius and depth of 80% of the wall thickness were machined. The highest erosion corrosion occurs at a pipe elbow bend, where the fluid changes its direction, as shown in Figure 1.3 [21]. Therefore, a far-surface (internal) cylindrical defect of 5 mm radius and depth of 80% of wall thickness was machined at the specified maximum erosion corrosion location on the pipe elbow for experimental validation. The Ref, Hin and Opt circuits were used, and the leakage magnetic flux density in the x-direction ($\mathbf{B}_x$) was measured numerically and experimentally at nine inspection points while keeping the magnetiser lift-off zero and with a 2 mm sensor lift-off from the surface of the inspection components. Figure 5.6 shows experimental and simulation results obtained for the Ref circuit on a defect-free plate. The

leakage signal is minimal at the centre and increases towards the edges due to the MFL magnets. The same profile was obtained for the defect-free inspection component in a previous study [116].

In Figure 5.7 (a), (b) and (c), simulation and experimental results are compared by measuring the leakage magnetic flux density from defects on the plate using the three magnetic circuits, Ref, Hin and Opt circuits, respectively. Figure 5.8 (a), (b) and (c) illustrate validation of simulation results on the pipe using the Ref, Hin and Opt circuits, respectively. In Figure 5.9 (a), (b) and (c), the leakage magnetic flux density is measured in simulation and experiment using the Ref, Hin and Opt circuits, respectively, on the pipe elbow. The results comprehensively compare modelled and observed leakage magnetic flux densities across these inspection components, and the discrepancy between experimental and simulation results was below 2% for all test cases. The strongest signal of the leakage is seen in the area of imperfection, and the leakage signal deteriorates away from the centre of the imperfection, reaching its minimum at around 7.2 mm away from the centre of the imperfection. Any increase in signal strength beyond 7.2 mm is attributable to the proximity of MFL magnets and can be disregarded. When comparing the performance of the Ref, Hin and Opt circuits experimentally for the three inspection components, plate, pipe and pipe elbow, the Opt circuit provides the highest performance in all cases, as shown in Figure 5.7 (d), Figure 5.8 (d) and Figure 5.9 (d), respectively. The significant increase in the performance of the Opt circuit on the pipe and the pipe elbow is due to optimised circuit design and the introduced hinge in the Opt circuit. Moreover, the leakage signals are weaker for pipe elbow compared to the plate and pipe since far-surface defect is considered for the pipe elbow, and the effect of defect location will be discussed in section 5.4.2.

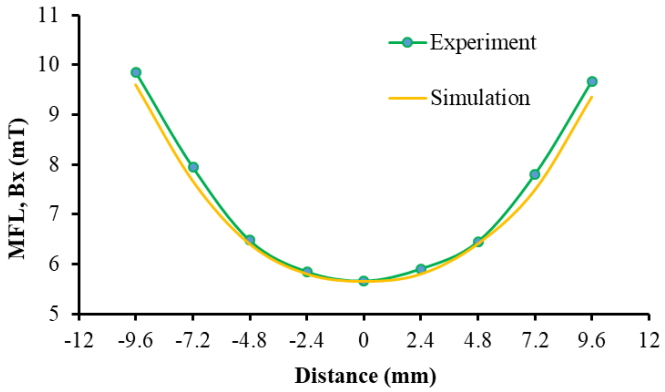


**Figure 5.6.** Experimental and simulation results of leakage signal distribution across a defect-free plate using the Ref circuit. The signal is weakest at the centre and increases toward the edges due to the magnet.

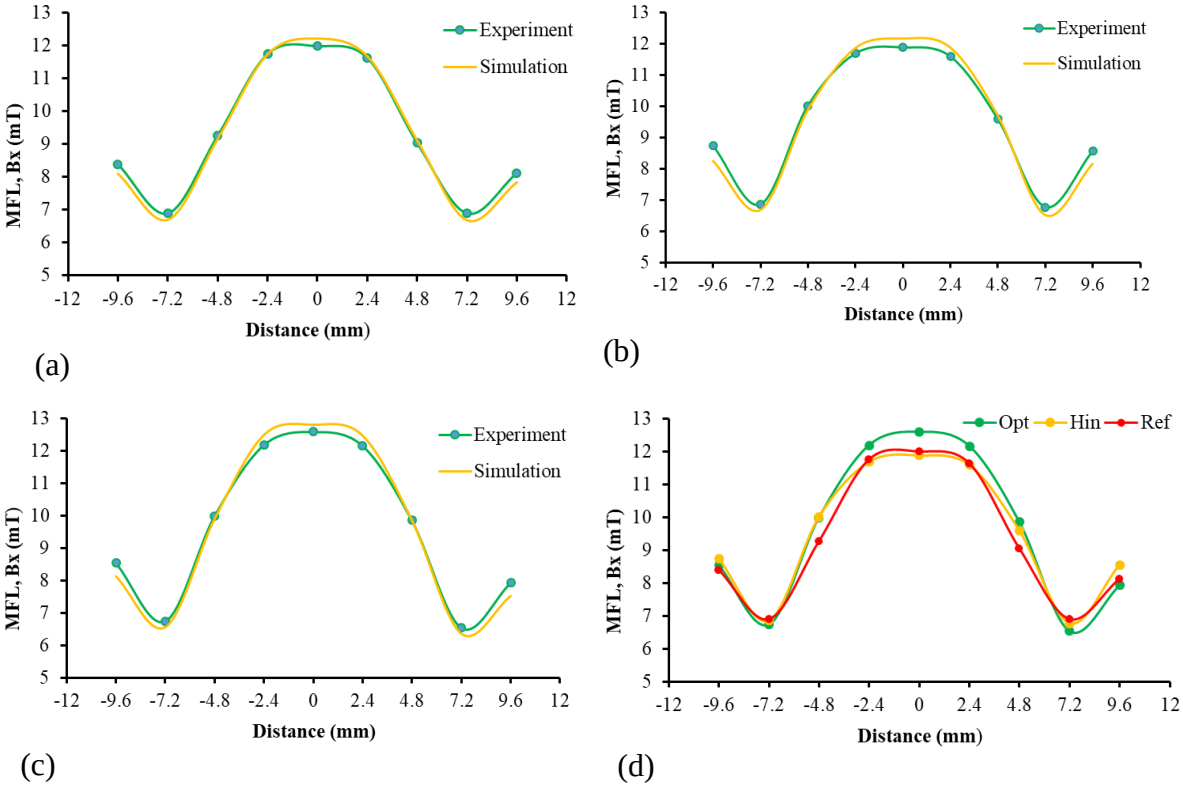


**Figure 5.7.** Validation of simulation results experimentally on the flat plate using (a) the Ref circuit, (b) the Hin circuit and (c) the Opt circuit. And (d) experimental results using the Ref, Hin and Opt circuits on the flat plate.

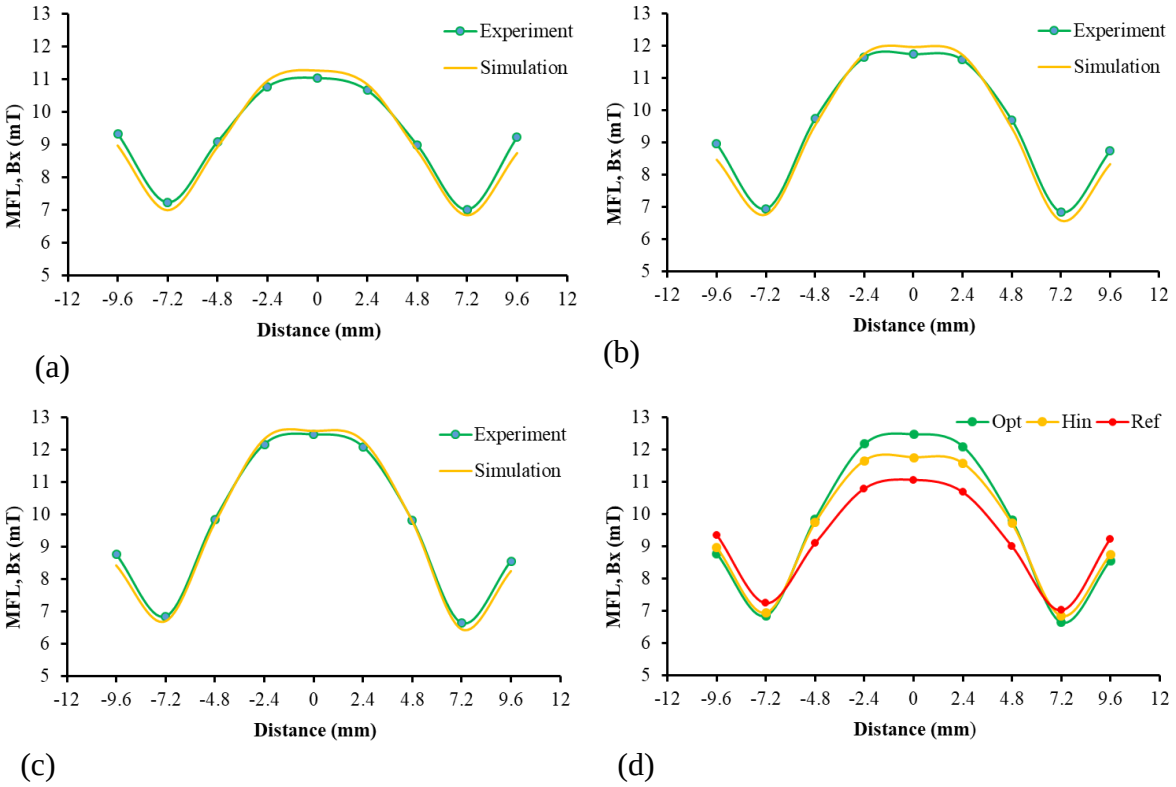


**Figure 5.8.** Simulation and experimental results on the pipe using (a) the Ref circuit, (b) the Hin circuit and (c) the Opt circuit. And (d) experimental results of the Ref, Hin and Opt circuits on the pipe.

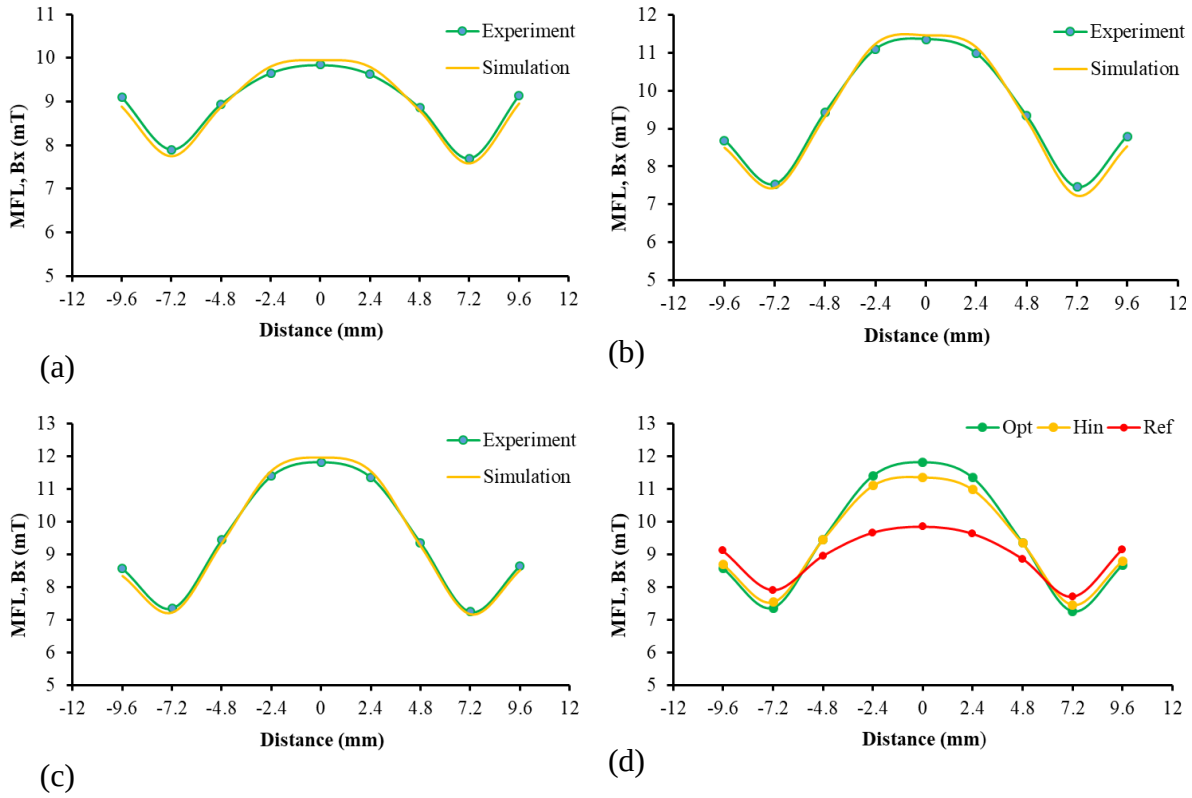


**Figure 5.9.** Comparison of simulation and experimental results on the pipe elbow using (a) the Ref circuit, (b) the Hin circuit and (c) the Opt circuit. And (d) experimental results of the Ref, Hin and Opt circuits on the pipe elbow.

## 5.4. Sensitivity Analysis of defects

### 5.4.1. Defect Depth

The effect of defect depth on the MFL signals ($\mathbf{B}_x$ and $\mathbf{B}_z$) was studied by machining near-surface cylindrical defects of 5 mm radius and depth of 0%, 20%, 40%, 60% and 80% of the wall thickness on the plate and pipe. The $\mathbf{B}_x$ and $\mathbf{B}_z$ were measured experimentally using the Ref, Hin and Opt circuits.

Figure 5.10 (a) and (b) show the $\mathbf{B}_x$ and $\mathbf{B}_z$ leakage signals, respectively, obtained on the plate for different defect depths using the Ref circuit. Similarly, Figure 5.11 (a) and (b) illustrate the $\mathbf{B}_x$ and $\mathbf{B}_z$ leakage signals using the Hin circuit, and Figure 5.12 (a) and (b) present the $\mathbf{B}_x$ and **B**z leakage signals using the Opt circuit. Figure 5.13 (a) and (b) compare $\mathbf{B}_x$ and $\mathbf{B}_z$ leakage signals obtained using the Ref, Hin and Opt circuits for a 5 mm defect radius and depth of 80% of wall thickness on the plate.

The effect of defect depth was analysed by measuring $\mathbf{B}_x$ and $\mathbf{B}_z$ signals for a 5 mm defect radius by increasing defect depth from 0% of wall thickness to 80% with a 20% gap using the

Ref circuits on the pipe, as shown in Figure 5.14 (a) and (b), respectively. Likewise, Figure 5.15 (a) and (b) present the $\mathbf{B}_x$ and $\mathbf{B}_z$ leakage signals using the Hin circuit, and Figure 5.16 (a) and (b) show the $\mathbf{B}_x$ and $\mathbf{B}_z$ leakage signals using the Opt circuit. Figure 5.17 (a) and (b) compare the performance of the three circuits on the pipe for a 5 mm defect radius and depth of 80% of wall thickness by measuring $\mathbf{B}_x$ and $\mathbf{B}_z$, respectively.

For the defect-free inspection components, the leakage signal is weak in the centre and increases further away from the centre due to the MFL magnets. The leakage signals increase with increasing defect depths for all test cases. On average, a 20% increase in defect depth results in approximately a 19% rise in peak leakage signal across the 20% to 80% depth range. As the depth of a defect increases, the increased defect volume causes a more significant interruption in the continuity of the magnetic path within the ferromagnetic material. The defect causes flux lines to divert from the material into the surrounding air. The disruption results in more magnetic flux leaking out of the material. Then, the stronger signals are more easily detected by the sensors. The increase in magnetic flux leakage signals with defect depth due to enhanced disruption of magnetic field continuity aligns with findings in earlier studies [176], [177], [178]. The $\mathbf{B}_x$ signals are greater than $\mathbf{B}_z$ signals because $\mathbf{B}_x$ aligns in the direction of magnetisation. This alignment causes $\mathbf{B}_x$ to be more responsive to disruptions in the magnetic field caused by defects.

When the depth of a defect is 20% of the wall thickness (minimal defect depth or shallow defect), the $\mathbf{B}_x$ leakage signal splits into two peaks due to the leakage field being concentrated at the edges of the defect. When comparing the performance of the three circuits, the Opt circuit has the highest performance. The performance of the Ref circuit on the pipe significantly drops due to the curvature of the pipe. The relationship between defect depth and leakage signals is crucial for quantitative analysis and sizing defects in pipelines and other structures using MFL testing.

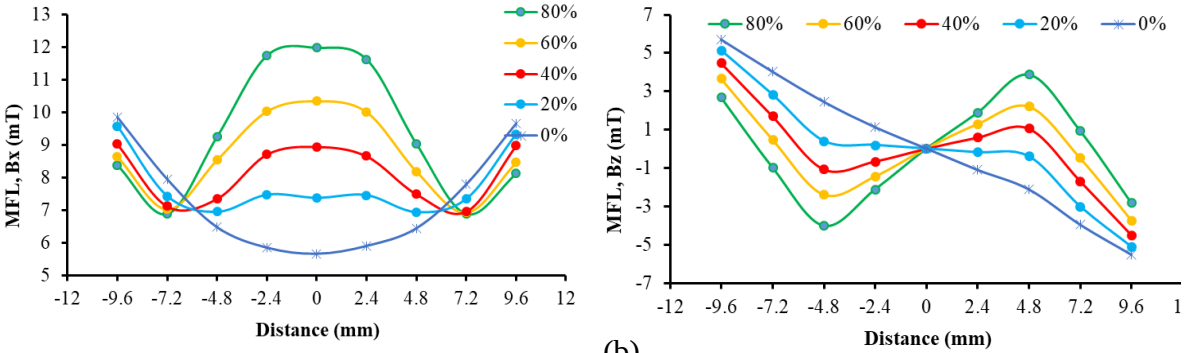


(a) (b)

**Figure 5.10.** Effect of defect depths on (a) the $\mathbf{B}_x$ and (b) $\mathbf{B}_z$ leakage signals using the Ref circuit on the plate for a 5 mm defect radius and depth of 0%, 20%, 40%, 60% and 80% of the wall thickness.

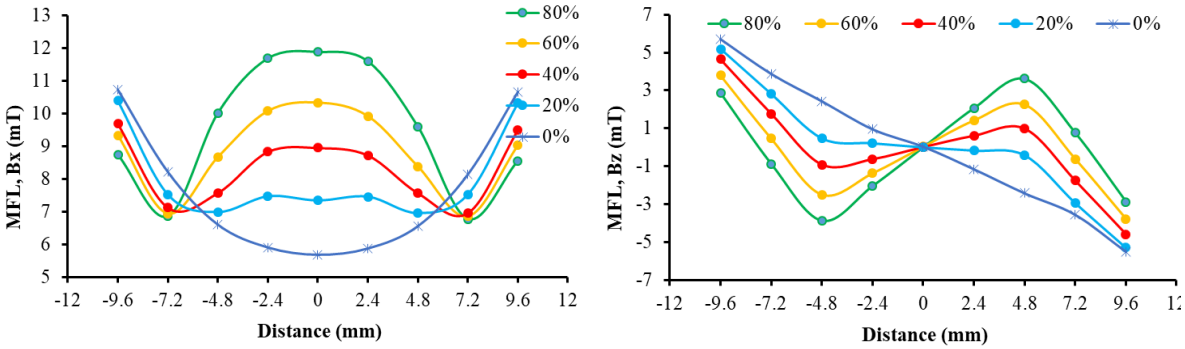


(a) (b)

**Figure 5.11.** Impact of defect depths on (a) the $\mathbf{B}_x$ and (b) $\mathbf{B}_z$ leakage signals using the Hin circuit on the plate for a 5 mm defect radius and depth of 0%, 20%, 40%, 60% and 80% of the wall thickness.

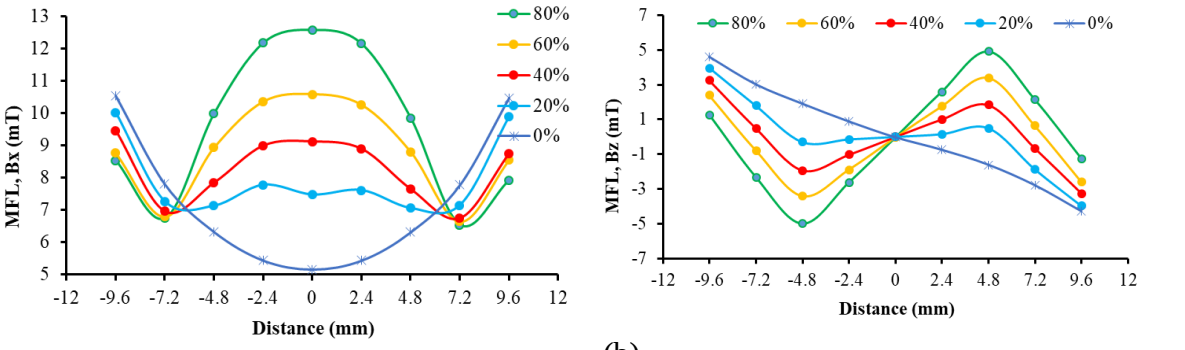


(a) (b)

**Figure 5.12.** Influence of defect depths on (a) the $\mathbf{B}_x$ and (b) $\mathbf{B}_z$ leakage signals using the Opt circuit on the plate for a 5 mm defect radius and depth of 0%, 20%, 40%, 60% and 80% of the wall thickness.

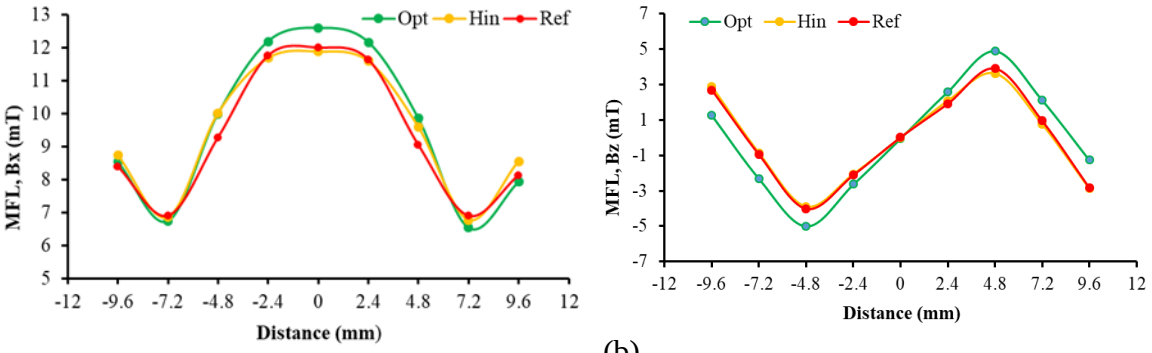


**Figure 5.13.** (a) The $\mathbf{B}_x$ and (b) $\mathbf{B}_z$ leakage signals using the Ref, Hin and Opt circuits for a 5 mm defect radius and depth of 80% of wall thickness on the plate.

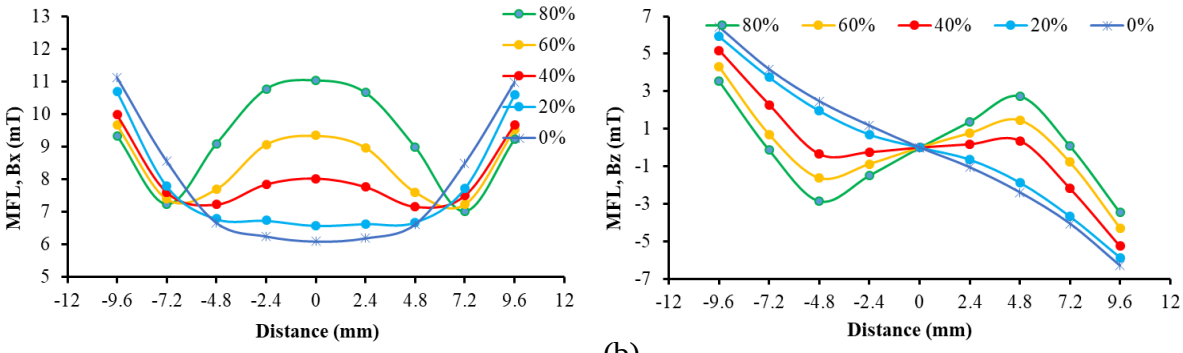


**Figure 5.14.** Effect of defect depths on the MFL signals using the Ref circuit on the pipe for a 5 mm defect radius and depth of 0%, 20%, 40%, 60% and 80% of the wall thickness measuring: (a) $\mathbf{B}_x$ leakage signals and (b) $\mathbf{B}_z$ leakage signals.

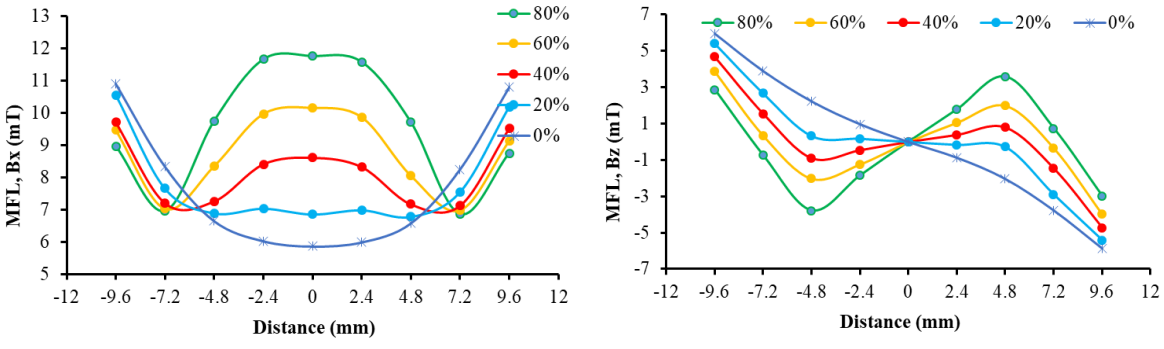


**Figure 5.15.** Impact of defect depths on (a) the $\mathbf{B}_x$ and (b) $\mathbf{B}_z$ leakage signals using the Hin circuit on the pipe for a 5 mm defect radius and depth of 0%, 20%, 40%, 60% and 80% of the wall thickness.

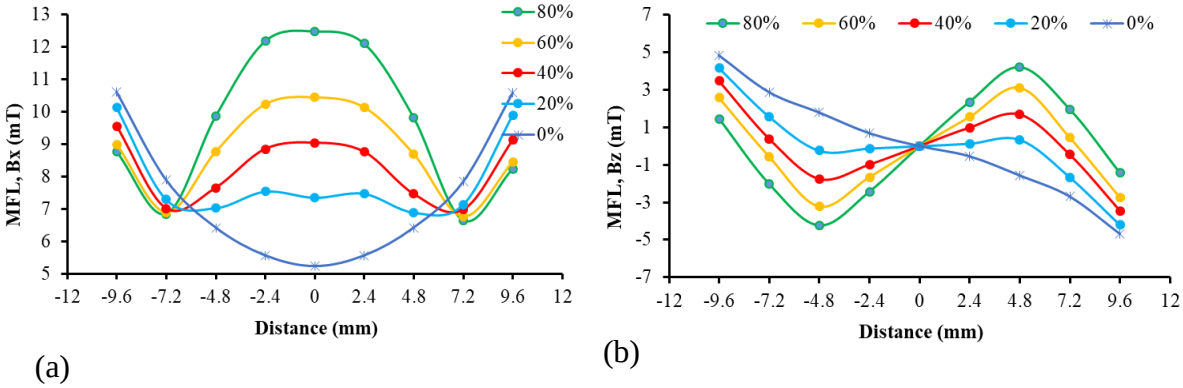


**Figure 5.16.** Influence of defect depths on (a) the $\mathbf{B}_x$ and (b) $\mathbf{B}_z$ leakage signals using the Opt circuit on the pipe for a 5 mm defect radius and depth of 0%, 20%, 40%, 60% and 80% of the wall thickness.

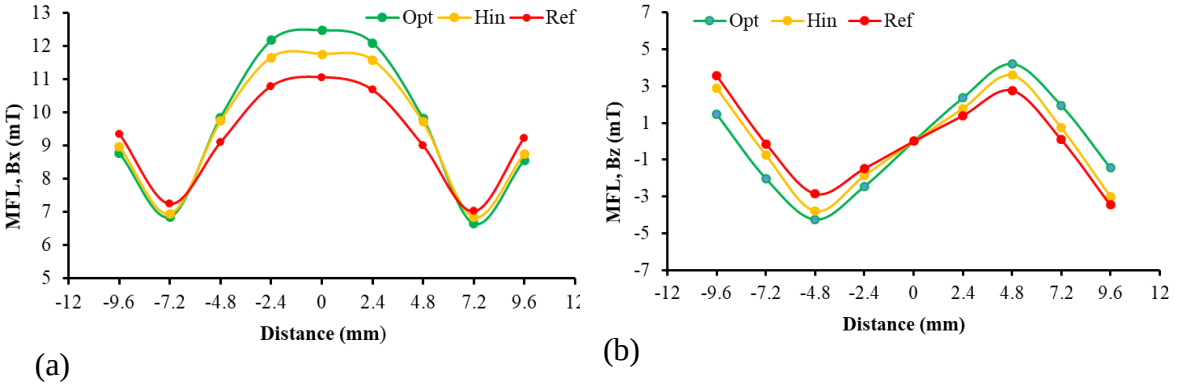


**Figure 5.17.** (a) The $\mathbf{B}_x$ and (b) $\mathbf{B}_z$ leakage signals using the Ref, Hin and Opt circuits for a 5 mm defect radius and depth of 80% of wall thickness on the pipe.

### 5.4.2. Defect Location

Sensitivity to defect location was analysed by considering far-surface defects of 5 mm radius and depth of 0%, 20%, 40%, 60% and 80% of the wall thickness using the Ref, Hin and Opt circuits on the plate and pipe, and comparing experimentally measured leakage signals from far-surface defects using the three circuits and with leakage signals obtained from near-surface defects. Figure 5.18 (a), (b) and (c) show $\mathbf{B}_x$ MFL signals measured from a far-surface 5 mm defect radius and depth of 0%, 20%, 40%, 60% and 80% of the wall thickness on the plate using the Ref, Hin and Opt circuits, respectively. Figure 5.18 (d) shows $\mathbf{B}_x$ MFL signals measured from a far-surface 5 mm defect radius and depth of 80% of wall thickness on the plate using the Ref, Hin and Opt circuits. Figure 5.19 shows $\mathbf{B}_x$ MFL signals obtained for near and far-surface defects of 5 mm radius and depth of 80% of wall thickness using the Opt circuit on the plate.

Figure 5.20 (a), (b) and (c) show $\mathbf{B}_x$ MFL signals measured from a far-surface 5 mm defect radius and depth of 0%, 20%, 40%, 60% and 80% of the wall thickness on the pipe using the Ref, Hin and Opt circuits, respectively. Figure 5.20 (d) shows $\mathbf{B}_x$ MFL signals measured from a far-surface 5 mm defect radius and depth of 80% of wall thickness on the pipe using the Ref, Hin and Opt circuits. Figure 5.21 shows $\mathbf{B}_x$ MFL signals obtained for near and far-surface defects of 5 mm radius and depth of 80% of wall thickness on the pipe using the Opt circuit.

The MFL signal obtained for near-surface defects is higher than for far-surface defects. On average, a reduction of approximately 10% in peak signal amplitude is observed for far-surface defects. This is because near-surface defects are closer to the sensors and the surface of the material, where the MFL signal strength is highest. MFL signals are more concentrated near the surface of the defects, making detecting leakage fields from defects close to the surface easier. For far-surface defects, the MFL signal must penetrate the material before reaching the sensor. This causes attenuation or weakening of the MFL signals. The path the leaked magnetic flux needs to travel to reach the sensors is shorter for near-surface defects, which means less flux is lost or dispersed before detection, resulting in a stronger signal. Far-surface defects have a longer path for the leaked magnetic flux to travel. When the flux travels this longer path, it can spread out and weaken, leading to reduced MFL signals. The observed increase in magnetic flux leakage signal for near-surface defects compared to far-surface defects agrees with previous studies. As reported in [189], [190], far-surface defects produce weaker signals since the defects are further from the sensor and the presence of a ferromagnetic wall between them.

When comparing the performance of the three circuits on the plate and pipe, the Opt circuit has the highest performance, as shown in Figure 5.18 (d) and Figure 5.20 (d). The performance of the Ref circuit on the pipe significantly drops due to the curvature of the pipe. The $\mathbf{B}_x$ signal obtained from a defect with a depth of 20% of wall thickness is roughly similar to that with no defect, see Figure 5.20 (a).

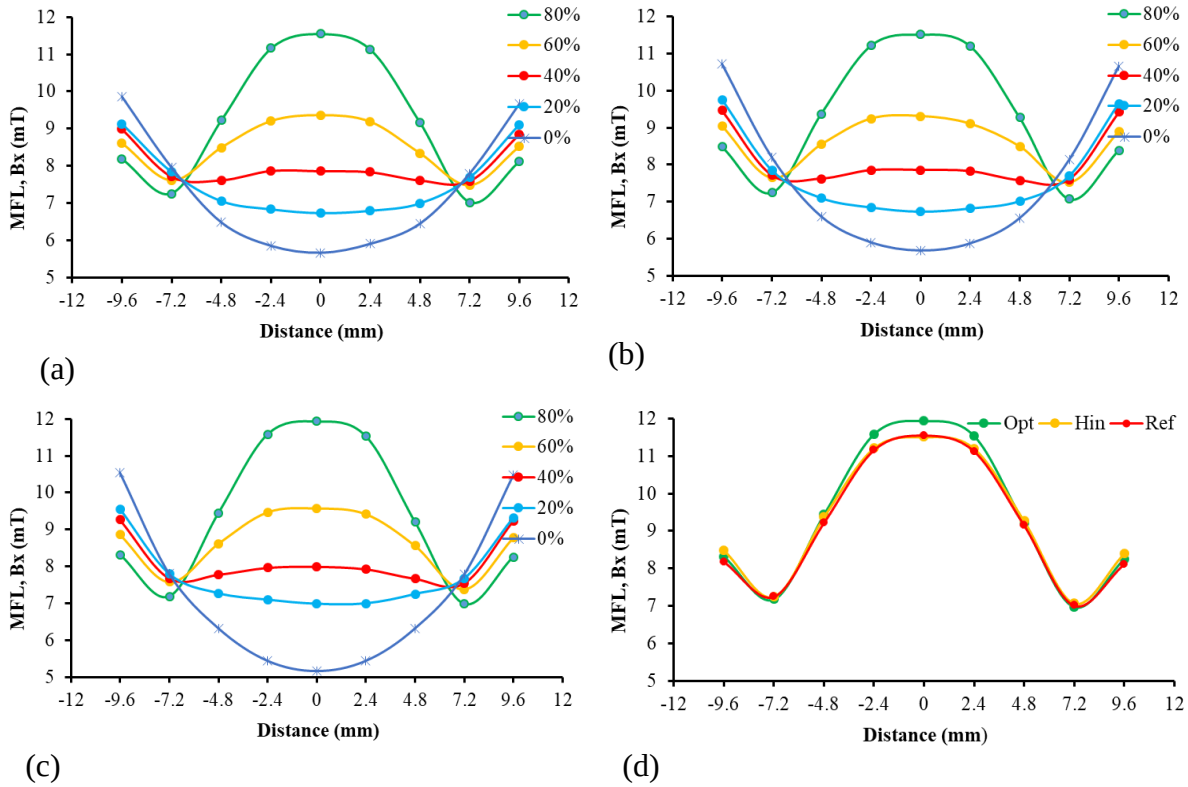


**Figure 5.18.** The $\mathbf{B}_x$ MFL signals obtained from a far-surface 5 mm defect radius and depth of 0%, 20%, 40%, 60% and 80% of the wall thickness using (a) the Ref, (b) the Hin and (c) the Opt circuits on the plate. And (d) the $\mathbf{B}_x$ MFL signals obtained for a far-surface 5 mm defect radius and depth of 80% of the wall thickness using the Ref, Hin and Opt circuits on the plate.

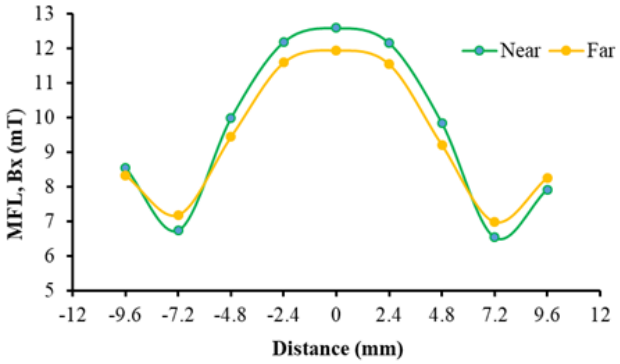


**Figure 5.19.** The $\mathbf{B}_x$ MFL signals for near and far-surface defect of a 5 mm defect radius and depth of 80% of the wall thickness using the Opt circuit on the plate.

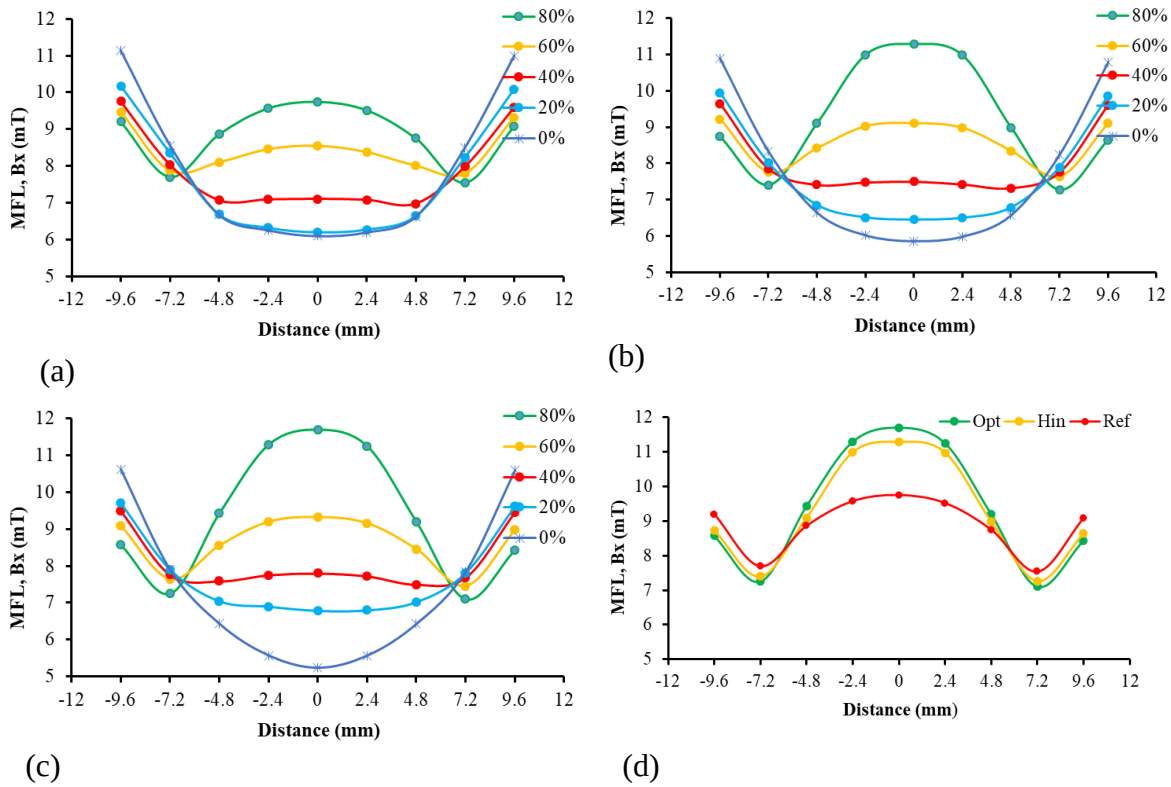


**Figure 5.20.** The $\mathbf{B}_x$ MFL signals obtained from a far-surface 5 mm defect radius and depth of 0%, 20%, 40%, 60% and 80% of the wall thickness using (a) The Ref, (b) The Hin and (c) The Opt circuits on the pipe. And (d) the $\mathbf{B}_x$ leakage signals obtained for a far-surface 5 mm defect radius and depth of 80% of the wall thickness using the Ref, Hin and Opt circuits on the pipe.

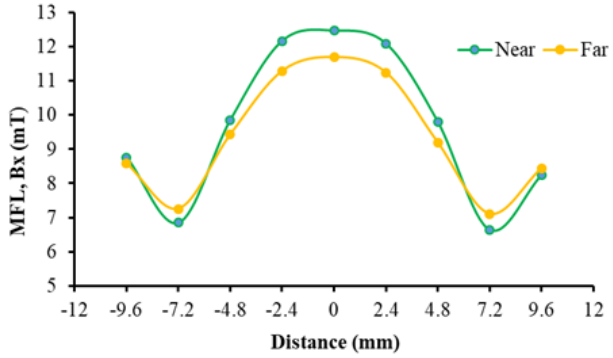


**Figure 5.21.** The $\mathbf{B}_x$ MFL signals for near and far-surface defect of a 5 mm defect radius and depth of 80% of the wall thickness using the Opt circuit on the pipe.

### 5.4.3. Defect Radius

The radius of the defect with a depth of 80% wall thickness was varied to 2 mm, 5 mm, 8 mm and 11 mm to experimentally analyse the effect of defect radius on the MFL signal using the Ref, Hin and Opt circuits on the plate. The number of inspection points for 2 mm, 5 mm, 8 mm and 11 mm defect radii was seven, nine, eleven and fifteen, respectively, with a 2.4 mm gap

between the inspection points. Figure 5.22 (a), (b) and (c) show that the $\mathbf{B}_x$ MFL signal increases with increasing defect radius because a larger defect radius causes significant disruption/ perturbation in the magnetic path, resulting in stronger and more detectable MFL signals. The observed increase of MFL signal with defect radius/width agrees with previous studies [172], [261]. Moreover, the $\mathbf{B}_x$ MFL signal splits into two peaks for larger defect radii due to the nature of the magnetic flux distribution around the defect. The magnetic flux lines are only slightly disrupted for a small defect radius. The flux leakage is concentrated in a small area directly above the defect, resulting in a single, centralised peak in the $\mathbf{B}_x$ MFL signal. For a larger defect radius, the disruption to the magnetic flux lines is more significant and spread over a larger area. The magnetic flux lines are pushed further apart and concentrate more around the edges of the defect (edge effect). This causes the $\mathbf{B}_x$ signal to split into two peaks and form double peaks. The central area directly above the defect has lower flux density because the flux lines bend around the defect edge rather than leak directly upward. The distance between the peaks can provide information about the size of the defect. A larger defect radius will have peaks further apart than smaller defects. The height and shape of the peaks can also help in assessing the severity and nature of the defect.

Figure 5.22 (d) shows $\mathbf{B}_x$ signals obtained with the Ref, Hin, and Opt circuits for an 8 mm defect radius and a depth of 80% of the wall thickness on the plate. The results show the highest $\mathbf{B}_x$ signal obtained using the Opt circuit.

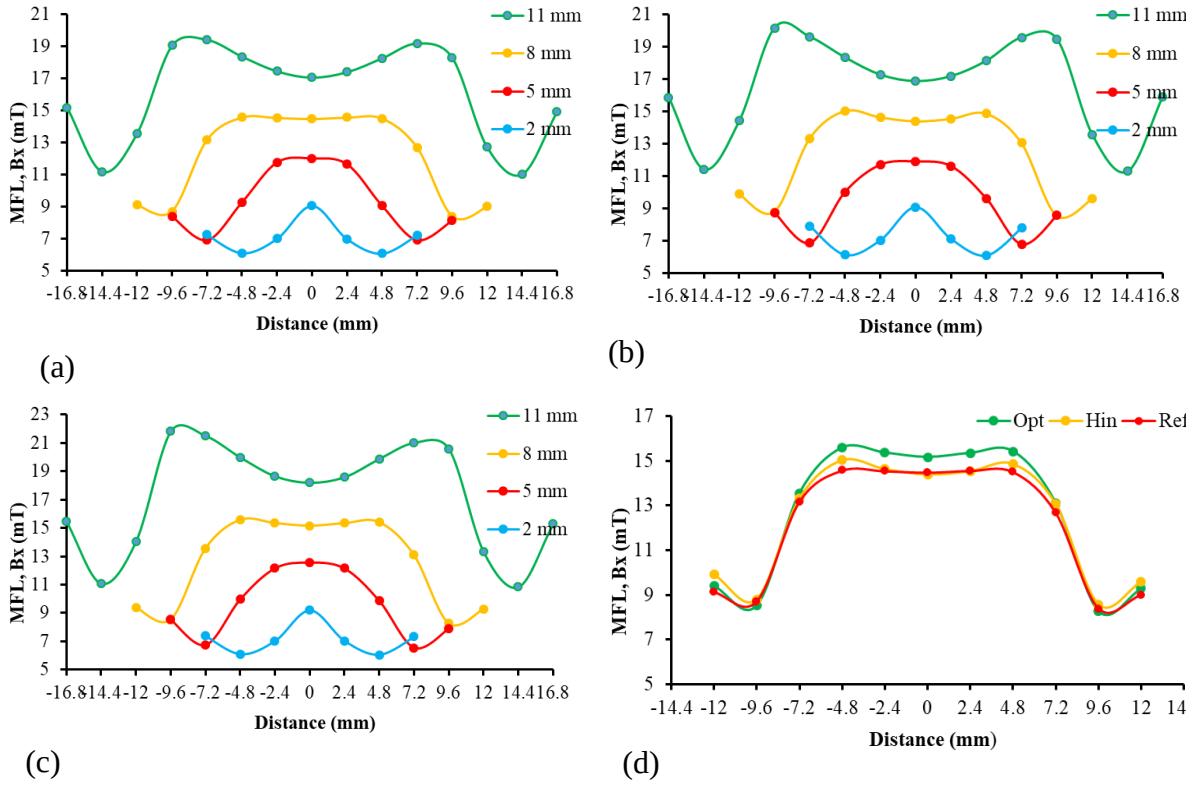


**Figure 5.22.** Effect of defects radii on $\mathbf{B}_x$ signals on the plate using (a) the Ref circuit, (b) the Hin circuit and (c) the Opt circuit. And (d) the $\mathbf{B}_x$ signals obtained with the Ref, Hin and Opt circuits for an 8 mm defect radius and depth of 80% of wall thickness on the plate.

### 5.4.4. Sensor Lift-off

The effect of sensor lift-off was analysed by varying the sensor lift-off and measuring leakage signals from defects. Figure 5.23 (a) and (b) show that the $\mathbf{B}_x$ and $\mathbf{B}_z$ MFL signals measured using the Opt circuit for a near-surface defect on the plate with a 5 mm defect radius and depth of 60% of wall thickness with 0.5 mm, 1 mm, 2 mm, 3 mm, 4 mm and 5 mm sensor lift-offs. Figure 5.23 (c) and (d) show that the $\mathbf{B}_z$ signals measured using the Opt circuit on the plate with a near-surface defect of 5 mm radius and depth of 0%, 20%, 40%, 60% and 80% of the wall thickness with 2 mm and 0.5 mm sensor-offs, respectively. The signals were measured experimentally for all 2 mm sensor lift-offs and in simulation for the rest of the sensor lift-offs.

As the sensor lift-off increases, the sensor is moved further away from the surface. The detected MFL signals weaken because the field lines spread out and diminish in strength. This is due to the increased distance from the defect (signal coming from defects), causing the leakage field to traverse a longer path, leading to greater attenuation and a weaker signal at the sensor. The further the sensor is from the surface where the magnetic flux leakage occurs, the more the magnetic signal attenuates, resulting in weaker MFL signals. With a bigger lift-off, the signal

strength decreases while background noise (leakage field without any defect) remains relatively constant, leading to a lower signal-to-noise ratio (SNR). When SNR is lower, it is harder to distinguish the defect signal from the noise, and the sensor becomes less effective at detecting small changes in the magnetic flux density. This results in a challenge to identify and characterise defects. Previous studies by Valentine [161], Yang et al. [163] and Azizzadeh and Safizadeh [162], [164] have demonstrated that increasing the sensor lift-off significantly decreases the MFL signal. Therefore, minimising sensor lift-off is essential.

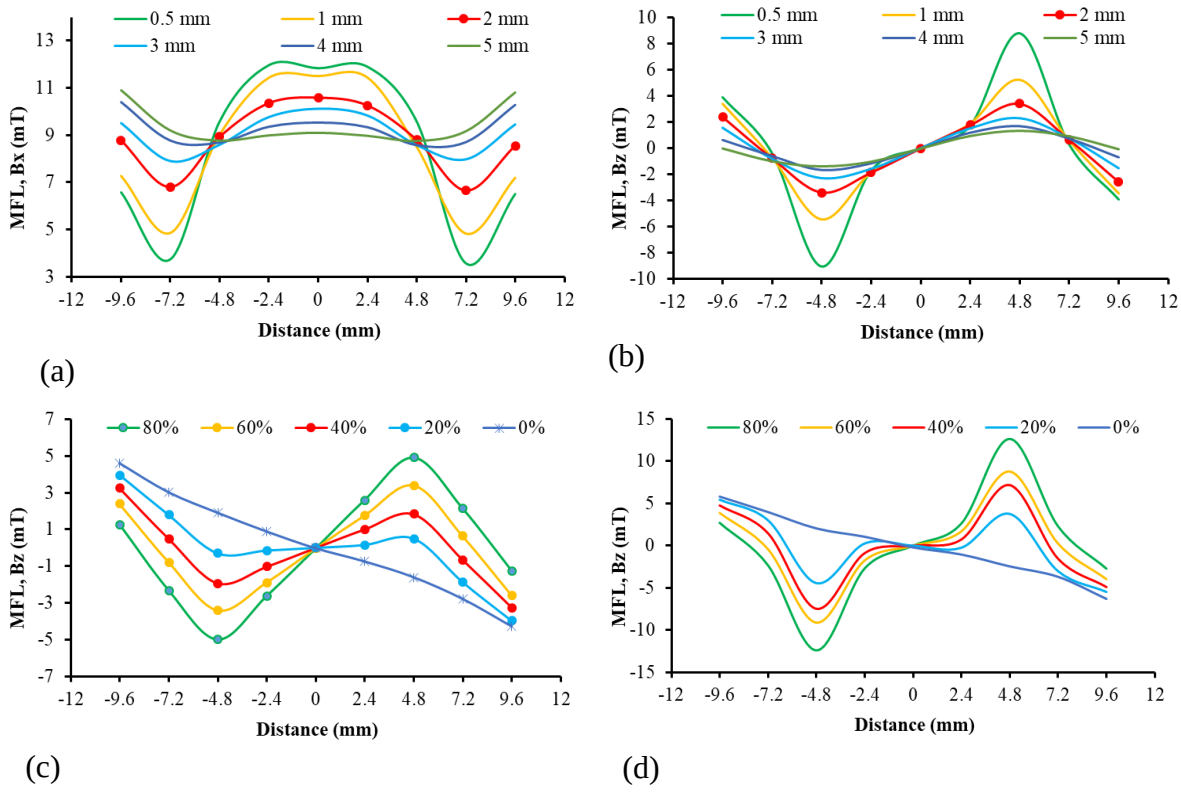


**Figure 5.23.** Effect of sensor lift-off on (a) the $\mathbf{B}_x$ and (b) $\mathbf{B}_z$ MFL signals measured using the Opt circuit for a 5 mm defect radius and depth of 60% of wall thickness with 0.5 mm, 1 mm, 2 mm, 3 mm, 4 mm and 5 mm sensor lift-offs. The $\mathbf{B}_z$ signal measured using the Opt circuit for a 5 mm defect radius and depth of 0%, 20%, 40%, 60% and 80% of the wall thickness with (c) 2 mm and (d) 0.5 mm sensor-offs.

## 5.5. Summary

In this chapter, simulation results were validated for the new MFL systems by experimentally introducing manufactured cylindrical defects and conducting sensitivity analysis on defect depths, radii, locations, and sensor lift-offs. This was to validate and ensure that the simulation models perform reliably under different scenarios. The validation was carried out experimentally for all three (Ref, Hin and Opt) circuits used on a flat plate, a pipe and a pipe

elbow with a manufactured cylindrical defect. The discrepancy between experimental and simulation results was below 2% for all test cases. When comparing the three types of circuits, the Opt circuit performs the best for all inspection components: the plate, pipe and pipe elbow. There was a significant increase in the performance of the Opt circuit on the pipe and the pipe elbow compared to the Ref circuit due to the introduced hinge and optimised circuit design, which allowed the MFL circuit to be installed on curved surfaces easily and improved the performance significantly.

The sensitivity analysis of defects in terms of their depths, radii, locations and sensor lift-offs was done. The results indicated that the magnetic flux leakage signals increase with increasing defect depth and radius because deeper and wider defects cause more disruptions in the magnetic path. The $\mathbf{B}_x$ MFL signal splits into two peaks for shallow defect depth (depth of 20% of the wall thickness) and larger defect radii (8 mm and 11 mm defect radius) because the magnetic flux lines concentrate and bend around the edges of the shallow and wider defects, creating two distinct regions of increased magnetic flux density. This results in a characteristic double peak in the $\mathbf{B}_x$ MFL signal, which helps identify and characterise smaller depth and larger radius defects in ferromagnetic materials.

It was observed that the near-surface defects have higher leakage signals because the magnetic field strength is higher near the surface, the path for leaked flux to travel to the sensors is shorter, the sensors are more sensitive to changes close to the surface/sensor, and the magnetic field concentration is higher. These factors make the disruptions caused by near-surface defects more pronounced, resulting in a stronger MFL signal. Increasing sensor lift-off decreases the MFL signal primarily due to the attenuation of the magnetic field strength with distance, the sensor's reduced sensitivity to the leakage flux, and a lower signal-to-noise ratio. Therefore, it is essential to maintain a minimum sensor lift-off distance for effective MFL testing.

# 6. CONCLUSIONS AND RECOMMENDATIONS

## 6.1. Summary

The research work reported in this thesis investigated the magnetic circuit design optimisation of the MFL system for continuous and long-term remote monitoring in corrosion-susceptible, hazardous and difficult-to-access areas such as pipe elbows, critical areas of pipes and tank floors. The investigation covers the simulation-led design of the MFL system using numerical analysis and optimisation algorithms, as well as experimental validation and sensitivity analysis of the new MFL designs. Three MFL systems, Ref, Hin and Opt circuits, were developed, and experimental validation was performed by introducing cylindrical defects of known dimensions on a range of inspection components, plate, pipe and pipe elbow. Sensitivity analysis of the new MFL systems was performed experimentally by introducing a range of defect parameters such as depth, radius, location, and sensor configurations.

The summary and conclusions of each chapter were given at the end of the respective chapters. Therefore, a brief conclusion of the entire thesis is put forward as follows:

- The latest advancements in the MFL describe the effect of a limited number of magnetic circuit parameters on the magnetisation, uniform flux distribution, defect detection and compactness of the device.
- To date, little research has been conducted in 3D on the design optimisation and comprehensive effect of multiple magnetic circuit parameters of the MFL system for a range of sample geometries, such as plates, pipes and elbows.
- The methodology proposed in this work consists of a simulation-led design based on 3D finite element analysis using COMSOL Multiphysics and optimisation algorithms and experimental work for validation and sensitivity analysis.
- An improved Ref circuit was designed based on the specified sample magnetisation level, recommended operation points on the **B-H** curve and increased uniformity of magnetic flux density inside the sample.
- A novel Hin circuit with a hinged magnet bridge was designed, which improved the performance of the system for non-planar surfaces.
- A novel Opt circuit was developed to optimise the performance and reduce the fringing, unintended leakage field and overall weight and size of the device. The Opt circuit has optimal performance in magnetising the inspection objects, is more compact and

lighter, has less fringing and unintended leakage field and can be used on flat and curved inspection components such as plates, pipes and pipe elbows.

- The validation was carried out experimentally for all three circuits (Ref, Hin and Opt circuits) used on a flat plate, a pipe and a pipe elbow with a manufactured cylindrical defect. The discrepancy between experimental and simulation results was below 2% for all test cases.
- The novel Opt circuit performs the best in defect detection for all inspection components: the plate, pipe and pipe elbow, and there was a significant increase in the performance of the Opt circuit on the pipe and the pipe elbow due to optimised circuit design and the introduced hinge in the Opt circuit, which allowed the MFL circuit to be installed on curved surfaces easily and improved the performance significantly.
- The defect depth, radius, location and sensor lift-off affect MFL signals. The MFL signals increase with increasing defect depth and radius because deeper and wider defects cause more disturbances in the magnetic flow in the circuit.
- The $\mathbf{B}_x$ MFL signal splits into two peaks for shallow defect depth and larger defect radii since the magnetic flux lines concentrate and bend around the edges of the shallow and wider defects.
- When considering defect locations, the near-surface defects have higher leakage signals than the far-surface defects. This is because the magnetic field strength is higher near the surface, the path for leaked flux to travel to the sensors is shorter, the sensors are more sensitive to changes close to the sensor, and the magnetic field concentration is higher.
- It is important to keep the sensor lift-off minimum since increasing sensor lift-off decreases the MFL signals. This is due to the attenuation of the magnetic field strength with sensor lift-off distance, reduced sensor sensitivity to the leakage flux, and a lower signal-to-noise ratio.

## 6.2. Deployment Prospects of the Developed MFL Device

The developed MFL device for continuous long-term remote defect monitoring offers significant potential for enhancing the integrity management of pipelines and tank floors. In practice, the device will be installed in pipelines and tank floors to magnetise the ferromagnetic structures, and it uses sensors to detect magnetic flux leakage caused by defects. Before in-service deployment, the system must undergo extensive validation with actual defects under

real-world operating conditions, be thoroughly calibrated and establish reliable data interpretation protocols to ensure reliable defect quantification. The developed MFL system is generally reliable and well-suited for remote, continuous defect monitoring, with a few manageable challenges typical of practical deployment. One limitation is its sensitivity to lift-off variations caused by surface debris, coatings, welds, or surface irregularities, which can affect signal accuracy. This issue can be mitigated through surface cleaning prior to installation, the use of adaptive sensor positioning to maintain consistent spacing, the implementation of lift-off compensation mechanisms, or the inclusion of ferromagnetic supports to reduce magnetic reluctance. Another consideration is the long-term stability of the magnets, as their performance may degrade over time due to environmental exposure. This can be addressed using high-quality rare-earth magnets, such as NdFeB, with protective coatings to maintain magnetic strength. When inspecting components of varying thicknesses, the system allows for simple dimensional adjustments to ensure effective magnetisation, with its cost-effective design making such customisation feasible. The MFL system also struggles to distinguish between internal and external defects. However, this can be improved by applying techniques designed to identify defect locations. For permanent installations, ensuring power efficiency is essential, which can be achieved through energy harvesting methods, such as using pipeline vibrations, or by incorporating long-life batteries to minimise maintenance.

## 6.3. Recommendations for Future Work

This thesis presents a comprehensive work combining simulation-led design development, experimental validation and sensitivity analysis of the novel MFL circuit designs. However, it is recommended that the following additional research work may be a suitable follow-up:

- Using the new MFL systems, characterising actual defects of different dimensions, geometries, locations and orientations to understand how the new MFL system responds to a range of actual defects. This helps to understand the system's defect characterisation accuracy and the effect of a range of defect parameters such as shape, dimensions, orientation and locations on the MFL signals.

- Comparing the performance of the new MFL system with other NDT techniques such as ultrasonic testing, eddy current inspection and acoustic emission testing to benchmark the accuracy and reliability of the new MFL system.

- Performing a probability of detection (POD) study of the new MFL system to quantify the likelihood of detecting defects of various sizes and geometries. POD helps identify the smallest defect the new MFL system can reliably find and the biggest flaw that it could miss. This helps to understand the new MFL system's sensitivity and detection capabilities, especially for small subsurface defects.

# RFERENCES


[1] International Energy Agency (IEA), “Statistics report: Key World Energy Statistics 2020,” Aug. 2020.

[2] International Energy Agency (IEA), “Net Zero Roadmap: A Global Pathway to Keep the 1.5 °C Goal in Reach - 2023 Update,” 2023. [Online]. Available: www.iea.org/t&c/

[3] K. D. Prasanta, “Oil pipelines,” Encyclopedia of energy series, Elsevier, no. 36, pp. 673–690, May 2004, doi: 10.1016/B0-12-176480-X/00260-6.

[4] Y. Shi, C. Zhang, R. Li, M. Cai, and G. Jia, “Theory and application of magnetic flux leakage pipeline detection,” Dec. 10, 2015, MDPI AG. doi: 10.3390/s151229845.

[5] N. Saeed and H. R. Ronagh, “Design of fibre-reinforced polymer overwraps for pipe pressure,” in Rehabilitation of Pipelines Using Fiber-reinforced Polymer (FRP) Composites, Elsevier, 2015, pp. 211–223. doi: 10.1016/B978-0-85709-684-5.00010-2.

[6] J. G. Speight, “Corrosion Monitoring and Control,” Oil and Gas Corrosion Prevention, pp. 109–149, Jan. 2014, doi: 10.1016/B978-0-12-800346-6.00006-5.

[7] W. D. Callister and D. G. Rethwisch, Materials science and engineering. WILEY, 2007.

[8] European Gas Pipeline Data Group (EGIG), “GAS PIPELINE INCIDENTS,” 2020. [Online]. Available: https://www.EGIG.eu

[9] Thomas Industrial Coatings, “The different types of corrosion.” Accessed: Jul. 10, 2024. [Online]. Available: https://www.thomasindcoatings.com/the-different-types-of-corrosion/

[10] A. Adhithya, P. Sidharth, and T. P. Nagar, “EFFECT OF PITTING CORROSION ON ULTIMATE STRENGTH AND BUCKLING STRENGTH OF PLATES-A REVIEW,” Dig J Nanomater Biostruct, vol. 4, no. 4, pp. 783–788, Dec. 2009.

[11] J. Bhandari, F. Khan, R. Abbassi, V. Garaniya, and R. Ojeda, “Modelling of pitting corrosion in marine and offshore steel structures - A technical review,” J Loss Prev Process Ind, vol. 37, pp. 39–62, Sep. 2015, doi: 10.1016/j.jlp.2015.06.008.

[12] T. Satoh, Y. Shao, W. G. Cook, D. H. Lister, and S. Uchida, “Flow-assisted corrosion of carbon steel under neutral water conditions,” Corrosion, vol. 63, no. 8, pp. 770–780, 2007, doi: 10.5006/1.3278426.

[13] L. Giourntas, T. Hodgkiess, and A. M. Galloway, “Comparative study of erosion-corrosion performance on a range of stainless steels,” Wear, vol. 332–333, pp. 1051–1058, Sep. 2014, doi: 10.1016/j.wear.2014.12.052.

[14] Y. Yang and Y. F. Cheng, “Parametric effects on the erosion-corrosion rate and mechanism of carbon steel pipes in oil sands slurry,” Wear, vol. 276–277, pp. 141–148, Feb. 2012, doi: 10.1016/j.wear.2011.12.010.

[15] Y. Xu and M. Y. Tan, “Probing the initiation and propagation processes of flow accelerated corrosion and erosion corrosion under simulated turbulent flow conditions,” Corros Sci, vol. 151, pp. 163–174, May 2019, doi: 10.1016/j.corsci.2019.01.028.

[16] R. C. Ireland and C. R. Torres, “Finite element modelling of a circumferential magnetiser,” Sens Actuators A Phys, vol. 129, no. 1-2 SPEC. ISS., pp. 197–202, May 2006, doi: 10.1016/j.sna.2005.11.066.

[17] Kurita America Inc., “Flow Accelerated Corrosion.” Accessed: Oct. 12, 2024. [Online]. Available: https://www.kuritaamerica.com/the-splash/flow-accelerated-corrosion

[18] J. Bhandari, F. Khan, R. Abbassi, V. Garaniya, and R. Ojeda, “Modelling of pitting corrosion in marine and offshore steel structures - A technical review,” Sep. 01, 2015, Elsevier Ltd. doi: 10.1016/j.jlp.2015.06.008.

[19] N. Anita, R. M. Joany, J. A. Dorothy, A. S. S. Rajendran, G. Singh, and C. Verma, Electrochemical and analytical techniques for sustainable corrosion monitoring. Cambridge, United States: Elsevier , 2023.

[20] E. V. Senatore et al., “Evaluation of high shear inhibitor performance in CO2-containing flow-induced corrosion and erosion-corrosion environments in the presence and absence of iron carbonate films,” Wear, vol. 404–405, pp. 143–152, Jun. 2018, doi: 10.1016/j.wear.2018.03.014.

[21] R. E. Vieira, A. Mansouri, B. S. McLaury, and S. A. Shirazi, “Experimental and computational study of erosion in elbows due to sand particles in air flow,” Powder Technol, vol. 288, pp. 339–353, Jan. 2016, doi: 10.1016/j.powtec.2015.11.028.

[22] M. Parsi, K. Najmi, F. Najafifard, S. Hassani, B. S. McLaury, and S. A. Shirazi, “A comprehensive review of solid particle erosion modeling for oil and gas wells and pipelines applications,” J Nat Gas Sci Eng, vol. 21, pp. 850–873, Oct. 2014, doi: 10.1016/j.jngse.2014.10.001.

[23] V. Kain, “Flow accelerated corrosion: Forms, mechanisms and case studies,” in 1st International Conference on Structural Integrity, ICONS_2014, Procedia Engineering, 2014, pp. 576–588. doi: 10.1016/j.proeng.2014.11.083.

[24] L. Zeng, G. Chen, and H. Chen, “Comparative study on flow-accelerated corrosion and erosion-corrosion at a 90° carbon steel bend,” Materials, vol. 13, no. 7, Apr. 2020, doi: 10.3390/MA13071780.

[25] X. C. Song, S. L. Huang, and W. Zhao, “Optimization of the magnetic circuit in the MFL inspection system for storage-tank floors,” Russian Journal of Nondestructive Testing, vol. 43, no. 5, pp. 326–331, May 2007, doi: 10.1134/S1061830907050063.

[26] S. Hassan, J. Wang, C. Kontovas, and M. Bashir, “An assessment of causes and failure likelihood of cross-country pipelines under uncertainty using bayesian networks,” Reliab Eng Syst Saf, vol. 218, Feb. 2022, doi: 10.1016/j.ress.2021.108171.

[27] X. Li, J. Wang, R. Abbassi, and G. Chen, “A risk assessment framework considering uncertainty for corrosion-induced natural gas pipeline accidents,” J Loss Prev Process Ind, vol. 75, Feb. 2022, doi: 10.1016/j.jlp.2021.104718.

[28] G. Koch, “Cost of corrosion,” Trends in Oil and Gas Corrosion Research and Technologies: Production and Transmission, pp. 3–30, Jan. 2017, doi: 10.1016/B978-0-08-101105-8.00001-2.

[29] M. v. Biezma, M. A. Andrés, D. Agudo, and E. Briz, “Most fatal oil & gas pipeline accidents through history: A lessons learned approach,” Eng Fail Anal, vol. 110, Mar. 2020, doi: 10.1016/j.engfailanal.2020.104446.

[30] J. Carter, P. Dawson, and R. Nixon, “EXPLOSION AT THE CONOCO HUMBER REFINERY-16TH APRIL 2001,” 2006.

[31] Health and Safety Executive (HSE), “Public Report of The Fire and Explosion at the Conoco Phillips HSE,” Apr. 2001.

[32] Y. Wang, Y. Xu, B. Wang, S. Ding, J. Xu, and M. Zheng, “Research on metal atmospheric storage tank inspection method for standard in China,” in The ASME 2009 Pressure Vessels and Piping Division Conference (PVP2009), Prague, Czech Republic: ASME, Jun. 2009. [Online]. Available: http://asmedigitalcollection.asme.org/PVP/proceedings-pdf/PVP2009/43642/447/2745162/447_1.pdf

[33] Y. Ye, K. Ji, and P. Wang, “Influences of Magnetization Direction on the Flux Leakage Field of Weld Defects,” Coatings, vol. 13, no. 6, Jun. 2023, doi: 10.3390/coatings13061005.

[34] S. Liu, Y. Sun, X. Jiang, and Y. Kang, “A Review of Wire Rope Detection Methods, Sensors and Signal Processing Techniques,” Dec. 01, 2020, Springer. doi: 10.1007/s10921-020-00732-y.

[35] American petroleum Institute (API), “Piping Inspection Code Inspection, Repair, Alteration, and Rerating of In-service Piping Systems,” 1998.

[36] American Society of Mechanical Engineers, “ASME B318S: Managing System Integrity of Gas Pipelines,” 2005.

[37] B. T. Lu, J. F. Lu, and J. L. Luo, “Erosion-corrosion of carbon steel in simulated tailing slurries,” Corros Sci, vol. 53, no. 3, pp. 1000–1008, Mar. 2011, doi: 10.1016/j.corsci.2010.11.034.

[38] M. Ahammed, “Probabilistic estimation of remaining life of a pipeline in the presence of active corrosion defects,” International Journal of Pressure Vessels and Piping, vol. 75, pp. 321–329, Jan. 1998.

[39] American Petroleum Institute (API), “Risk-Based Inspection: API RECOMMENDED PRACTICE 580,” Nov. 2009.

[40] M. Kutz, Handbook of Environmental Degradation of Materials. Delmar, New York, USA: William Andrew Publishing, 2005. [Online]. Available: www.williamandrew.com

[41] H. Woldesellasse and S. Tesfamariam, “Risk analysis of onshore oil and gas pipelines: Literature review and bibliometric analysis,” Journal of Infrastructure Intelligence and Resilience, vol. 2, no. 4, Nov. 2023, doi: 10.1016/j.iintel.2023.100052.

[42] W. K. Muhlbauer, “Pipeline Risk Management Manual: Ideas, Techniques, and Resources,” Pipeline Risk Management Manual: Ideas, Techniques, and Resources, pp. 1–395, Jan. 2003, doi: 10.1016/B978-0-7506-7579-6.X5000-6.

[43] L. Yang and K. T. Chiang, “On-line and real-time corrosion monitoring techniques of metals and alloys in nuclear power plants and laboratories,” Understanding and Mitigating Ageing in Nuclear Power Plants: Materials and Operational Aspects of Plant Life Management (Plim); Woodhead Publishing Series in Energy, pp. 417–455, 2010, doi: 10.1533/9781845699956.3.417.

[44] “Part I: General Aspects of Corrosion, Corrosion Control, and Corrosion Prevention,” Corrosion Atlas Case Studies, pp. xxv–xli, Jan. 2020, doi: 10.1016/B978-0-12-818760-9.02002-X.

[45] C. M. Pietersen, “ANALYSIS OF THE LPG-DISASTER IN MEXICO CITY,” J Hazard Mater, vol. 20, pp. 85–107, 1988.

[46] G. Arturson, “The tragedy of San Juanico—the most severe LPG disaster in history,” Burns, vol. 13, no. 2, pp. 87–102, Apr. 1987, doi: 10.1016/0305-4179(87)90096-9.

[47] C. M. Pletersen, The two largest industrial disasters with hazardous material. Gelling publishing, 2007.

[48] Ir. C. M. Pietersen and S. Cendejas Huerta, “TNO Environment, Energy and process Innovation: Analysis of the LPG incident in San Juan Ixhautepec, Mexico City, 19 November 1984,” Nov. 1984.

[49] The Hon Lord Cullen, “The Public Inquiry into the Piper Alpha Disaster,” London, Oct. 1990.

[50] Oil and Gas UK, “Piper Alpha: Lessons Learnt,” 2008.

[51] M. Christou and Konstantinidou, “JRC Scientific and Policy Reports Safety of offshore oil and gas operations: Lessons from past accidents analysis,” 2012.

[52] D. C. A. Washington, “Natural Gas Pipeline Rupture and Fire Near Carlsbad, New Mexico National Transportation Safety Board,” 2000.

[53] ASNT, “Discover Nondestructive Testing.” Accessed: Jul. 16, 2024. [Online]. Available: https://asnt.org/MajorSiteSections/About/Discover_Nondestructive_Testing

[54] Charles. J. Hellier, HANDBOOK OF NONDESTRUCTIVE EVALUATION. McGraw, 2003.

[55] S. Zhong and W. Nsengiyumva, Nondestructive Testing and Evaluation of Fiber-Reinforced Composite Structures. Springer, 2022.

[56] R. Prakash, Non-Destructive Testing Techniques New Academic Science. New Academic Science Limited, 2012.

[57] D. E. Bray and D. McBride, Nondestructive Testing Techniques . Wiley, 1992.

[58] N. Meyendorf, N. Ida, R. Singh, and J. Vrana, Handbook of Nondestructive Evaluation 4.0. Springer, 2022.

[59] M. W. Allgaier, S. Ness, P. McIntire, and P. O. Moore, Nondestructive Testing Handbook, Visual and Optical Testing, vol. 8. Columb.Ohio: American Society for Nondestructive Testing (ASNT), 1993.

[60] E. D. Megaw, “Factors affecting visual inspection accuracy,” Appl Ergon, vol. 10, pp. 27–32, Mar. 1979.

[61] J. F. Norman, J. T. Todd, and G. A. Orban, “Perception of Three-Dimensional Shape From Specular Highlights, Deformations of Shading, and Other Types of Visual Information,” 2004. [Online]. Available: www.psy.ohio-state.edu/

[62] G. A. Matzkanin, “Selecting a Nondestructive Testing Visual testing,” in AMMTIAC Q, 1(3), 2006, pp. 7–10.

[63] TFHRC, “Reliability of Visual Inspection for Highway Bridges, Volume I: Final Report,” May 2001. [Online]. Available: http://www.tfhrc.gov/hnr20/nde/home.htm

[64] F. A. Iddings, Visual Inspection, vol. MaterialsEval 56. 2004.

[65] J. E. See, “Visual Inspection Reliability for Precision Manufactured Parts,” Hum Factors, vol. 57, no. 8, pp. 1427–1442, Dec. 2015, doi: 10.1177/0018720815602389.

[66] Carosena. Meola, Simone. Boccardi, and G. M. . Carlomagno, Infrared thermography in the evaluation of aerospace composite materials : infrared thermography to composites. Woodhead Publishing, 2017.

[67] J. Krautkrämer and H. Krautkrämer, Ultrasonic Testing of Materials. Springer Berlin Heidelberg, 1983. doi: 10.1007/978-3-662-02357-0.

[68] The Welding Institute (TWI), "What is Ultrasonic Testing and How Does it Work? - TWI." Accessed: Sep. 01, 2024. [Online]. Available: https://www.twi-global.com/technical-knowledge/faqs/ultrasonic-testing

[69] C. for N. E. N.-Ed. org Iowa State University, "Nondestructive Evaluation Techniques : Ultrasound." Accessed: Sep. 01, 2024. [Online]. Available: https://www.nde-ed.org/NDETechniques/Ultrasonics/index.xhtml

[70] P. Grosser, "ULTRASONIC DETECTION AND MEASURING OF ISOLATED OR PITTING CORROSION (IPC)," in 12th A-PCNDT 2006 - Asia -Pacific Conference on NDT, Oct. 2006. [Online]. Available: https://www.ndt.net/?id=4242

[71] Q. Qian, H. Hanachi, J. Liu, and J. Gu, "Simulation of Ultrasonic Testing for Resolution of Corrosion Detection in Pipes," in 2016 IEEE International Conference of Prognostics and Health Management, IEEE, 2016.

[72] S. C. Olisa, M. A. Khan, and A. Starr, "Review of current guided wave ultrasonic testing (GWUT) limitations and future directions," Sensors (Switzerland), vol. 21, no. 3, pp. 1–28, Feb. 2021, doi: 10.3390/s21030811.

[73] S. Sharma and A. Mukherjee, "Monitoring Corrosion in Oxide and Chloride Environments Using Ultrasonic Guided Waves," Journal of Materials in Civil Engineering, Feb. 2011, doi: 10.1061/ASCEMT.1943-5533.0000144.

[74] R. Mohammadkhani et al., "Improving depth resolution of ultrasonic phased array imaging to inspect aerospace composite structures," Sensors (Switzerland), vol. 20, no. 2, Jan. 2020, doi: 10.3390/s20020559.

[75] R. N. P. Gunarathna and V. Sivahar, "Challenges in Monitoring Metallic Pipeline Corrosion Using Ultrasonic Waves – A Review Article," Engineer: Journal of the Institution of Engineers, Sri Lanka, vol. 54, no. 1, p. 67, May 2021, doi: 10.4038/engineer.v54i1.7436.

[76] C. U. Grosse and M. Ohtsu, Acoustic emission testing: Basics for Research-Applications in Civil Engineering. Springer Berlin Heidelberg, 2008. doi: 10.1007/978-3-540-69972-9.

[77] The Japanese Society of Non-destructive Inspection, Practical Acoustic Emission Testing. Springer JAPAN, 2016.

[78] C. for N. E. N.-Ed. org Iowa State University, "Nondestructive Evaluation Techniques : Acoustic Emission Testing." Accessed: Sep. 01, 2024. [Online]. Available: https://www.nde-ed.org/NDETechniques/AcousticEmission/AE_Theory-Sources.xhtml

[79] The Welding Institute (TWI), "What Is Acoustic Emission Testing? A Definitive Guide - TWI." Accessed: Sep. 01, 2024. [Online]. Available: https://www.twi-global.com/technical-knowledge/faqs/acoustic-emission-testing

[80] M. Huang, L. Jiang, P. K. Liaw, C. R. Brooks, R. Seeley, and D. L. Klarstrom, "Using Acoustic Emission in Fatigue and Fracture Materials Research," Nondestructive Evaluation, Nov. 1998, Accessed: Sep. 01, 2024. [Online]. Available: https://www.tms.org/pubs/journals/jom/9811/huang/huang-9811.html

[81] L. . Hollaway and J. G. . Teng, Strengthening and rehabilitation of civil infrastructures using fibre-reinforced polymer (FRP) composites. Woodhead Pub. ; Maney Pub. ; CRC Press, 2008.

[82] Patrick. O. Moore, Nondestructive Testing Handbook: Radiographic Testing, Third., vol. 4. ASNT, 2002.

[83] The Welding Institute (TWI), "Radiography Testing - NDT Inspection - TWI." Accessed: Sep. 01, 2024. [Online]. Available: https://www.twi-global.com/what-we-do/services-and-support/asset-management/non-destructive-testing/ndt-techniques/radiography-testing

[84] NDT Group, "Radiographic testing: advantages and disadvantages." Accessed: Sep. 01, 2024. [Online]. Available: https://www.ndtgroup.co.uk/latest-news/radiographic-testing-adv-disadv/

[85] C. Mr and P. Ashb, "Non-Destructive Testing and Radiation in Industry," 2001.

[86] S. K. Dwivedi, M. Vishwakarma, and A. Soni, “Advances and Researches on Non Destructive Testing: A Review,” Mater Today Proc, vol. 5, pp. 3690–3698, 2018, [Online]. Available: www.sciencedirect.comwww.materialstoday.com/proceedings

[87] M. Gupta, M. A. Khan, R. Butola, and R. M. Singari, “Advances in applications of Non-Destructive Testing (NDT): A review,” Advances in Materials and Processing Technologies, vol. 8, no. 2, pp. 2286–2307, 2022, doi: 10.1080/2374068X.2021.1909332.

[88] R. Heidersbach, Metallurgy and Corrosion Control in Oil and Gas Production, Second. John Wiley and Sons, 2018. [Online]. Available: http://www.wiley.com/go/permissions.

[89] R. Singh, Applied Welding Engineering: Processes, Codes, and Standards, Third. Butterworth-Heinemann, 2020.

[90] G. A. . Antaki, Piping and pipeline engineering : design, construction, maintenance, integrity, and repair. Ebrary, 2007.

[91] “Liquid penetrant Testing (PT or LPT).” Accessed: Aug. 29, 2024. [Online]. Available: https://www.linkedin.com/pulse/liquid-penetrant-testing-pt-lpt-mehdi-mehdizadeh/

[92] BINDT, “Liquid penetrant inspection.” Accessed: Sep. 01, 2024. [Online]. Available: https://www.bindt.org/What-is-NDT/Liquid-penetrant-inspection/

[93] C. Chris Roshan, H. Vasanth Ram, and J. Solomon, “Non-destructive testing by liquid penetrant testing and ultrasonic testing-A review,” International Journal of Advance Research, pp. 694–697, 2019, [Online]. Available: www.IJARIIT.com

[94] X. Guirong, G. Xuesong, Q. Yuliang, and G. Yan, “Analysis and Innovation for Penetrant Testing for Airplane Parts,” in Procedia Engineering, Elsevier Ltd, 2015, pp. 1438–1442. doi: 10.1016/j.proeng.2014.12.681.

[95] N. Bowler, Eddy-Current Nondestructive Evaluation. Springer, 2019. [Online]. Available: http://www.springer.com/series/13337

[96] J. García-Martín, J. Gómez-Gil, and E. Vázquez-Sánchez, “Non-destructive techniques based on eddy current testing,” Sensors, vol. 11, no. 3, pp. 2525–2565, Mar. 2011, doi: 10.3390/s110302525.

[97] The Welding Institute (TWI), “Eddy Current Testing (Includes Eddy Current Array) - TWI.” Accessed: Sep. 07, 2024. [Online]. Available: https://www.twi-global.com/technical-knowledge/job-knowledge/eddy-current-testing-123

[98] C. for N. E. N.-Ed. O. IOWA STATE UNIVERSITY, “Nondestructive Evaluation Techniques : Eddy Current Testing.” Accessed: Sep. 07, 2024. [Online]. Available: https://www.nde-ed.org/NDETechniques/EddyCurrent/index.xhtml

[99] R. Pohl, A. Erhard, H. J. Montag, H. M. Thomas, and H. Wüstenberg, “NDT techniques for railroad wheel and gauge corner inspection,” in NDT and E International, Mar. 2004, pp. 89–94. doi: 10.1016/j.ndteint.2003.06.001.

[100] J. M. Buckley, “An introduction to Eddy Current Testing theory and technology,” technical paper eddyc, 2003, Accessed: Oct. 30, 2024. [Online]. Available: http://joe.buckley.net/papers

[101] P. Dominique and D. Isabelle Member, “Eddy Current Sensors for Nondestructive Inspection of Graphite Composite Materials,” in In Conference Record of the IEEE Industry Applications Society Annual Meeting, 1992.

[102] D. G. . Moore and P. O. . Moore, Nondestructive Testing Handbook: Magnetic testing, vol. 8. American Society for Nondestructive Testing, 2008.

[103] J. Blitz, Electrical and Magnetic Methods of Non-destructive Testing, vol. 3. in Non-Destructive Evaluation Series, vol. 3. Dordrecht: Springer Netherlands, 1997. doi: 10.1007/978-94-011-5818-3.

[104] Q. Wu, K. Dong, X. Qin, Z. Hu, and X. Xiong, “Magnetic particle inspection: Status, advances, and challenges — Demands for automatic non-destructive testing,” NDT and E International, vol. 143, Apr. 2024, doi: 10.1016/j.ndteint.2023.103030.

[105] A. Zolfaghari, A. Zolfaghari, and F. Kolahan, “Reliability and sensitivity of magnetic particle nondestructive testing in detecting the surface cracks of welded components,” Nondestructive Testing and Evaluation, vol. 33, no. 3, pp. 290–300, Jul. 2018, doi: 10.1080/10589759.2018.1428322.

[106] General Inspection Technical Office GITO, “Magnetic Particle Inspection.” Accessed: Sep. 09, 2024. [Online]. Available: https://general-ito.com/gallery-details/71/1

[107] D. Lovejoy, Magnetic particle inspection: A Pra. Dordrecht: Springer, 1993. doi: 10.1007%2F978-94-011-1536-0.

[108] One Stop NDT, “Basic Principles of Magnetic Particle Testing.” Accessed: Sep. 09, 2024. [Online]. Available: https://www.onestopndt.com/ndt-articles/magnetic-particle-testing-principles

[109] The National Board of Boiler and Pressure Vessel Inspections, “Magnetic Particle Examination.” Accessed: Sep. 09, 2024. [Online]. Available: https://www.nationalboard.org/Index.aspx?pageID=164&ID=377

[110] B. Feng, J. Wu, H. Tu, J. Tang, and Y. Kang, “A Review of Magnetic Flux Leakage Nondestructive Testing,” Oct. 01, 2022, MDPI. doi: 10.3390/ma15207362.

[111] F. I. Al-Naemi, J. P. Hall, and A. J. Moses, “FEM modelling techniques of magnetic flux leakage-type NDT for ferromagnetic plate inspections,” J Magn Magn Mater, vol. 304, no. 2, Sep. 2006, doi: 10.1016/j.jmmm.2006.02.225.

[112] A. Sophian, G. Y. Tian, and S. Zairi, “Pulsed magnetic flux leakage techniques for crack detection and characterisation,” Sens Actuators A Phys, vol. 125, no. 2, pp. 186–191, Jan. 2006, doi: 10.1016/j.sna.2005.07.013.

[113] J. Feng, F. Li, S. Lu, J. Liu, and D. Ma, “Injurious or noninjurious defect identification from MFL images in pipeline inspection using convolutional neural network,” IEEE Trans Instrum Meas, vol. 66, no. 7, pp. 1883–1892, Jul. 2017, doi: 10.1109/TIM.2017.2673024.

[114] P. Chandra and R. Bhagi, “Magnetic Flux Leakage Testing: Basics,” Journal of Non Destructive Testing and Evaluation, vol. 11, Dec. 2012, [Online]. Available: https://www.researchgate.net/publication/258936176

[115] Z. Du et al., “3-D FEM simulation of velocity effects on magnetic flux leakage testing signals,” IEEE Trans Magn, vol. 44, no. 6, pp. 1642–1645, Jun. 2008, doi: 10.1109/TMAG.2007.915955.

[116] O. K. W. Chukwunonso and C. K. W. Okolo, “Modelling and Experimental Investigation of Magnetic Flux Leakage Distribution for Hairline Crack Detection and Characterization,” Cardiff University, Cardiff, 2018.

[117] M. E. . Orazem, Underground pipeline corrosion : detection, analysis and prevention. Elsevier, Woodhead Publishing, 2014.

[118] J. C. Drury and A. Marino, “A Comparison of the Magnetic Flux Leakage and Ultrasonic Methods in the detection and measurement of corrosion pitting in ferrous plate and pipe,” in 15th World Conference on Nondestructive Testing, Roma, Italy, Oct. 2000. Accessed: Sep. 18, 2024. [Online]. Available: https://www.ndt.net/article/wcndt00/papers/idn701/idn701.htm

[119] A. L. Pullen, P. C. Charlton, N. R. Pearson, and N. J. Whitehead, “Practical evaluation of velocity effects on the magnetic flux leakage technique for storage tank inspection,” Insight: Non-Destructive Testing and Condition Monitoring, vol. 62, no. 2, pp. 73–80, 2020, doi: 10.1784/insi.2020.62.2.73.

[120] A. L. Pullen, P. C. Charlton, N. R. Pearson, and N. J. Whitehead, “Magnetic flux leakage scanning velocities for tank floor inspection,” IEEE Trans Magn, vol. 54, no. 9, Sep. 2018, doi: 10.1109/TMAG.2018.2853117.

[121] M. S. Safizadeh and T. Azizzadeh, “Corrosion detection of internal pipeline using NDT optical inspection system,” NDT and E International, vol. 52, pp. 144–148, Nov. 2012, doi: 10.1016/j.ndteint.2012.07.008.

[122] J. W. Wilson and G. Y. Tian, “Pulsed electromagnetic methods for defect detection and characterisation,” NDT and E International, vol. 40, no. 4, pp. 275–283, 2007, Accessed: Sep. 02, 2024. [Online]. Available: https://research.manchester.ac.uk/en/publications/pulsed-electromagnetic-methods-for-defect-detection-and-character

[123] O. Kara and H. H. Çelik, “A Novel Nonlinear Magnetic Equivalent Circuit Model for Magnetic Flux Leakage System,” Applied Sciences (Switzerland), vol. 14, no. 10, May 2024, doi: 10.3390/app14104071.

[124] C.-G. Stefanita, Magnetism Basics and Applications. Springer, 2012.

[125] B. D. Cullity and C. D. Graham, INTRODUCTION TO MAGNETIC MATERIALS, Second. Wiley, 2009.

[126] David. Jiles, Introduction to magnetism and magnetic materials. CRC Press, Taylor & Francis Group, 2016.

[127] J. R. Riba Ruiz, A. Garcia Espinosa, and L. Romeral, “A computer model for teaching the dynamic behavior of ac contactors,” IEEE Transactions on Education, vol. 53, no. 2, pp. 248–256, May 2010, doi: 10.1109/TE.2009.2014153.

[128] Electrical Academia, “Hysteresis Loop | Magnetization Curve | Electrical Academia.” Accessed: Jan. 30, 2022. [Online]. Available: https://electricalacademia.com/electromagnetism/hysteresis-loop-magnetization-curve/

[129] O. H. . Wyatt and David. Dew-Hughes, Metals, ceramics, and polymers; an introduction to the structure and properties of engineering materials. Cambridge University Press, 1974.

[130] F. Cardarelli, Materials Handbook, Third. Cham: Springer International Publishing, 2018.

[131] K. Fabian, V. P. Shcherbakov, and S. A. McEnroe, “Measuring the Curie temperature,” Geochemistry, Geophysics, Geosystems, vol. 14, no. 4, pp. 947–961, Apr. 2013, doi: 10.1029/2012GC004440.

[132] P. Mohnt and E. P. Wohlfarth, “The Curie temperature of the ferromagnetic transition metals and their compounds,” Journal of Physics F: Metal Physics J. Phys. F: Met. Phys, vol. 17, pp. 2421–2430, 1987.

[133] Y. Zhang, Z. Ye, and C. Wang, “A fast method for rectangular crack sizes reconstruction in magnetic flux leakage testing,” NDT and E International, vol. 42, no. 5, pp. 369–375, Jul. 2009, doi: 10.1016/j.ndteint.2009.01.006.

[134] A. N. Pechenkov, V. E. Shcherbinin, and J. G. Smorodinskiy, “Analytical model of a pipe magnetization by two parallel linear currents,” NDT and E International, vol. 44, no. 8, pp. 718–720, Dec. 2011, doi: 10.1016/j.ndteint.2011.07.014.

[135] J. B. Nestleroth, “CIRCUMFERENTIAL MFL IN-LINE INSPECTION FOR CRACKS IN PIPELINES FINAL REPORT,” 2003.

[136] S. Huang, L. Peng, Q. Wang, S. Wang, and W. Zhao, “An opening profile recognition method for magnetic flux leakage signals of defect,” IEEE Trans Instrum Meas, vol. 68, no. 6, pp. 2229–2236, Jun. 2019, doi: 10.1109/TIM.2018.2869438.

[137] J. W. Kim and S. Park, “Magnetic flux leakage–based local damage detection and quantification for steel wire rope non-destructive evaluation,” J Intell Mater Syst Struct, vol. 29, no. 17, pp. 3396–3410, Oct. 2018, doi: 10.1177/1045389X17721038.

[138] A. D. Eslamlou, A. Ghaderiaram, E. Schlangen, and M. Fotouhi, “A review on non-destructive evaluation of construction materials and structures using magnetic sensors,” Constr Build Mater, vol. 397, Sep. 2023, doi: 10.1016/j.conbuildmat.2023.132460.

[139] J. Yousaf, R. W. Harseno, S. H. Kee, and J. J. Yee, “Evaluation of the Size of a Defect in Reinforcing Steel Using Magnetic Flux Leakage (MFL) Measurements,” Sensors, vol. 23, no. 12, Jun. 2023, doi: 10.3390/s23125374.

[140] Y. Li, C. Sun, and Y. Liu, “Magnetic Flux Leakage Testing Method for Pipelines with Stress Corrosion Defects Based on Improved Kernel Extreme Learning Machine,” Electronics (Switzerland), vol. 12, no. 17, Sep. 2023, doi: 10.3390/electronics12173707.

[141] Y. Chang, J. Jiao, G. Li, X. Liu, C. He, and B. Wu, “Effects of excitation system on the performance of magnetic-flux-leakage-type non-destructive testing,” Sens Actuators A Phys, vol. 268, pp. 201–212, Dec. 2017, doi: 10.1016/J.SNA.2017.08.009.

[142] S. Mukhopadhyay and G. P. Srivastava, “Characterisation of metal loss defects from magnetic flux leakage signals with discrete wavelet transform,” NDT and E International, 2000, [Online]. Available: www.elsevier.com/locate/ndteint

[143] F. Xu, X. Wang, and H. Wu, “Inspection method of cable-stayed bridge using magnetic flux leakage detection: Principle, sensor design, and signal processing,” Journal of Mechanical Science and Technology, vol. 26, no. 3, pp. 661–669, Mar. 2012, doi: 10.1007/s12206-011-1234-x.

[144] E. Norouzi and H. Ravanbod, “Optimisation of the flux distribution in magnetic flux leakage testing,” Insight: Non-Destructive Testing and Condition Monitoring, vol. 51, no. 10, pp. 563–567, 2009, doi: 10.1784/INSI.2009.51.10.563.

[145] C. Xiuli, Z. Dechang, and L. Guixiong, “Study on Simulation and Experiment of the Magnetizer in Magnetic Flux Leakage Testing,” in The IEEE International Conference on Mechatronics and Automation, Harbin, China, Jul. 2007.

[146] J. Cui et al., “Manufacturing Processes for Permanent Magnets: Part I—Sintering and Casting,” 2022, Springer. doi: 10.1007/s11837-022-05156-9.

[147] I. Petrov, D. Egorov, J. Link, R. Stern, S. Ruoho, and J. Pyrhönen, “Hysteresis Losses in Different Types of Permanent Magnets Used in PMSMs,” IEEE Transactions on Industrial Electronics, vol. 64, no. 3, pp. 2502–2510, Mar. 2017, doi: 10.1109/TIE.2016.2548440.

[148] J. J. Croat, J. F. Herbst, R. W. Lee, and F. E. Pinkerton, “Pr-Fe and Nd-Fe-based materials: A new class of high-performance permanent magnets (invited),” J Appl Phys, vol. 55, no. 6, pp. 2078–2082, 1984, doi: 10.1063/1.333571.

[149] O. Gutfleisch, M. A. Willard, E. Brück, C. H. Chen, S. G. Sankar, and J. P. Liu, “Magnetic materials and devices for the 21st century: Stronger, lighter, and more energy efficient,” Advanced Materials, vol. 23, no. 7, pp. 821–842, Feb. 2011, doi: 10.1002/adma.201002180.

[150] X. Zhou, A. Huang, B. Cui, and J. W. Sutherland, “Techno-economic Assessment of a Novel SmCo Permanent Magnet Manufacturing Method,” in Procedia CIRP, Elsevier B.V., 2021, pp. 127–132. doi: 10.1016/j.procir.2021.01.017.

[151] E. A. Grunditz, T. S. Lundmark, M. Alatalo, T. Thiringer, and A. Nordelof, “Three Traction Motors with Different Magnet Materials - Influence on Cost, Losses, Vehicle, Performance, Energy Use and Environmental Impact,” in 2018 Thirteenth International Conference on Ecological Vehicles and Renewable Energies (EVER), IEEE, Apr. 2018.

[152] G. J. Long and F. Grandjean, Supermagnets, Hard Magnetic Materials, vol. 331. Springer Science and Business, 2012.

[153] G. S. , J. P. W. , R. W. Y. Park, “Optimum Design of the Non-Destructive Testing System to Maximize the Magnetic Flux Leakages,” Journal of Magnetics, vol. 6(1), pp. 31–35, 2001.

[154] J. A. Parra-Raad and S. Roa-Prada, “Multi-Objective Optimization of a Magnetic Circuit for Magnetic Flux Leakage-Type Non-destructive Testing,” J Nondestr Eval, vol. 35, no. 1, pp. 1–12, Mar. 2016, doi: 10.1007/S10921-015-0329-1/FIGURES/13.

[155] H. Q. Pham, Q. T. Trinh, D. T. Doan, and Q. H. Tran, “Importance of Magnetizing Field on Magnetic Flux Leakage Signal of Defects,” IEEE Trans Magn, vol. 54, no. 6, Jun. 2018, doi: 10.1109/TMAG.2018.2809671.

[156] Y. Sun and Y. Kang, “Magnetic compression effect in present MFL testing sensor,” Sens Actuators A Phys, vol. 160, no. 1–2, pp. 54–59, 2010, doi: 10.1016/j.sna.2010.03.038.

[157] H. J. M. Jansen, M. Van de Camp, and M. Geerdink, “Magnetisation as a key parameter of magnetic flux leakage pigs for pipeline inspection,” in NDT, Insight, Sep. 1994, p. pp.672-677.

[158] H. A. Leupold and E. I. Potenziani, “A Permanent Magnet Circuit Design Primer,” Jun. 1996.

[159] ASME, “PIPELINE TRANSPORTATION SYSTEMS FOR LIQUIDS AND SLURRIES B31.4 - 2019.” Accessed: Jan. 31, 2022. [Online]. Available: https://www.asme.org/codes-standards/find-codes-standards/b31-4-pipeline-transportation-systems-liquids-slurries

[160] J. Tang, R. Wang, B. Liu, and Y. Kang, “A novel magnetic flux leakage method based on the ferromagnetic lift-off layer with through groove,” Sens Actuators A Phys, vol. 332, Dec. 2021, doi: 10.1016/j.sna.2021.113091.

[161] F. Louis Valentine, “Effect of debris-induced lift-off on magnetic flux leakage inspection results,” West Virginia University, 2000. Accessed: Jan. 31, 2022. [Online]. Available: https://researchrepository.wvu.edu/etd/1035

[162] T. Verleun, “CLEANING OF OIL & GAS PIPELINES ON-LINE & OFF-LINE,” 2003.

[163] L. Yang, G. Zhang, G. Liu, and S. Gao, “Effect of Lift-off on Pipeline Magnetic Flux Leakage Inspection,” in 17th World Conference on Nondestructive Testing, Shanghai, China, 2008, pp. 25–28.

[164] T. Azizzadeh and M. S. Safizadeh, “Investigation of the lift-off effect on the corrosion detection sensitivity of three-axis MFL technique,” Journal of Magnetics, vol. 23, no. 2, pp. 152–159, 2018, doi: 10.4283/JMAG.2018.23.2.152.

[165] X. Wang, X. Wu, J. Xu, and H. Ba, “Study on the lift-off effect on MFL signals with magnetic circuit model and 3D FEM,” Insight: Non-Destructive Testing and Condition Monitoring, vol. 54, no. 9, pp. 505–510, 2012, doi: 10.1784/insi.2012.54.9.505.

[166] K. Reber and A. Belanger, “Reliability of Flaw Size Calculation based on Magnetic Flux Leakage Inspection of Pipelines,” in ECNDT, Feb. 2006.

[167] V. Suresh and A. Abudhair, “Dipole model to predict the rectangular defect on ferromagnetic pipe,” Journal of Magnetics, vol. 21, no. 3, pp. 437–441, 2016, doi: 10.4283/JMAG.2016.21.3.437.

[168] N. R. Pearson, M. A. Boat, R. H. Priewald, M. J. Pate, and J. S. D. Mason, “A study of MFL signals from a spectrum of defect geometries,” in 18th World Conference on Nondestructive Testing, Durban, South Africa, May 2012. [Online]. Available: http://www.ndt.net/?id=12649

[169] H. M. Kim and G. S. Park, “A study on the estimation of the shapes of axially oriented cracks in CMFL Type NDT system,” IEEE Trans Magn, vol. 50, no. 2, pp. 109–112, 2014, doi: 10.1109/TMAG.2013.2283343.

[170] S. Saha, S. Mukhopadhyay, U. Mahapatra, S. Bhattacharya, and G. P. Srivastava, “Empirical structure for characterizing metal loss defects from radial magnetic flux leakage signal,” NDT and E International, vol. 43, no. 6, pp. 507–512, Sep. 2010, doi: 10.1016/j.ndteint.2010.05.006.

[171] M. A. Siebert and J. E. Sutherland, “Application of the circumferential component of magnetic flux leakage measurement for in-line inspection,” in NACE International Conference, 1999.

[172] L. Xiucheng, W. Yujue, W. Bin, G. Zhen, and H. Cunfu, “Design of Tunnel Magnetoresistive-Based Circular MFL Sensor Array for the Detection of Flaws in Steel Wire Rope,” J Sens, vol. 2016, 2016, doi: 10.1155/2016/6198065.

[173] Y. Wang et al., “Rail Magnetic Flux Leakage Detection and Data Analysis Based on Double-Track Flaw Detection Vehicle,” Processes, vol. 11, no. 4, Apr. 2023, doi: 10.3390/pr11041024.

[174] H. M. Kim, D. W. Jeong, S. H. Im, J. H. Park, J. S. Lee, and G. Soo Park, “A Study on the Estimation of Defect Depth in MFL type NDT System,” in 20th International Conference on the Computation of Electromagnetic Fields, 2015, pp. 6–8.

[175] H. Zuoying, Q. Peiwen, and C. Liang, “3D FEM analysis in magnetic flux leakage method,” NDT and E International, vol. 39, no. 1, pp. 61–66, Jan. 2006, doi: 10.1016/j.ndteint.2005.06.006.

[176] D. L. Atherton and M. G. Daly, “Finite element calculation of magnetic flux leakage detector signals,” NDT International, vol. 20, Aug. 1987.

[177] J. Qi, “Experimental Study of Interference Factors and Simulation on Oil-Gas Pipeline Magnetic Flux Leakage Density Signal,” in International Conference on Mechatronics and Automation, IEEE Xplore, Aug. 2007.

[178] P. Karuppasamy, A. Abudhahir, M. Prabhakaran, S. Thirunavukkarasu, B. P. C. Rao, and T. Jayakumar, “Model-Based Optimization of MFL Testing of Ferromagnetic Steam Generator Tubes,” J Nondestr Eval, vol. 35, no. 1, pp. 1–9, Mar. 2016, doi: 10.1007/s10921-015-0320-x.

[179] Q. Jiang, Q. Sui, Q. Lu, P. Zachariades, and J. Wang, “Detection and Estimation of Oil-gas Pipeline Corrosion Defects,” in Eighteenth International conference on System Engineering (ICSE2006), 2006, pp. 173–177.

[180] D. H. Saunderson, “THE MFE TANK-FLOOR SCANNER-A CASE HISTORY,” IEEE Xplore, 1983.

[181] P. C. Charlton, “A Theoretical and Experimental Study of the Magnetic Flux Leakage Method for the Analysis of Corrosion Defects in Carbon Steel Plate,” University of the West of England, Bristol, 1995.

[182] H. Aldosari, R. Elfouly, and R. Ammar, “Evaluation of Machine Learning-Based Regression Techniques for Prediction of Oil and Gas Pipelines Defect,” in Proceedings - 2020 International Conference on Computational Science and Computational Intelligence, CSCI 2020, Institute of Electrical and Electronics Engineers Inc., Dec. 2020, pp. 1452–1456. doi: 10.1109/CSCI51800.2020.00271.

[183] M. Shi, M. Ni, L. Qin, Y. Liang, and Z. Huang, “Quantification method of tubing defects based on machine learning algorithm and magnetic flux leakage signals,” Review of Scientific Instruments, vol. 94, no. 1, Jan. 2023, doi: 10.1063/5.0122436.

[184] A. David Trevino Garcia, “Modeling and Interpretation of Magnetic Flux Leakage,” Rice University, 2012.

[185] P. Chen et al., “A cascaded deep learning approach for detecting pipeline defects via pretrained YOLOv5 and ViT models based on MFL data,” Mech Syst Signal Process, vol. 206, Jan. 2024, doi: 10.1016/j.ymssp.2023.110919.

[186] N. Afandi Sharif, R. Ramli, M. Zaki Nuawi, M. Soleimani Amiri, A. Zawawi Mohamed, and K. Ahmad, “MAGNETIC FLUX LEAKAGE (MFL) DEFECT CHARACTERIZATION USING I-KAZ STATISTICAL ANALYSIS FOR NON-DESTRUCTIVE TEST (NDT) APPLICATION,” Journal of Engineering Science and Technology, vol. 16, no. 4, pp. 3015–3024, 2021.

[187] M. Layouni, M. S. Hamdi, and S. Tahar, “Detection and sizing of metal-loss defects in oil and gas pipelines using pattern-adapted wavelets and machine learning,” Applied Soft Computing Journal, vol. 52, pp. 247–261, Mar. 2017, doi: 10.1016/j.asoc.2016.10.040.

[188] M. Boat, N. Pearson, R. Lieb, J. Davies, R. James, and B. Woodhead, “Factors that affect the defect sizing capabilities of the Magnetic Flux Leakage Technique.”

[189] Z. Usarek, M. Chmielewski, and L. Piotrowski, “A Comparative Study on Methods of Distinction Between Near- and Far-Side Defects as Techniques Used Alongside with the Magnetic Flux Leakage Testing,” J Nondestr Eval, vol. 41, no. 1, Mar. 2022, doi: 10.1007/s10921-022-00844-7.

[190] J. Wu, W. Wu, E. Li, and Y. Kang, “Magnetic Flux Leakage Course of Inner Defects and Its Detectable Depth,” Chinese Journal of Mechanical Engineering (English Edition), vol. 34, no. 1, Dec. 2021, doi: 10.1186/s10033-021-00579-y.

[191] N. Pearson, “Discrimination of top and bottom discontinuities with MFL and the Surface Topology Air-gap Reluctance System (STARS),” Nondestructive Testing Australia, 2012.

[192] N. Pearson and M. Boat, “A novel approach to discriminate top and bottom discontinuities with the Floormap3D.” [Online]. Available: https://www.ndt.net/?id=13924

[193] A. Romero Ramírez, J. S. D. Mason, and N. Pearson, “Experimental study to differentiate between top and bottom defects for MFL tank floor inspections,” NDT and E International, vol. 42, no. 1, pp. 16–21, Jan. 2009, doi: 10.1016/j.ndteint.2008.08.005.

[194] J. Wu, Y. Sun, Y. Kang, and Y. Yang, “Theoretical analyses of MFL signal affected by discontinuity orientation and sensor-scanning direction,” IEEE Trans Magn, vol. 51, no. 1, Jan. 2015, doi: 10.1109/TMAG.2014.2350460.

[195] Y. Sun and Y. Kang, “The feasibility of MFL inspection for omni-directional defects under a unidirectional magnetization,” International Journal of Applied Electromagnetics and Mechanics, vol. 33, no. 3–4, pp. 919–925, Jan. 2010, doi: 10.3233/JAE-2010-1202.

[196] K. Song, Y. Kang, Y. Sun, C. Qiu, and J. Su, “MFL testing of omni-directional cracks in steel strip using strong longitudinal magnetization,” International Journal of Applied Electromagnetics and Mechanics, vol. 33, no. 3–4, pp. 1231–1236, Jan. 2010, doi: 10.3233/JAE-2010-1243.

[197] “How It Works: Pipeline Pigging | SLB.” Accessed: Aug. 09, 2024. [Online]. Available: https://www.slb.com/resource-library/article/valve-insights/how-it-works-pipeline-pigging

[198] Q. Ma et al., “Pipeline in-line inspection method, instrumentation and data management,” Jun. 01, 2021, MDPI AG. doi: 10.3390/s21113862.

[199] S. Shailesh and S. Sengar, “A Review of MFL Technique in Inspection of Steel Pipelines,” in International Conference on Quality, Productivity, Reliability, Optimization and Modeling (ICQPROM), IEEE, Jan. 2017, pp. 143–147.

[200] H. Zhu et al., “In-Line Inspection (ILI) Techniques for Subsea Pipelines: State-of-the-Art,” Mar. 01, 2024, Multidisciplinary Digital Publishing Institute (MDPI). doi: 10.3390/jmse12030417.

[201] H. Song et al., “Comparative Analysis of In-line Inspection Equipments and Technologies,” in IOP Conference Series: Materials Science and Engineering, Institute of Physics Publishing, Jul. 2018. doi: 10.1088/1757-899X/382/3/032021.

[202] Greg Palast, “The Pig that Burst the Keystone Pipeline.” Accessed: Jan. 31, 2022. [Online]. Available: https://www.gregpalast.com/pig-burst-keystone-pipeline/

[203] X. Peng, U. Anyaoha, Z. Liu, and K. Tsukada, “Analysis of Magnetic-Flux Leakage (MFL) Data for Pipeline Corrosion Assessment,” IEEE Trans Magn, vol. 56, no. 6, Jun. 2020, doi: 10.1109/TMAG.2020.2981450.

[204] M. Xie and Z. Tian, “A review on pipeline integrity management utilizing in-line inspection data,” Eng Fail Anal, vol. 92, pp. 222–239, Oct. 2018, doi: 10.1016/j.engfailanal.2018.05.010.

[205] S. Sampath, K. L. Chaurasiya, P. Aryan, and B. Bhattacharya, “An innovative approach towards defect detection and localization in gas pipelines using integrated in-line inspection methods,” J Nat Gas Sci Eng, vol. 90, Jun. 2021, doi: 10.1016/j.jngse.2021.103933.

[206] J. Quarini and S. Shire, “A review of fluid-driven pipeline pigs and their applications,” 2007, Professional Engineering Publishing. doi: 10.1243/0954408JPME108.

[207] K. Reber and M. Beller, “IN-LINE INSPECTION OF NEW PIPELINES,” Stutensee, Germany, 2004.

[208] United Kingdom Onshore Pipeline’ Association (UKOPA), “UKOPA Good Practice Guide: In Line Inspection (ILI),” Derbyshire, Mar. 2020. [Online]. Available: www.UKOPA.co.uk

[209] G. Callar and M. Brown, “Technical Policy: In-line Inspection Transmission Pressure Pipelines,” Feb. 2015.

[210] J. Costain, N. R. Pearson, and M. A. Boat, “Capability of modern tank floor scanning with Magnetic Flux Leakage,” in 19th World Conference on Non-Destructive Testing, Bad Nieniszcz, 2016.

[211] MST Scanner, “Alphanetics - Tank Floor Scanner, Mfl Scanner, Api 653, Ndt.” Accessed: Aug. 17, 2024. [Online]. Available: https://mstscanner.com/

[212] “Gulf Pipe line Testing & Inspection.” Accessed: Aug. 17, 2024. [Online]. Available: https://www.gptigroup.com/Mfl-Storage-Tank.html

[213] Eddyfi, “User’s Manual Floormap ® X MFL Array Tank Floor Inspection Solution FloormapX User Manual Version A_07 SIMS GO Software version 1.0R1 SIMS PRO Software version 1.0R1.”

[214] Arora Technologies, “Distribution – Magnetic Flux Leakage.” Accessed: Aug. 28, 2024. [Online]. Available: https://arorandt.com/distribution-magnetic-flux-leakage/

[215] Z. Ou, Z. Han, and D. Du, “Magnetic Flux Leakage Testing for Steel Plate Using Pot-Shaped Excitation Structure,” IEEE Trans Magn, vol. 58, no. 9, Sep. 2022, doi: 10.1109/TMAG.2022.3187341.

[216] Y. Sun, Y. Kang, and C. Qiu, “A permanent magnetic perturbation testing sensor,” Sens Actuators A Phys, vol. 155, no. 2, pp. 226–232, Oct. 2009, doi: 10.1016/j.sna.2009.08.023.

[217] J. A. Stratton, Electromagnetic Theory - A Classic Reissue. John Wiley & Sons, 2007. Accessed: Sep. 02, 2024. [Online]. Available: https://books.google.com/books/about/Electromagnetic_Theory.html?id=zFeWdS2luE4C

[218] Y. Sun and Y. Kang, “A new MFL principle and method based on near-zero background magnetic field,” NDT and E International, vol. 43, no. 4, pp. 348–353, Jun. 2010, doi: 10.1016/j.ndteint.2010.01.005.

[219] J. Wu, H. Fang, X. Huang, H. Xia, Y. Kang, and C. Tang, “An online MFL sensing method for steel pipe based on the magnetic guiding effect,” Sensors (Switzerland), vol. 17, no. 12, Dec. 2017, doi: 10.3390/s17122911.

[220] J. Tang, R. Wang, G. Qiu, Y. Hu, and Y. Kang, “Mechanism of Magnetic Flux Leakage Detection Method Based on the Slotted Ferromagnetic Lift-Off Layer,” Sensors, vol. 22, no. 9, May 2022, doi: 10.3390/s22093587.

[221] G. S. Park and S. H. Park, “Analysis of the velocity-induced eddy current in MFL type NDT,” IEEE Trans Magn, vol. 40, no. 2 II, pp. 663–666, 2004, doi: 10.1109/TMAG.2004.824717.

[222] Masteel, “4 Different Types of Construction Steel.” Accessed: Oct. 08, 2024. [Online]. Available: https://masteel.co.uk/news/4-different-types-construction-steel/

[223] I. Hajro and D. Hodzic, “Basic Comparison of selected structural steel strength influence on total welding fabrication costs of oil storage tanks,” in 12th International Research/Expert Conference “‘Trends in the Development of Machinery and Associated Technology’” TMT 2008, Istanbul, Turkey, Aug. 2008.

[224] The Piping Mart, “S275 Grade Steel - Composition, Properties, and Uses.” Accessed: Oct. 08, 2024. [Online]. Available: https://blog.thepipingmart.com/grades/s275-grade-steel-composition-properties-and-uses/

[225] H. I. Ünal, H. Atapek, B. G. Beleli, S. Polat, S. Gümüs, and E. Erisir, “Characterization of the fracture behaviour of X42 microalloyed pipeline steel,” International Journal of Structural Integrity, vol. 6, no. 5, pp. 567–577, Oct. 2015, doi: 10.1108/IJSI-09-2013-0020/FULL/XML.

[226] S. M. Beden, “Reliability of the Installation and Operation of pipeline system,” Basrah Journal for Engineering Science, vol. 16, no 2, vol. 16, 2016.

[227] Precise Pipepedia, “API 5L X42 Pipe: Specifications - Precise.” Accessed: Oct. 08, 2024. [Online]. Available: https://precisepipe.com/api-5l-x42-pipe-specifications/

[228] Union Victory, “What is API 5L X42 Material? - Knowledge.” Accessed: Oct. 08, 2024. [Online]. Available: https://www.vicsteelpipe.com/info/what-is-api-5l-x42-material-97445196.html

[229] A. Cahyono, A. Irawan, and B. Munir, “A failure analysis study on the flange of submersible vertical pump ASTM A234 operated in offshore platform,” AIP Conf Proc, vol. 2338, no. 1, Nov. 2021, doi: 10.1063/5.0066655/1027291.

[230] America Piping Products, “A234 fitting specifications | American Piping Products.” Accessed: Oct. 09, 2024. [Online]. Available: https://amerpipe.com/products/fittings-and-flanges/a234-fitting-specifications/

[231] R. Zahedi and A. Babaee Rad, “Numerical and experimental simulation of gas-liquid two-phase flow in 90-degree elbow,” Alexandria Engineering Journal, vol. 61, no. 3, pp. 2536–2550, Mar. 2022, doi: 10.1016/j.aej.2021.07.011.

[232] Y. Li, X. Wang, S. Yuan, and S. K. Tan, “Flow development in curved rectangular ducts with continuously varying curvature,” Exp Therm Fluid Sci, vol. 75, pp. 1–15, Jul. 2016, doi: 10.1016/j.expthermflusci.2016.01.012.

[233] BS EN 60404-04:1997 +A2:2008, “Methods of measurement of D.C. magnetic properties of magnetically soft materials.”

[234] P. Anderson, “A universal DC characterisation system for hard and soft magnetic materials,” J Magn Magn Mater, vol. 320, no. 20, Oct. 2008, doi: 10.1016/j.jmmm.2008.04.034.

[235] N. Zatsepin and V. Shcherbinin, Calculation of the magneto-static field of surface defects. I. Field topology of defect models. Defektoskopiya, vol. 5. Defektoskopiya, 1996.

[236] Z. Huang and P. Que, “Three modeling methods in MFL testing,” in 17th World Conference on Nondestructive Testing, Shanghai, China, Oct. 2008. [Online]. Available: https://www.ndt.net/?id=6578

[237] S. M. Dutta, F. H. Ghorbel, and R. K. Stanley, “Dipole modeling of magnetic flux leakage,” IEEE Trans Magn, vol. 45, no. 4, pp. 1959–1965, Apr. 2009, doi: 10.1109/TMAG.2008.2011895.

[238] F. Forster, “New findings in the field of non-destructive magnetic leakage field inspection,” NDT International, Elsevier, vol. vol 19 No 1., Feb. 1986.

[239] C. Edwards and S. B. Palmer, “The magnetic leakage field of surface-breaking cracks,” Journal of Physics D: Applied Physics J. Phys. D: Appl. Phys, vol. 19, pp. 657–673, 1986.

[240] K. F. Bainton, “Characterizing defects by determining magnetic leakage fields,” NDT International, Elsevier, vol. Vol. 10, Issue 5, pp. 253–257, Oct. 1977.

[241] Y. Li, J. Wilson, and G. Y. Tian, “Experiment and simulation study of 3D magnetic field sensing for magnetic flux leakage defect characterisation,” NDT and E International, vol. 40, no. 2, pp. 179–184, Mar. 2007, doi: 10.1016/j.ndteint.2006.08.002.

[242] X. Li and L. Chen, “FEA of Pipeline Magneti Flux Leakage NDE,” in International Conference on Applied Superconductivity and Electromagnetic Devices, Chengdu,

China: IEEE International Conference on Applied Superconductivity and Electromagnetic Devices, Sep. 2009, p. 406.

[243] D. A. G. Trevino, S. M. Dutta, F. H. Ghorbel, and M. Karkoub, “An Improved Dipole Model of 3-D Magnetic Flux Leakage,” IEEE Trans Magn, vol. 52, no. 12, pp. 1–7, Dec. 2016, doi: 10.1109/TMAG.2015.2475429.

[244] D. Minkov, Y. Takeda, T. Shoji, and J. Lee, “Estimating the sizes of surface cracks based on Hall element measurements of the leakage magnetic field and a dipole model of a crack,” Appl Phys A Mater Sci Process, vol. 74, no. 2, pp. 169–176, Feb. 2002, doi: 10.1007/s003390100899.

[245] Z. Wu, Y. Deng, and L. Wang, “A Pinning Actor-Critic Structure-Based Algorithm for Sizing Complex-Shaped Depth Profiles in MFL Inspection with High Degree of Freedom,” Complexity, vol. 2021, 2021, doi: 10.1155/2021/9995033.

[246] C. A. Felippa, INTRODUCTION to FINITE ELEMENT METHODS. Boulder, Colorado: University of Colorado, 2004.

[247] W. Lord and J. H. Hwang, “Finite element modelling of magnetic field/defect interactions,” ASTM J.Testing & Evaluation , vol. Volume 3., pp. 21–25, 1975.

[248] Y. Li, G. Y. Tian, and S. Ward, “Numerical simulation on magnetic flux leakage evaluation at high speed,” NDT and E International, vol. 39, no. 5, pp. 367–373, Jul. 2006, doi: 10.1016/j.ndteint.2005.10.006.

[249] COMSOL, “The AC/DC Module User’s Guide,” 2022. Accessed: Oct. 14, 2024. [Online]. Available: http://doc.comsol.com/6.1/doc/com.comsol.help.acdc/ACDCModuleUsersGuide.pdf

[250] J. C. Maxwell, A Treatise on Electricity and Magnetism, vol. 2. London: Clarendon Press google schola, 1873.

[251] COMSOL, “Optimization Module User’s Guide,” 2023. [Online]. Available: www.comsol.com/blogs

[252] COMSOL, “Performing Optimization in COMSOL Multiphysics®.” Accessed: Jun. 18, 2024. [Online]. Available: https://www.comsol.com/support/learning-center/article/Performing-Optimization-in-comsolmph-55751

[253] M. P. Bendsøe and O. Sigmund, Topology Optimization, Theory, Methods, and Applications. 2004. doi: 10.1007/978-3-662-05086-6.

[254] L. M. Cohen, E. J. Rolph, and L. D. Steffey, Statistics, Testing, and Defense Acquisition. National Academies Press, 1998. doi: 10.17226/6037.

[255] Newnes, Hall-Effect Sensors Theory and Applications, Second Edition. Elsevier, 2006.

[256] E. H. Hall, "On a New Action of the Magnet on Electric Currents," 1879. [Online]. Available: https://www.jstor.org/stable/2369245

[257] N. P. K and A. Q. M, "Finite Element Modelling & Experimental Simulation of Magnetic Leakage Flux from Metal Loss Defects in Steel Pipelines," Open access data base www.ndt.new, [Online]. Available: www.ndt.net/?id=15189

[258] E. P. Herbert A. Leupold, A Permanent Magnet Circuit Design. 1996. Accessed: Jan. 31, 2022. [Online]. Available: https://www.amazon.co.uk/Permanent-Magnet-Circuit-Design-Primer/dp/1423579070

[259] DAVANTECH, "What is Reaming: a Precision Machining Operation. - Davantech." Accessed: Jun. 02, 2025. [Online]. Available: https://www.davantech.com/what-is-reaming-a-precision-machining-operation/

[260] HMT, "Spark Erosion | EDM Machining Of Press & Mould Tools UK." Accessed: Jun. 02, 2025. [Online]. Available: https://www.hmtooling.co.uk/toolmaking/spark-erosion-edm/

[261] W. Liu, L. Ren, and G. Tian, "Study on the Impact of Pole Spacing on Magnetic Flux Leakage Detection under Oversaturated Magnetization," Sensors, vol. 24, no. 16, Aug. 2024, doi: 10.3390/s24165195.

[262] Master Magnetics Inc., "How to Separate STRONG Magnets - YouTube." Accessed: Jul. 09, 2024. [Online]. Available: https://www.youtube.com/watch?v=ynhSd2Bskzc

This page intentionally left blank

# APPENDICES

# Appendix A: Chemical Compositions and Susceptibility Ranges of Plate, Pipe and Elbow

**Table A.1**. Composition of plate, pipe and elbow.

| Element (%) | C | Si | Mn | P | S | Cr | Ni | Cu | Al | Mo | Nb |
|---|---|---|---|---|---|---|---|---|---|---|---|
| Plate | 0.06 | 0.01 | 0.62 | 0.015 | 0.008 | 0.09 | 0.09 | 0.25 | 0.025 | 0.017 | 0.02 |
| Pipe | 0.20 | 0.19 | 0.92 | 0.007 | 0.003 | 0.11 | 0.09 | 0.15 | 0.021 | 0.029 | 0.001 |
| Elbow | 0.10 | 0.19 | 1.23 | 0.01 | 0.002 | 0.08 | 0.03 | 0.09 | 0.023 | 0.01 | 0.00 |

| Element (%) | V | Ti | B | N | Sn |
|---|---|---|---|---|---|
| Plate | 0.003 | 0.015 | 0.001 | 0.005 | 0.012 |
| Pipe | 0.013 | 0.001 | 0.0004 | 0.0117 | 0.008 |
| Elbow | 0.00 | 0.00 | 0.0002 | 0.00 | 0.00 |

**Table A.2.** Magnetic susceptibility range calculated using central difference formula for the plate, pipe and elbow.

| Sample | Magnetic susceptibility range |
|---|---|
| Plate | 4.44 to 519 |
| Pipe | 3.15 to 381 |
| Elbow | 3.96 to 577 |

## Appendix B: Parametric Optimisation Results

**Table B.1.** Parametric optimisation results. Where a is an initial value for pole piece height.

| a (mm) | Pole piece height (m) | Bridge length (m) | Bridge height (m) | Magnetic flux density norm (T) |
|---|---|---|---|---|
| 5 | 0.005 | 0.15 | 0.04 | 1.5489 |
| 5 | 0.006 | 0.15 | 0.04 | 1.5501 |
| 5 | 0.005 | 0.154 | 0.04 | 1.5216 |
| 5 | 0.005 | 0.15 | 0.041 | 1.5498 |
| 5 | 0.007 | 0.15 | 0.04 | 1.5447 |
| 5 | 0.005 | 0.146 | 0.04 | 1.5889 |
| 5 | 0.005 | 0.15 | 0.039 | 1.5479 |
| 5 | 0.005093 | 0.14202 | 0.040023 | 1.6265 |
| 5 | 0.005 | 0.13804 | 0.040019 | 1.668 |
| 5 | 0.005 | 0.13081 | 0.03993 | 1.7574 |
| 5 | 0.005071 | 0.13657 | 0.040947 | 1.6881 |
| 5 | 0.005 | 0.13594 | 0.041932 | 1.6969 |
| 5 | 0.005288 | 0.13576 | 0.041837 | 1.6961 |
| 5 | 0.005121 | 0.13576 | 0.04175 | 1.6946 |
| 5 | 0.005 | 0.13508 | 0.04199 | 1.7064 |
| 5 | 0.005099 | 0.13582 | 0.04213 | 1.6962 |
| 5 | 0.005 | 0.13565 | 0.042144 | 1.6937 |
| 5 | 0.005 | 0.13681 | 0.041875 | 1.6786 |
| 5 | 0.005 | 0.13533 | 0.04177 | 1.7045 |
| 5 | 0.005079 | 0.13563 | 0.041939 | 1.6981 |

| | | | | |
|---|---|---|---|---|
| 5 | 0.005032 | 0.13561 | 0.041954 | 1.6986 |
| 5 | 0.005 | 0.13566 | 0.041929 | 1.6992 |
| 5 | 0.005 | 0.13566 | 0.041928 | 1.7 |
| 10 | 0.01 | 0.15 | 0.04 | 1.5388 |
| 10 | 0.011 | 0.15 | 0.04 | 1.5327 |
| 10 | 0.01 | 0.154 | 0.04 | 1.5116 |
| 10 | 0.01 | 0.15 | 0.041 | 1.5421 |
| 10 | 0.009 | 0.15 | 0.04 | 1.5447 |
| 10 | 0.01 | 0.146 | 0.04 | 1.57 |
| 10 | 0.01 | 0.15 | 0.039 | 1.5403 |
| 10 | 0.009745 | 0.14214 | 0.040037 | 1.607 |
| 10 | 0.008862 | 0.135 | 0.040224 | 1.6848 |
| 10 | 0.009969 | 0.12858 | 0.039771 | 1.75 |
| 10 | 0.008571 | 0.13239 | 0.040925 | 1.7146 |
| 10 | 0.008229 | 0.13161 | 0.040006 | 1.727 |
| 10 | 0.009025 | 0.13315 | 0.040837 | 1.7062 |
| 10 | 0.008901 | 0.13329 | 0.040354 | 1.7028 |
| 10 | 0.008957 | 0.1332 | 0.039416 | 1.703 |
| 10 | 0.008923 | 0.13328 | 0.039922 | 1.7035 |
| 10 | 0.008699 | 0.13368 | 0.040355 | 1.6993 |
| 10 | 0.008785 | 0.13345 | 0.040291 | 1.7027 |
| 10 | 0.008745 | 0.13367 | 0.040457 | 1.6976 |
| 10 | 0.008666 | 0.13381 | 0.040371 | 1.6985 |
| 10 | 0.008682 | 0.13365 | 0.040379 | 1.7021 |

| | | | | |
|---|---|---|---|---|
| 10 | 0.008669 | 0.13354 | 0.040333 | 1.6998 |
| 10 | 0.008662 | 0.1336 | 0.040286 | 1.6973 |
| 10 | 0.008669 | 0.13354 | 0.040333 | 1.6998 |
| 15 | 0.015 | 0.15 | 0.04 | 1.5282 |
| 15 | 0.016 | 0.15 | 0.04 | 1.5244 |
| 15 | 0.015 | 0.154 | 0.04 | 1.5009 |
| 15 | 0.015 | 0.15 | 0.041 | 1.529 |
| 15 | 0.014 | 0.15 | 0.04 | 1.528 |
| 15 | 0.015 | 0.146 | 0.04 | 1.5522 |
| 15 | 0.015 | 0.15 | 0.039 | 1.5274 |
| 15 | 0.014904 | 0.14202 | 0.040042 | 1.588 |
| 15 | 0.014228 | 0.13464 | 0.040408 | 1.6599 |
| 15 | 0.015348 | 0.12865 | 0.039699 | 1.7174 |
| 15 | 0.014617 | 0.12759 | 0.040328 | 1.7324 |
| 15 | 0.015098 | 0.12849 | 0.039267 | 1.7193 |
| 15 | 0.015543 | 0.12898 | 0.039625 | 1.713 |
| 15 | 0.015709 | 0.12947 | 0.039709 | 1.7071 |
| 15 | 0.01608 | 0.12966 | 0.039954 | 1.7027 |
| 15 | 0.016176 | 0.13011 | 0.039532 | 1.6966 |
| 15 | 0.016029 | 0.13014 | 0.040134 | 1.6977 |
| 15 | 0.016088 | 0.12998 | 0.040346 | 1.6992 |
| 15 | 0.016107 | 0.13009 | 0.040567 | 1.6973 |
| 15 | 0.016084 | 0.13087 | 0.04033 | 1.6888 |
| 15 | 0.015874 | 0.1298 | 0.040393 | 1.7035 |

| | | | | |
|---|---|---|---|---|
| 15 | 0.016155 | 0.12963 | 0.040321 | 1.7027 |
| 15 | 0.016135 | 0.13005 | 0.040346 | 1.697 |
| 15 | 0.016054 | 0.12984 | 0.040333 | 1.6983 |
| 15 | 0.016088 | 0.12998 | 0.040346 | 1.6992 |
| 20 | 0.02 | 0.15 | 0.04 | 1.5148 |
| 20 | 0.021 | 0.15 | 0.04 | 1.5126 |
| 20 | 0.02 | 0.154 | 0.04 | 1.4906 |
| 20 | 0.02 | 0.15 | 0.041 | 1.5155 |
| 20 | 0.019 | 0.15 | 0.04 | 1.5171 |
| 20 | 0.02 | 0.146 | 0.04 | 1.54 |
| 20 | 0.02 | 0.15 | 0.039 | 1.514 |
| 20 | 0.0199 | 0.14202 | 0.040033 | 1.5694 |
| 20 | 0.019544 | 0.13416 | 0.040149 | 1.6404 |
| 20 | 0.020888 | 0.11919 | 0.039716 | 1.78 |
| 20 | 0.018092 | 0.12898 | 0.04061 | 1.6995 |
| 20 | 0.017811 | 0.12701 | 0.040152 | 1.7214 |
| 20 | 0.018217 | 0.12797 | 0.041023 | 1.7066 |
| 20 | 0.017916 | 0.12912 | 0.040742 | 1.6987 |
| 20 | 0.018142 | 0.12888 | 0.040817 | 1.699 |
| 20 | 0.01805 | 0.12883 | 0.040718 | 1.7019 |
| 20 | 0.018256 | 0.12841 | 0.040557 | 1.7036 |
| 20 | 0.017913 | 0.12938 | 0.040699 | 1.6952 |
| 20 | 0.018055 | 0.12869 | 0.040687 | 1.7011 |
| 20 | 0.018113 | 0.12886 | 0.040644 | 1.7007 |

| | | | | |
|---|---|---|---|---|
| 20 | 0.018128 | 0.12911 | 0.040598 | 1.6972 |
| 20 | 0.018065 | 0.12885 | 0.040582 | 1.7008 |
| 20 | 0.018057 | 0.12894 | 0.040644 | 1.7011 |
| 20 | 0.018111 | 0.12911 | 0.040641 | 1.6991 |
| 20 | 0.018092 | 0.12904 | 0.040657 | 1.699 |
| 20 | 0.018092 | 0.12898 | 0.04061 | 1.6995 |
| 25 | 0.025 | 0.15 | 0.04 | 1.5047 |
| 25 | 0.026 | 0.15 | 0.04 | 1.5017 |
| 25 | 0.025 | 0.154 | 0.04 | 1.4803 |
| 25 | 0.025 | 0.15 | 0.041 | 1.5054 |
| 25 | 0.024 | 0.15 | 0.04 | 1.5068 |
| 25 | 0.025 | 0.146 | 0.04 | 1.5271 |
| 25 | 0.025 | 0.15 | 0.039 | 1.504 |
| 25 | 0.024865 | 0.14204 | 0.040037 | 1.5543 |
| 25 | 0.024068 | 0.13476 | 0.040272 | 1.6123 |
| 25 | 0.024824 | 0.11924 | 0.039658 | 1.7564 |
| 25 | 0.021467 | 0.11799 | 0.041811 | 1.7894 |
| 25 | 0.025398 | 0.12179 | 0.037852 | 1.7292 |
| 25 | 0.026259 | 0.12302 | 0.036073 | 1.7116 |
| 25 | 0.024652 | 0.12379 | 0.034898 | 1.7097 |
| 25 | 0.024165 | 0.12374 | 0.034025 | 1.7126 |
| 25 | 0.023735 | 0.1253 | 0.035025 | 1.7011 |
| 25 | 0.022741 | 0.12496 | 0.034949 | 1.7092 |
| 25 | 0.023619 | 0.12587 | 0.034559 | 1.6959 |

| | | | | |
|---|---|---|---|---|
| 25 | 0.023796 | 0.12597 | 0.03516 | 1.696 |
| 25 | 0.023619 | 0.12554 | 0.035103 | 1.6996 |
| 25 | 0.023768 | 0.12545 | 0.03504 | 1.6989 |
| 25 | 0.023667 | 0.12488 | 0.035247 | 1.7045 |
| 25 | 0.023634 | 0.12553 | 0.035318 | 1.6995 |
| 25 | 0.023696 | 0.12548 | 0.035182 | 1.6991 |
| 25 | 0.023571 | 0.12551 | 0.035094 | 1.7001 |
| 25 | 0.023537 | 0.12558 | 0.035126 | 1.6991 |
| 25 | 0.02357 | 0.12566 | 0.035062 | 1.6984 |
| 25 | 0.02361 | 0.12547 | 0.035123 | 1.7004 |
| 25 | 0.023571 | 0.12551 | 0.035094 | 1.7001 |
| 30 | 0.03 | 0.15 | 0.04 | 1.4944 |
| 30 | 0.029 | 0.15 | 0.04 | 1.4965 |
| 30 | 0.03 | 0.154 | 0.04 | 1.4724 |
| 30 | 0.03 | 0.15 | 0.041 | 1.4951 |
| 30 | 0.028 | 0.15 | 0.04 | 1.4984 |
| 30 | 0.03 | 0.146 | 0.04 | 1.5156 |
| 30 | 0.03 | 0.15 | 0.039 | 1.4937 |
| 30 | 0.029886 | 0.14203 | 0.040036 | 1.542 |
| 30 | 0.029417 | 0.13426 | 0.040134 | 1.6024 |
| 30 | 0.029867 | 0.11837 | 0.040278 | 1.7389 |
| 30 | 0.02613 | 0.11268 | 0.040176 | 1.7986 |
| 30 | 0.029117 | 0.11774 | 0.042125 | 1.7485 |
| 30 | 0.029276 | 0.11797 | 0.039477 | 1.7446 |

| | | | | |
|---|---|---|---|---|
| 30 | 0.029741 | 0.12076 | 0.04107 | 1.7199 |
| 30 | 0.03 | 0.12647 | 0.042449 | 1.6693 |
| 30 | 0.029288 | 0.12291 | 0.041264 | 1.7034 |
| 30 | 0.029367 | 0.12353 | 0.041124 | 1.6968 |
| 30 | 0.029422 | 0.12336 | 0.041247 | 1.6986 |
| 30 | 0.029355 | 0.12299 | 0.041167 | 1.701 |
| 30 | 0.029364 | 0.12341 | 0.041235 | 1.6982 |
| 30 | 0.029186 | 0.12245 | 0.041115 | 1.7061 |
| 30 | 0.02939 | 0.1232 | 0.041184 | 1.6997 |
| 30 | 0.029382 | 0.12303 | 0.041212 | 1.7013 |
| 30 | 0.029415 | 0.12302 | 0.041176 | 1.7018 |
| 30 | 0.029383 | 0.12321 | 0.041192 | 1.7003 |

a is the initial value for pole piece height.

## Appendix C: Drawing of the Hinge Design 1 Female Part

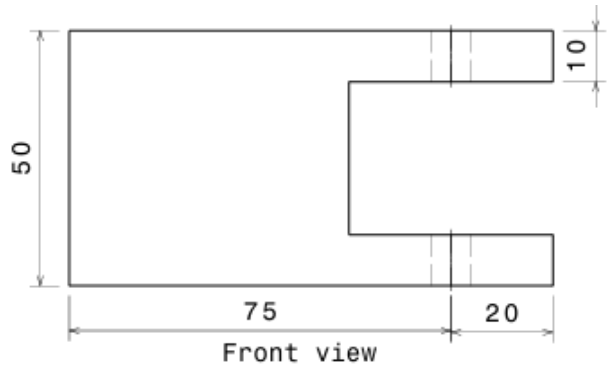


Front view
Scale: 1:1

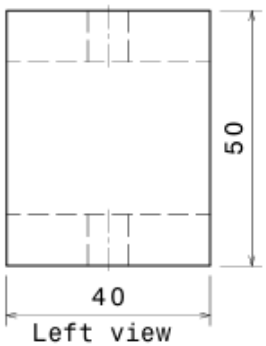


Left view
Scale: 1:1

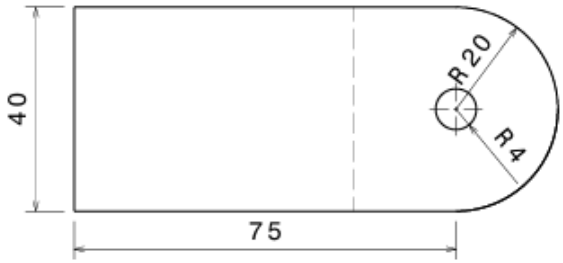


Top view
Scale: 1:1

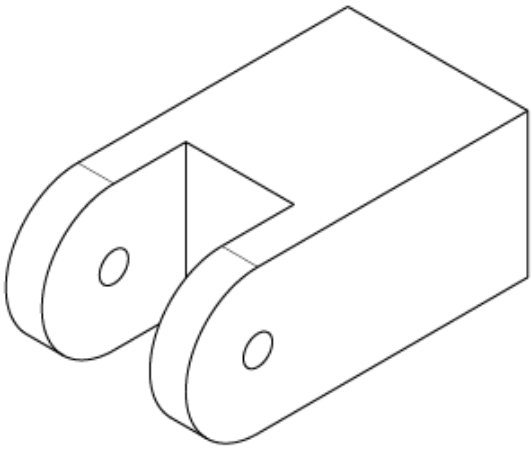

Isometric view
Scale: 1:1

## Appendix D: Drawing of the Hinge Design 1 Male Part


Front view
Scale: 1:1

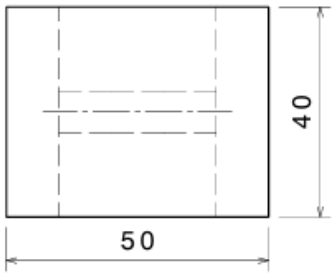


Left view
Scale: 1:1

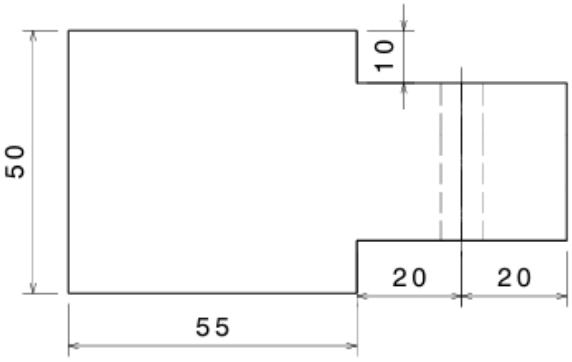


Top view
Scale: 1:1

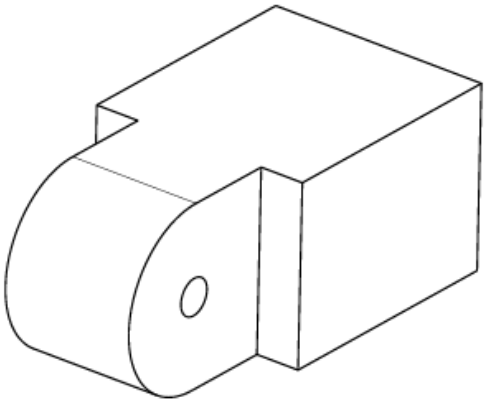

Isometric view
Scale: 1:1

## Appendix E: Drawing of the Hinge Design 2 Female Part

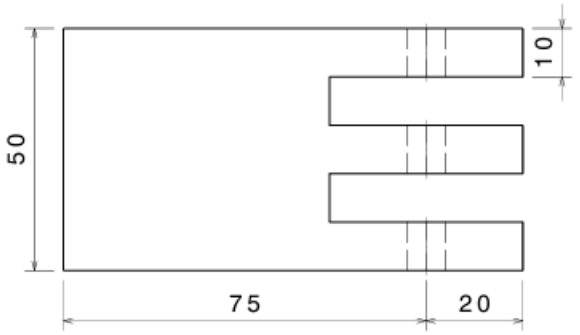


Front view
Scale: 1:1

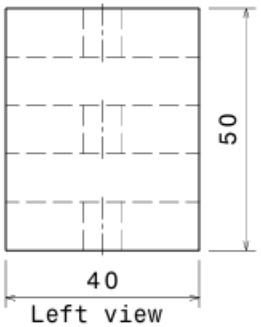


Left view
Scale: 1:1

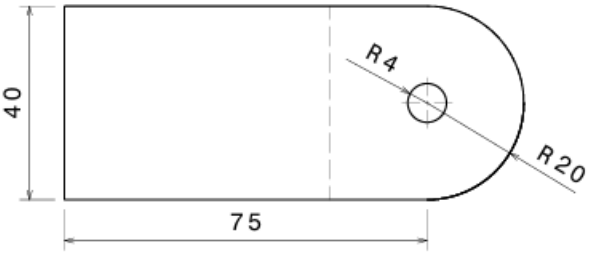


Top view
Scale: 1:1

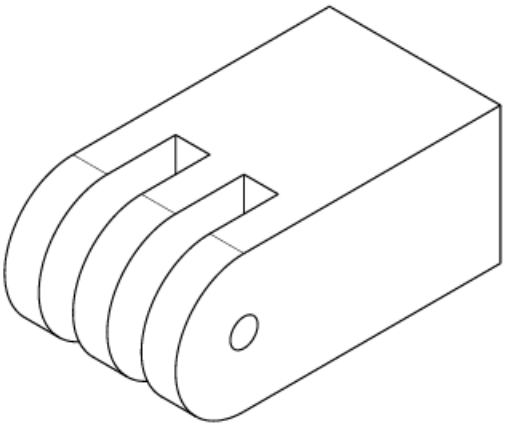

Isometric view
Scale: 1:1

## Appendix F: Drawing of the Hinge Design 2 Male Part

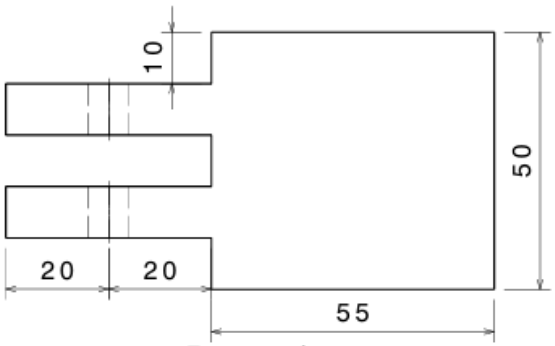


Front view
Scale: 1:1

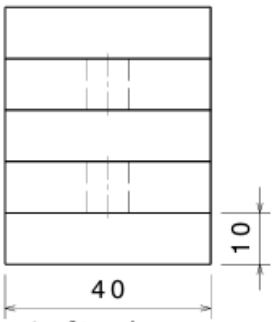


Left view
Scale: 1:1

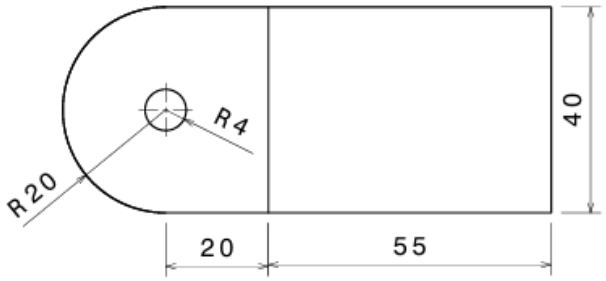


Top view
Scale: 1:1

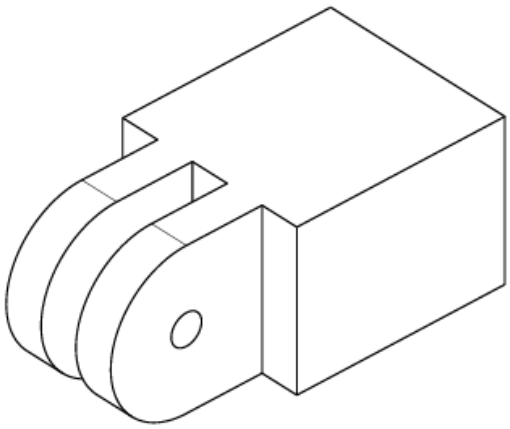

Isometric view
Scale: 1:1

## Appendix G: Drawing of the Hinge Design 3 Female Part

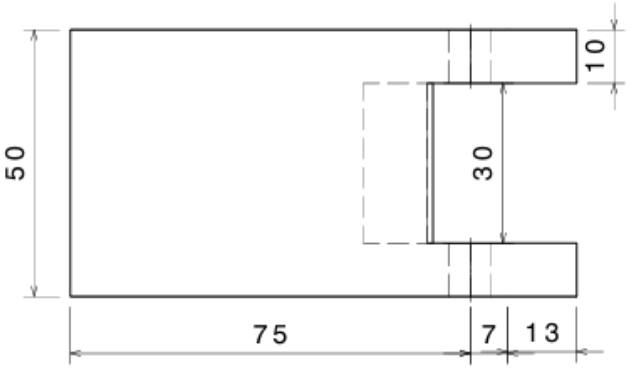


Front view
Scale: 1:1

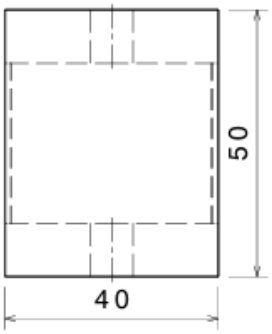


Left view
Scale: 1:1

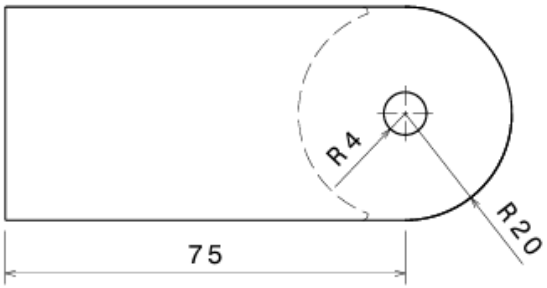


Top view
Scale: 1:1

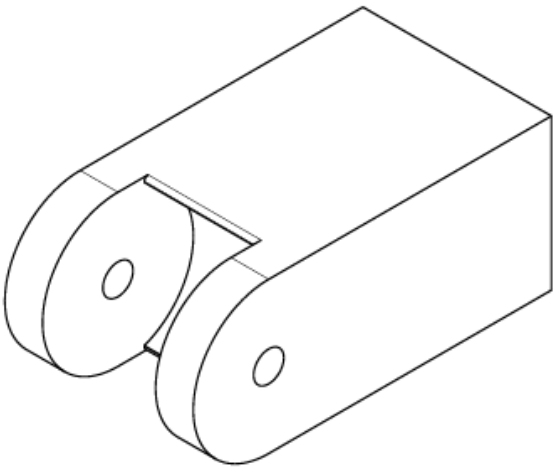

Isometric view
Scale: 1:1

## Appendix H: Drawing of the Hinge Design 3 Male Part

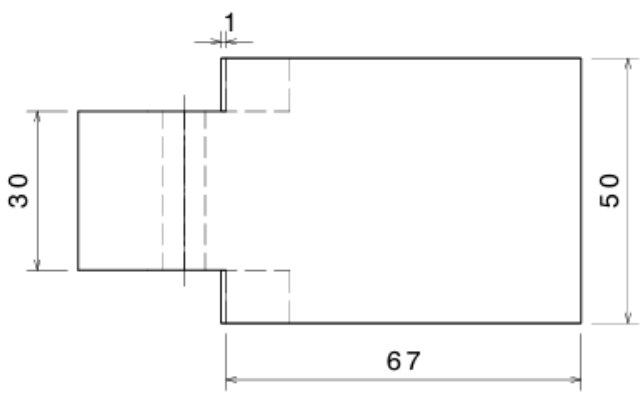


Front view
Scale: 1:1

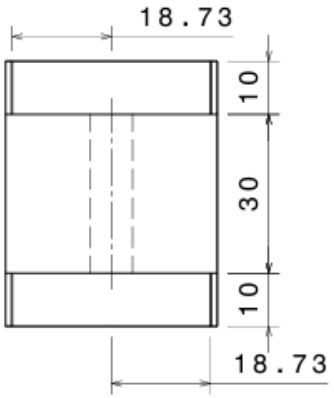


Left view
Scale: 1:1

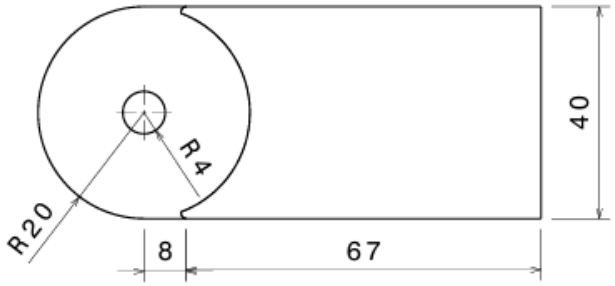


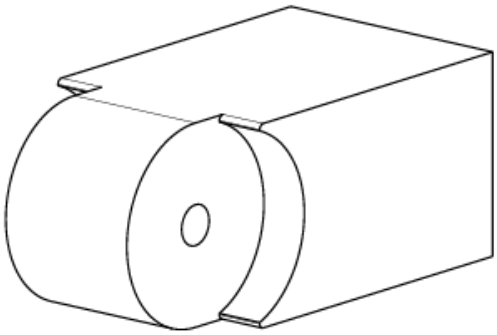

## Appendix I: Drawing of the Hinge Design 4 Female Part

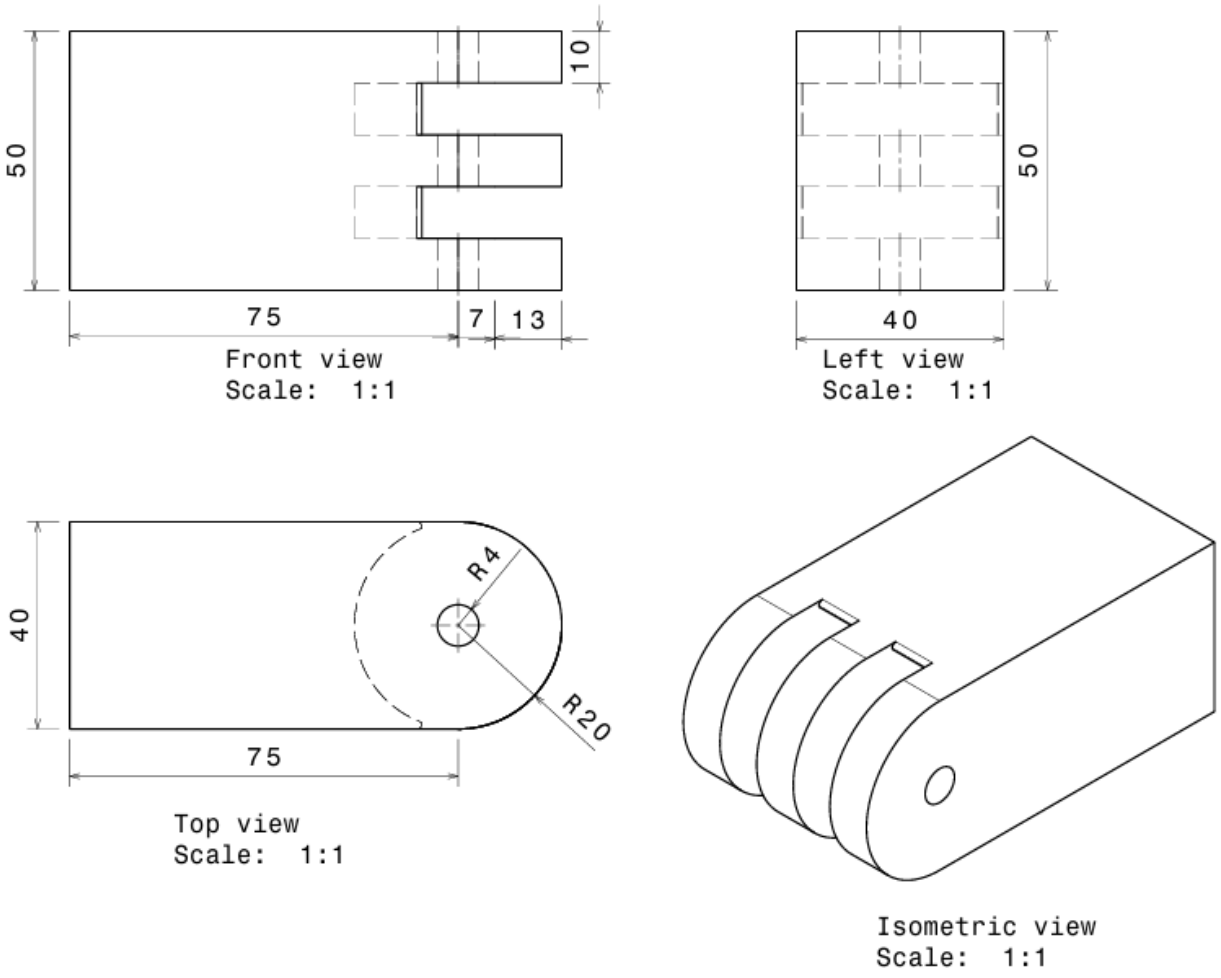

## Appendix J: Drawing of the Hinge Design 4 Male Part

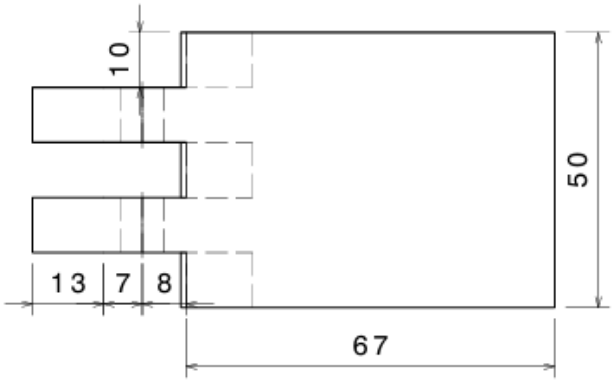


Front view
Scale: 1:1

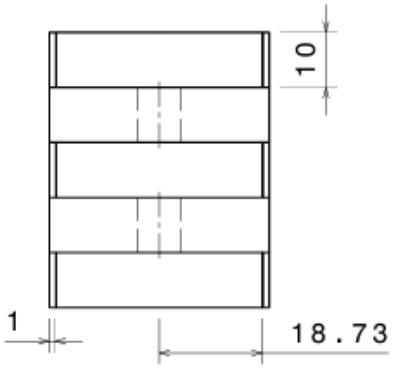


Left view
Scale: 1:1

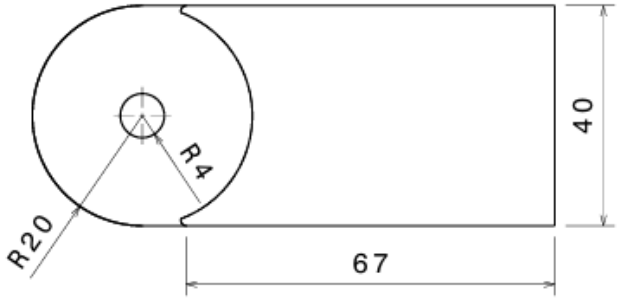


Top view
Scale: 1:1

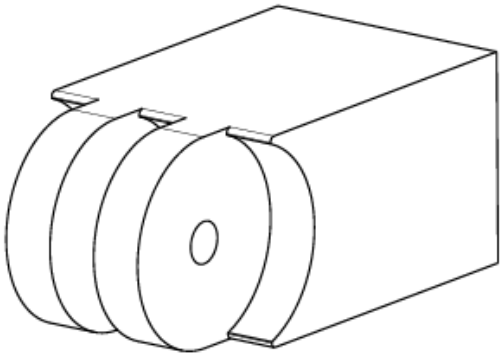

Isometric view
Scale: 1:1

## Appendix K: Drawing of the Optimised Design Female Part

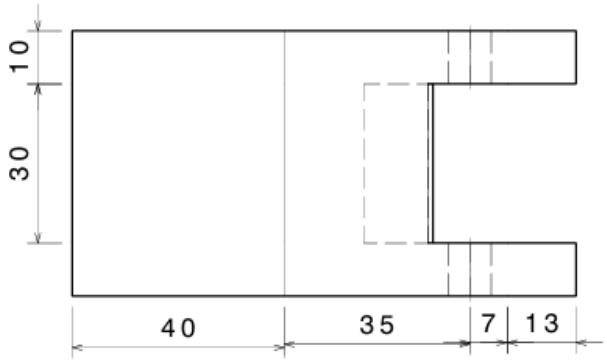


Front view
Scale: 1:1

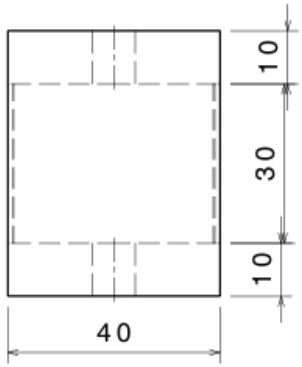


Left view
Scale: 1:1

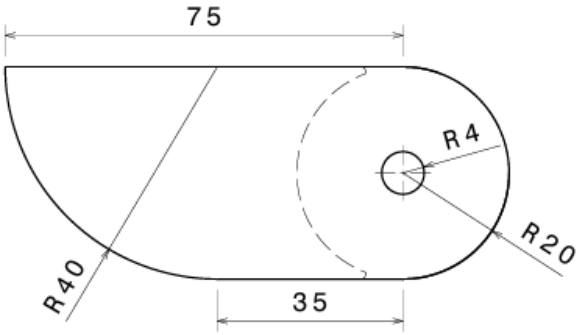


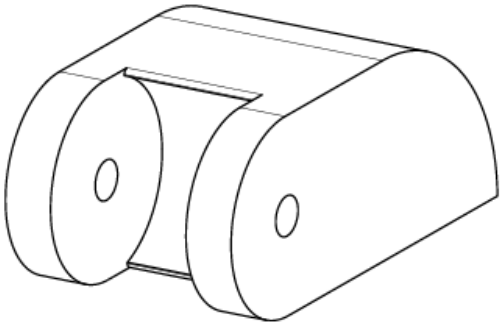

## Appendix L: Drawing of the Optimised Design Male Part

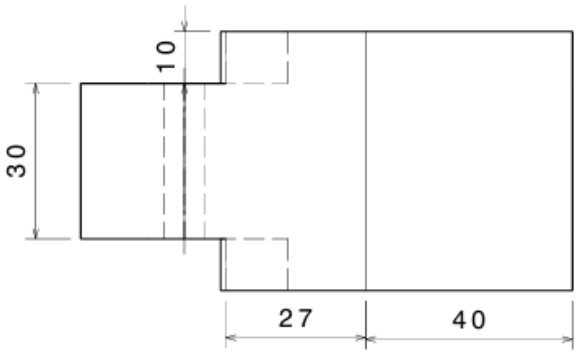


Front view
Scale: 1:1

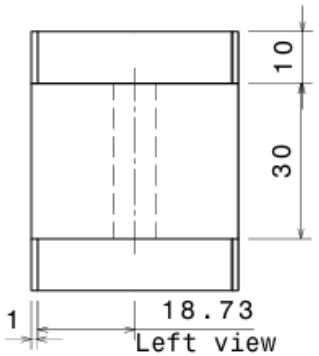


Left view
Scale: 1:1

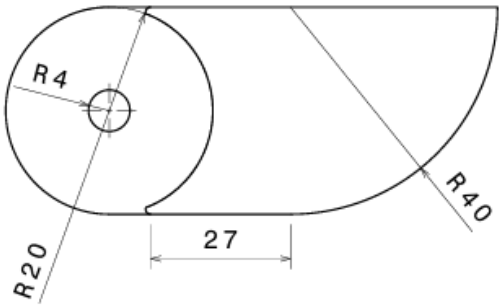


Top view
Scale: 1:1

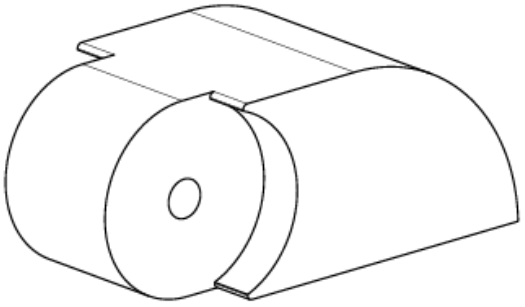

Isometric view
Scale: 1:1

# Appendix M: Target and Measured Cylindrical Defect Dimensions

**Table M.1**. Target and measured cylindrical defect dimensions, including uncertainties.

| Component | Target depth (mm) | Measured depth with uncertainty (mm) | Target radius (mm) | Measured radius with uncertainty (mm) |
|---|---|---|---|---|
| Plate | 6.28 | 6.25 ± 0.02 | 5.00 | 5.02 ± 0.01 |
| Plate | 4.71 | 4.69 ± 0.03 | 5.00 | 5.00 ± 0.01 |
| Plate | 3.14 | 3.18 ± 0.02 | 5.00 | 5.01 ± 0.02 |
| Plate | 1.57 | 1.55 ± 0.03 | 5.00 | 5.02 ± 0.01 |
| Pipe | 5.69 | 5.66 ± 0.02 | 5.00 | 5.00 ± 0.01 |
| Pipe | 4.27 | 4.26 ± 0.01 | 5.00 | 5.00 ± 0.01 |
| Pipe | 2.84 | 2.81 ± 0.02 | 5.00 | 5.01 ± 0.01 |
| Pipe | 1.42 | 1.43 ± 0.01 | 5.00 | 5.00 ± 0.01 |
| Plate | 6.28 | 6.26 ± 0.02 | 11.00 | 11.02 ± 0.01 |
| Plate | 6.28 | 6.27 ± 0.02 | 8.00 | 8.01 ± 0.02 |
| Plate | 6.28 | 6.25 ± 0.02 | 5.00 | 5.00 ± 0.01 |
| Plate | 6.28 | 6.29 ± 0.02 | 2.00 | 2.01 ± 0.01 |

## Appendix N: Safe Handling and Installation Techniques for N52 Magnet

Magnet shear force, the force required to slide magnets, is around five times weaker than the pull force [262]. Therefore, a sliding technique was adopted to install and remove the magnetic circuit using wooden wedges of different shapes and a mallet.

The wedge was carefully inserted between the circuit and the inspection surface, and the mallet was used to gently tap the circuit from the wedge to the inspection component. When removing/installing the circuit from/to the inspection component, the edge technique was used by sliding the circuit towards the edge of a table and removing the circuit/installing (for curved surfaces). These methods allowed for controlled and safe installation and removal of the circuits, reducing the likelihood of injuries.